

Politecnico di Torino

ScuDo
Scuola di Dottorato ~ Doctoral School
WHAT YOU ARE, TAKES YOU FAR

Doctoral Dissertation
Doctoral Program in Electrical, Electronics and Communications Engineering (37^{th}cycle)

Multi-Defect Localization and Evaluation Techniques for Distribution Cables Based on Time-Domain Reflectometry

By

Kun Zhao

******

Supervisor(s):
Prof. Stefano Grivet-Talocia and Prof. Hongjie Li, Supervisor
Prof. Paolo Manfredi, Co-Supervisor

Doctoral Examination Committee:
Prof. Shengchang Ji, Referee, Xi'an Jiaotong University
Prof. Yanzhao Xie, Referee, Xi'an Jiaotong University
Prof. Haibao Mu, Referee, Xi'an Jiaotong University
Prof. Lei Pang, Referee, Xi'an Jiaotong University
Prof. Wanzhao Cui, Referee, China Academy of Space Technology
Prof. Jiandong Duan, Referee, Xi'an University of Technology
Prof. Carlo Stefano Ragusa, Referee, Politecnico di Torino

Politecnico di Torino
2025

Declaration

I hereby declare that, the contents and organization of this dissertation constitute my own original work and does not compromise in any way the rights of third parties, including those relating to the security of personal data.

Kun Zhao
2025

* This dissertation is presented in partial fulfillment of the requirements for **Ph.D. degree** in the Graduate School of Politecnico di Torino (ScuDo).

I would like to dedicate this thesis to my loving family

Acknowledgements

First and foremost, I would like to express my deepest gratitude to my supervisor, Professor Hongjie Li, for his continuous support, insightful guidance, and patient encouragement throughout the course of my doctoral research. His professionalism and dedication have been a constant source of inspiration to me.

I am also sincerely thankful to my international supervisors, Professor Stefano Grivet-Talocia and Professor Paolo Manfredi, for their invaluable academic guidance and generous support during my stay at Politecnico di Torino. Their expertise and mentorship have significantly contributed to the depth and quality of my research.

I would like to thank the reviewers for their constructive feedback and valuable suggestions, which helped improve the quality of this dissertation.

My heartfelt thanks go to my colleagues for their insightful discussions and support. I am also grateful to my friends including Song Huang, Zhaoyu Zhang, Stefano Schubert and so on who have accompanied me throughout this journey.

I sincerely thank the China Scholarship Council for funding my study at Politecnico di Torino, and Zhuhai Power Supply Bureau, Guangdong Power Grid Co., Ltd., for supporting my research.

I am deeply grateful to my family for their unconditional love and support, especially to my fiancée, Li Man, for her patience and encouragement.

Lastly, I would like to thank Xi'an Jiaotong University and Politecnico di Torino for providing an excellent academic environment.

This dissertation would not have been possible without all of your support. Thank you.

Abstract

Power distribution cables are essential components of power distribution systems, responsible for delivering electric energy to support social production and daily life, and playing a foundational role in economic development and societal operation. However, during manufacturing, installation, and operation, cables are often subject to various forms of damage, such as mechanical stress, corrosion, and water ingress, which may lead to defects. These defects can cause failures that seriously threaten power supply security and the stable operation of the power system. Therefore, the development of efficient and reliable methods for defect detection and localization in power cables is of great practical significance. Time Domain Reflectometry (TDR) is widely used for detecting and localizing cable defects. By injecting a pulse signal into the cable and analyzing the reflected signal, TDR enables the detection and localization of defects. However, due to limited understanding of defect-related signal propagation characteristics, the lack of advanced signal processing techniques, and performance limitations of detection equipment, traditional TDR methods struggle to accurately detect, localize, and evaluate defects under conditions such as signal distortion and multiple reflections. These limitations restrict the practical effectiveness of TDR and pose challenges to cable operation and maintenance. To address these issues, this dissertation focuses on several key challenges in cable defect detection and proposes comprehensive research solutions covering modeling, defect localization, severity assessment, and system implementation.

To address the limitation that current cable defect reflection signal modeling mainly focuses on single-defect modeling, a general multiple-defect cable reflection signal modeling and simulation method was proposed, which achieved accurate modeling and simulation of reflection signals in multiple-defect and multiple-joint cables. Based on the frequency-dependent distributed parameter model of the cable body, a transmission line model was established to accurately represent the propagation characteristics. Furthermore, for different types of defects, equivalent circuit models and S-parameter models were established using equivalent circuit methods and finite element methods, respectively. By combining these models, the reflection coefficient spectrum of multiple-defect cables was constructed, from which the time-domain reflection signals were obtained. The modeling results demonstrated a quantitative relationship between defect type, severity, and propagation characteristics, providing an important basis

for defect type discrimination and severity assessment. This research provides a theoretical foundation for subsequent analysis of defect reflection signals under complex conditions.

To address the problem of interference in defect detection and localization caused by multiple reflections under multi-defect conditions, a pulse reconstruction-based method for multi-defect detection and localization was developed. This method effectively suppressed the interference of multiple reflections and achieved accurate detection and localization of defects in multi-defect environments. First, the TDR-based estimation method for the cable's characteristic impedance and propagation constants was improved to enable precise evaluation of cable parameters. Then, using the estimated cable parameters, a defect detection and localization algorithm based on time-varying matched filtering was proposed, which effectively suppresses the influence of cable attenuation, dispersion, and environmental noise on localization accuracy. Finally, by combining the evaluation results with the reflection coefficient spectrum, a pulse-reconstruction-based framework for multi-defect detection and localization was developed to accurately identify and locate multiple defect reflections. Simulation and experimental results demonstrated that, compared to existing methods, the proposed approach could accurately determine the number of multiple defects and exhibited superior localization accuracy and robustness.

To address the problem that defect severity cannot be accurately and quantitatively evaluated in TDR measurements, an evaluation method based on double-frequency Time-Frequency Domain Reflectometry (TFDR) was proposed. The method quantitatively evaluates defect severity by estimating the characteristic impedance and physical size of defects. First, a chirp signal was employed as the excitation source to enhance the sensitivity of the measurement to variations in defect severity. Then, the influence of defect parameters—such as characteristic impedance and physical size—on the reflected signal and localization results was analyzed. Based on this, a double-frequency dual-injection measurement strategy was designed to enable independent estimation of characteristic impedance and physical size, thereby enabling quantitative evaluation of defect severity. Simulation and experimental results demonstrated that the proposed double-frequency TFDR method is accurate and robust, enabling accurate estimation of the characteristic impedance of defects and the physical size of short defects with lengths ranging from about ten centimeters to several meters.

To address the problem of weak reflected signals and limited detection distance in multiple-defect cable TDR measurements, a TDR system with high-voltage (HV) pulse injection and fast range switching was developed. By combining HV pulse injection with fast range switching multi-ratio signal measurement, the system significantly enhanced the strength of the reflected signal and the signal-to-noise ratio (SNR), and extended the detectable range in multiple-defect cables. Specifically, an HV pulse generator based on a series-stacked MOSFET architecture was designed, capable of generating HV pulses with adjustable amplitudes from 0 to 4.93 kV and pulse width from 200 ns to 1 μs, to meet the testing requirements of different cables. In addition,

a fast range switching voltage divider with 4 different ratios was developed, which can rapidly change the division ratio during signal acquisition, thereby expanding the dynamic range of the TDR system. Based on these modules, a complete TDR system for multiple-defect cable detection and localization was constructed. Experimental results demonstrated that the system significantly enhanced the TDR capability for detecting weak and distant defects, exhibiting high practicality and strong engineering applicability.

Contents

List of Figures **xi**

List of Tables **xvii**

1 Introductions **1**

1.1 Research Background and Significance 1

1.2 Current Research Status 2

1.2.1 Current Status of Cable Defect Detection 2

1.2.2 Current Status of Reflection Technology in Cable Defect Detection . 4

1.2.3 Current Status of Defect Localization and Assessment Based on TDR 8

1.3 Main Research Contents 15

2 Modeling of Reflected Signals in Multiple-Defect Cables Based on RCS **17**

2.1 Modeling and Analysis of Cable Defects 17

2.1.1 Principle of Cable Distributed Parameter Model 17

2.1.2 Modeling and Analysis of Cable Joints 19

2.1.3 Modeling and Analysis of Lumped Defects in Cable 23

2.1.4 Modeling and Analysis of Distributed Defects in Cable 24

2.2 Propagation Characteristics Measurement of Cable Defects 34

2.2.1 Fundamentals of S-Parameters Measurement 34

2.2.2 Cable Defect S-Parameter Measurement 36

2.2.3 Analysis of Cable Defect Characteristics Using S-Parameters 38

2.3 Modeling of Reflectometry Signal in Mulitple-Defect Cables 38

2.3.1 Principle of TDFD Method 39
2.3.2 RCS General Model for Multiple-Defect Cables 40
2.4 Summary 45

3 Pulse-Reconstruction-Based TDR for Multi-Defect Detection and Localization 46
3.1 Estimation Method of Cable Characteristic Parameters 47
3.1.1 Analysis of TDR Signal Propagation 47
3.1.2 Estimation of Characteristic Parameters 48
3.1.3 Simulation and Validation 51
3.2 Defect Localization Based on TVMF 53
3.2.1 Principle and Implementation of TVMF 54
3.2.2 Construction of Time-Varying Matched Filter Bank 55
3.2.3 Selection of TVMF Filtering Results 57
3.2.4 Comparison and Validation of Localization Methods 62
3.3 Reflection Pulse Reconstruction for Multi-Defect Cables 64
3.3.1 Influence of Multiple Defects on Detection and Localization 64
3.3.2 Estimation of Defect Characteristic Parameters 65
3.3.3 Implementation of Pulse Reconstruction 71
3.3.4 Simulation and Validation 72
3.4 Experimental Verification 79
3.4.1 Experimental Setup Measurement Platform 79
3.4.2 Experimental Results and Analysis 80
3.5 Summary 87

4 Quantitative Severity Evaluation of Cable Defects Based on Double-Frequency TFDR 89
4.1 Principles of TFDR-Based Cable Defect Detection 89
4.1.1 Principles of Detection and Localization 89
4.1.2 Design for Injected Signal Parameters 92
4.2 Principles of Double-Frequency TFDR for Defect Severity Estimation 94

4.2.1 Analytical Modeling of TFDR Defect Measurement Results 95
4.2.2 Implementation of Double-Frequency TFDR Method 100
4.2.3 Quantitative Estimation of Severity Defects 102
4.2.4 Simulation and Validation 105
4.3 Experimental Verification 113
4.3.1 Experimental Setup and Measurement Platform 114
4.3.2 Experimental Results and Analysis 115
4.4 Summary 123

5 Development of a TDR System with HV Pulse Injection and Fast Range Switching 124
5.1 Tunable HV Pulse Generator 124
5.1.1 Hardware Design and Simulation Analysis 125
5.1.2 Signal Integrity Simulation and Parameter Optimization 130
5.1.3 Experimental Testing and Performance Evaluation 131
5.2 Fast-Switching Multiple-Ratio Voltage Divider 132
5.2.1 Topology and Operational Principle of the FSMRVD 133
5.2.2 Key Parameter Selection and System Implementation 134
5.2.3 Experimental Testing and Performance Evaluation 139
5.3 Experimental Validation of HVFRS-TDR System 142
5.3.1 Experimental Platform and Testing Procedure 142
5.3.2 Experimental Results and Analysis 144
5.4 Summary 146

6 Conclusions and Future Work 148
6.1 Conclusions 148
6.2 Future Work 150

References 151

Achievements 160

List of Figures

1.1 Failure rates and causes of distribution cable faults 2
1.2 Common defects in distribution cables 2
1.3 Step TDR testing a cable network 5
1.4 Chirp signal 6
1.5 Schematic of NDR 7
1.6 Two Models of water tree defects 10
1.7 Diagram of piecewise method 11
1.8 Typical topologies of pulse generator 14
1.9 Typical topologies of gate driver circuit for series-stacked MOSFETs 14
1.10 Dissertation outline 16

2.1 Structure of a typical single-core cable and its cross-section 17
2.2 Frequency-dependent parameters of the cable 18
2.3 Cross-section of a cable joint 19
2.4 Cable joint subdivided into 15 segments 19
2.5 Distributed parameters of the cable joint at 2 MHz 21
2.6 Distribution of electric and magnetic field in the cable joint 22
2.7 S-parameter of the cable joint with 50 Ω reference impedance 22
2.8 Input impedance of the cable joint 23
2.9 Classification of cable defects 23
2.10 Equivalent circuit of lumped defects 23
2.11 Cable shield with corrosion defect 24

2.12 Distributed-parameter model of cable with shield corrosion. 25
2.13 Geometric parameters of the spiral shield. 26
2.14 Distribution of electric and magnetic fields in cables with and without shield corrosion defects 27
2.15 A typical shield hole caused by the corrosion in the cable 28
2.16 FEM model of the cable with shield hole 29
2.17 Electric and magnetic field distribution in the cable with and without a shield hole 29
2.18 Distributed parameters of the cable with shield hole 31
2.19 FEM model of the cable with water ingress defect 32
2.20 Distributed parameters of the cable with light water ingress defect 33
2.21 Water tree defect in the insulation of the cable 34
2.22 Distributed parameters of the cable with various water tree defect 35
2.23 S-parameter measurement using VNA 36
2.24 Fixture Components 36
2.25 Cable defect samples with different degrees of moisture ingress 37
2.26 Measured S-parameters of the cable samples 37
2.27 Characteristic parameters of cable with water ingress defects. (a) and (b) are the 0.5 m-long cable, (c) and (d) are 1 m, and (e) and (f) are 2 m. 39
2.28 The distributed-parameter model of a long cable with a lumped defect 41
2.29 Distributed-parameter model of a long cable with a distributed defect 42
2.30 Long cable with multiple defects 42
2.31 Cascading network of a long cable with a defect 43
2.32 S11 parameters of cables with a joint, with shield corrosion, and with a shield hole 45

3.1 Signal propagation process in TDR system 47
3.2 Lattice diagram of signal propagation when measuring a cable using TDR system 48
3.3 A typical TDR measurement result at port V_o in Fig. 3.1. 49
3.4 The results of the auxiliary measurement. 50
3.5 The TDR measurement results of a 100-meter-long healthy power cable . . . 52

3.6 Comparison of the refitting values, initial values and reference values of the cable characteristic parameters 53
3.7 Model of the distributed defect on a cable 56
3.8 The TDR measurement results of the cable with defects. 58
3.9 The results of the TVMF. 58
3.10 The 1D CNN model for defect type recognition. 59
3.11 Loss and accuracy curves of the 1D CNN model. 60
3.12 The confusion matrix of the 1D CNN model. 61
3.13 The classification result of the 1D CNN model. 61
3.14 The TDR measurement results of defects at various locations. 62
3.15 Location error comparison: TVMF and matched filtering. 63
3.16 TDR simulation results with varying noise intensities. 63
3.17 Localization results comparison: the TVMF and commonly used methods. . . 64
3.18 Lattice diagram of the pulse propagation in the cable. 65
3.19 Two typical TDR measurement results of cable with lumped defects 66
3.20 The procedure of the signal propagating along a cable with two lumped defects 67
3.21 The frequency-dependent behavior of the reflection coefficient for distributed defects is illustrated. The solid lines represent the accurate results obtained from (3.24), while the dashed lines show the approximated results based on (3.40). 69
3.22 The procedure of the signal propagating along a distributed defect 69
3.23 The schematic of the TDR measurement system for a cable with a defect. . . 71
3.24 Case I: A model of long cable with multiple defects 73
3.25 TDR simulation results 73
3.26 Reconstruction of reflection pulses by the first Defect 74
3.27 The TVMF location results of the second actual reflection pulse 74
3.28 Reconstruction of reflection pulses by the first and second defects 75
3.29 The TVMF location results of the third actual reflection pulse 75
3.30 Reconstruction of reflection pulses by the first, second defects and cable end . 76

3.31 Flowchart of multiple defect identification and localization. Note: the reference cable is a cable segment of the same type as the tested cable. 77
3.32 The schematic of the cable with a lumped defect and a distributed defect . . . 77
3.33 TDR simulation results of the cable in case II 77
3.34 Reconstruction of reflection pulses in case II cable 78
3.35 The schematic of the experiment 80
3.36 The TDR measurement results of the 200-meter-long cable with an open-circuit. 81
3.37 The schematic of VNA measurement for cable characteristic parameters . . . 81
3.38 Comparison of cable characteristic parameters: estimation results by the improved method and measurement results from the VNA 82
3.39 Resistors used as lumped defects in experiments 82
3.40 The TDR measurement results of two lumped defects 83
3.41 The reconstruction reflection pulses by the first defect in Case II and Case III 84
3.42 The TVMF location results of the second defects 84
3.43 The reconstruction reflection pulses by the first and second defects in Case II and Case III 85
3.44 The TVMF location results of the third defects 86
3.45 The reconstruction reflection pulses by all defects and cable ends in Case II and Case III 86

4.1 Chirp signal with a 40 MHz bandwidth, a 40 MHz center frequency and a 200 ns duration time 90
4.2 A typical TFDR measurement result 92
4.3 The TFCC of the reflected signal 92
4.4 The reflected signal and TFCC of distributed defects with different lengths . . 100
4.5 Flowchart of the estimation of distributed defect 104
4.6 Diagram of cable detection using TFDR 105
4.7 Reflected signals from shield corrosion defects with different lengths 106
4.8 Effect of various shield corrosion sizes on the location of the peak in TFCC curves 106

4.9 Effect of the defect length on the location: comparison between simulations and equations . . . 107
4.10 Comparison of Z_{cf1} between the estimated value and the reference value . . . 107
4.11 Assessment results of shield corrosion size using the double-frequency TFDR 108
4.12 Reflected signals for various shield hole defects . . . 109
4.13 Magnitude surface of the reflected signal for various defects . . . 109
4.14 TFCC curves of reflected signals from shield corrosion hole defects of various sizes . . . 110
4.15 Reference characteristic impedance Z_{cf1} and reference ρ of the shield hole defects 110
4.16 Size evaluation of shield hole defects . . . 111
4.17 Size evaluation of shield hole defects under the signals with various SNR . . 112
4.18 Irregular shield hole defects in Table 4.1 . . . 112
4.19 Size evaluation of irregular shield corrosion holes . . . 113
4.20 Experiment setup . . . 114
4.21 Experiment platform . . . 114
4.22 Cable samples with defects . . . 115
4.23 Measured results of shield corrosion defects by the first injected signal . . . 116
4.24 Comparison between the reflected signals obtained with the experiment and in simulation for shield corrosion defects . . . 117
4.25 TFCC curves of the defect location in the experiment . . . 117
4.26 The TFDR measurement results of cables with shield hole defects . . . 118
4.27 Comparison between the reflected signals obtained with the experiment and in simulation for shield hole defects . . . 119
4.28 TFCC curves showing the location of cable defects . . . 120
4.29 Reference sets of Z_{cf1} and ρ_1 for evaluating the size of the shield hole defects 120

5.1 TDR simulation results of a cable with a joint at 5 km . . . 126
5.2 Topology of the HV negative pulse generator . . . 127
5.3 Circuit of the pulse generator in charging and discharging phase . . . 127
5.4 Design circuit of the HV pulse generator . . . 128

5.5 PCB model of the HV pulse generator for signal integrity simulation 130
5.6 Simulation of the HV pulse generator with various parameters of the buffer circuit 131
5.7 Simulation of the HV pulse generator with various parameters of the gate resistance 132
5.8 Prototype of the HV pulse generator 132
5.9 Test results of the HV pulse generator 133
5.10 Topology of the FSMRVD 134
5.11 PCB model of the FSMRVD 135
5.12 Current simulation results of the active protection circuits 138
5.13 Prototype of the FSMRVD 140
5.14 Bandwidth test results of FSMRVD 141
5.15 Schematic of the switching speed test of the FSMRVD 141
5.16 Switching speed test results of the FSMRVD 142
5.17 Experiment platform of the HVFRS-TDR system 143
5.18 The first measurement result of the Case 1 144
5.19 The second measurement result of the Case 1 145
5.20 The measurement result of the Case 2 145
5.21 The measurement result of the Case 3 146

List of Tables

2.1 Electrical Parameters of a Typical Cable Joint 19

2.2 Parameters of the 8.7/15 kV Single-core Cable 22

2.3 Comparison of L_{sc} values calculated by FEM and the analytical equation . . . 28

3.1 Parameters of the SYV50 Cable 51

3.2 Location and estimation results of defects in Case I 76

3.3 Location and estimation results of defects in Case II 79

3.4 Parameters of defects in experiments 80

3.5 The location results of the defects in Case II and III 87

3.6 Equivalent resistance estimation results of defects in Case II and III 87

4.1 Angle and length parameters of the samples in the simulation 113

4.2 Comparison of actual and estimated defect sizes 117

4.3 Comparison between simulated and measured values of Z_{cf1} 118

4.4 Comparison of ρ_1 between reference and measured values in experiments . . 121

4.5 Comparison of Z_{cf1} between the reference and measured values in experiments 121

4.6 Comparison of defect sizes between actual and estimated values 122

4.7 Comparison between actual sizes and estimation results of irregular shield holes 122

5.1 Designed parameters of the voltage dividers. 136

5.2 Designed parameters of the voltage dividers. 137

5.3 Required Parameters of MOSFETs in the Active Protection Circuit. 137

5.4 Required Parameters of MOSFETs in the Active Protection Circuit. 139

5.5 Tested cases in the experiment 143

5.6 Localization results of defects in three test cases. 146

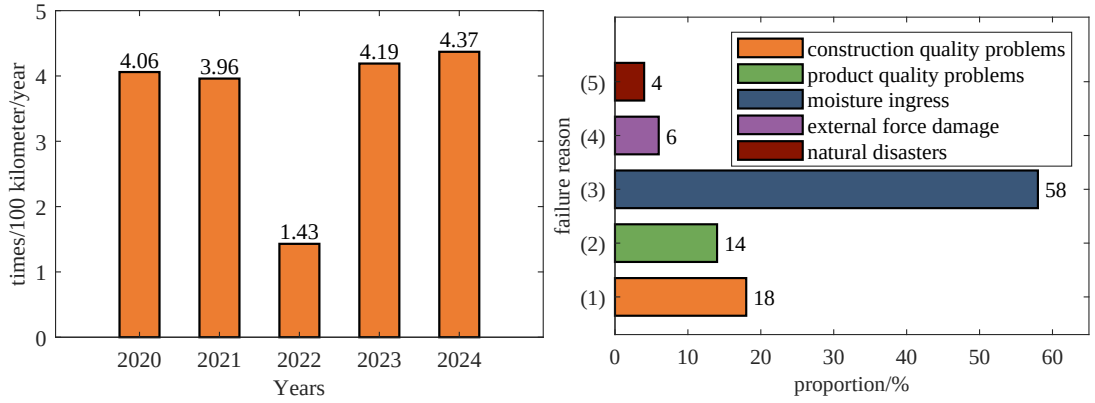
Chapter 1

Introductions

1.1 Research Background and Significance

Cables possess the advantages of compact structure, high reliability, large transmission capacity, and low power loss, and are thus widely used in urban power distribution systems. In recent years, with the rapid advancement of urbanization and the growing demand for electricity, the construction of distribution networks has accelerated. In some major cities, the proportion of underground distribution networks has reached 95 % or more [1, 2]. According to public reports from the National Energy Administration, by 2020 the total length of 10 kV distribution cables in China had reached 1.006 million kilometers, and this figure has continued to grow at an annual rate of 15 % [3]. With the increasing length of cables and the growing complexity of distribution networks, the failure rate of distribution cables has also risen. According to the National Annual Report on Power System Reliability released by the National Energy Administration, the average annual failure rate of distribution cables in China over the past five years is shown in Fig. 1.1a [3]. The reported failure rate is 3.6 times/100 km/year, which is significantly higher than the 1.18 times/100 km/year observed in the United States and European countries [4]. Under these circumstances, the reliability of distribution cables has attracted increasing attention. Therefore, developing effective methods for defect detection and localization in distribution cables is of vital importance for ensuring the reliability and safety of power distribution systems and for achieving the goal of high-quality development of power distribution networks.

Based on statistics from a power supply company in southern China [5], shown in Fig. 1.1b, the common failures in distribution cables are primarily attributed to the following factors: (1) poor construction quality, (2) product quality issues, (3) moisture ingress, (4) external mechanical damage, and (5) natural disasters, which are shown in Fig. 1.2. Among these causes, moisture ingress accounts for the largest proportion, nearly 58 %. According to existing



(a) Failure Rate (b) Failure Reasons

Fig. 1.1 Failure rates and causes of distribution cable faults

research [6], reflectometry techniques have been proven effective for detecting and localizing moisture-related defects. Therefore, investigating accurate and effective reflectometry methods and developing cost-effective, high-performance reflectometry systems are of great significance for improving the reliability of distribution cables and ensuring the safe operation of power distribution networks.



(a) Shield aperture (b) Deformation (c) Moisture Ingress (d) Neutral Corrosion

Fig. 1.2 Common defects in distribution cables

1.2 Current Research Status

1.2.1 Current Status of Cable Defect Detection

Overview of Cable Defect Detection Methods

From manufacture to operation, cables need to undergo various tests to ensure their quality and reliability. According to state standards for power cables with extruded insulation and their accessories for rated voltages from 1 kV (Um = 1.2 kV) up to 35 kV (Um = 40.5 kV), cables are required to undergo type tests, sampling tests, and routine tests [7]. Before leaving the factory, cables must pass withstand voltage tests, impulse tests, insulation resistance tests, and partial discharge tests. After installation, cables need to undergo similar tests. During operation, cables

are subject to various periodic tests. These tests are classified into three categories—withstand voltage tests, partial discharge tests, and parameter diagnostic tests—according to IEEE Std 400.2 [8]. With the expansion of cable networks and the advancement of detection technologies, online monitoring of cables has been increasingly adopted. Online monitoring mainly includes partial discharge monitoring and parameter diagnostic monitoring. In current cable maintenance practices, offline and online methods together constitute the cable defect detection system.

Withstand Voltage Tests

Cable withstand voltage tests have long been employed in cable testing. To date, they remain an authoritative method for assessing cable health. According to the type of power source used, withstand voltage tests can be divided into direct current (DC) withstand voltage tests and alternating current (AC) withstand voltage tests [9]. DC withstand voltage tests are rarely used due to the problem of space charge accumulation. Power-frequency AC withstand voltage tests are performed only in some key procedures because of the large volume of the required test equipment. In routine outage maintenance, very low-frequency withstand voltage tests and damped AC withstand voltage tests have replaced power-frequency AC withstand voltage tests [10]. Withstand voltage tests are closest to the actual operating conditions of cables and are able to detect most cable defects. However, their testing equipment is usually bulky and expensive, and the testing process is time-consuming, making them unsuitable for routine rapid maintenance. Consequently, they are often replaced by other two methods.

Partial Discharge Tests

Partial discharge (PD) tests can detect and localize small defects in cables. According to the operating status of the cable, PD tests are divided into offline PD tests and online PD tests [11]. Offline PD tests are usually combined with very low-frequency and damped AC tests, while online PD tests are performed during normal operation. The pulse current method is mainly used to detect cable PD signals [12], and the double-terminal PD localization technique is commonly applied to locate PD sources. Since PD tests are based on partial discharge phenomena, they can detect defects associated with PD activity. However, defects such as cable aging, moisture ingress, copper corrosion, and some types of mechanical damage do not generate partial discharge and are therefore undetectable by PD tests [13].

Parameter Diagnosing Tests

Parameter diagnosing tests assess the condition of cables by measuring cable parameters. These tests include insulation resistance tests, tan-δ tests, leakage current tests, reflectometry tests,

and others [14]. The results can be used to evaluate the health condition of cables and determine whether they suffer from insulation aging, water ingress, copper corrosion, or mechanical damage. Among these methods, reflectometry tests are the only approach capable of localizing cable defects, while the others provide only a global evaluation of cable health. Therefore, in IEEE Std 1617 [15], reflectometry tests are recommended as the primary method for detecting and localizing cable moisture ingress and copper corrosion defects. Due to their fast testing speed and localization capability, reflectometry testing has been widely used for cable defect detection and localization in routine maintenance.

Based on the statistical analysis of cable fault causes, in which moisture ingress defects account for the largest proportion, and on the characteristics of various testing methods, it can be concluded that reflectometry tests provide the fastest and most effective means of detecting and localizing moisture-related cable defects. Therefore, research on reflectometry techniques for cable defect detection is of significant practical importance.

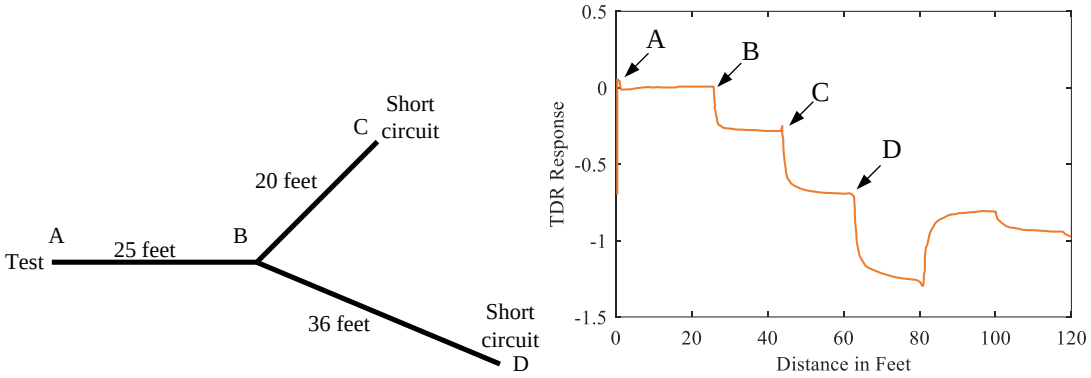
1.2.2 Current Status of Reflection Technology in Cable Defect Detection

Reflectometry diagnoses cable parameters by injecting a signal into the cable and then measuring and analyzing the reflected signals. Due to parameter differences between healthy and defective cables, the characteristic impedance changes in defective sections, and the injected signal is reflected at these impedance discontinuities. Owing to their small size, light weight, relatively low cost, and fast testing speed, reflectometry tests have been widely used for cable defect detection in daily maintenance. Reflectometry tests can be divided into time-domain reflectometry (TDR), frequency-domain reflectometry (FDR), and noise-domain reflectometry (NDR), according to the domain of the measured signals [16]. TDR methods mainly include pulse TDR, sequence TDR (STDR) and spread spectrum TDR (SSTDR) [17], orthogonal multi-tone TDR (OMTDR) [18], chaos TDR (CTDR) [19], binary TDR (BTDR) [20], and time-frequency TDR (TFDR) [21]. FDR mainly include frequency-modulated carrier wave (FMCW) [22], phase detection FDR (PD-FDR) [23], standing wave ratio reflectometry (SWR) [24], mixed signal reflectometry (MSR) [25], multicarrier reflectometry (MCR), and broadband impedance spectroscopy (BIS). The details of these methods are introduced in the following subsections.

TDR Cable Defect Detection

TDR was employed in the early stages of cable testing. Initially, it was mainly used to detect short and open circuits faults. With the development of signal sources and measurement technologies, TDR has been extended to cable defect detection. In a typical TDR test, a pulse is injected into the cable to detect and localize defects. The equipment is simple, cost-effective,

and widely applied in cable defect detection [26]. However, the injected pulse has low energy and a simple waveform, making it susceptible to noise and less effective in detecting multiple defects or faults in long cables. To improve injection energy, step TDR was proposed. It injects a step signal into cables, thereby increasing the signal energy and enabling detection of longer cables [27]. Step TDR is particularly suitable for measuring cable networks, as it can also reveal the characteristic impedance of each cable section. An example of step TDR testing in a cable network is shown in Fig. 1.3. However, for power cable detection, high-magnitude



(a) a RG58 cable network (b) Step TDR signal

Fig. 1.3 Step TDR testing a cable network

step TDR is still required. The step signal with short rise time and high voltage is difficult to generate. Therefore, step TDR is mainly used to detect signal cables, while pulse TDR is more commonly used to detect power cables.

When detecting cable defects using reflectometry, high-frequency signals are more sensitive to defects. In TDR detection, however, the high-frequency components in pulse and step signals are limited. To improve the high-frequency components of the injected signal and enhance the sensitivity of TDR, STDR and SSTDR were proposed [17]. STDR uses a pseudo-noise (PN) code as the injected signal, while SSTDR uses a PN code modulated by a sine or square wave. STDR and SSTDR can be used on online cables because the injection signal is a high-frequency signal. Due to the complexity of signal generation, however, STDR and SSTDR with high magnitude are difficult to achieve. Moreover, the attenuation caused by multiple defects and long-distance transmission reduces the signal-to-noise ratio (SNR) of the reflected signals. Therefore, STDR and SSTDR are mainly applied to signal cables, while their application to power cables is still in the exploratory stage. To improve the SNR of TDR using high-frequency signals, TFDR was proposed [21]. It injects a linear frequency-modulated signal with a Gaussian envelope (chirp signal), as shown in Fig. 1.4, and uses the time-frequency cross-correlation (TFCC) method to localize cable defects, which enhances the anti-noise performance of TDR.

As cable networks expand, the requirement of cable network detection is also increasing. CTDR is proposed to detect defects in cable networks [19]. This method injects a pseudo-

random signal generated by a chaotic process into cables. Through the chaotic process, CTDR can generate multiple injection signals that are mutually non-interfering. Therefore, CTDR allows online simultaneous multi-point detection in cable networks. BTDR is the digital version of CTDR [20]. It eliminates the analog circuit in CTDR and uses digital circuits to generate pseudo-random signals. Compared with power cable networks, signal cable networks have more complex topologies. Therefore, CTDR and BTDR are mainly used in signal cable networks. Nevertheless, with the development of power cable networks, CTDR and BTDR are regarded as key development directions of TDR for power cable defect detection.

Besides the above general TDR methods, OMTDR is a special TDR method for online detection of broadband signal cables [18]. It is based on the principle of orthogonal frequency division multiplexing (OFDM). It injects a time-domain signal with multiple frequencies into cables, where the frequencies depend on the availability of the channel. OMTDR does not occupy the current working channel and obtains the measurement results of the entire channel by measuring at different times. It can avoid the interference between transmission signals and the injected signal. Therefore, this technique is usually used for online detection in signal cable networks. Among the TDR methods, pulse TDR is the main method for detecting power cables, while TFDR has only a few applications.

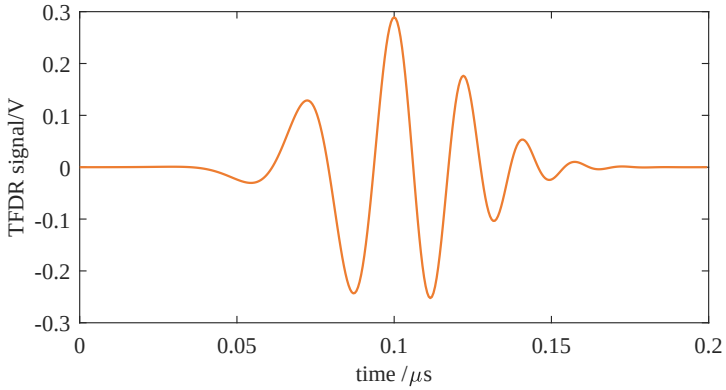


Fig. 1.4 Chirp signal

FDR Cable Defect Detection

FDR methods detect and localize cable defects by measuring the frequency-domain information of reflection signals. They use impedance analyzers and vector network analyzers (VNA) to measure cables. Compared to TDR, the equipment is more complex and expensive. Therefore, the development of FDR occurred later than that of TDR. FMCW is a typical FDR method. It sweeps the frequency of the sine wave over time and measures the frequency difference between the injected and reflected signals to localize targets [22]. However, due to limitations in sweep speed and localization accuracy, FMCW is only used for cable length measurement and not for

cable defect detection. Nevertheless, FMCW has a relatively fast testing speed among FDR methods. PD-FDR measures the phase difference between the injected and reflected sine signals and uses the relationship between frequency and phase to localize defects [23]. However, due to cable attenuation, the sweep frequency range may not be sufficient. In addition, the phase is restricted to the range of $(0, 2\pi)$, making it difficult to determine the number of phase cycles. Consequently, PD-FDR is not suitable for long cables. SWR measures the magnitude of the standing wave formed by the injected and reflected sine signals. By measuring the variation of peaks and nulls, SWR can localize defects [24]. However, because the peaks and nulls are not obvious for soft defects, SWR is only applicable to localizing hard defects. MSR is similar to SWR but measures the squared magnitude of the standing wave. MSR is more accurate than SWR and can be used to localize soft defects [25]. BIS measures the impedance spectrum of cables and then applies time-frequency and integral transformations to localize defects [28]. Since impedance can directly reflect the variation of cable parameters, and with the maturity of impedance measurement equipment, BIS is increasingly applied in cable defect detection. FDR methods are sensitive to cable defects. However, for sweep-frequency-based FDR, the testing speed is relatively slow, which becomes more significant for long cables. Moreover, the localization accuracy depends on the maximum frequency reached in the sweep: higher accuracy requires a higher frequency range. As a result, the localization accuracy of FDR in on-site measurements is usually lower than that of TDR.

NDR Cable Defect Detection

NDR is different from TDR and FDR in that it does not require an external signal source. Instead, it utilizes the inherent noise signals in cables to detect and localize defects. It measures two signals separated by a time interval of λ and applies the correlation method to localize defects from the two measurements [29]. The schematic of NDR is shown in Fig. 1.5, where the random source represents the noise source in the cable system. NDR is a passive method, and its measurements exhibit high randomness. Therefore, it is not suitable for offline testing.

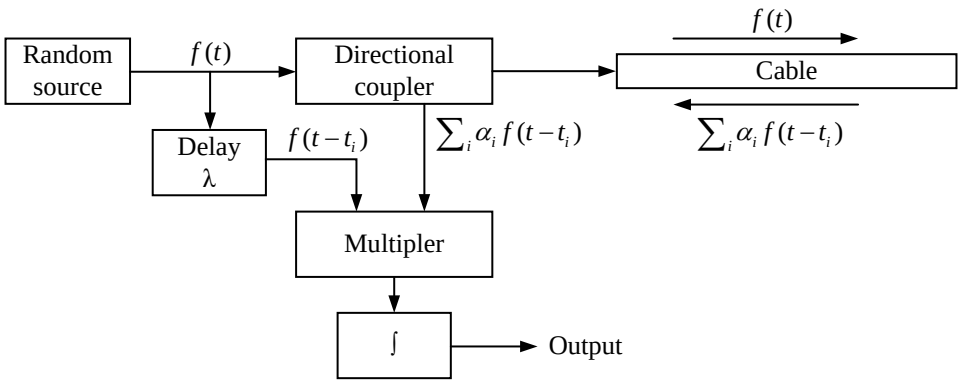


Fig. 1.5 Schematic of NDR

Among existing reflectometry methods, due to the propagation characteristics of power cables and the performance limitations of test equipment, pulse TDR remains the most widely used technique for power cable detection. BIS and TFDR techniques are rapidly evolving. Other methods, especially those relying on high-frequency signals, are mainly applied to signal cables, as such signals suffer from severe attenuation in power cables and cannot propagate over long distances.

1.2.3 Current Status of Defect Localization and Assessment Based on TDR

In cable defect detection based on TDR, defect identification, localization, and evaluation are the three key steps. To achieve accurate detection and evaluation, cable and defect models have been developed and analyzed, methods for defect localization and evaluation have been proposed, and TDR systems have been designed and implemented. The current research progress in these aspects is summarized below.

Modeling and Analyzing of Cables and Defects

The analysis of signal propagation along the cable line is fundamental to TDR-based detection. The cable body is typically modeled as a coaxial transmission line using a distributed-parameter representation. Breien [30] and Wedepohl [31] developed accurate distributed-parameter models for power cables, but these models are computationally intensive due to the involvement of Bessel functions. To improve practicality, Wielen [32] simplified the models in 2005.

Joints are critical components in cable systems. Due to differences in structure and materials, their propagation characteristics differ significantly from those of the cable body. Typically, the diameter of a joint is larger than that of the cable body, leading to changes in equivalent capacitance. Wang [33] represented the joint using a lumped capacitance, a simple but coarse model that is unsuitable for accurately analyzing propagation characteristics. To achieve higher accuracy, Norouzi [34] applied the Finite Element Method (FEM) to calculate the equivalent resistance, inductance, conductance, and capacitance of joints. However, this lumped model still fails to describe propagation behavior. Hu [35] adopted a piecewise approach by dividing the joint into several axial sections, each approximated as uniform, with distributed parameters derived from cable models. Although this method captures propagation characteristics, its precision depends on the number of sections and requires substantial computation. To balance accuracy and efficiency, Yu [36] employed S-parameters to characterize joint behavior. From existing research, it is evident that S-parameter-based modeling is the most suitable approach for reflectometry simulations of cable joints [37].

Open and short circuit faults, corrosion defects, moisture ingress, and mechanical damage are common types detected by reflectometry in distribution cables. Tang [38], based on the continuity of voltage and current at defect locations, classified defects into two categories: lumped and distributed. Lumped defects include two types: ground defects and series resistance defects. Distributed defects include shield corrosion, moisture ingress, and external mechanical damage. Sommervogel [39] and Wang [40] proposed using lumped resistances to represent lumped defects.

Chen [41] analyzed the mechanism of corrosion influence on cable propagation characteristics and found that corrosion can also affect the inductance of the cable, mainly because it alters the conductor geometry. The cable shield is composed of wrapped copper tape, where two adjacent layers contact each other to form a cylindrical shield. However, when water enters the cable and slight corrosion occurs, patina forms between adjacent layers, altering the current path and causing changes in cable inductance. Based on this phenomenon, Guo [42] proposed a model for slight corrosion but they did not analyze the influence of corrosion on cable propagation characteristic.

Both severe shield corrosion and damage caused by external mechanical forces can create a hole in the shield. Therefore, shield corrosion holes and external force damage can be modeled using the same approach. For small holes, Taylor [43] proposed an analytical method and used the transmission matrix of the defect to calculate propagation characteristics. However, these methods involve complex derivations and are limited by hole shape and size. Cerri [44] employed the method of moments to compute propagation characteristics of shield holes, which reduces computational complexity but is still suitable only for small, regular-shaped holes. With the development of the Finite-Difference Method (FDM) and the FEM, arbitrary-shaped shield holes have been analyzed, as demonstrated in [45, 46].

Water ingress defects can be divided into two categories: light water ingress and heavy water ingress. In light water ingress, water accumulates outside the outer semiconductive layer after sheath damage, and its impact on propagation characteristics is limited due to the thin water layer. A typical heavy water ingress defect is the water tree, which forms when water penetrates into the insulation layer. Steennis [47] investigated water tree behavior within insulation and analyzed their dielectric properties and influence on the overall dielectric characteristics of insulation. Ohki [48] measured space charge distribution to study water trees and proposed an equivalent circuit model. Ma [49] used polarization–depolarization current (PDC) measurements to evaluate dielectric properties of water trees and proposed a three-branch Debye model to fit the data, as shown in Fig. 1.6a. Based on this approach, water tree defects can be diagnosed; however, the PDC method is not suitable for long-distance cable detection. Mugala [50] used a VNA to measure dielectric properties of water trees and established the relationship between equivalent permittivity, water content, and tree volume. The equivalent model of a measured water tree sample is shown in Fig. 1.6b. Zhou [51] applied FEM to

analyze the effect of water trees on electric field distribution in cable insulation but did not study their influence on propagation characteristics.



(a) Three-branch Debye model (b) Equivalent model of water tree

Fig. 1.6 Two Models of water tree defects

In summary, cable modeling has a solid foundation and can accurately describe the propagation characteristics of distribution cables. Joint modeling based on S-parameters is particularly suitable for cable reflectometry simulations. For defect modeling, lumped defects can be represented by lumped resistances, whereas distributed defects are usually analyzed using FEM or FDM to capture their propagation characteristics. However, for the research of reflectometry on multiple-defect cables, models of multiple-defect cables are required. Therefore, it is necessary to develop a general modeling approach for the reflected signals of multiple-defect cables based on the above methods.

Defect Detection and Localization Based on TDR

The principles of TDR-based detection and localization are founded on the traveling wave method. To get the arrival time of reflected siganls, Kreuger [52] in 1993 proposed the threshold method, Sleeman and Akaike [53] in 1999 proposed the Akaike Information Criterion (AIC) method, Kurz [54] in 2005 proposed the Energy Criterion (EC) method, and Wagenaars [55] in 2008 proposed the Gabor centroid method. These methods are simple and easy to implement, but they are sensitive to noise, and their localization accuracy degrades in noisy environments. To mitigate the influence of noise, Mardian [56] in 2010 proposed a phase-based method that utilizes the phase difference between the injected and reflected signals to locate defects. This method demonstrates strong noise resistance and provides good localization accuracy. However, it is effective only in uniform cables without secondary or multiple reflections and refractions, which can cause abrupt phase shifts. Cross-correlation-based methods [57, 58] are also used for defect localization. These methods are mainly applied in non-pulse TDR techniques such as TFDR, STDR, and SSTDR. They offer strong noise immunity and can locate defects across the entire measured signal without requiring pre-selection, but they involve higher computational complexity.

For multiple-defect detection, multiple reflections among defects can interfere with defect identification. Bruckstein [59] in 1987 proposed a layer-peeling method to localize multiple

defects. However, this method is based on the assumption that the cable is lossless; therefore, it is mainly suitable for short cables and printed circuit board (PCB) layouts. Hsue [60] in 1997 proposed a piecewise method to identify multiple defects, as shown in Fig. 1.7. This method divides the cable into short sections and assumes that each section can reflect signals. Defects are then determined by calculating the impedance of each section based on TDR measurements. In this method, the derivation of reflections is complex, and its accuracy is limited by the number of sections. Since it provides the characteristic impedance of each section, this method is mainly used to estimate PCB parameters.

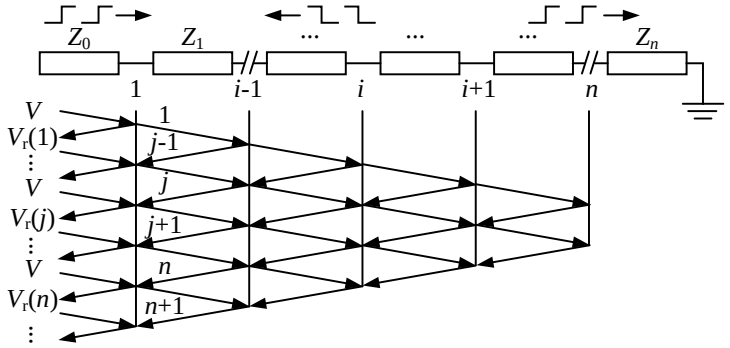


Fig. 1.7 Diagram of piecewise method

Smail [61] employed a genetic algorithm and particle swarm optimization to detect defects in multiple-reflection signals of cable networks. However, this method requires knowledge of the cable network topology and can only detect hard defects. To overcome the limitation of requiring known network topology, Blum [62] proposed a method based on a continuous cost function to reconstruct cable networks using TDR results. However, this method cannot detect defects. Lee [63] in 2021 applied a classification approach based on a Faster Region-Based Convolutional Neural Network (R-CNN) to distinguish real defects from false ones in measurement results. However, their training method did not account for the influence of propagation characteristics caused by multiple defects and joints within the cable. Wang [40] improved the piecewise method and proposed a frequency-domain iterative algorithm to localize multiple defects. Although effective, the method was only validated on lumped defects, and its effectiveness for distributed defects remains unknown.

In summary, existing TDR-based methods for defect detection and localization face two main challenges: (1) most existing methods primarily focus on identifying the arrival time of reflected signals, without accounting for waveform distortion induced by the propagation characteristics of cables and defects; (2) in TDR measurements, effective and practical methods for defect identification and localization in the presence of multiple reflections and refractions are still lacking.

Estimation of Cable Defects Based on TDR

The severity of defects determines the maintenance strategy for power cables, and estimating defect severity is an important aspect of TDR detection. Ho [64] used equivalent resistance to represent defect severity. Lee and Kwon [65, 66] in 2019 employed TDR methods to measure the reflection coefficient and subsequently the equivalent resistance, achieving accurate results. However, these studies could not estimate the severity of distributed defects and did not consider the influence of multiple defects. Compared with lumped defects, estimating the severity of distributed defects is more complex, as they involve more parameters such as characteristic impedance, length, width, and central angle. Buccella [45] in 2003 showed that the amplitude of the reflected signal increases with shield-hole defect size. Griffiths [67] tested cables with fraying defects and observed similar trends. Cozza [68] analyzed the relationship between the input reflection coefficient and the defect length or central angle, while Manet [69] used FEM to model shield hole defects and proposed an equivalent circuit model. Nevertheless, these studies only demonstrated correlations between defect size and signal characteristics without providing quantitative estimation methods. More recently, Hua [70] and Zou [71] employed TFDR to detect damage defects and qualitatively analyzed the relationship between TFCC results and defect size, but quantitative estimation methods are still lacking.

In summary, existing methods can accurately estimate the severity of lumped defects but neglect the influence of multiple defects, leading to significant errors when measuring the cable with multiple defects. For distributed defects, current approaches mainly analyze the variation of measurement results with defect size but cannot get an estimation results for defect severity from measurement and still lack effective and practical methods for quantitative estimation.

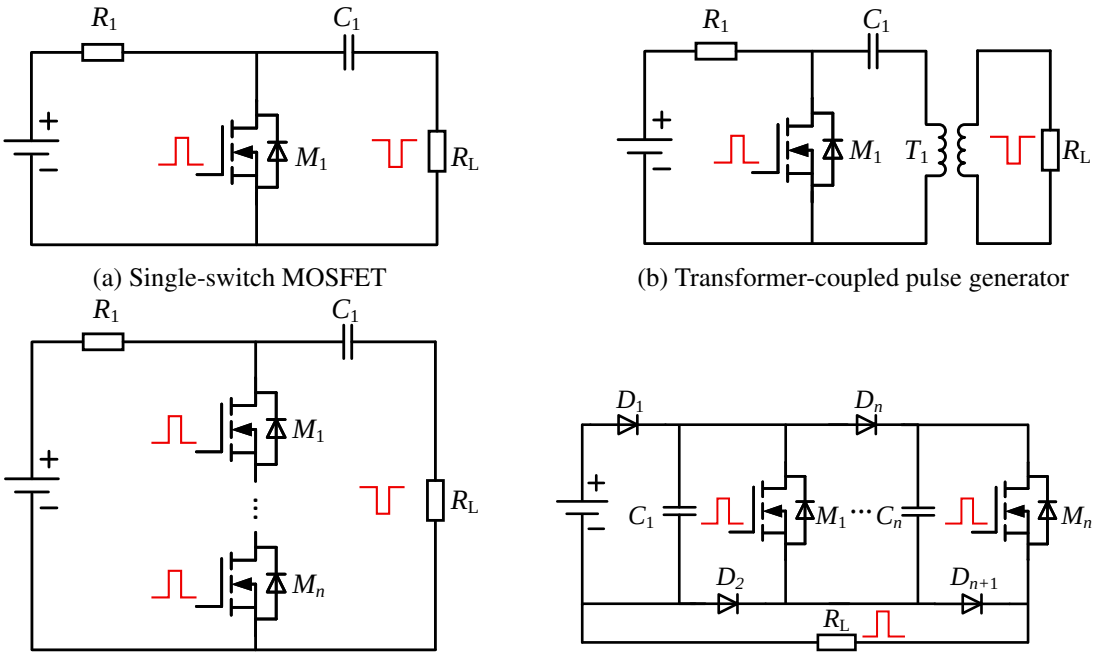
Development of TDR System

As the length and scale of cables increase, conventional pulse TDR is no longer sufficient to meet the requirements of defect detection. To extend the detection range and improve system performance, various methods have been proposed. One approach is to amplify the received signal using TDR equipment [72]. However, since both signal and noise are amplified simultaneously, weak reflections from small defects remain obscured. To mitigate noise interference, methods that increase the amplitude and pulse width of the injected signal have been investigated to enhance long-cable detection capability [73]. Increasing the amplitude, however, may saturate the TDR measurement device, resulting in incomplete data. To address this, Cataldo [74] proposed an optimization method that adjusts the amplitude and pulse width of the injected signal according to the defect location to maximize detection performance. Nevertheless, the improvement of TDR magnitude is limited by the safety voltage of the measurement device. To

increase the pulse voltage and enable high-voltage (HV) TDR measurements, the HV pulse signal is typically measured using voltage dividers [75].

In HV pulse TDR, a HV pulse source with adjustable magnitude and width is required. Early HV pulse sources were mainly based on spark gaps [76], but with the development of semiconductor technology, semiconductor-switch-based pulse sources have become widely used. Silicon carbide metal-oxide-semiconductor field-effect transistors (SiC MOSFETs) offer high breakdown voltage and fast switching speed, making them suitable for HV pulse generation [77]. To generate HV pulses, various circuit topologies have been proposed. Chaney [78] presented a simple MOSFET-based HV pulse circuit, as shown in Fig. 1.8a. It is straightforward and easy to implement, but the output voltage is limited by the MOSFET breakdown voltage. To increase the output voltage, a pulse transformer can be connected to the MOSFET output to enhance the pulse amplitude [79], as shown in Fig. 1.8b. This method is simple and effective but tends to increase the rise time of the pulse. A more advanced approach is the series-stacked MOSFET circuit [80], shown in Fig. 1.8c, which increases the effective breakdown voltage by connecting MOSFETs in series while maintaining a short rise time. However, it requires a complex driver circuit to ensure synchronized operation of all MOSFETs, and a single HV power source to supply the circuit. To simplify the structure, solid-state Marx generators have been proposed [81], as shown in Fig. 1.8d. These circuits share the advantages of conventional Marx generators in not requiring a single HV power source while still producing HV pulses. Nevertheless, for TDR applications, solid-state Marx generators are unsuitable because they cannot measure reflected signals of opposite polarity, as such signals are short-circuited inside the generator. Therefore, series-stacked MOSFET circuits are more appropriate as HV pulse sources in TDR applications.

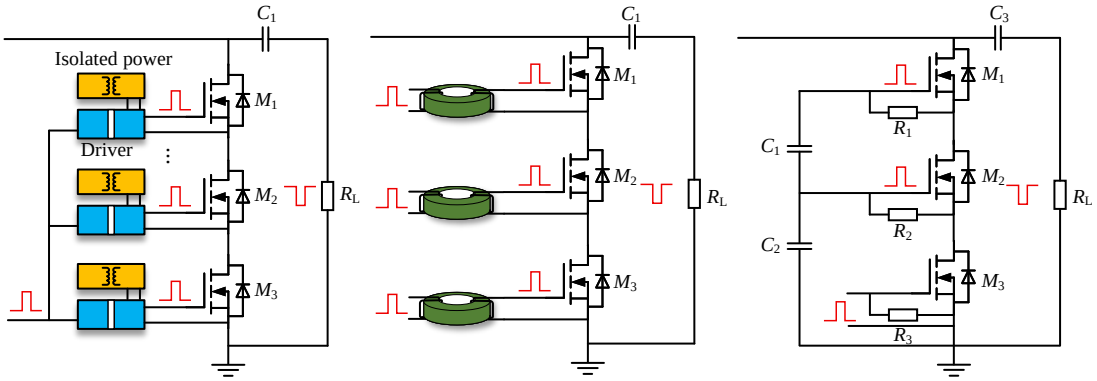
In series-stacked MOSFET circuits, each MOSFET must be driven by an isolated gate driver. The commonly used solution is an active gate drive circuit, as shown in Fig. 1.9a. It employs a commercial isolated gate driver IC together with an isolated power supply. This method provides high control accuracy and fast switching speed, but the cost is high and the circuit is complex. A simplified alternative is the toroidal-core-based driver [82], shown in Fig. 1.9b. In this method, a strong drive signal is transmitted through a toroidal core, while the MOSFET gate circuit limits and maintains the signal amplitude. This approach features a simple structure and high isolation capability, making it suitable for extra-high-voltage applications. However, the use of a toroidal core increases the pulse rise time, making it unsuitable for applications that require steep pulses. Another option is the self-triggered gate driver [80], shown in Fig. 1.9c. It uses an RC network connected to the MOSFET gates, offering a simple structure and fast switching speed. However, the parameters of the RC network depend on the output pulse amplitude, making it unsuitable for adjustable-amplitude pulses. Therefore, for HV pulse sources requiring short rise time and stable operation, active gate drive circuits remain the most suitable choice.



(a) Single-switch MOSFET (b) Transformer-coupled pulse generator

(c) Series-stacked MOSFET (d) Solid-state Marx generator

Fig. 1.8 Typical topologies of pulse generator



(a) Isolated driver (b) Toroidal core driver (c) Self-triggered driver

Fig. 1.9 Typical topologies of gate driver circuit for series-stacked MOSFETs

The use of HV pulses increases the SNR of reflection signals. However, HV pulse injection also introduces new challenges for voltage dividers. In HV TDR measurements, the injected HV pulse and the weak defect reflections coexist. A fixed-ratio voltage divider is no longer suitable, since it attenuates both the HV pulse and the weak reflections by the same ratio, causing the reflections to become too small to detect [83]. To overcome this limitation, a variable-ratio voltage divider is required for HV pulse TDR measurements. In 2005, Greig [84] designed a three-stage voltage divider for measuring 1000 V/50 Hz signals, which provided three output channels with different attenuation ratios. However, the channels could not be independently selected, and the low-ratio divider still produced a HV output. More recently, Maslan [85] developed a selectable multi-ratio voltage divider that allows the attenuation ratio

to be chosen according to application requirements. Nevertheless, this design relies on signal relays for switching, and the switching speed does not satisfy the microsecond-level timing requirements of TDR measurements. Therefore, for current HV pulse TDR applications, a fast range-switching voltage divider is essential.

In summary, existing TDR systems face two main challenges: (1) the amplitude of the injected pulse is relatively low, which cannot satisfy the detection requirements for weak defects or long cable distances; and (2) the dynamic range of the measurement system is limited, making it difficult to simultaneously capture strong injected pulses and weak defect reflections.

1.3 Main Research Contents

To address the shortcomings of conventional TDR in defect localization and severity evaluation for multiple-defect cables, this work proposes a multiple-defect localization method based on pulse reconstruction and a quantitative defect severity evaluation method based on dual-frequency TFDR. To enhance the performance of TDR and extend its detectable distance, this dissertation develops a HV pulse TDR system with fast range switching. The main research contents of this dissertation are as follows:

(1) A general modeling method for multiple-defect cables is researched. Cable defects are classified according to their propagation characteristics. Using FEM, the propagation characteristics of various defects and joints are analyzed, and equivalent models of defects and joints are established. By applying the transmission line theory and the network cascading method, multiple-defect cable models are constructed and the reflection coefficient spectra are calculated. The reflected signals of multiple-defect cables are then simulated from the reflection coefficient spectra using the time-domain to frequency-domain transformation (TDFD) method.

(2) A multiple-defect detection and localization method is researched. A TDR-based method for estimating the characteristic impedance and propagation constant of cables is developed based on the analysis of pulse signal propagation along the tested cables. Using the estimated cable parameters, a time-varying matched filtering (TVMF)-based method for defect detection and localization is proposed, which demonstrates strong resistance to noise and waveform distortion. By combining the time-varying matched filtering method with the general multiple-defect cable modeling method, a pulse reconstruction method is further proposed to identify and localize defects in multiple-defect cables. The effectiveness and localization accuracy of the proposed method are verified through simulations and experiments.

(3) A defect severity quantitative evaluation method is researched. A chirp signal is employed to test cables, thereby enhancing the sensitivity of the injected signal to defect severity.

The relationship between defect parameters and reflected signals is analyzed through analytical derivation. Based on the analysis results, a double-frequency TFDR method is proposed to evaluate the characteristic impedance and physical size of defects. The characteristic impedance and physical size quantitatively represent defect severity. The double-frequency TFDR method is validated through simulations and experiments.

(4) A TDR system with HV pulse injection and fast range switching is designed. Based on the requirements of multiple-defect cable TDR measurements, a series-stacked MOSFET HV pulse generator with adjustable pulse width and amplitude is developed, and its component parameters are optimized through signal integrity simulation. A fast range-switching multi-ratio voltage divider is also designed to measure both the strong and weak reflections during TDR measurements. The performance of the HV pulse source and the fast range-switching multi-ratio voltage divider is verified through experiments. The overall effectiveness and localization accuracy of the designed TDR system is further validated experimentally.

Fig. 1.10 shows the structure of this dissertation.

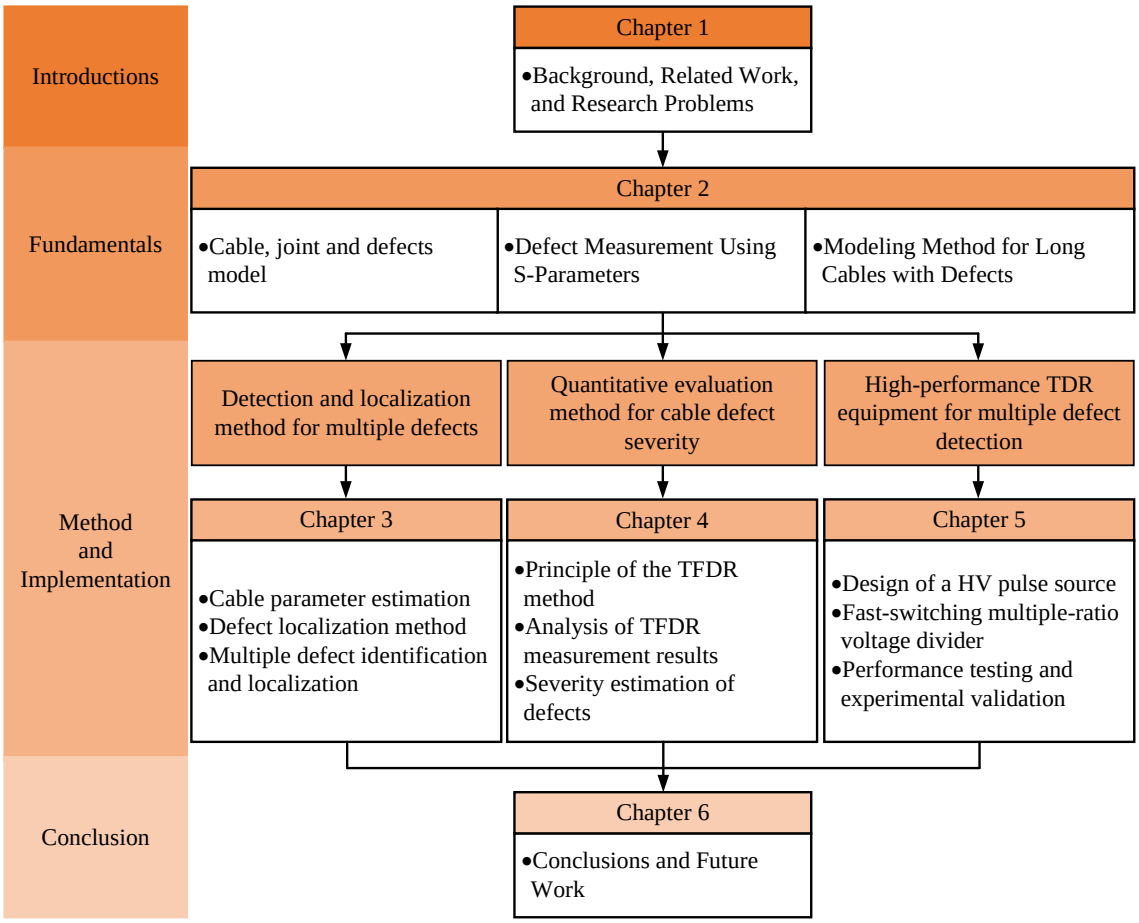


Fig. 1.10 Dissertation outline

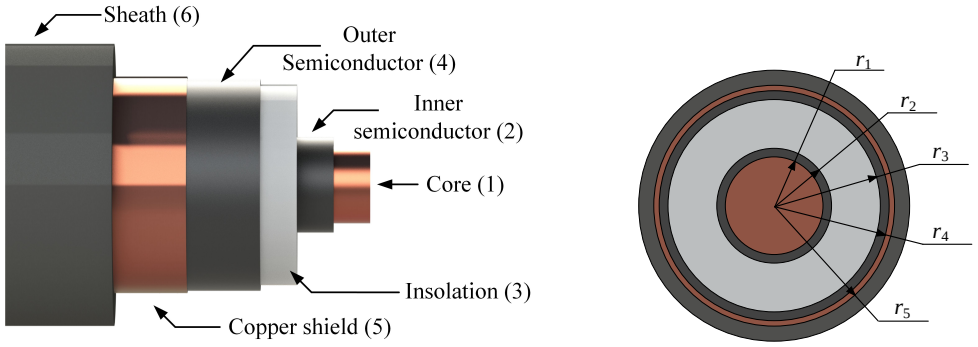
Chapter 2

Modeling of Reflected Signals in Multiple-Defect Cables Based on RCS

Accurate propagation characteristics are key to detecting and localizing cable defects. To investigate the influence of joints and various defect types on reflectometry signals, this chapter develops models for common cable defects, analyzes their propagation characteristics, and experimentally measures the characteristics of typical defects. Based on these cable and defect models, a general modeling method for cables with multiple defects based on the reflection coefficient spectrum (RCS) is proposed to simulate their reflectometry signals.

2.1 Modeling and Analysis of Cable Defects

2.1.1 Principle of Cable Distributed Parameter Model



(a) Structure of a typical single-core cable (b) Cross-section of cable and its sizes.

Fig. 2.1 Structure of a typical single-core cable and its cross-section

The structure of a typical single-core power cable is shown in Fig. 2.1a, and the geometric details of its cross-section are illustrated in Fig. 2.1b. The distributed-parameter model of a power cable is shown in Fig. 2.2. It consists of two parts: the series impedance Z and the shunt admittance Y. The series impedance of the cable can be expressed as

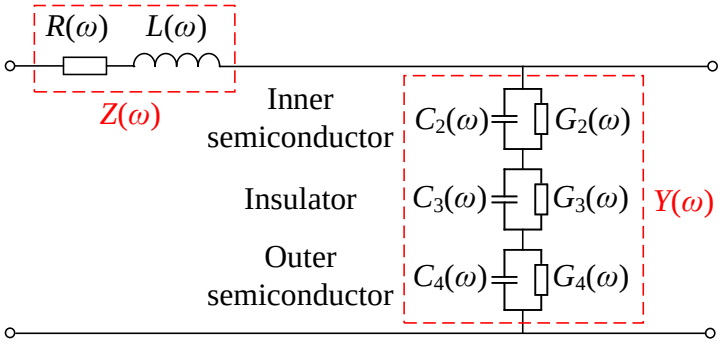


Fig. 2.2 Frequency-dependent parameters of the cable

$$Z = Z_1 + Z_5 + Z_{\text{ex}} \tag{2.1}$$

where Z_1, Z_5 and Z_{ex} are calculated as follows [86]:

$$Z_1 = \frac{m_1}{2\pi r_1 \sigma_1} \frac{I_0(m_1 r_1)}{I_1(m_1 r_1)} \tag{2.2}$$

$$Z_5 = \frac{m_5}{2\pi r_4 \sigma_5} \frac{I_0(m_5 r_4)K_1(m_5 r_5) + I_1(m_5 r_5)K_0(m_5 r_4)}{I_1(m_5 r_5)K_1(m_5 r_4) - I_1(m_5 r_4)K_1(m_5 r_5)} \tag{2.3}$$

$$Z_{\text{ex}} = \mathrm{j}\omega \frac{\mu_0}{2\pi} \ln\left(\frac{r_4}{r_1}\right) \tag{2.4}$$

where σ_1 and σ_5 are the conductivities of the core and copper shield, respectively. I_0 and I_1 are the modified Bessel functions of the first kind and its first derivative, respectively. K_0 and K_1 are the modified Bessel functions of the second kind and its first derivative. μ_0 is the permeability of free space. The parameters m_1 and m_5 are given by:

$$m_1 = \sqrt{\mathrm{j}\omega\mu_0\sigma_1} \tag{2.5}$$

$$m_5 = \sqrt{\mathrm{j}\omega\mu_0\sigma_5} \tag{2.6}$$

The shunt admittance Y of the power cable is given as follows:

$$Y = \frac{1}{\sum_{k=1}^{n} \frac{1}{Y_k}} \tag{2.7}$$

$$Y_k = \mathrm{j}\omega \frac{2\pi\varepsilon_0\varepsilon_k^*}{\ln \frac{r_k}{r_{k-1}}} \tag{2.8}$$

where ε_0 is the permittivity of vacuum, ε_k^* is the complex permittivity of the k-th layer, r_k and r_{k-1} denote the outer radii of the k-th and $(k-1)$-th layers, respectively.

2.1.2 Modeling and Analysis of Cable Joints

Cable joints are used to connect two cable sections and have a complex structure composed of the cable body and joint components. Fig. 2.3 shows the cross-section of a typical cable joint.

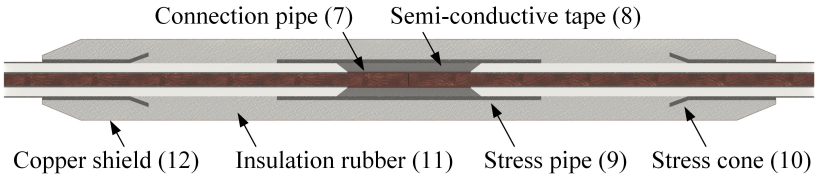


Fig. 2.3 Cross-section of a cable joint

Piecewise Model of Cable Joints

As shown in Fig. 2.3, the joint is a heterogeneous structure along the axial direction, and its distributed parameters cannot be derived in the same way as those of the cable body. Therefore, a piecewise method is employed [35]. Fig. 2.4 shows the joint divided into 15 segments. Each segment has approximately uniform structure and can be modeled individually using distributed parameters.

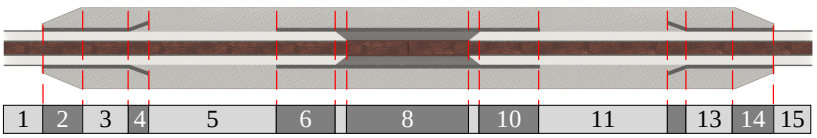


Fig. 2.4 Cable joint subdivided into 15 segments

The material parameters of a typical 35 mm^2, 8.7/15 kV cable joint are listed in Table 2.1.

Table 2.1 Electrical Parameters of a Typical Cable Joint

Components	Electric parameters
Copper shield	$\sigma = 5.98 \times 10^7\ \mathrm{S\,m^{-1}}$
Insulation rubber	$\varepsilon = 3.2$
Stress pipe	$\varepsilon = 15 - \mathrm{j}2.5$
Stress cone	$\varepsilon = 100 - \mathrm{j}600$
Connection pipe	$\sigma = 5.98 \times 10^7\ \mathrm{S\,m^{-1}}$
Semi-conductive tape	$\varepsilon = 360 - \mathrm{j}850$

Based on (2.1) and (2.7), the distributed parameters of the each cable joint segment are calculated. At a frequency of 2 MHz, the spatial variation of these parameters along the length of the joint is depicted in Fig. 2.5.

As illustrated in the figure, the distributed parameters are not constant but vary continuously along the joint, exhibiting a symmetrical pattern with respect to the joint's midpoint. This symmetry arises from the geometrically and electrically symmetric structure of the joint itself. However, despite the symmetric nature, the distributed parameters remain significantly non-uniform across the joint region. This non-uniformity introduces complexity in analyzing the signal propagation behavior using conventional transmission line theory. To address this difficulty, the scattering parameter (S-parameter) method is employed to evaluate the influence of the cable joint on signal propagation.

S-Parameter of Cable Joints

Cable joints are two-port networks, and their influence on signal propagation can be characterized using S-parameters [87]. In the S-parameters of two-port networks, S_{11} and S_{22} are the reflection coefficients at ports 1 and 2, respectively. The input impedance of a cable joint can indicate the mismatch between the joint and the cable body. The input impedance of the cable joint when connected to a cable can be calculated using the S_{11} and shown as:

$$Z_{\text{in}} = Z_{\text{ref}} \frac{1 + S_{11}}{1 - S_{11}} \tag{2.9}$$

where Z_{in} is the input impedance of the cable joint, Z_{ref} is the cable characteristic impedance (35 Ω), and S_{11} is referenced to 35 Ω.

To calculate the S-parameters of joints, the cable joint is modeled using the FEM. Owing to its centrosymmetric structure, a two-dimensional axisymmetric model is adopted to reduce computational cost. The material parameters used in the FEM simulation are listed in Table 2.1. The transient FEM simulation results of the cable joint are shown in Fig. 2.6. In the figure, the color map represents the magnitude of the electric field at a signal frequency of 2 GHz. The red arrows indicate the direction of the magnetic field, while the black arrows represent the direction of the electric field.

S_{11} and S_{21} of the cable joint are calculated using Fourier transform, and their curves as functions of frequency are illustrated in Fig. 2.7. To compare the differences in S-parameters between the cable joint and the cable body, the S-parameters of a typical 35 mm^2, 8.7/15 kV cable, as listed in Table 2.2, are calculated. Using (2.9), the input impedance of the cable joint is shown in Fig. 2.8. The characteristic impedance of a typical 10 kV cable shown in Table 2.2 is approximately 35 Ω and input impedance of a joint is frequency-dependent and is

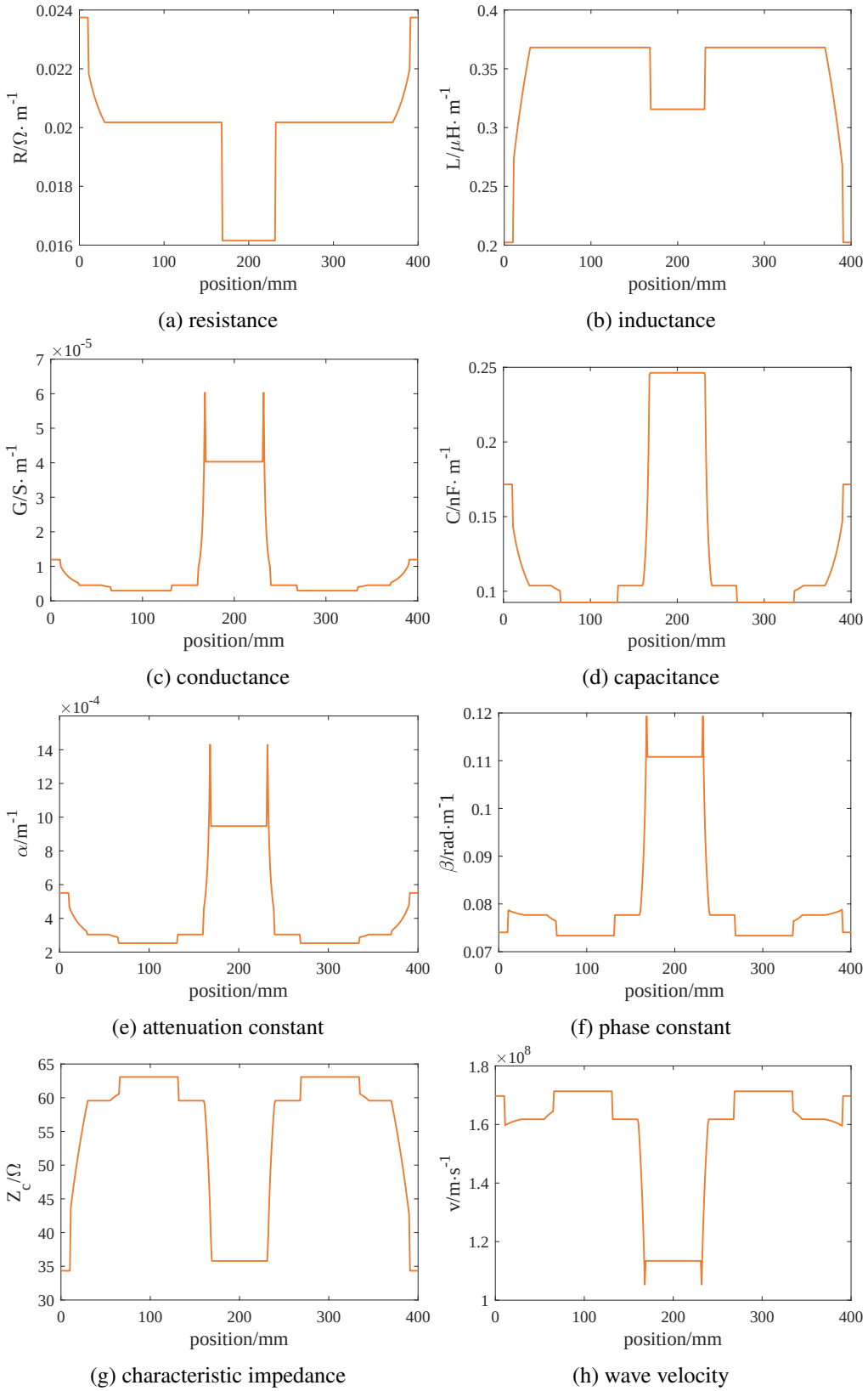


Fig. 2.5 Distributed parameters of the cable joint at 2 MHz

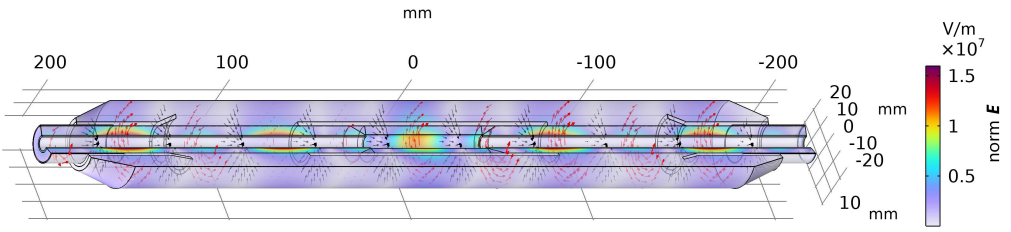
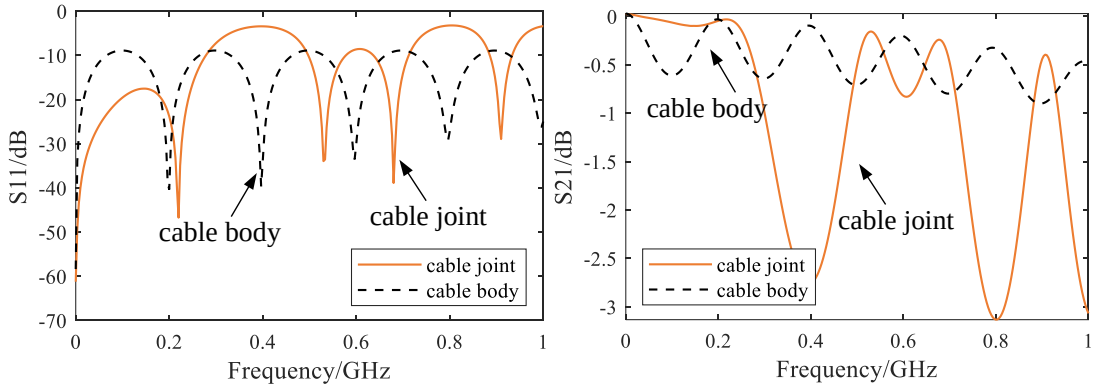


Fig. 2.6 Distribution of electric and magnetic field in the cable joint

approximately 38.6 Ω at 20 MHz. As a result, signal reflection occurs at the cable joint during propagation.

Table 2.2 Parameters of the 8.7/15 kV Single-core Cable

Components	radius/mm	Electric parameters
Core	3.335	$\sigma = 5.98 \times 10^7\,\mathrm{S\,m^{-1}}$
Inner-semiconductor	4.115	$\varepsilon = 500$
XLPE	8.635	$\varepsilon' = 2.3, \quad \varepsilon'' = -0.001$
Outer-semiconductor	9.125	$\varepsilon = 500$
Shield	9.325	$\sigma = 5.98 \times 10^7\,\mathrm{S\,m^{-1}}$
Sheath	12.115	$\varepsilon = 2.25$



(a) S_{11} of the cable joint

(b) S_{21} of the cable joint

Fig. 2.7 S-parameter of the cable joint with 50 Ω reference impedance

Prior to cable defect modeling, cable defects are systematically classified into lumped or distributed types based on their electrical behavior [38]. When the pulse's electrical length l_{tw} is much greater than the defect length Δl_{f}, the defect is modeled as a distributed defect if both voltage and current remain continuous across it. If voltage or current is discontinuous under the same condition, it is treated as a lumped defect. When the pulse is shorter than the defect, the two ends of the defect are individually modeled as lumped defects. The classification is illustrated in Fig. 2.9.

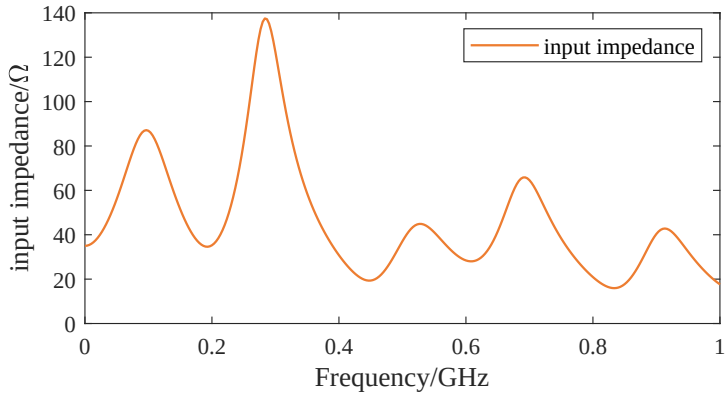


Fig. 2.8 Input impedance of the cable joint

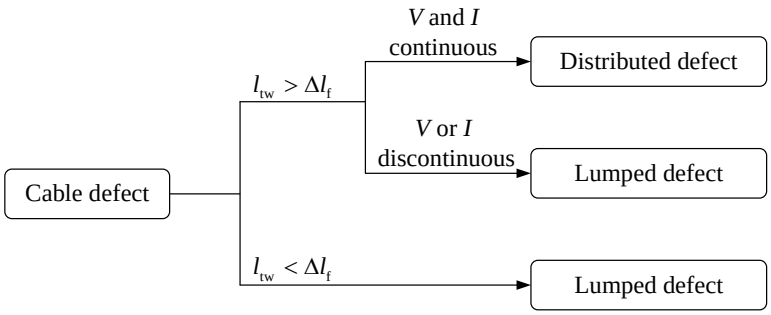


Fig. 2.9 Classification of cable defects

2.1.3 Modeling and Analysis of Lumped Defects in Cable

Lumped defects are modeled using lumped elements and typically classified as ground or series resistance defects [39, 64]. A ground defect results from insulation damage, leading to a direct or resistive connection between the conductor and ground, as shown in Fig. 2.10a, where R_g is the equivalent ground resistance. A series resistance defect is modeled by a resistor R_s in series with the conductor, as shown in Fig. 2.10b.



(a) Ground defect (b) Serial resistance defect

Fig. 2.10 Equivalent circuit of lumped defects

The reflection coefficients of the defect can be calculated as follows:

$$\Gamma_g = \frac{R_g // Z_{c2} - Z_{c1}}{R_g // Z_{c2} + Z_{c1}} \tag{2.10}$$

$$\Gamma_s = \frac{R_s + Z_{c2} - Z_{c1}}{R_s + Z_{c2} + Z_{c1}} \tag{2.11}$$

Usually, cable I and cable II are the same cable type. Therefore (2.10) and (2.11) can be simplified as

$$\Gamma_{\mathrm{g}} = \frac{R_{\mathrm{g}} // Z_{\mathrm{c}} - Z_{\mathrm{c}}}{R_{\mathrm{g}} // Z_{\mathrm{c}} + Z_{\mathrm{c}}} \tag{2.12}$$

$$\Gamma_{\mathrm{s}} = \frac{R_{\mathrm{s}}}{R_{\mathrm{s}} + 2Z_{\mathrm{c}}} \tag{2.13}$$

where Γ_{g} and Γ_{s} denote the reflection coefficients of the ground defect and the series resistance defect, respectively. The symbol "//" represents a parallel connection of impedances. Equations (2.12) and (2.13) describe the reflection coefficients of lumped defects.

2.1.4 Modeling and Analysis of Distributed Defects in Cable

Modeling and Analysis of Shield Corrosion Defects

Shield corrosion is a common defect in power cables, particularly those buried underground. Once the outer sheath is damaged, water can infiltrate the cable and corrode the copper shield. The shield is constructed as a tape-wrapped layer, where copper tape is wound around the outer semiconductor. The structure of the shield is illustrated in Fig. 2.11, which clearly shows the overlapping tape-wrapped configuration. After water ingress, the shield undergoes gradual corrosion. In the early stage, patina forms only on the surface of the shield, causing minimal impact on the cable [88]. As corrosion progresses, patina begins to accumulate between adjacent layers of the shielding tape, altering the current path within the shield. Once corrosion fully occupies the gaps between layers, the current follows a helical trajectory along the shield.

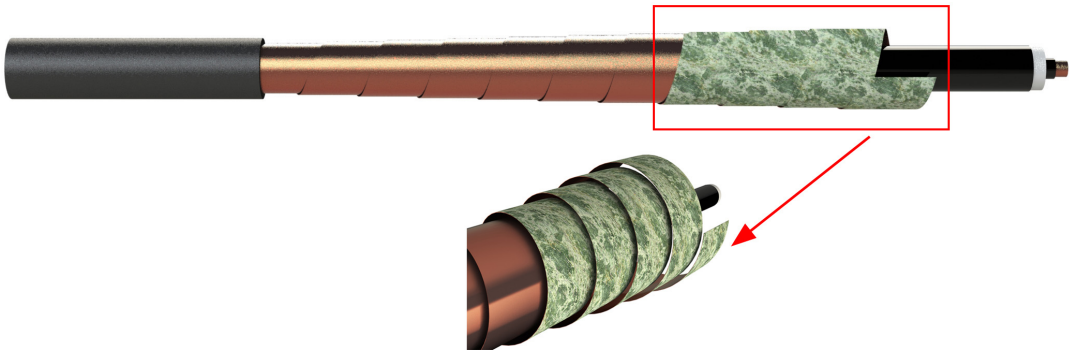


Fig. 2.11 Cable shield with corrosion defect

Modeling of Shield Corrosion Defect To analyze the influence of shield corrosion defects on signal propagation, the distributed parameters of the affected cable must be calculated. Due to the spiral path of the current in the corroded shield, an additional equivalent inductance is

introduced [42]. The distributed parameter model of the cable with shield corrosion is therefore modified, as shown in Fig. 2.12, where L_{sc} represents the additional inductance caused by the shield corrosion defect.

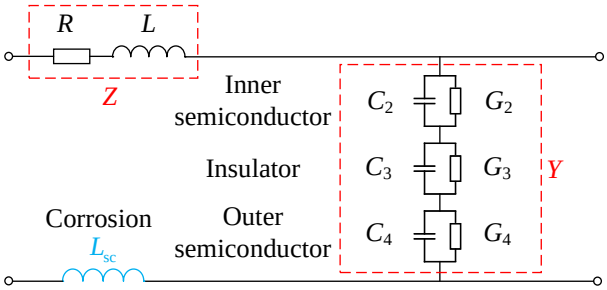


Fig. 2.12 Distributed-parameter model of cable with shield corrosion.

The corroded shield can be modeled as a solenoid coil, which enables the application of standard solenoid inductance formulas to estimate the additional equivalent inductance introduced by corrosion. To perform this calculation accurately, it is essential to define the detailed geometry of the spiral shield structure. The relevant geometric parameters are illustrated in Fig. 2.13, where M_w and M_h represent the width and pitch of the spirally wound copper tape, respectively, and r_4 denotes the radius of the cable's outer semiconductor layer.

The equations for calculating the inductance of a solenoid coil are as follows [89].

$$L_{sc} = N_4 \frac{\Phi_4}{I_4} \tag{2.14a}$$

$$\Phi_4 = B_4 S_4. \tag{2.14b}$$

where Φ_4 is the magnetic flux in the solenoid coil, and I_4 is the current. N_4 denotes the number of turns of the copper shield in a 1 m length of cable, B_4 is the magnetic flux density, and S_4 is the cross-sectional area of the solenoid coil. These quantities are defined as follows.

$$N_4 = \frac{1}{M_h} \tag{2.15}$$

$$B_4 = 2\mu_0 J_4 \tag{2.16}$$

$$S_4 = \pi r_4^2 \tag{2.17}$$

$$J_4 = \frac{I_4}{M_a} \tag{2.18}$$

where J_4 is the line current density in the shield. The magnetic flux density B_4 consists of two components: the current in the single-layer region M_h and the overlap current in the overlapping region M_p. By substituting (2.15), (2.16), and (2.17) into (2.14), the additional equivalent

inductance induced by the shield corrosion defect can be expressed as follows:

$$L_{\mathrm{sc}} = \frac{2\mu_0 S_4}{M_{\mathrm{h}} M_{\mathrm{a}}} \tag{2.19}$$

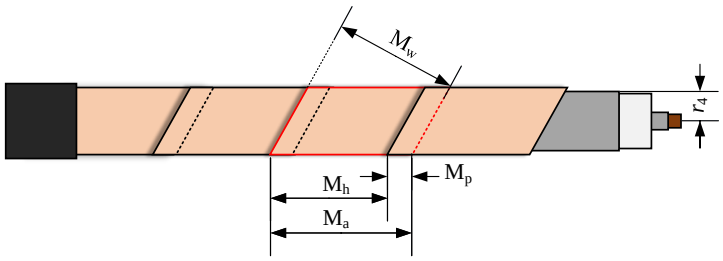


Fig. 2.13 Geometric parameters of the spiral shield.

In (2.19), L_{sc} is related to the shield structural parameters M_{h} and M_{p}. Typically, M_{h} and M_{p} are not directly known; however, the overlap ratio $\eta = M_{\mathrm{p}}/M_{\mathrm{a}}$ and the tape width M_{w} are usually provided in cable handbooks [90]. Therefore, M_{h} and M_{a} can be derived from η as follows:

$$M_{\mathrm{h}} = \frac{2\pi r_4 (1-\eta) M_{\mathrm{w}}}{\sqrt{(2\pi r_4)^2 - (1-\eta)^2 M_{\mathrm{w}}^2}} \tag{2.20}$$

$$M_{\mathrm{a}} = \frac{M_{\mathrm{h}}}{1-\eta} \tag{2.21}$$

By substituting (2.20) into (2.19), the additional equivalent inductance induced by the corroded shield can be expressed as:

$$L_{\mathrm{sc}} = \frac{\mu_0}{2\pi} \frac{(2\pi r_4)^2 - (1-\eta)^2 M_{\mathrm{w}}^2}{(1-\eta) M_{\mathrm{w}}^2} \tag{2.22}$$

Considering the small overlap ratio η and the large inter-turn spacing of a solenoid equivalent to overlapping currents, the magnetic flux density B_4 can be simplified as follows:

$$B_4 = \mu_0 \frac{I_4}{M_{\mathrm{h}}}. \tag{2.23}$$

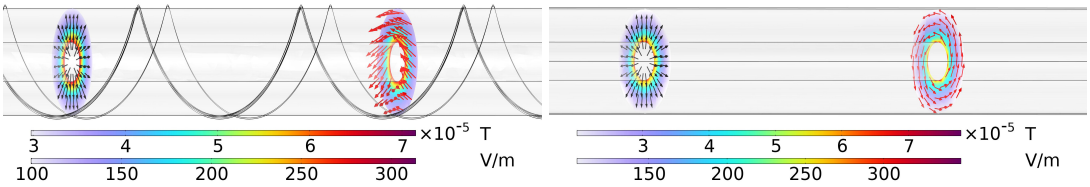
Therefore, L_{sc} can be further simplified as follows:

$$L_{\mathrm{sc}} = \frac{\mu_0}{4\pi} \frac{(2\pi r_4)^2 - (1-\eta)^2 M_{\mathrm{w}}^2}{(1-\eta)^2 M_{\mathrm{w}}^2} \tag{2.24}$$

Based on the distributed-parameter model of cables, the distributed inductance of a cable with shield corrosion can be approximated as

$$L_{\mathrm{s}} \approx \frac{1}{2\sqrt{2}\pi r_1}\sqrt{\frac{\mu_0}{\omega\sigma_1}} + \frac{1}{2\sqrt{2}\pi r_5}\sqrt{\frac{\mu_0}{\omega\sigma_5}} + \frac{\mu_0}{2\pi}\ln\frac{r_5}{r_1} + \frac{\mu_0}{4\pi}\frac{(2\pi r_4)^2 - (1-\eta)^2 M_{\mathrm{w}}^2}{(1-\eta)^2 M_{\mathrm{w}}^2} \tag{2.25}$$

Validation of Shield Corrosion Model Equation (2.25) provides a method for calculating the distributed inductance of a shield corrosion defect. To validate this equation, a shield corrosion defect was modeled and analyzed using the FEM. In the FEM simulation, the rust-filled regions between adjacent layers of the shield are represented as air-filled gaps. To enable comparison with a perfect cable, a defect-free cable was also modeled in the FEM simulation software. After the simulations, the electric and magnetic field distributions in both the corroded and perfect cables were compared, as shown in Fig. 2.14. In the figure, the black arrows represent the direction of the electric field, with the surrounding color map indicating its magnitude. The red arrows denote the direction of the magnetic flux density, and the corresponding color map illustrates its strength.



(a) Cable with shield corrosion (b) Cable without shield corrosion

Fig. 2.14 Distribution of electric and magnetic fields in cables with and without shield corrosion defects

Comparing Fig. 2.14a and Fig. 2.14b, the magnetic flux density in the corroded cable shows a spiral distribution with a notable axial component, unlike the perfect cable where it mainly encircles the conductor. This axial component contributes to additional equivalent inductance. In contrast, the electric field distribution remains similar in both cases. Further, the additional equivalent inductance L_{sc} is calculated using FEM simulation. For a cable with a shield overlap ratio of $\eta = 15\,\%$, the inductance L_{sc} due to shield corrosion is computed as $356.8\,\mathrm{nH\,m^{-1}}$ in the FEM simulation. In comparison, the value derived from the analytical equation (2.25) is $364.4\,\mathrm{nH\,m^{-1}}$. Furthermore, a comparative analysis between the simulation and analytical results for various shield overlap ratios is presented in Table 2.3.

From Table 2.3, the FEM results and the analytical equation for the distributed inductance due to shield corrosion show excellent agreement, with a maximum discrepancy of only 2.1 %, indicating that the proposed equation accurately models the additional inductance introduced by such defects. Furthermore, based on the distributed-parameter model, the characteristic

Table 2.3 Comparison of L_{sc} values calculated by FEM and the analytical equation

Samples	η/%	L_{FEM}/nH	L_{s}/nH	Error/%
Cable I	5	266.6	271.8	2.0
	10	307.9	314.2	2.1
	15	356.8	364.4	2.1

impedance of a shield corrosion defect with $\eta = 15\,\%$ is calculated as $52.7\,\Omega$, significantly higher than that of an intact cable ($35\,\Omega$).

Modeling and Analysis of Cable Shield Hole Defects

Among the various defects that can occur in cables, shield breaches or holes are another common type encountered during cable diagnostics. These defects typically arise from external mechanical damage or severe corrosion of the shield. Shield holes can exhibit diverse shapes, such as circular, oval, rectangular, or other irregular forms. However, in the context of defect analysis, the exact shape of the hole is less critical than its dimensions—specifically, its length and width. Therefore, for modeling purposes, the shield hole is simplified as a rectangular aperture [69]. A typical example is shown in Fig. 2.15, which illustrates a shield hole resulting from corrosion or damage. The hole is represented as a rectangle projected onto the surface of a cylinder, characterized by a length d and a width defined by the central angle θ.

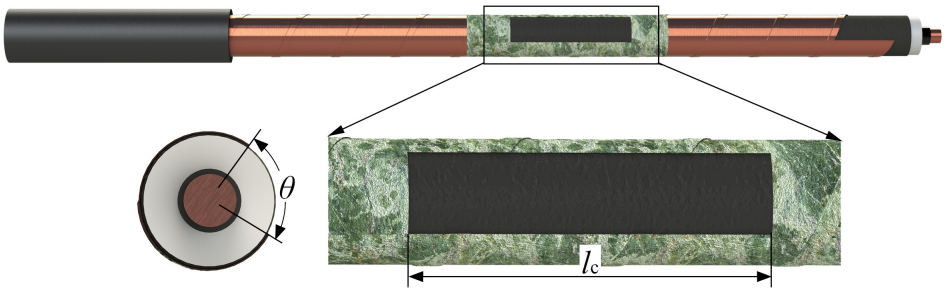


Fig. 2.15 A typical shield hole caused by the corrosion in the cable

Modeling of Shield Hole Defects Using FEM Shield holes compromise the structural integrity of the cable, making it difficult to model using traditional analytical methods. To address this, FEM simulations are employed to calculate the distributed parameters of cables with shield corrosion holes, including resistance R_{s}, inductance L_{s}, conductance G_{s}, and capacitance C_{s}. A two-dimensional cross-sectional FEM model is shown in Fig. 2.16. In the 2D cross-sectional simulation, the defect length is set to 1 m.

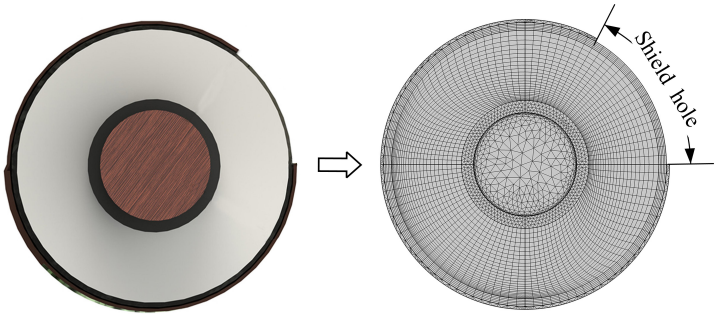
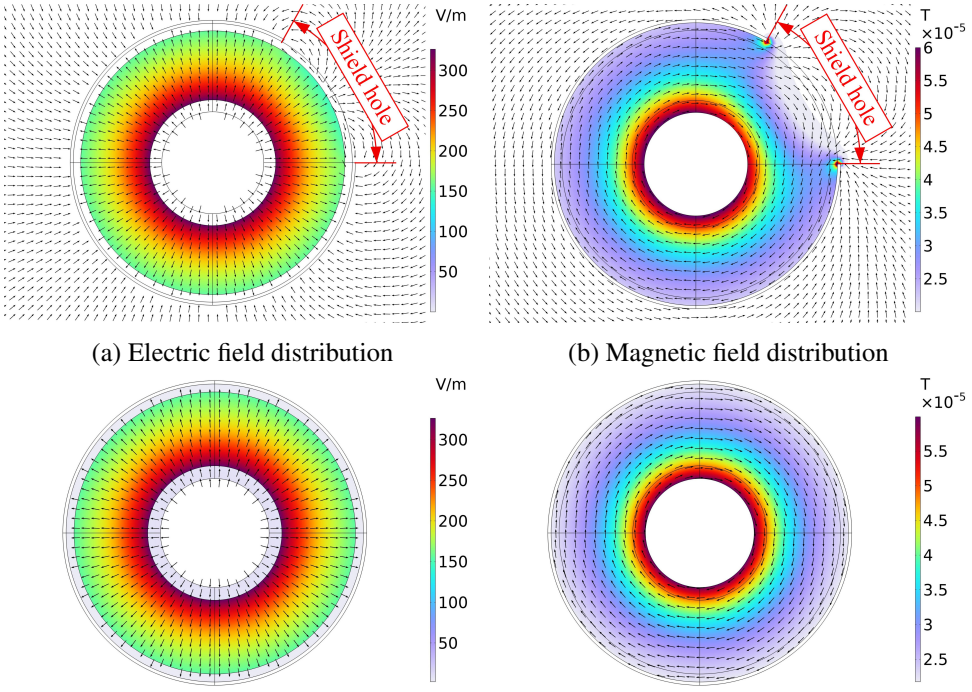


Fig. 2.16 FEM model of the cable with shield hole

Fig. 2.17 presents the FEM simulation results, showing the electromagnetic field distribution in the cross-section of a cable with a shield hole. To highlight the differences between cables with and without shield holes, the electric and magnetic field distributions of the defective cable are compared with those of a perfect cable, which are also shown in Fig. 2.17. The comparison reveals significant leakage of both electric and magnetic fields in the cable with a shield hole, indicating that such defects substantially affect signal propagation along the cable.



(a) Electric field distribution

(b) Magnetic field distribution

(c) Electric field distribution

(d) Magnetic field distribution

Fig. 2.17 Electric and magnetic field distribution in the cable with and without a shield hole

The distributed parameters of the cable with shield holes of various central angles are calculated [91], and the results are shown in Fig. 2.18. The comparison reveals that as the central angle increases, the distributed resistance R and inductance L increase, while the distributed conductance G and capacitance C decrease. Additionally, the attenuation constant α and the characteristic impedance Z_c increase with the central angle of the shield hole, whereas

the wave velocity v decreases. For example, as the central angle increases from 0° to 300°, Z_c rises from 35 Ω to 61.8 Ω.

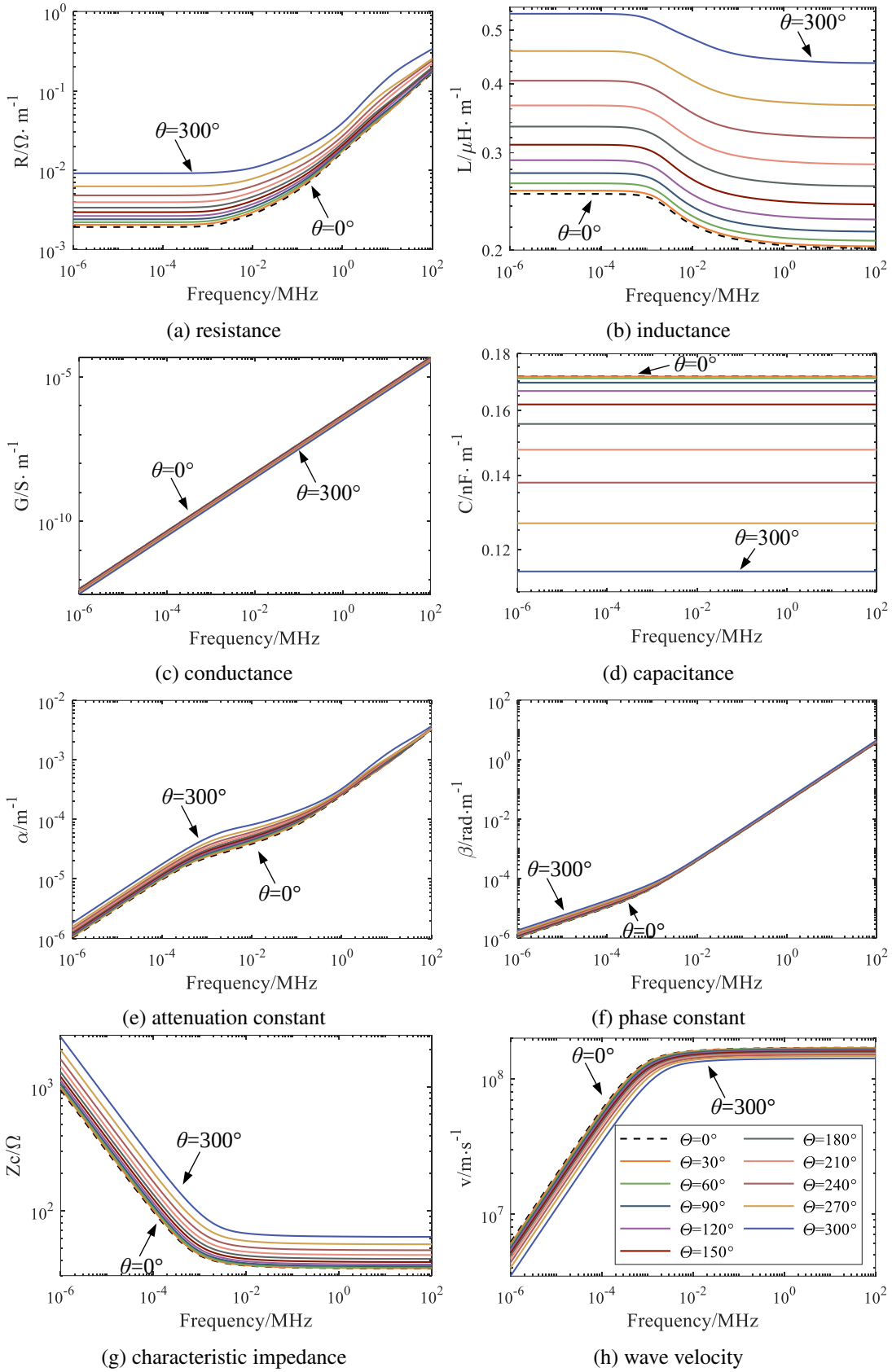
Modeling and Analysis of Water Ingress Defects in Cables

Water ingress is another common defect in cables. When the cable sheath is damaged, water can enter the cable and degrade the insulation layer. Based on the extent of water ingress, it can be classified into two types: light water ingress and heavy water ingress. In light water ingress, water only covers the surface of the insulation layer, exerting minimal impact on signal propagation characteristics. However, it can corrode the shield, leading to shield corrosion defects. In heavy water ingress, water penetrates the insulation layer in the form of water trees. This type of ingress significantly affects the cable's propagation characteristics and weakens the insulation layer.

Simulation of Light Water Ingress Defect To analyze the changes in the cable's propagation characteristics due to water ingress, the cable with a water ingress defect is modeled and simulated using FEM. First, the defect caused by light water ingress is analyzed. Considering the distribution of ingressed water on the surface of the insulation layer, various water distribution scenarios are modeled in FEM [92]. In the FEM model, the water is represented as a thin layer between the shield and the outer semiconductor. The thickness of the water layer is set to 0.1 mm. The distribution of the water layer on the insulation surface is described using the central angle θ of the water layer in the cable cross-section. Six different central angles are considered in the simulation: 60°, 120°, 180°, 240°, 300°, and 360°. The FEM model of the cable with a light water ingress defect is shown in Fig. 2.19a.

The simulation results of the distributed parameters are shown in Fig. 2.20. As observed, the light water ingress defect has minimal impact on the distributed resistance and inductance, indicating that these parameters are relatively insensitive to such localized moisture intrusion. However, the distributed conductance and capacitance exhibit noticeable increases as the central angle of the defect expands. Regarding the propagation constants, both the attenuation constant and the phase constant increase with the central angle of the defect, indicating higher signal loss and slower phase propagation. In contrast, the characteristic impedance and wave velocity gradually decrease as the central angle increases, which suggests stronger impedance mismatch in the affected cable segment.

Simulation of Water Tree Defect Water tree defects are a form of heavy water ingress, caused by moisture penetrating the insulation layer of the cable under the influence of an electric field. Water trees grow along the direction of the electric field, and their impact on the cable's propagation characteristics is related to their volume [93]. In addition to volume, the



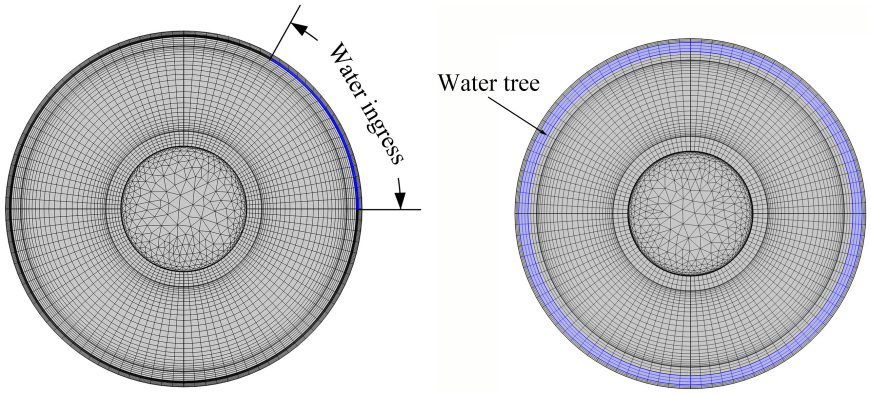
(a) resistance (b) inductance

(c) conductance (d) capacitance

(e) attenuation constant (f) phase constant

(g) characteristic impedance (h) wave velocity

Fig. 2.18 Distributed parameters of the cable with shield hole



(a) Light water ingress defect (b) Water tree

Fig. 2.19 FEM model of the cable with water ingress defect

water content within the water tree also significantly affects signal propagation. To analyze this influence, the cable with a water tree defect is modeled using FEM simulation software. When a water tree forms in the insulation layer, the permittivity of the insulation changes. The equivalent permittivity of the insulation layer with a water tree defect can be calculated based on the structure of the defect. The structure of insulation with a water tree defect is illustrated in Fig. 2.21.

Assuming the ratio of the water tree area to the water-treed XLPE area gives the water tree concentration c_{wt}, and the water contained in each water tree as a percentage of its total volume is denoted as m_{wt}, the water content W_{wt} in the water-treed XLPE is given by [50]:

$$W_{\mathrm{wt}} = c_{\mathrm{wt}} m_{\mathrm{wt}} \tag{2.26}$$

According to an effective medium theory [94], the equivalent permittivity of the water-treed XLPE can be expressed as follows:

$$\varepsilon_{wt} = \varepsilon_{\mathrm{PE}} \left(1 + \frac{W_{\mathrm{wt}}(\varepsilon_{\mathrm{w}} - \varepsilon_{\mathrm{PE}})}{\varepsilon_{\mathrm{PE}} + D(1 - W_{\mathrm{wt}})(\varepsilon_{\mathrm{w}} - \varepsilon_{\mathrm{PE}})} \right) \tag{2.27}$$

where ε_{w} is the permittivity of water, $\varepsilon_{\mathrm{PE}}$ is the permittivity of XLPE, and D is the dimensionless depolarization factor, which depends on the shape of the water tree. When the shape is spheroidal, $D = 1/3$.

In the simulation, water tree defects with various water tree concentrations c_{wt} and different ratios t_{wt}—defined as the ratio of the thickness of water-treed XLPE to the total insulation thickness—are analyzed. The concentration c_{wt} ranges from 0.05 to 1.00 in increments of 0.05, while the thickness ratio t_{wt} ranges from 0.05 to 0.95 with the same step size. The FEM simulation model is shown in Fig. 2.19a, and the simulation results for the distributed parameters of the water tree defects are presented in Fig. 2.22.

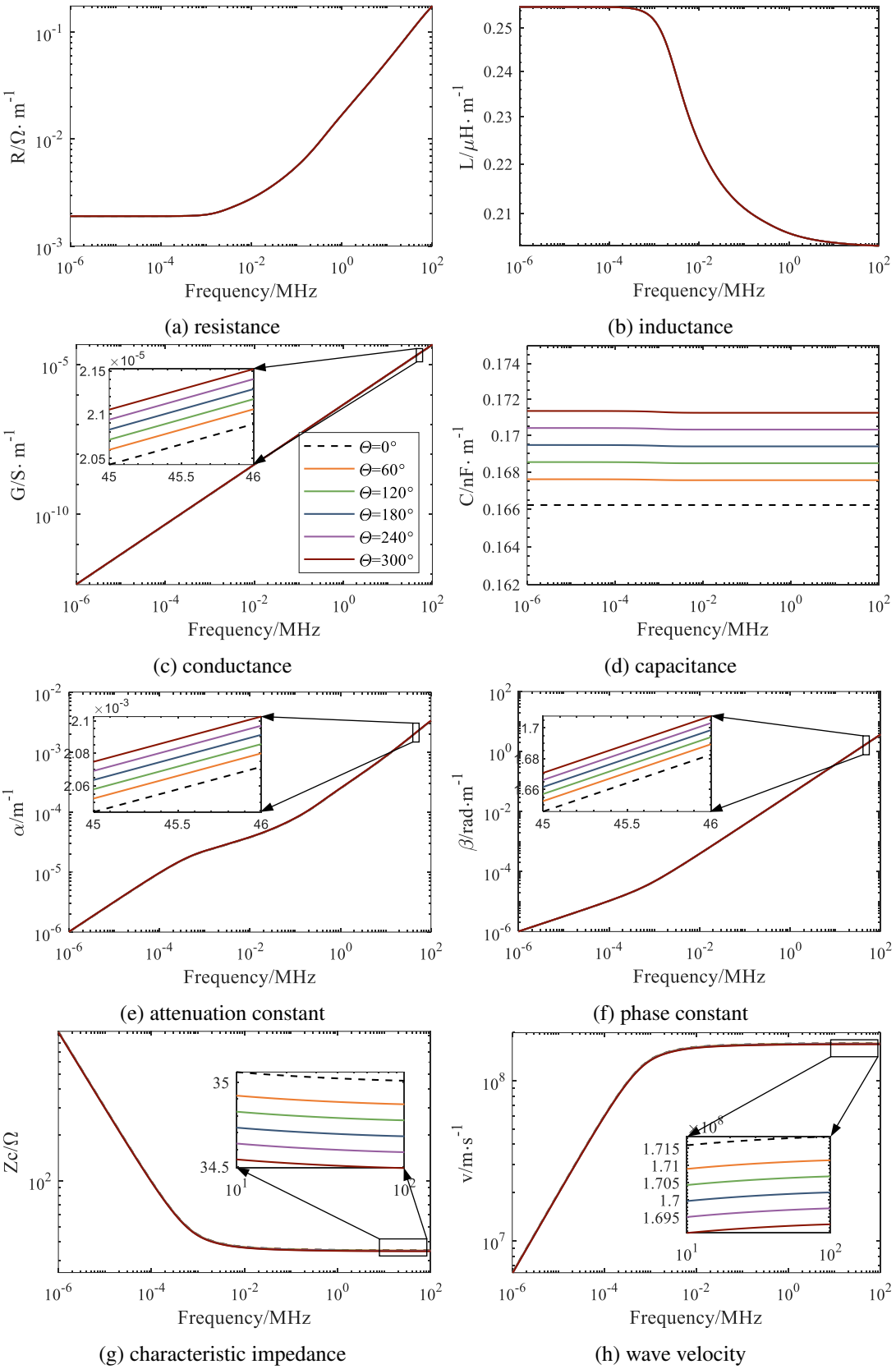


Fig. 2.20 Distributed parameters of the cable with light water ingress defect

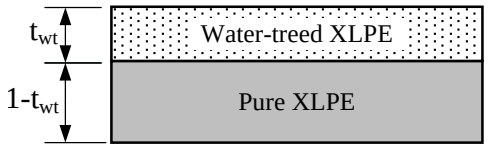


Fig. 2.21 Water tree defect in the insulation of the cable

From the simulation results shown in Fig. 2.22, it can be observed that the distributed resistance R and inductance L are scarcely affected by the presence of water tree defects. In contrast, the distributed conductance G and capacitance C are significantly influenced. As the water tree concentration c_{wt} and thickness ratio t_{wt} increase, both G and C exhibit a corresponding increase. Similarly, the attenuation constant α and phase constant β also increase with the severity of the water tree defect. Conversely, Z_c and v decrease as the defect becomes more pronounced. Specifically, when the water tree concentration c_{wt} increases from 0.05 to 1.00 and the thickness ratio t_{wt} increases from 0.05 to 0.95, Z_c drops from 35 Ω to 11 Ω.

2.2 Propagation Characteristics Measurement of Cable Defects

To validate the modeling and simulation results, cable samples with water ingress defects are fabricated and measured, using water ingress as a representative example. In this experiment, the S-parameters of the defected samples are measured using a VNA. Based on the measured S-parameters, the characteristic parameters of the cables with water ingress defects are derived. By comparing the characteristic parameters of cables with varying degrees of water ingress, the impact of water ingress on signal propagation characteristics is analyzed.

2.2.1 Fundamentals of S-Parameters Measurement

The S-parameters are measured using a VNA, and the schematic of the measurement setup is shown in Fig. 2.23a [95]. The device under test (DUT) is connected to the two ports of the VNA, and the S-parameters are obtained accordingly. Typically, the DUT is connected to the VNA via coaxial cables. For standard DUTs, coaxial connectors such as subminiature version A (SMA) connectors are used. However, for certain special DUTs, dedicated fixtures are required to establish the connection. Due to the influence of fixtures, the direct measurement results obtained from the VNA contain the combined propagation characteristics of the two fixtures and the DUT, as illustrated in Fig. 2.23b. To extract the intrinsic propagation characteristics of the DUT alone, the measured results need to be de-embedded.

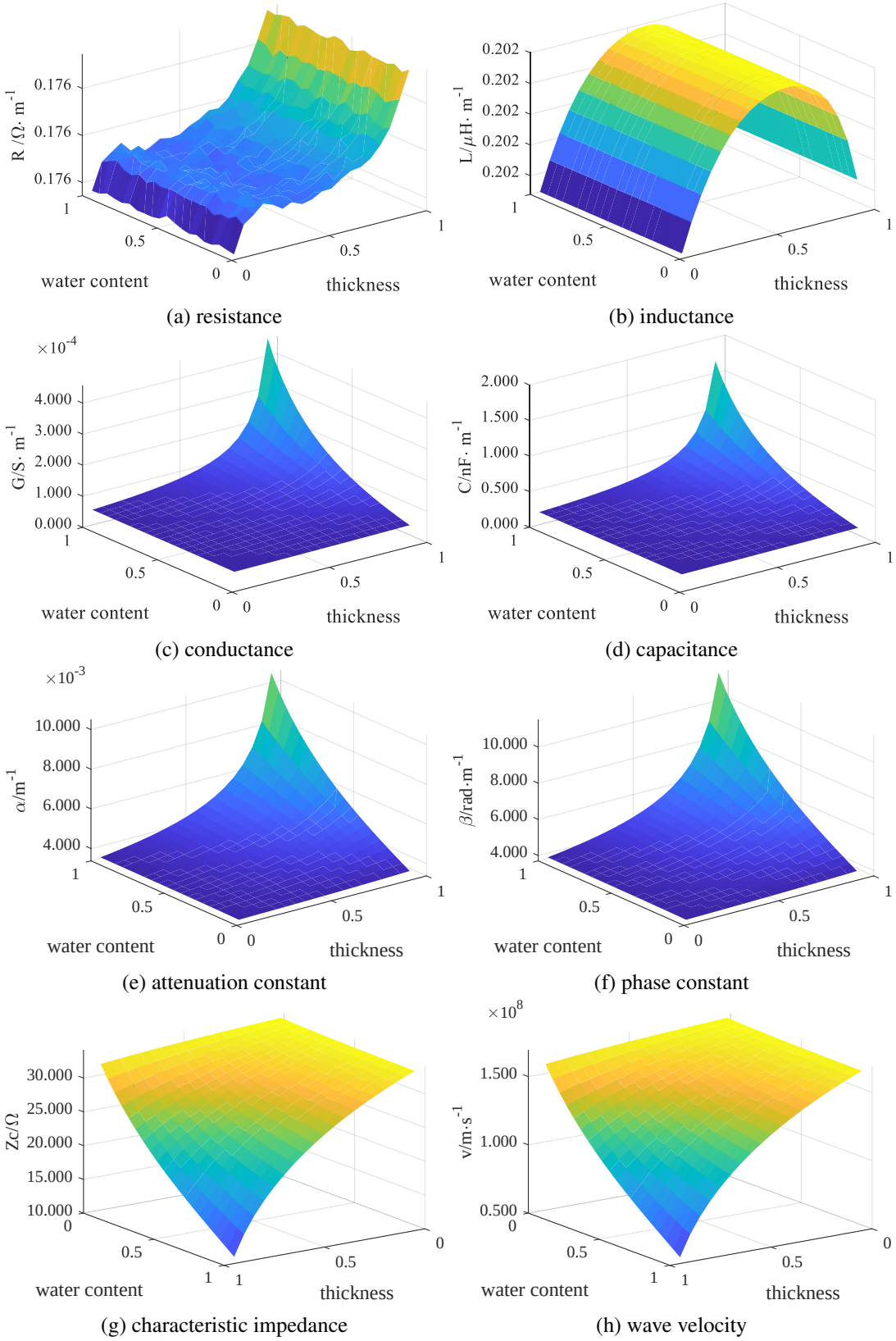
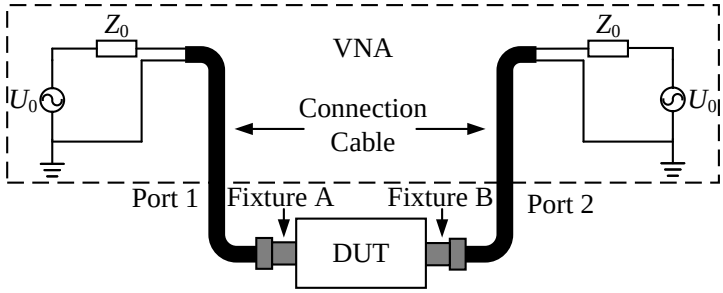
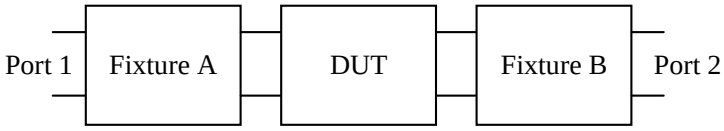


Fig. 2.22 Distributed parameters of the cable with various water tree defect



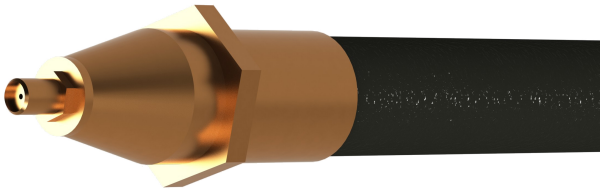
(a) Principle of S-parameter measurement



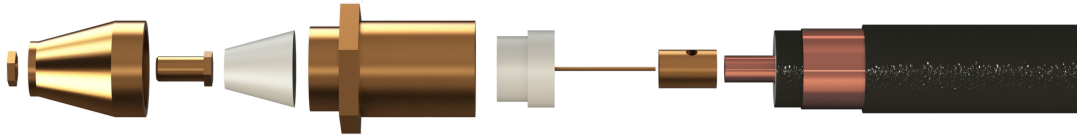
(b) The connection of two fixtures and DUT

Fig. 2.23 S-parameter measurement using VNA

To measure the S-parameters of power cables with defects, a dedicated fixture is designed to interface the cable with the VNA. The fixture and its structural details are illustrated in Fig. 2.24. For standard DUTs with coaxial connectors, de-embedding can be performed using the short-open-load-through (SOLT) calibration method with standard calibration kits. Since the fixture does not conform to standard coaxial connector interfaces. For the special fixtures, the de-embedding is carried out using the time-domain gating method [96].



(a) Fixture for cable defect S-parameter measurement



(b) Structure of the fixture

Fig. 2.24 Fixture Components

2.2.2 Cable Defect S-Parameter Measurement

Because water ingress accounts for a large proportion of cable faults, water ingress defects were specifically tested in the experiment. To investigate the impact of moisture ingress on cable propagation characteristics, an experiment was conducted to measure the S-parameters of cables with varying degrees of moisture ingress. Cable samples with different defect lengths

were fabricated. To simulate moisture ingress, the cable sheath was cut and the cable was placed in water-filled pipes for a designated duration. The fabricated samples are shown in Fig. 2.25. Three defect lengths were prepared: 0.5 m, 1 m, and 2 m. Each sample includes custom fixture at both ends and 0.5 m of intact cable on each side. A PicoVNA 106 VNA was used to measure the S-parameters across the frequency range from 0.3 MHz to 600 MHz, with a frequency resolution of 0.3 MHz.

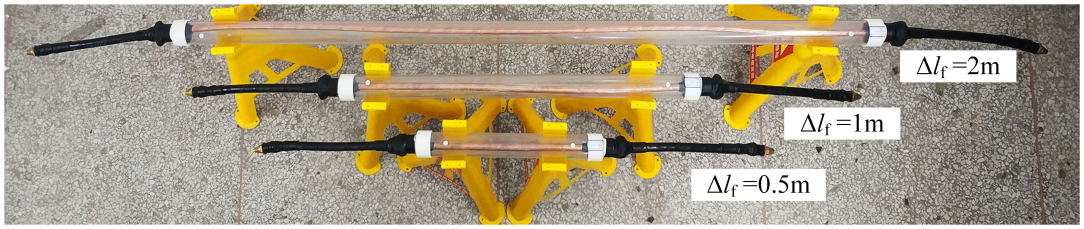
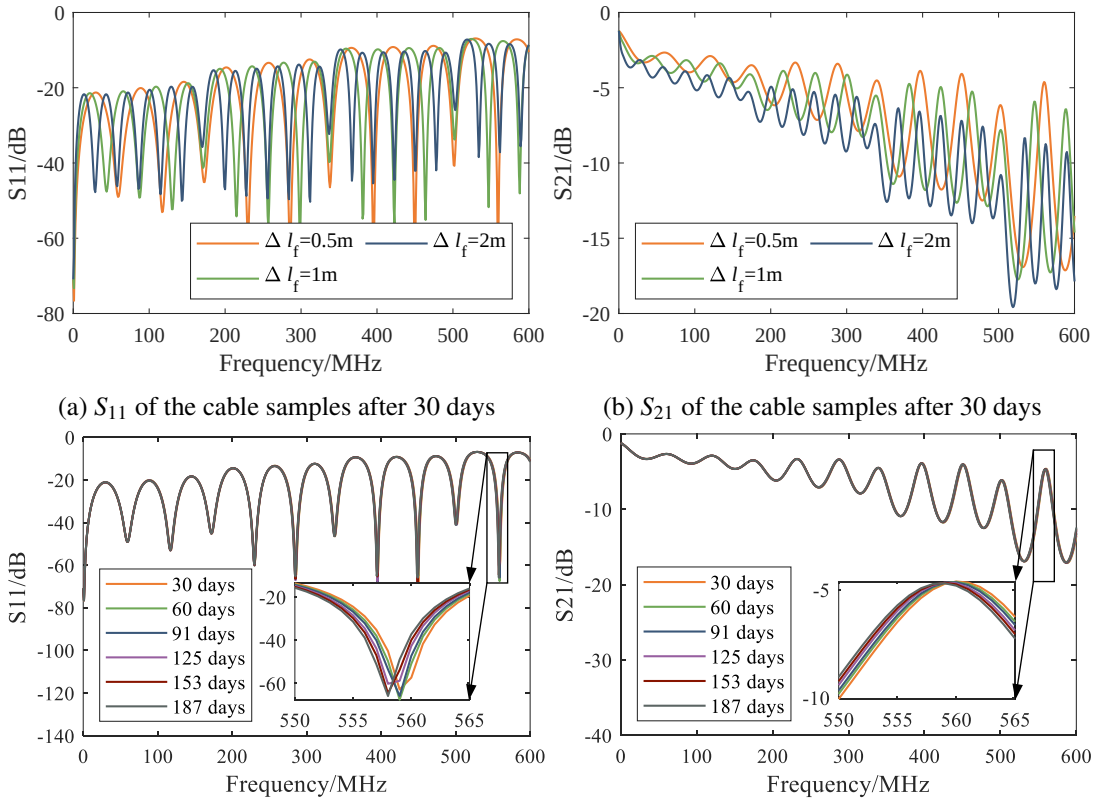


Fig. 2.25 Cable defect samples with different degrees of moisture ingress

The experiment lasted for six months, during which the cables were measured at approximately 30-day intervals. As the immersion time increased, the extent of moisture ingress gradually increased, enabling the evaluation of samples with different levels of water ingress. The measured S-parameters of typical cable samples are presented in Fig. 2.26.



(a) S_{11} of the cable samples after 30 days

(b) S_{21} of the cable samples after 30 days

(c) S_{11} of the 0.5 m-long cable

(d) S_{21} of the 0.5 m-long cable

Fig. 2.26 Measured S-parameters of the cable samples

Figures 2.26a and 2.26b show the measured S_{11} and S_{21} of cables with different defect lengths. Figures 2.26c and 2.26d present the S_{11} and S_{21} of cables with varying moisture levels. As shown, slight variations in S_{11} and S_{21} indicate gradual water penetration into the cable. Moreover, the influence of moisture ingress on propagation characteristics becomes more pronounced at higher frequencies.

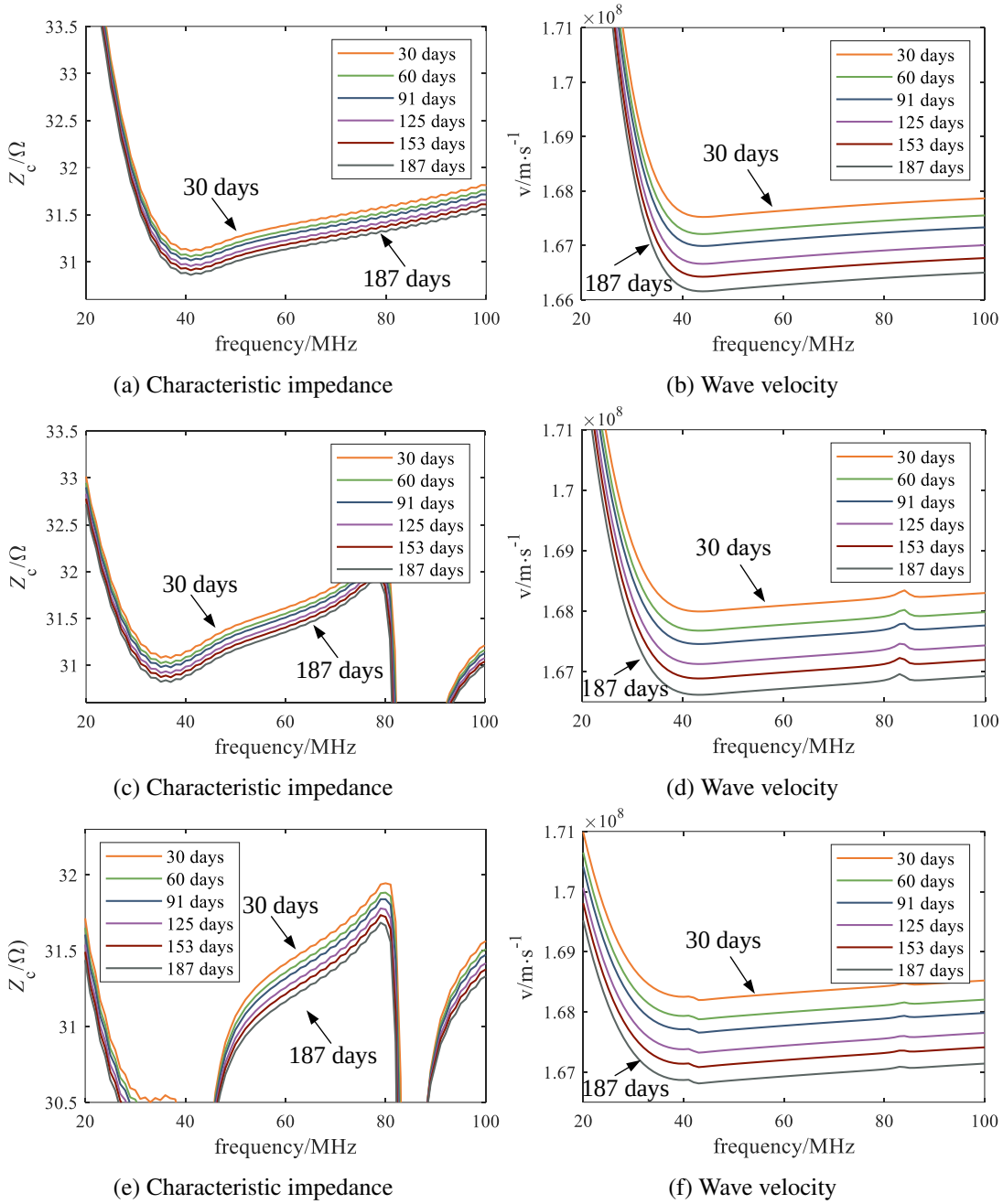
2.2.3 Analysis of Cable Defect Characteristics Using S-Parameters

By applying the time-domain gating method, the fixture contributions are removed from the measured S-parameters of the cable samples. The de-embedded S-parameters are then used to calculate the characteristic parameters of the cables. Fig. 2.27 presents the calculated results, including the characteristic impedance Z_c and wave velocity v, for cable samples with varying degrees of moisture ingress.

Analyzing the characteristic parameters of the cable samples with varying degrees of moisture ingress reveals that the Z_c and v decrease as the moisture level increases. This behavior is attributed to the rise in the dielectric constant of the insulation layer caused by moisture ingress, which reduces both Z_c and v. The Z_c curves exhibit irregularities, particularly around 85 MHz for the 1 m and 2 m cable samples. These anomalies are due to the sensitivity of Z_c calculations to resonant nulls in the S_{21} and S_{12}. The irregular points correspond to the resonance frequencies in the S_{21} and S_{12} curves, resulting in local fluctuations in the Z_c plots. Furthermore, as the cable length increases, the resonant nulls shift to lower frequencies and become more closely spaced, leading to more frequent irregularities in the Z_c curves. In conclusion, moisture ingress significantly alters the propagation characteristics of cables, causing reductions in both Z_c and v, with more severe effects observed at higher levels of moisture.

2.3 Modeling of Reflectometry Signal in Mulitple-Defect Cables

This section presents a method for calculating the reflection signals of multi-defect cables based on the RCS and analyzes the impact of defects on cable propagation characteristics. First, the RCS of multi-defect cables is computed using distributed-parameter models and S-parameter models. Then, the frequency-domain reflection signal is obtained from the RCS and the time-domain reflection signal is obtained using using the TDFD method. Finally, the RCS is employed to analyze and compare the propagation characteristics of cables with different defects.



(a) Characteristic impedance (b) Wave velocity

(c) Characteristic impedance (d) Wave velocity

(e) Characteristic impedance (f) Wave velocity

Fig. 2.27 Characteristic parameters of cable with water ingress defects. (a) and (b) are the 0.5 m-long cable, (c) and (d) are 1 m, and (e) and (f) are 2 m.

2.3.1 Principle of TDFD Method

The TDFD method is a simple yet powerful approach for solving the time-domain response of a frequency-domain system. Its principle is based on the inverse fast Fourier transform (IFFT). The input signal is decomposed into its sinusoidal harmonic components. Treating the system as a “black box", the steady-state response to each harmonic can be calculated using phasor analysis. Each component is individually processed by the system, and the

corresponding responses are obtained. These responses are then summed and transformed back to the time domain to yield the final time-domain output. The main steps of the TDFD method are summarized by the following equations [86]:

$$S(\omega) = \mathscr{F}\left(s(t)\right) \tag{2.28a}$$

$$R(\omega) = S(\omega) \cdot H(\omega) \tag{2.28b}$$

$$r(t) = \mathscr{F}^{-1}\left(R(\omega)\right) \tag{2.28c}$$

In (2.28), $s(t)$ denotes the input signal, and $S(\omega)$ is its frequency spectrum. $H(\omega)$ is the system transfer function, which corresponds to the RCS of the cable in the context of reflected signal calculation. $R(\omega)$ is the frequency spectrum of the response signal, and $r(t)$ is the time-domain response. $\mathscr{F}$ and $\mathscr{F}^{-1}$ represent the Fourier and inverse Fourier transforms, respectively.

The frequency selection in (2.28) depends on the required time resolution and signal length of the reflected waveform in the time domain. Assuming that the signal length is T and the time resolution is t_s, the frequency parameters can be determined as follows:

$$f_\mathrm{max} = \frac{1}{2t_\mathrm{s}} \tag{2.29a}$$

$$f_\mathrm{s} = \frac{1}{T} \tag{2.29b}$$

where f_max is the maximum frequency used in the frequency-domain representation, and f_s is the frequency resolution. In (2.28), RCS plays a central role and depends on the specific object under investigation. In the following subsection, the RCS for a cable is derived.

2.3.2 RCS General Model for Multiple-Defect Cables

Since different types of defects are modeled using different approaches, the RCS is computed in accordance with the respective modeling method. For the cable body and simple defects, distributed-parameter models are employed. In contrast, joints and complex defects, such as shield-hole defects and water ingress, are characterized using S-parameters. Accordingly, two methods for calculating the RCS of a multiple-defect cable are proposed.

RCS Calculation based on transmission line equations

Assuming that the reflection coefficient at the interface between the cable body and a defect is denoted by Γ, the coefficient Γ_l at a distance l from the interface is given by:

$$\Gamma_\mathrm{l} = \Gamma \mathrm{e}^{-2\gamma l} \tag{2.30}$$

The input impedance Z_{in} at a distance l from the interface is expressed as:

$$Z_{\text{in}} = Z_{\text{c}} \frac{1+\Gamma_{\text{l}}}{1-\Gamma_{\text{l}}} \tag{2.31}$$

where Z_c is the characteristic impedance of the cable.

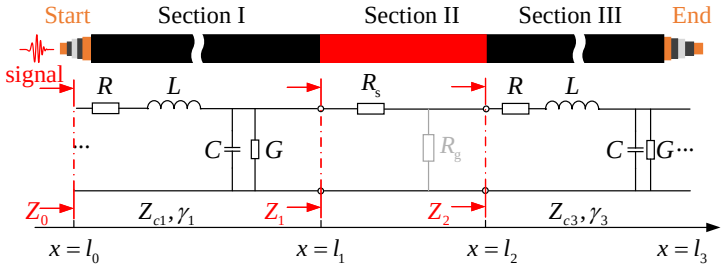


Fig. 2.28 The distributed-parameter model of a long cable with a lumped defect

Fig. 2.28 show a simple scenario where the cable has a lumped defect. Assuming the end of Section III is open-circuited, the reflection coefficient at the end is 1. According to (2.30), the reflection coefficient at $x = l_2$ within Section III can be calculated as follows:

$$\Gamma_{2\text{r}} = \text{e}^{2\gamma_3(l_2-l_3)} \tag{2.32}$$

The input impedance Z_2 of Section III at $x = l_2$ can then be calculated as:

$$Z_2 = Z_{\text{c3}} \frac{1+\Gamma_{2\text{r}}}{1-\Gamma_{2\text{r}}} \tag{2.33}$$

The reflection coefficient Γ_1 in Section I at $x = l_1$ can be derived based on (2.12) and (2.13). Finally, the reflection coefficient Γ_0 at the input of the cable is given by:

$$\Gamma_0 = \Gamma_1 \text{e}^{2\gamma_1(l_0-l_1)} \tag{2.34}$$

A cable with a distributed defect is shown as Fig. 2.29. The derivation of the input impedance Z_2 follows the same procedure as in (2.33). According to (2.31), the reflection coefficient Γ_2 at the interface $x = l_2$ is expressed as:

$$\Gamma_2 = \frac{Z_2 - Z_{\text{c2}}}{Z_2 + Z_{\text{c2}}} \tag{2.35}$$

where Z_{c2} is the characteristic impedance of Section II. By repeating the procedures in (2.32), (2.33), and (2.35), the reflection coefficient $\Gamma_{1\text{r}}$ in Section II at $x = l_1$, the input impedance Z_1 of Section II at $x = l_1$, and the reflection coefficient Γ_1 at the interface $x = l_1$ can be derived as

follows:

$$\Gamma_{1\mathrm{r}} = \Gamma_2 \mathrm{e}^{2\gamma_2(l_1-l_2)} \tag{2.36}$$

$$Z_1 = Z_{\mathrm{c}2}\frac{1+\Gamma_{1\mathrm{r}}}{1-\Gamma_{1\mathrm{r}}} \tag{2.37}$$

$$\Gamma_1 = \frac{Z_1 - Z_{\mathrm{c}1}}{Z_1 + Z_{\mathrm{c}1}} \tag{2.38}$$

The reflection coefficient of the cable at $x = 0$ can be derived by (2.34).

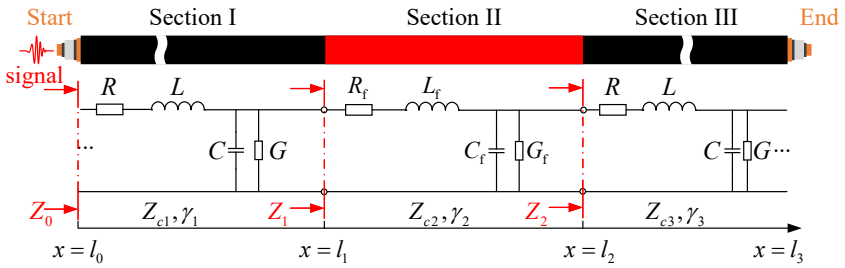
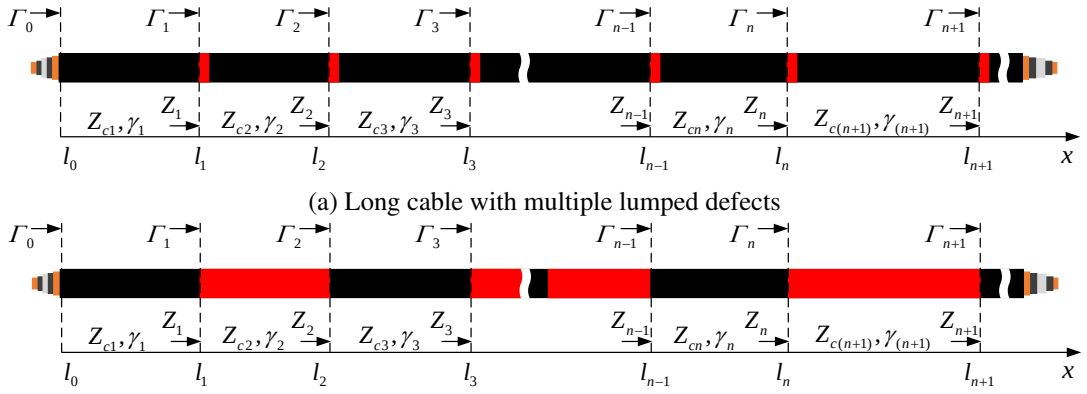


Fig. 2.29 Distributed-parameter model of a long cable with a distributed defect

Γ_0 serves as the RCS of the cable, describing the relationship between the reflected signal and the incident signal. Therefore, the reflected signal can be derived as follows:

$$r(t) = \mathscr{F}^{-1}\left(\Gamma_0 S(\omega)\right) \tag{2.39}$$



(a) Long cable with multiple lumped defects

(b) Long cable with multiple distributed defects

Fig. 2.30 Long cable with multiple defects

A typical multiple-defect scenario is illustrated in Fig. 2.30. In the diagram, Γ_n denotes the input reflection coefficient at location l_n, and Z_n is the input impedance at l_n. The parameters $Z_{\mathrm{c}n}$ and γ_n represent the characteristic impedance and propagation constant of the cable section between l_n and l_{n+1}, respectively. The transfer function Γ_0 at l_0 can be derived using (2.34), where the reflection coefficient Γ_1 is computed recursively. The recursive equations are given as

follows:

$$\Gamma_n = \frac{Z_n - Z_{cn}}{Z_n + Z_{cn}} \tag{2.40a}$$

$$Z_n = \begin{cases} Z_{c(n+1)} \dfrac{1+\Gamma_{n+1}e^{2\gamma_{c(n+1)}(l_n - l_{n+1})}}{1-\Gamma_{n+1}e^{-2\gamma_{c(n+1)}(l_n - l_{n+1})}} // R_p, & \text{ground defects} \\ Z_{c(n+1)} \dfrac{1+\Gamma_{n+1}e^{2\gamma_{c(n+1)}(l_n - l_{n+1})}}{1-\Gamma_{n+1}e^{-2\gamma_{c(n+1)}(l_n - l_{n+1})}} + R_s, & \text{series resistance defects} \end{cases} \tag{2.40b}$$

$$Z_n = Z_{c(n+1)} \frac{1+\Gamma_{n+1}e^{2\gamma_{c(n+1)}(l_n - l_{n+1})}}{1-\Gamma_{n+1}e^{-2\gamma_{c(n+1)}(l_n - l_{n+1})}}, \text{distributed defects.} \tag{2.40c}$$

RCS Calculation Based on S-parameter

Joints and certain types of defects are modeled using S-parameter matrices. In this approach, a long cable containing joints and defects is represented as a cascaded network of healthy and defective cable segments. A typical cascaded network configuration is illustrated in Fig. 2.31. The S-parameter matrix of each segment is obtained individually and then cascaded to yield the S-parameter matrix of the entire network.

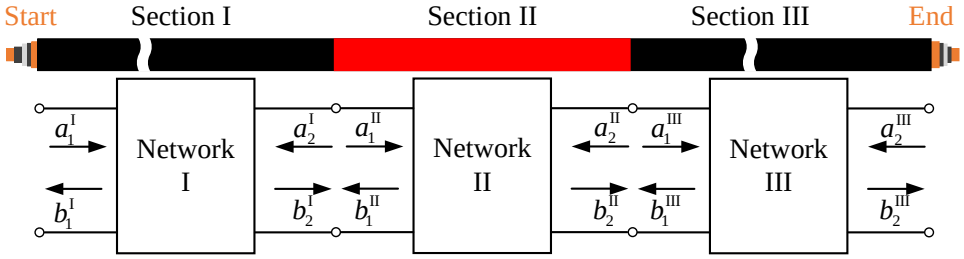


Fig. 2.31 Cascading network of a long cable with a defect

To obtain the S-parameters of the cascaded network, the S-parameter matrices are first converted into ABCD matrices, also known as transmission matrices, which characterize the transmission properties of the network. For healthy cable segments, the ABCD matrix for a cable of length l can be derived from its distributed-parameter model and equations are expressed as follows:

$$\begin{bmatrix} A & B \\ C & D \end{bmatrix} = \begin{bmatrix} \cosh(\gamma l) & Z_c \sinh(\gamma l) \\ \frac{1}{Z_c}\sinh(\gamma l) & \cosh(\gamma l) \end{bmatrix} \tag{2.41}$$

For cable joints and certain defects, the S-parameter matrix can be obtained through measurement or simulation. The corresponding ABCD matrix can then be derived from the S-parameter matrix. The relationship between the S-parameter matrix and the ABCD matrix is

given as follow [87]:

$$A = \frac{(1+S_{11})(1-S_{22})+S_{12}S_{21}}{2S_{21}} \tag{2.42a}$$

$$B = Z_0\frac{(1+S_{11})(1+S_{22})-S_{12}S_{21}}{2S_{21}} \tag{2.42b}$$

$$C = \frac{1}{Z_0}\frac{(1-S_{11})(1-S_{22})-S_{12}S_{21}}{2S_{21}} \tag{2.42c}$$

$$D = \frac{(1-S_{11})(1+S_{22})+S_{12}S_{21}}{2S_{21}} \tag{2.42d}$$

where Z_0 is the reference impedance of the S-parameters. The cascading of multiple ABCD matrices can be expressed as:

$$\begin{bmatrix} A_{\text{total}} & B_{\text{total}} \\ C_{\text{total}} & D_{\text{total}} \end{bmatrix} = \begin{bmatrix} A_1 & B_1 \\ C_1 & D_1 \end{bmatrix} \begin{bmatrix} A_2 & B_2 \\ C_2 & D_2 \end{bmatrix} \cdots \begin{bmatrix} A_n & B_n \\ C_n & D_n \end{bmatrix} \tag{2.43}$$

where A_{total}, B_{total}, C_{total}, and D_{total} are the total ABCD parameters of the cascaded network. After obtaining the ABCD matrices of the cascading network, the S_{11} of the entire network can be calculated as follows:

$$S_{11}^{\text{total}} = \frac{A_{\text{total}} + B_{\text{total}}/Z_0 - C_{\text{total}}Z_0 - D_{\text{total}}}{A_{\text{total}} + B_{\text{total}}/Z_0 + C_{\text{total}}Z_0 + D_{\text{total}}} \tag{2.44}$$

where the S_{11}^{total} is the S_{11} of the entire cable. The RCS of the long cable can be derived from its S-parameters, as given by the following equation:

$$\Gamma_0 = \frac{Z_0\left(1+S_{11}^{\text{total}}\right) - Z_c\left(1-S_{11}^{\text{total}}\right)}{Z_0\left(1+S_{11}^{\text{total}}\right) + Z_c\left(1-S_{11}^{\text{total}}\right)} \tag{2.45}$$

where Z_c is characteristic impedance of the long cable at the input section, Z_0 is the reference impedance.

Fig. 2.32 shows the RCS of a cable with different types of defects at the same location. The curves overlap in the low-frequency range (0 to approximately 5 MHz), indicating that the responses of defects excited by pulse signals are similar, since the main frequency components of a pulse signal lie within this range. Consequently, defect classification and severity estimation based on pulse signals are challenging. As the frequency increases, the curves diverge and exhibit distinct characteristics, suggesting that a higher-frequency injection signal can be used to estimate defect severity. Therefore, for defect-severity estimation, high-frequency injected signals are recommended to improve the discrimination among different defect types.

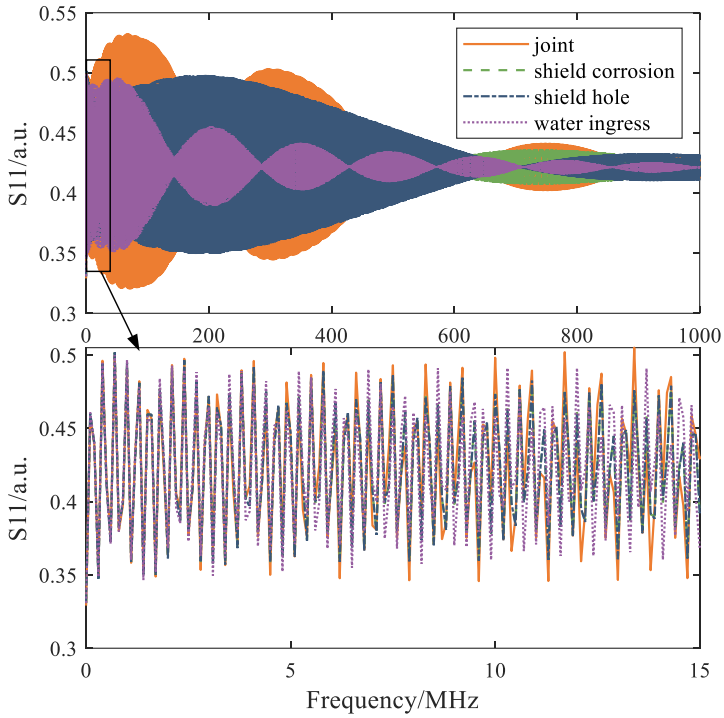


Fig. 2.32 S11 parameters of cables with a joint, with shield corrosion, and with a shield hole

2.4 Summary

In this chapter, propagation models for joints and defects are established and a general computational model for reflected signals in cables with multiple defects is developed. According to their propagation characteristics, defects are classified into lumped and distributed types. Lumped defects are modeled using equivalent circuits, whereas distributed defects are represented by distributed-parameter models and S-parameter matrices. The propagation characteristics of the defects, such as characteristic impedance and propagation constant, are analyzed based on the above models. The proposed computational model is applicable to cables with defects represented by either distributed-parameter models or S-parameters, enabling unified analysis across different defect types. These analyses, together with the general modeling approach, provide a theoretical foundation for subsequent research on reflectometry-based detection of multiple defects in cables.

Chapter 3

Pulse-Reconstruction-Based TDR for Multi-Defect Detection and Localization

In TDR testing, noise and signal distortion can significantly affect the accuracy of defect localization. Multiple reflections in TDR measurements of multiple-defect cables interfere with defect identification and localization. To address these challenges, this chapter proposes a TVMF method to suppress noise and distortion, enabling accurate defect localization. A pulse reconstruction technique is further developed to eliminate the influence of multiple reflections and to identify and localize multiple defects in a cable.

Before proceeding with the following analysis, several types of reflection coefficients are defined as follows:

(1) **Interface reflection coefficient** $\Gamma_*^{\pm}$: This coefficient represents the reflection at a interface, where the cable beyond the interface is assumed to be either infinitely long or sufficiently long relative to the spatial extent of the signal. The superscript $\pm$ indicates the direction of wave propagation, and the subscript $*$ denotes the location of the interface.

(2) **Local reflection coefficient** Γ_*': This coefficient represents the input reflection coefficient at a defect, under the assumption that the cable segment beyond the defect is infinitely long. The subscript $*$ denotes the defect location.

(3) **Reflection coefficient** Γ_*: This represents the reflection coefficient at a specific port of the cable, with the subscript $*$ indicating the port location.

For lumped defects, the interface reflection coefficient $\Gamma_*^{\pm}$ at the boundary between the defect and the adjacent cable equals the local reflection coefficient Γ_*'.

3.1 Estimation Method of Cable Characteristic Parameters

This section first introduces the basic principles of TDR technology, including the composition of the TDR system, the principles of TDR measurement, and the signal propagation process during the measurement. Then, a method for estimating cable characteristic parameters, such as the propagation constant and characteristic impedance, based on the measured TDR results is presented. Finally, a simulation is conducted to validate the improved estimation method.

3.1.1 Analysis of TDR Signal Propagation

A typical TDR system is illustrated in Fig. 3.1. V_s denotes the pulse signal source, R_w is the output impedance of the source, R_m is the input impedance of the sampling oscilloscope, T is a three-port connector, and D is the connector between the connecting cable and the tested cable. R_w and R_m are usually matched. For clarity, key points are labeled 1 through 5: Point 1 is the output of the signal source and the first port of connector T; Point 2 is the input of the connecting cable and the second port of connector T; Point 3 is the input of the oscilloscope and the third port of connector T; Point 4 is the output of the connecting cable; Point 5 is the input of the tested cable; and E is the end of the tested cable. V^+ represents the forward-propagating signal (indicated by red arrows), and V^- denotes the reflected signal (black arrows). V_o is the sampled voltage output by the oscilloscope. Z_{c2}, γ_2, and l_2 are the characteristic impedance, propagation constant, and length of the connecting cable, respectively. Z_c, γ_c, and l_c are the corresponding parameters of the tested cable.

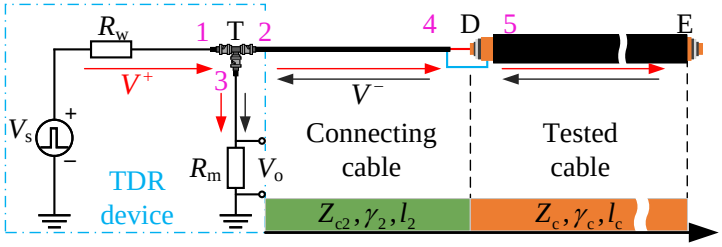


Fig. 3.1 Signal propagation process in TDR system

Since the cable characteristic parameters are frequency-dependent, the pulse signals at key points are analyzed in the frequency domain. Note that frequency-domain variables are denoted by uppercase letters, while their time-domain counterparts use lowercase letters. For simplicity, the frequency ω is omitted in frequency-domain expressions. The signal propagation process in the TDR system can be represented using a lattice diagram. The lattice diagram, shown in Fig. 3.2, depicts only the key signal propagation paths for clarity. In the lattice diagram, V_1^+ denotes the incident pulse at Point 1. V_2^+, V_4^+, V_5^+, and V_6^+ represent the measured injected signal at Points 2, 3, 4, 5, and 6, respectively. V_{2D}^-, V_{3D}^-, and V_{4D}^- are the reflected waves

generated by Connector D at Points 2, 3, and 4, respectively. V_{5E}^{-} is the reflected wave at Point 5 caused by the cable endpoint, and V_{E}^{-} denotes the reflection generated at the endpoint. The time axis is oriented vertically, increasing from top to bottom, indicating the signal propagation time to Point 3. Γ_{D}^{+} and Γ_{T}^{+} are the interface reflection coefficients at Connector D and Connector T, respectively. T_{D}^{+}, T_{D}^{-}, T_{T}^{+}, and T_{T}^{-} are the transmission coefficients at Connectors D and T, respectively.

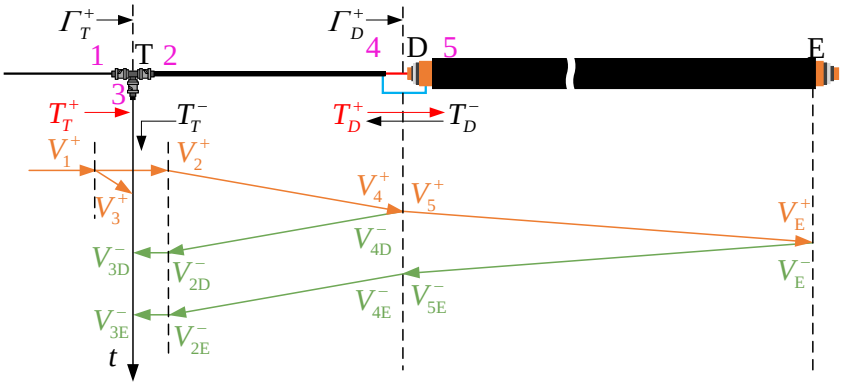


Fig. 3.2 Lattice diagram of signal propagation when measuring a cable using TDR system

3.1.2 Estimation of Characteristic Parameters

Estimating the cable's characteristic parameters is essential for defect detection and localization. These parameters include the propagation constant γ_c and the characteristic impedance Z_c. They can be estimated from TDR measurement results using the method described below. To accurately determine the cable's characteristic parameters, it is necessary to perform measurements on an intact cable beforehand.

Based on the signal propagation analysis in the TDR measurement, as illustrated in Fig. 3.2, the equations relating the cable's characteristic parameters to the voltage spectra at key points in Fig. 3.2 are given as follows [97]:

$$e^{-2\gamma_c l_c} = \frac{V_{5E}^{-}}{V_5^{+}} \tag{3.1}$$

$$\Gamma_{D}^{+} = \frac{Z_c - Z_{c2}}{Z_c + Z_{c2}} = \frac{V_{4D}^{-}}{V_4^{+}} \tag{3.2}$$

The variables in (3.1) and (3.2) are involved in the signal propagation process of the TDR system and cannot be directly measured. Therefore, (3.1) and (3.2) must be reformulated in terms of measurable quantities derived from the output results of the TDR measurement. According to the propagation principle illustrated in Fig. 3.1, a typical TDR measurement waveform observed at port V_o is shown in Fig. 3.3.

In the figure, $v_{\mathrm{oI}}(t)$, $v_{\mathrm{oD}}(t)$, and $v_{\mathrm{oE}}(t)$ represent the TDR measurement results corresponding to the injected signal, the signal reflected from connector D, and the signal reflected from cable endpoint E, respectively. Their corresponding frequency-domain spectra are denoted as V_{oI}, V_{oD}, and V_{oE}, which can be expressed in terms of the voltage spectra at port 3 in Fig. 3.2 as follows:

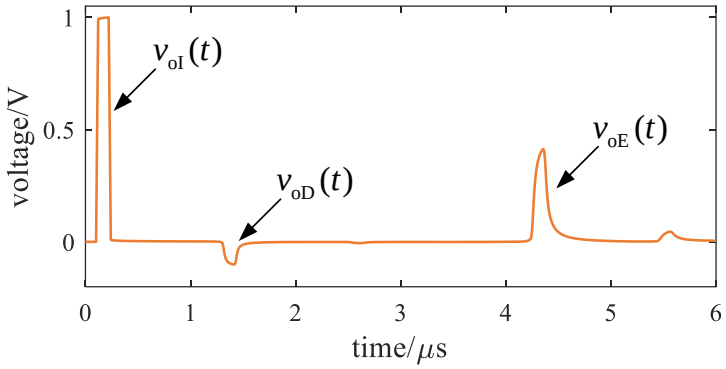


Fig. 3.3 A typical TDR measurement result at port V_{o} in Fig. 3.1.

$$V_{\mathrm{oI}} = V_3^+ \tag{3.3}$$

$$V_{\mathrm{oD}} = V_{3\mathrm{D}}^- \tag{3.4}$$

$$V_{\mathrm{oE}} = V_{3\mathrm{E}}^- \tag{3.5}$$

where $V_{\mathrm{o}*}$ is the pulse in TDR measured results. The relationship between $V_{5\mathrm{E}}^-$ and V_{oE} is:

$$V_{5\mathrm{E}}^- = \frac{V_{\mathrm{oE}}}{T_{\mathrm{D}}^- T_{\mathrm{T}}^- \mathrm{e}^{-\gamma_2 l_2}} \tag{3.6}$$

The relationship between V_5^+ and V_{oI} is expressed as follows:

$$V_5^+ = V_{\mathrm{oI}} T_{\mathrm{D}}^+ \mathrm{e}^{-\gamma_2 l_2} \tag{3.7}$$

By substituting (3.6) and (3.7) into (3.1), the propagation constant γ_{c} of the tested cable can be expressed as:

$$\mathrm{e}^{-2\gamma_{\mathrm{c}} l_{\mathrm{c}}} = \frac{V_{\mathrm{oE}}}{V_{\mathrm{oI}}} \frac{\mathrm{e}^{2\gamma_2 l_2}}{T_{\mathrm{D}}^+ T_{\mathrm{D}}^- T_{\mathrm{T}}^-} \tag{3.8}$$

In (3.8), T_{D}^+ and T_{D}^- can be expressed as follows:

$$T_{\mathrm{D}}^+ = 1 + \Gamma_{\mathrm{D}}^+ \tag{3.9}$$

$$T_{\mathrm{D}}^- = 1 - \Gamma_{\mathrm{D}}^+ \tag{3.10}$$

As introduced in (3.2), V_4^+ and $V_{4\mathrm{D}}^-$ are key variables for estimating Γ_{D}^+. Based on the relationship between $V_{4\mathrm{D}}^-$ and $V_{3\mathrm{D}}^-$, the relationship between $V_{4\mathrm{D}}^-$ and V_{oD} can be derived and is given as follows:

$$V_{4\mathrm{D}}^- = \frac{V_{\mathrm{oD}}}{T_{\mathrm{T}}^- \mathrm{e}^{-\gamma_2 l_2}} \tag{3.11}$$

Similarly, the relationship between V_4^+ and V_{oI} can be derived as follows:

$$V_4^+ = V_{\mathrm{oI}} \mathrm{e}^{-\gamma_2 l_2} \tag{3.12}$$

Therefore, by substituting (3.11) and (3.12) into (3.2), (3.2) can be expressed using V_{oI} and V_{oD} and rewritten as follows:

$$\frac{Z_{\mathrm{c}} - Z_{\mathrm{c2}}}{Z_{\mathrm{c}} + Z_{\mathrm{c2}}} = \frac{V_{\mathrm{oD}}}{V_{\mathrm{oI}}} \frac{1}{\mathrm{e}^{-2\gamma_2 l_2} T_{\mathrm{T}}^-} \tag{3.13}$$

Furthermore, by substituting (3.13) into (3.9) and (3.10), and then substituting the results into (3.8), the equation (3.8) can be rewritten as follows:

$$\mathrm{e}^{-2\gamma_{\mathrm{c}} l_{\mathrm{c}}} = \frac{V_{\mathrm{oE}} V_{\mathrm{oI}} \mathrm{e}^{-2\gamma_2 l_2} T_{\mathrm{T}}^-}{\left(V_{\mathrm{oI}} \mathrm{e}^{-2\gamma_2 l_2} T_{\mathrm{T}}^- + V_{\mathrm{oD}}\right)\left(V_{\mathrm{oI}} \mathrm{e}^{-2\gamma_2 l_2} T_{\mathrm{T}}^- - V_{\mathrm{oD}}\right)} \tag{3.14}$$

In (3.14) and (3.13), the term $\mathrm{e}^{-2\gamma_2 l_2} T_{\mathrm{T}}^-$ is unknown. To determine this term, an auxiliary measurement is performed on the connecting cable prior to the formal TDR measurement, as described in [32]. In this auxiliary setup, the connecting cable is disconnected from the tested cable, and the end of the connecting cable is short-circuited. The results of this auxiliary measurement are shown in Fig. 3.4. Here, $v_{\mathrm{os}}(t)$ represents the reflected signal from the short-circuited end of the connecting cable, and its corresponding frequency spectrum is denoted as V_{os}.

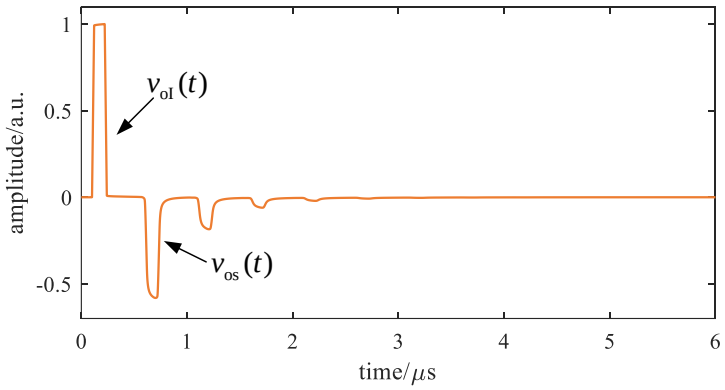


Fig. 3.4 The results of the auxiliary measurement.

V_{os} corresponds to V_{3E}^{-} in the lattice diagram shown in Fig. 3.2. Therefore, the relationship between V_{os} and V_{oI} can be expressed as follows:

$$V_{os} = -V_{oI} e^{-2\gamma_2 l_2} T_T^{-} \tag{3.15}$$

Equation (3.15) shows that the unknown term $e^{-2\gamma_2 l_2} T_T^{-}$ can be obtained from the auxiliary measurement. By substituting (3.15) into (3.14) and (3.13), the propagation constant γ_c and characteristic impedance Z_c of the cable can be estimated as follows:

$$e^{-2\gamma_c l_c} = \frac{V_{oE} V_{os}}{V_{oD}^2 - V_{os}^2} \tag{3.16}$$

$$Z_c = Z_{c2} \frac{V_{os} - V_{oD}}{V_{os} + V_{oD}} \tag{3.17}$$

According to (3.16) and (3.17), the characteristic impedance and propagation constant of the cable can be estimated using TDR testing. In these equations, the variables V_{os}, V_{oD}, and V_{oE}, the cable length l_c, and the characteristic impedance Z_{c2} of the connecting cable are required. Therefore, an auxiliary short-circuit test and a sufficiently long connecting cable are necessary when measuring cable characteristic parameters with TDR.

3.1.3 Simulation and Validation

To validate the improved method for estimating cable characteristic parameters, a series of simulations were conducted. The simulation circuit is designed with reference to Fig. 3.1. The output resistance R_w of the pulse source and the input impedance R_m of the sampling oscilloscope are both set to 50 Ω. The connecting cable is a 50 m-long SYV50 cable with a characteristic impedance of 50 Ω, and its parameters are listed in Table 3.1. The tested cable is a healthy 100 m-long power cable, and its parameters are given in Table 2.2. The pulse source generates pulses with a rise time and fall time of 20 ns and a pulse width of 100 ns.

Table 3.1 Parameters of the SYV50 Cable

Components	radius/mm	Electric parameters
Core	0.45	$\sigma = 5.98 \times 10^7\,\mathrm{S\,m^{-1}}$
Dielectric	1.475	$\varepsilon = 2.3$
Shield	1.8	$\sigma = 5.98 \times 10^7\,\mathrm{S\,m^{-1}}$
Sheath	2.475	$\varepsilon = 2.5$

The TDR measurement results of the healthy 100 m-long cable are shown in Fig. 3.5. In Fig. 3.5, $v_{oD}(t)$ and $v_{oE}(t)$ represent the reflected pulses from connector D and the open-

circuited end of the tested cable, respectively. According to (3.16), it is necessary to measure V_{os}. The measured waveform of $v_{os}(t)$ is shown in Fig. 3.4.

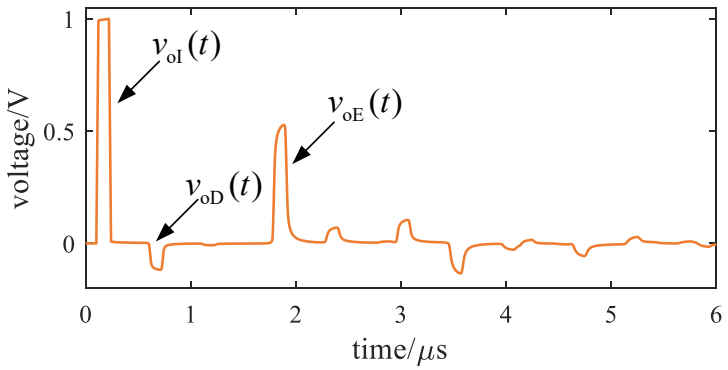


Fig. 3.5 The TDR measurement results of a 100-meter-long healthy power cable

To obtain V_{oD}, V_{oE}, and V_{os}, the $v_{oD}(t)$, $v_{oE}(t)$, and $v_{os}(t)$ are transformed into the frequency domain. The propagation constant γ_c and characteristic impedance Z_c of the power cable can then be estimated using (3.16) and (3.17) and $\gamma_c = \alpha_c + j\beta_c$. The initial estimates of α_c, β_c, Z_c and v are shown by the solid orange lines in Fig. 3.6.

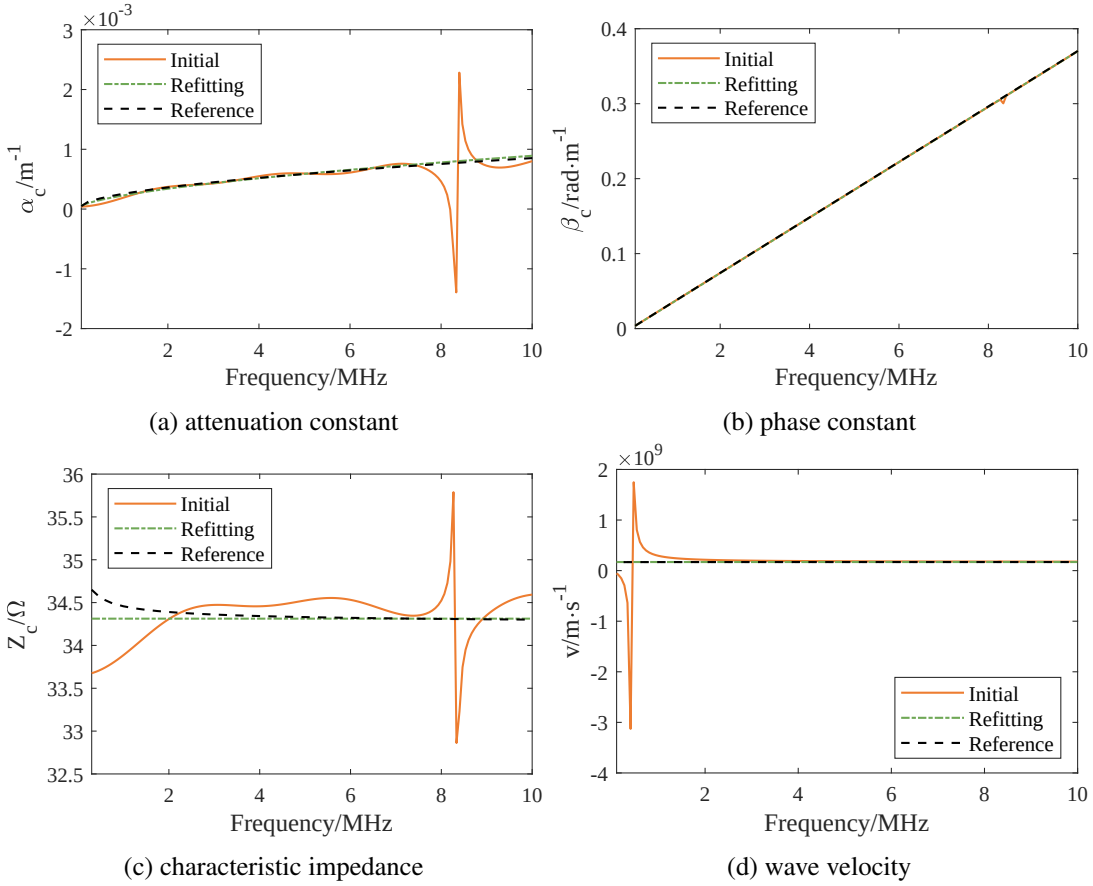
According to Fig. 3.6, some abnormal values appear in the estimated results—specifically around 8.2 MHz in Figures 3.6a, 3.6b, and 3.6c, and around 0.5 MHz in Fig. 3.6d. These anomalies are caused by division by zero in (3.16) and (3.17). Since the frequency spectrum of a pulse signal follows a sinc function, the signal spectrum approaches zero at certain frequencies. To resolve this issue, after the initial estimation, α_c, β_c, and Z_c are optimized based on their frequency-dependent characteristics. The optimization is performed by fitting the estimated values to known models of cable characteristic parameters. The attenuation constant α_c and phase constant β_c satisfy the following relationships [98]:

$$\alpha_c = K_a\sqrt{\omega} \tag{3.18a}$$

$$\beta_c = K_b\omega \tag{3.18b}$$

where K_a and K_b are the coefficients of the attenuation constant and phase constant, respectively. The characteristic impedance Z_c is typically constant in the high-frequency range and is therefore optimized as a fixed value.

The refitted values and reference values of the cable characteristic parameters are also shown in Fig. 3.6. In the comparison results, the reference values represent the distributed parameters of the tested cable used in the simulation model. As shown in Fig. 3.6, the estimated values closely match the reference values, confirming the effectiveness of the improved method for accurately estimating cable characteristic parameters. With these estimated parameters, a model of the tested cable can be established, and the reflected signals can be further modeled.



(a) attenuation constant

(b) phase constant

(c) characteristic impedance

(d) wave velocity

Fig. 3.6 Comparison of the refitting values, initial values and reference values of the cable characteristic parameters

In Fig. 3.6, the discrepancy between the estimated and reference values gradually increases above 10 MHz as the frequency increases. This is because the high-frequency components of the injected signal are weak, leading to reduced estimation accuracy at higher frequencies. However, this deviation has minimal impact on the simulation of reflected pulse signals, since the bandwidth of the injected pulse is limited and higher-frequency characteristics contribute little to the pulse response.

3.2 Defect Localization Based on TVMF

Defect localization is a critical aspect of reflectometry technology. In TDR measurements, noise affects the accuracy of signal arrival time determination. Power cables typically have a coaxial structure, which provides effective shielding; therefore, the dominant noise in TDR measurements is white noise. Another factor influencing localization accuracy is the distortion of the pulse signal due to attenuation and dispersion. Such distortion increases the rise time

of the TDR pulse and enlarges the error in determining the arrival time of reflected signals by traditional methods based on rising edges and abrupt energy changes.

Matched filtering is a signal processing technique used to detect known signals in the presence of noise. It is especially effective when the target signal is known [99]. When the measured original signal contains the target signal, the matched filtering output exhibits a prominent peak at the point where the target signal appears, as this corresponds to the highest similarity between the original signal and the matched filter [100]. The time of this peak indicates the arrival time of the target signal in the original signal. Therefore, matched filtering can be employed to detect and locate reflection signals in TDR measurement results.

3.2.1 Principle and Implementation of TVMF

The basic principle of matched filtering is to correlate the received signal with a template or reference signal that matches the expected shape of the target signal. Considering an original measurement result $x(t)$, its matched filtering output $y(t)$ can be expressed as follows [101]:

$$y(t) = \int_0^t h(\tau)x(t-\tau)d\tau \tag{3.19}$$

where $h(t)$ is the matched filter and can be designed based on the expected target signal, which is expressed as follows:

$$h(t) = Ks(T-t) \tag{3.20}$$

where K is the gain of the matched filter $h(t)$, which is typically set to 1. $s(t)$ for $t \in [0,T]$ is the target signal. The performance of matched filtering depends on the similarity between the target signal and the matched filter. Therefore, achieving more accurate defect localization requires more precise selection of the target signal.

As the pulse signal $s(t)$ propagates along the cable, two main factors affect its behavior. First, attenuation and dispersion gradually distort $s(t)$, altering both its amplitude and shape. Second, different defect types, such as lumped and distributed defects, exhibit distinct reflection characteristics, producing reflected pulses with varying waveforms and time-domain features. As a result, the matched filter $h(t)$, typically designed from the ideal injected signal $s(t)$, may become mismatched with the actual reflected signal. Therefore, a time-varying matched filter is required to adapt to the evolving target signal.

Assuming the cable has a defect at position l_{f1}, a reflected signal will appear in the TDR measurement $s(t)$ within the time interval $[t_{\mathrm{f1}}, t_{\mathrm{f1}}+T]$. To accurately detect this reflected signal, the matched filter $h(t)$ should be designed as a time-varying filter to adapt to the changing target signals. The time-varying matched filter can be designed based on (3.20) and is given as

follows:

$$H(\omega,t_{\mathrm{f1}}) = K\mathrm{e}^{-\mathrm{j}\omega T}S^{*}(\omega,t_{\mathrm{f1}}) = K\mathrm{e}^{-\mathrm{j}\omega T}S^{*}_{\mathrm{of1}}(\omega,t_{\mathrm{f1}})\cdot\Gamma'^{*}_{\mathrm{f1}}(\omega) \tag{3.21}$$

where $H(\omega,t_{\mathrm{f1}})$ is the frequency-domain representation of the time-varying matched filter, derived based on the convolution theorem. $S(\omega,t_{\mathrm{f1}})$ denotes the reflected signal from defect f1, which can be expressed as the product of the reflected signal $S_{\mathrm{of1}}(\omega,t_{\mathrm{f1}})$ from an open-circuited end located at defect f1 and the local reflection coefficient $\Gamma'_{\mathrm{f1}}(\omega)$ of defect f1. The symbol * denotes the complex conjugate.

3.2.2 Construction of Time-Varying Matched Filter Bank

As shown in (3.21), the time-varying matched filter $H(\omega,t_{\mathrm{f1}})$ consists of two components: the first is the reflected signal $S_{\mathrm{of1}}(\omega,t_{\mathrm{f1}})$ from an open-circuited end, and the second is the local reflection coefficient $\Gamma'_{\mathrm{f1}}(\omega)$. Since the propagation constant γ_{c} of the cable is known, (3.16) enables the calculation of the reflected signal $S_{\mathrm{of1}}(\omega,t_{\mathrm{f1}})$ corresponding to an open-circuited condition at defect f1. By substituting l_{f1} with $v_{\mathrm{c}}t_{\mathrm{f1}}/2$, the reflected signal $S_{\mathrm{of1}}(\omega,t_{\mathrm{f1}})$ can be derived from (3.16) as follows:

$$S_{\mathrm{of1}}(\omega,t_{\mathrm{f1}}) = \mathrm{e}^{-\gamma_{\mathrm{c}}t_{\mathrm{f1}}v_{\mathrm{c}}}\frac{V_{\mathrm{oD}}^{2}-V_{\mathrm{os}}^{2}}{V_{\mathrm{os}}} \tag{3.22}$$

where t_{f1} is the arrival time of the reflected signal from defect f1, and v_{c} is the propagation velocity of the cable.

The local reflection coefficient Γ'_{f1} depends on the type of defects. According to the analysis in Section 2.3, defects can be classified into two categories: lumped defects and distributed defects. The reflection characteristics of lumped and distributed defects differ significantly. For lumped defects, the reflection coefficient is a constant real number, and the reflected waveform is a single pulse whose amplitude is determined by the reflection coefficient. Distributed defects, on the other hand, typically exhibit complex reflection coefficients, and the corresponding reflected waveform generally consists of a double-pulse structure, characterized by one positive and one negative pulse. Therefore, the local reflection coefficient Γ'_{f1} can be categorized into two types. The first type, corresponding to lumped defects, is expressed as:

$$\Gamma'_{\mathrm{f1}} = K_{\mathrm{lumped}} \tag{3.23}$$

where K_{lumped} is a constant real number representing the reflection coefficient of the lumped defect.

The second type of Γ'_{f1} is the local reflection coefficient of the distributed defect. The distributed defect model on the cable is shown in Fig. 3.7. In the figure, the distributed defect

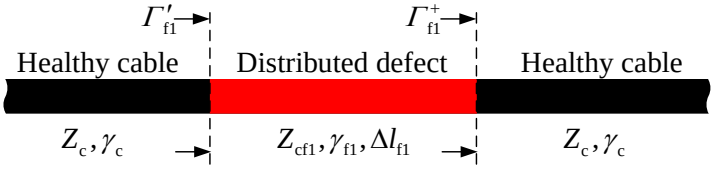


Fig. 3.7 Model of the distributed defect on a cable

is inserted between two healthy cable sections. Z_c and γ_c are the characteristic impedance and propagation constant of the healthy cable, respectively, while Z_{cf1} and γ_{f1} are those of the distributed defect. The length of the distributed defect is Δl_{f1}. The local reflection coefficient Γ'_{f1} of the distributed defect can be derived from (2.38) and is given by:

$$\Gamma'_{f1} = \frac{-\Gamma^{+}_{f1} + \Gamma^{+}_{f1} e^{-2\gamma_{f1}\Delta l_{f1}}}{1 - \Gamma^{+2}_{f1} e^{-2\gamma_{f1}\Delta l_{f1}}} \tag{3.24}$$

$$\Gamma^{+}_{f1} = \frac{Z_c - Z_{cf1}}{Z_c + Z_{cf1}} \tag{3.25}$$

Distributed defects exhibit the following characteristics:

(1) The characteristic impedance of the defect segment is usually close to that of the healthy cable, implying that $\Gamma^{+}_{f1} < 1$ and $\Gamma^{+2}_{f1} \ll 1$.

(2) The length of the distributed defect is typically much smaller than the the spatial length of the injected pulse signal, resulting in negligible signal attenuation.

Based on the above characteristics, two approximations are applied to (3.24): $\Gamma^{+2}_{f1} \approx 0$ and the defect attenuation constant $\alpha_{f1} \approx 0$. Therefore, Γ'_{f1} can be simplified as [68]:

$$\Gamma'_{f1} = \Gamma^{+}_{f1}\left(-1 + e^{-2j\beta_{f1}\Delta l_{f1}}\right) \tag{3.26}$$

where β_{f1} is the phase constant of the distributed defect. In (3.26), β_{f1} plays a similar role to the length of the distributed defect. This implies that different distributed defects with varying β_{f1} values may produce identical reflection results for certain lengths. In the absence of additional information, a given local reflection coefficient Γ'_{f1} may correspond to infinitely many distributed defects with different β_{f1} values. Therefore, assuming $\beta_{f1} = \beta_c$, the local reflection coefficient Γ'_{f1} can be expressed as:

$$\Gamma'_{f1} = \Gamma^{+}_{f1}\left(-1 + e^{-2j\beta_c\Delta l_{f1}}\right) \tag{3.27}$$

After the propagation coefficient β_{f1} is defined, the local reflection coefficient Γ'_{f1} given in (3.27) depends solely on the defect length Δl_{f1}. In this formulation, the coefficient Γ^{+}_{f1}

influences only the amplitude of the reflected signal, without altering its temporal waveform. Since Γ_{f1}^{+} only affects the magnitude of the reflected signal, it can be set to a non-zero constant within the range $(-1,1)$ when constructing time-varying matched filters. In (3.27), the defect length Δl_{f1} is the sole factor influencing the waveform of the reflected signal. To detect reflected signals with diverse waveforms, a single time-varying matched filter is insufficient. Therefore, a time-varying matched filter bank (TVMFB) is required. The TVMFB consists of a series of time-varying matched filters corresponding to reflected signals from lumped defects and distributed defects of various lengths. By substituting (3.16) and (3.27) into (3.21), the TVMFB for the reflected signal from defect f1 is expressed as follows:

$$H(\omega,t)=\begin{cases}\mathrm{e}^{-\mathrm{j}\omega T}\left(\mathrm{e}^{-\gamma_{\mathrm{c}}tv_{\mathrm{c}}\frac{V_{\mathrm{oD}}^2-V_{\mathrm{os}}^2}{V_{\mathrm{os}}}}\right)^{*}, & \text{lumped defect}\\ \mathrm{e}^{-\mathrm{j}\omega T}\left[\mathrm{e}^{-\gamma_{\mathrm{c}}tv_{\mathrm{c}}\frac{V_{\mathrm{oD}}^2-V_{\mathrm{os}}^2}{V_{\mathrm{os}}}}\left(-1+\mathrm{e}^{-2\mathrm{j}\beta_{\mathrm{c}}\Delta l_{\mathrm{f}}}\right)\right]^{*}, & \text{distributed defect.}\end{cases} \tag{3.28}$$

where the coefficient of $H(\omega,t_{\mathrm{f1}})$ is set to 1 in (3.28).

To eliminate the influence of reflected signal strength and filter amplitude, the outputs of the TVMF are normalized. Therefore, the output of the TVMF is expressed as:

$$y(t)=\frac{1}{E_{\mathrm{x}}(t)E_{\mathrm{H}}(t)}\int_{t}^{t+\mathrm{T}}h(\tau)x(t-\tau)d\tau \tag{3.29a}$$

$$E_{\mathrm{x}}(t)=\int_{t}^{t+\mathrm{T}}x(\tau)d\tau \tag{3.29b}$$

$$E_{\mathrm{H}}(t)=\int_{0}^{\mathrm{T}}h(\tau)d\tau. \tag{3.29c}$$

where $x(t)$ represents the TDR measurement results with noise, $E_{\mathrm{x}}(t)$ and $E_{\mathrm{H}}(t)$ are used to normalize the output of the TVMF, and $h(t)$ is the time-domain representation of $H(\omega,t)$. According to (3.29), the output of the TVMF consists of a series of peaks close to 1, with each peak time corresponding to the arrival time of a reflected signal.

3.2.3 Selection of TVMF Filtering Results

After filtering the TDR measurement results using the TVMFB, multiple filtering outputs are obtained. The location of defects must be identified based on these outputs. To illustrate the localization procedure, a simulation case is presented. Fig. 3.8 shows a TDR measurement result for a cable containing a lumped defect at 100 m and a distributed defect at 200 m. The reflected signal around 1.6 µs corresponds to the series resistance defect, while the reflected signal around 2.9 µs corresponds to the distributed defect. Based on (3.29), the TDR measurement results are processed using the TVMF. Taking the lumped defect filter and the 1 m-long distributed defect filter as examples, the corresponding filtering results of the TVMFB are shown in Fig. 3.9.

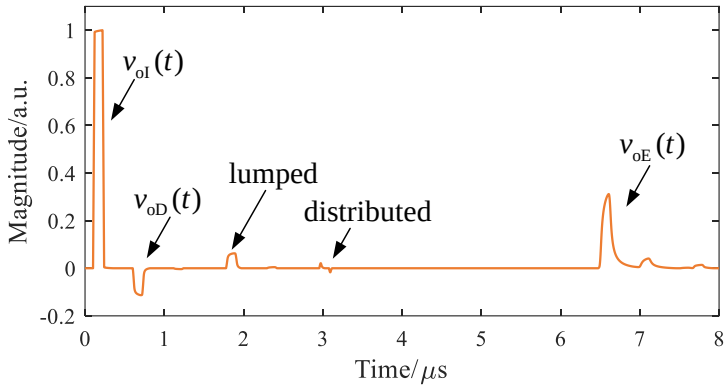
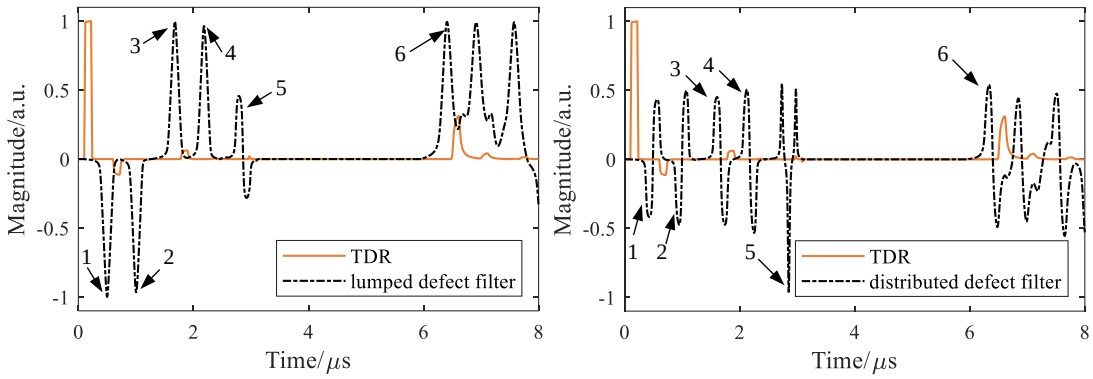


Fig. 3.8 The TDR measurement results of the cable with defects.



(a) lumped defect filter (b) distributed defect filter

Fig. 3.9 The results of the TVMF.

Principles for Selecting Filtering Results

In the filtering results, a series of peaks are observed. Peak 1 corresponds to the reflected signal from connector D, located between the connecting cable and the tested cable. Peak 2 corresponds to the second-order reflection from connector D. Peak 3 indicates the reflected signal from the series resistance defect, while Peak 4 is the subsequent reflection of Peak 3 by connector D. Peak 5 shows the reflected signal from the distributed defect, and Peak 6 corresponds to the reflection from the cable end. Among these signals, the reflections from connector D and the lumped defect appear as single pulses, whereas the reflection from the distributed defect exhibits a double-pulse waveform consisting of a positive and a negative pulse. In the filtering results shown in Fig. 3.9a using the lumped defect filter, the reflections from connectors and lumped defects appear as single pulses with magnitudes close to 1. In contrast, the reflected signal from the distributed defect appears as a double pulse with a lower magnitude. Fig. 3.9b shows the filtering results using the distributed defect filter. In this case, the reflections from connector D and the lumped defect appear as double pulses with low magnitudes. In contrast, the reflected signal from the distributed defect produces a distinct triple-pulse response, as shown by Peak 5 in Fig. 3.9b. The triple-pulse waveform resembles a

"Y" or inverted "Y" shape, with a central pulse of higher magnitude and two side pulses of lower magnitude and the same polarity. The central pulse has the opposite polarity to the side pulses.

1D CNN–Based Method for Selecting Filtering Results

Based on the above peak-identification principles in filtering results, an automatic approach involves employing deep learning techniques. One-dimensional convolutional neural networks (1D CNNs) are capable of extracting signal features and identifying signals. To train the 1D CNN, a dataset is constructed through simulation. The dataset includes reflected signals from both lumped and distributed defects at various locations and under different noise levels. The defect locations are set from 100 m to 1000 m in 200 m increments. Lumped defects include a 15 Ω series resistance defect and a 50 Ω ground defect. Distributed defects have five different lengths: 0.1 m, 0.2 m, 0.5 m, 1 m, and 2 m, each with two characteristic impedance values: 20 Ω and 50 Ω. Four noise levels are considered, with 10 signal realizations per level. A total of 2400 TDR simulation results are generated. These TDR signals are then filtered using the TVMFB. In the TVMFB, although the length of the distributed defect filter affects the peak time and peak value of the output, it does not alter the basic waveform shape. Therefore, for simplicity, the length of distributed defects is fixed at 1 m.

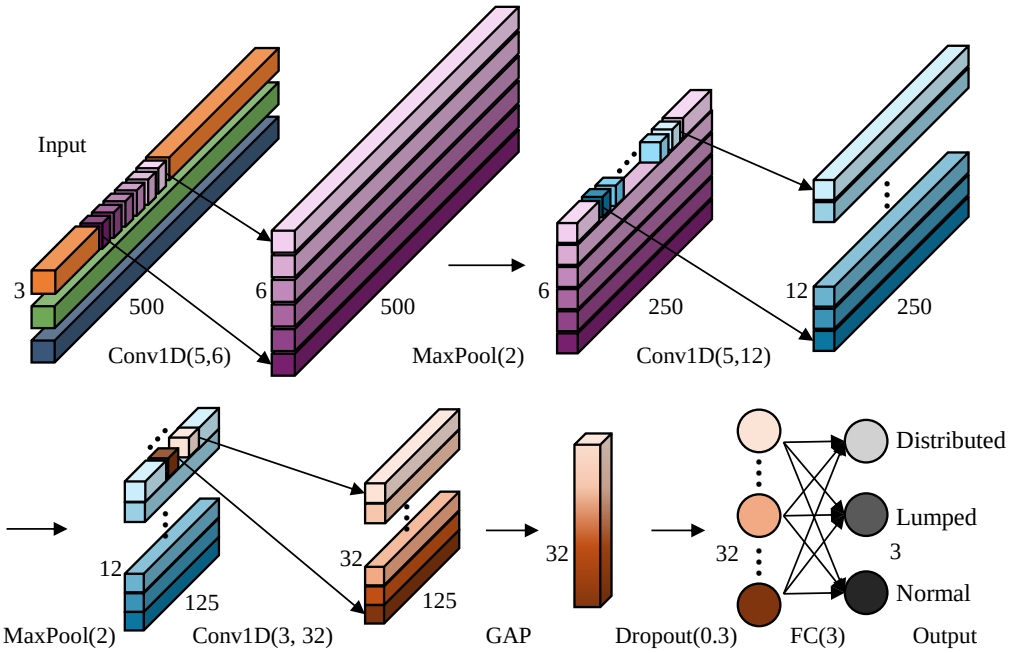
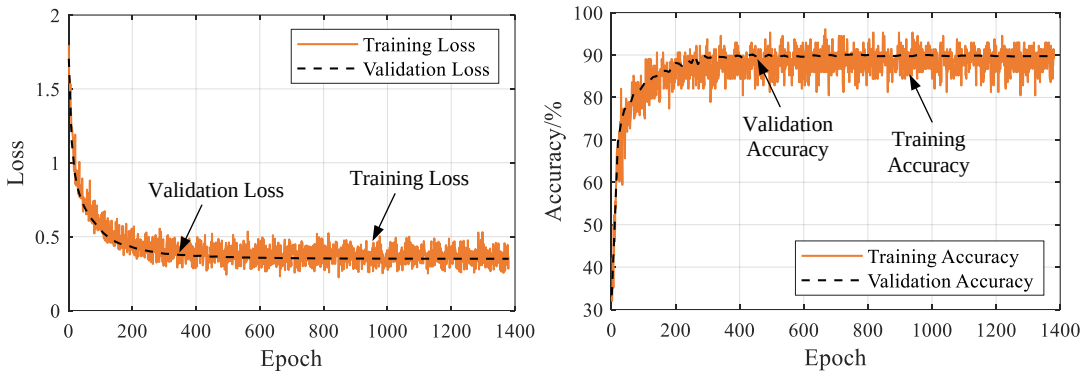


Fig. 3.10 The 1D CNN model for defect type recognition.

The 1D CNN is constructed based on the Visual Geometry Group Network (VGGNet) architecture, which employs multiple convolutional and pooling layers to extract features from the reflected signals [102]. The structure of the 1D CNN model is illustrated in Fig. 3.10. In this model, the input consists of three channels: the reflected signal and the outputs of the lumped

and distributed defect filters, each as a 500-point time sequence. The 1D CNN includes three convolutional layers and three pooling layers. The first convolutional layer has 6 kernels with a size of 5, the second layer has 12 kernels with a size of 5, and the third layer has 32 kernels with a size of 3. The first two are max pooling with a kernel size of 2, and the third is a global average pooling layer. A dropout layer follows the convolutional blocks to reduce overfitting. ReLU is used as the activation function, and softmax is applied in the output layer. The model is trained using categorical cross-entropy loss and the Adam optimizer (initial learning rate 0.001), with L2 regularization to further prevent overfitting. The batch size is 128, and the dataset is split 80 % for training and 20 % for testing.

Training loss and accuracy are shown in Fig. 3.11. The confusion matrix of the model is shown in Fig. 3.12. After training, the model achieves an accuracy of 89.93 % on the testing dataset. In the confusion matrix, it can be observed that the 1D CNN achieves high accuracy in recognizing reflected signals from both lumped and distributed defects, with recognition rates exceeding 90 %. However, for normal signals, 16.8 % are misclassified as distributed defects. This is mainly because normal signals consist of noise without reflection components, and some noise waveforms resemble those of distributed defect reflections. Since the 1D CNN classifies defect types based on waveform patterns, such similarities can lead to misclassification. However, in actual TDR measurements, noise waveforms vary over time. Therefore, this error can be mitigated through multiple TDR measurements and repeated classifications using the 1D CNN.



(a) Loss curve of the 1D CNN model.

(b) Accuracy curve of the 1D CNN model.

Fig. 3.11 Loss and accuracy curves of the 1D CNN model.

A typical classification result is shown in Fig. 3.13. In the classification results shown in Fig. 3.13, the 1D CNN processes TDR signals and their corresponding TVMFB filtering results using a sliding window approach. Each window contains 500 points, with a step size of 64 points. From the classification and localization results, it can be observed that the 1D CNN successfully identifies the defect types and gives the range of defect locations. Then based on the peak time of the filtering results, the defect locations can be determined. For lumped defects,

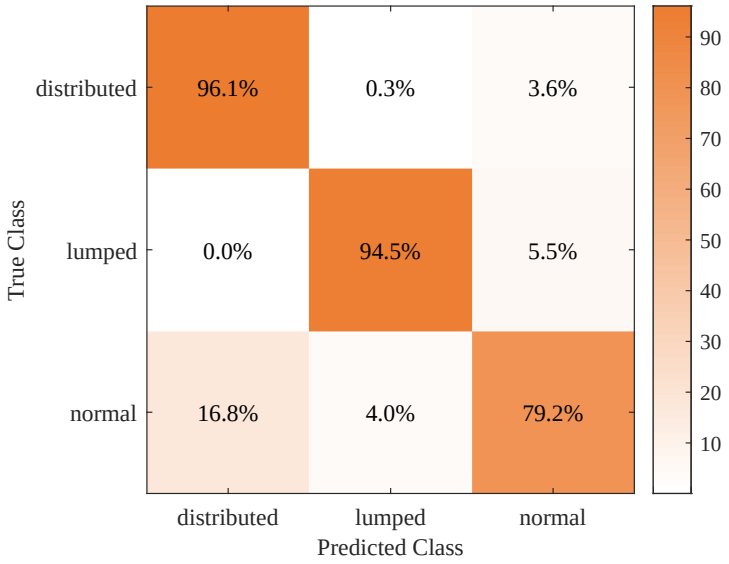


Fig. 3.12 The confusion matrix of the 1D CNN model.

their arrival times are the peak times of the lumped defect filter output. For distributed defects, multiple filters with different lengths are applied, and the arrival time is defined as the peak position of the filter output with the maximum amplitude among all results. The corresponding defect length of the optimal filter can be regarded as the equivalent length of the distributed defect. This length is an equivalent value instead of the actual physical length, representing the length that generates a similar reflection waveform for the distributed defect.

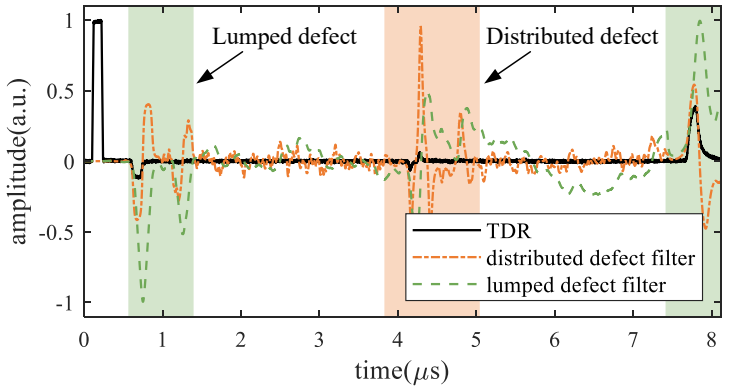


Fig. 3.13 The classification result of the 1D CNN model.

The waveforms of reflected signals from lumped and distributed defects are different, but they still show certain similarities to noise. Therefore, pulse noise may interfere with the classification performance of the 1D CNN. To further reduce the misclassification of normal signals, a post-processing rule is applied during 1D CNN classification: a defect type is confirmed only if it appears consistently in three or more consecutive windows. After classification, the defect can be located based on the peak time of the filtering result from the corresponding defect-type filter.

3.2.4 Comparison and Validation of Localization Methods

The effectiveness of the TVMF method is validated in this section. The validation focuses on three aspects: the necessity of the time-varying matched filter, the location accuracy of the TVMF, and its sensitivity to noise.

First, the necessity of the time-varying matched filter is verified by comparing its performance with that of conventional matched filtering, where the injected pulses are used as the target signals. For this comparison, a 10 kV power cable with a 10 Ω series resistance defect, as specified in Table 2.2, is modeled. The defect is placed at intervals of 50 m, ranging from 100 m to 500 m. The TDR measurement simulation follows the configuration shown in Fig. 3.1. The reflected signals from defects at various locations are shown in Fig. 3.14.

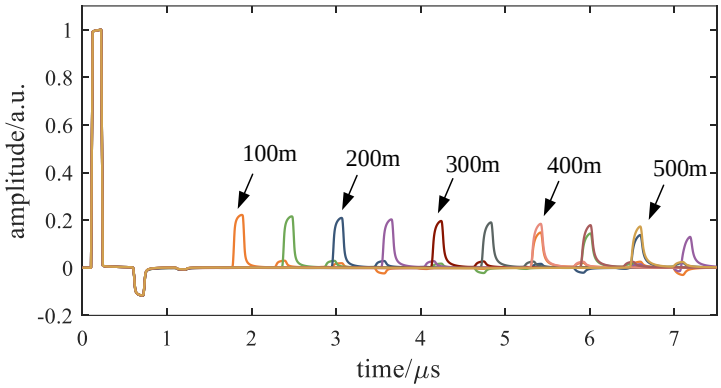


Fig. 3.14 The TDR measurement results of defects at various locations.

In Fig. 3.14, it can be observed that the waveforms of the reflected signals at different defect locations gradually deviate from the original injected pulse at $t = 0\,\mu s$. To demonstrate the necessity of the TVMF, these defects are localized using both the general matched filtering method and the TVMF, and their localization errors are compared. The localization errors of the general matched filtering method and the TVMF are shown in Fig. 3.15. In the figure, it can be observed that the localization errors of the TVMF are consistently smaller than those of the general matched filtering method. This result demonstrates that the TVMF effectively reduces localization errors and improves the performance of matched filtering in defect localization. However, some residual errors remain in the localization results of the TVMF. These errors are primarily attributed to inaccuracies in the estimated cable characteristic parameters, which arise from the use of fitting techniques to eliminate singular values during the estimation process. To address this issue, a pulse signal with a steeper rising edge can be used to improve the accuracy of the parameter fitting.

To evaluate the localization accuracy of the TVMF and its sensitivity to noise, the method is compared with several commonly used techniques, including the threshold method, Gabor centroid method, energy criterion method, and phase method. The simulation model consists

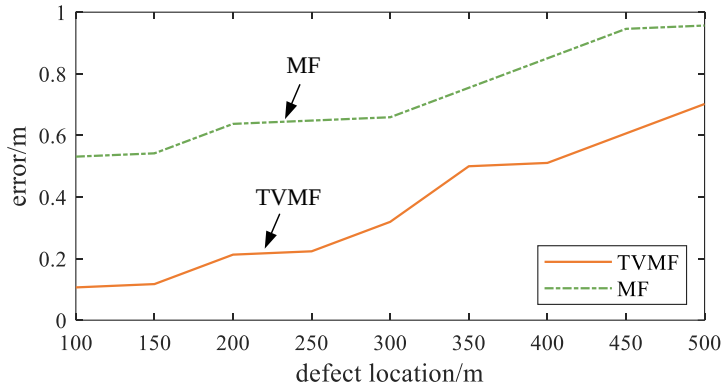


Fig. 3.15 Location error comparison: TVMF and matched filtering.

of a 700-meter-long cable with a 50 Ω series resistance defect located at 400 m. Four levels of white noise are added to the simulation results. The TDR responses under different noise conditions are shown in Fig. 3.16.

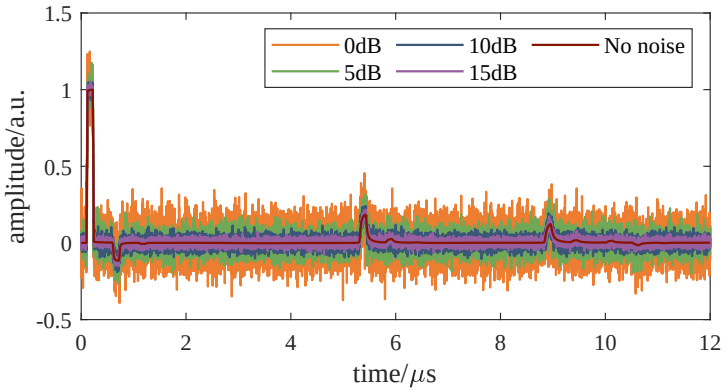
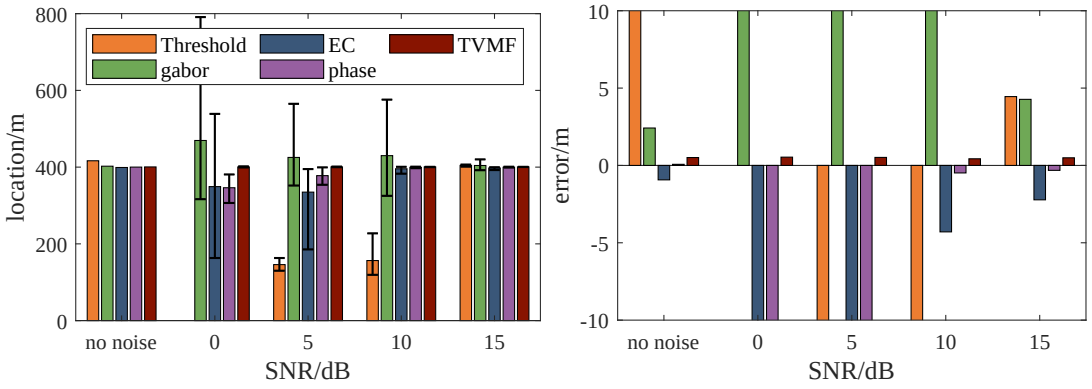


Fig. 3.16 TDR simulation results with varying noise intensities.

To statistically analyze the localization performance of each method, 10 sets of reflected signals were generated for each noise level. The defects in these signals were localized using different methods [55], and the results were statistically analyzed to evaluate the effectiveness of each approach. A comparison of the localization performance across the various methods is presented in Fig. 3.17. The average defect localization results obtained from each method are presented in Fig. 3.17a, with error bars indicating the maximum and minimum values. Fig. 3.17b shows the deviations between these average localization results and the reference values. The error range in Fig. 3.17b is limited to −10 m to 10 m. From Fig. 3.17, it can be observed that all five methods successfully localize the defect in the absence of noise. However, the threshold method performs poorly, with localization errors exceeding 10 meters, and fails entirely when the SNR is 0 dB. At SNRs below 5 dB, commonly used methods exhibit significant errors, often exceeding 10 meters. As the SNR increases, their accuracy improves. Notably, the TVMF method consistently achieves the highest localization accuracy. Within an SNR range of 0 dB to 15 dB, the localization error of TVMF decreases from 0.54 m to

0.49 m. In summary, the TVMF method not only provides high localization accuracy but also demonstrates low sensitivity to noise. In contrast, other methods suffer from large localization errors, particularly under low SNR conditions. The TVMF method consistently outperforms the commonly used approaches in terms of accuracy, exhibiting superior stability and robustness across various noise levels.



(a) Mean values and maximum errors

(b) Average errors

Fig. 3.17 Localization results comparison: the TVMF and commonly used methods.

Single-defect localization serves as the foundation for TDR-based diagnostics. However, in practical applications, cables often contain more than one defect. The presence of multiple defects generates numerous reflected signals in TDR measurements, which can interfere with defect identification and complicate localization. This necessitates the development of effective methods for accurately detecting and localizing multiple defects.

3.3 Reflection Pulse Reconstruction for Multi-Defect Cables

3.3.1 Influence of Multiple Defects on Detection and Localization

In practical cables, multiple defects often coexist, and at a minimum, each cable contains several joints. When TDR is used for defect detection, the injected pulse undergoes multiple reflections and refractions at both defects and joints. As a result, the TDR measurement contains more reflected pulses than the actual number of defects. These redundant reflections can lead to incorrect estimations of the number of defects and the misidentification of defects. To illustrate the cause and impact of these false reflections, the lattice diagram shown in Fig. 3.18 depicts the propagation process of the pulse within the cable.

The diagram displays only a subset of the reflections, and the pulse propagation paths are simplified to emphasize the occurrence of misidentification problems. In the lattice diagram, reflections marked in blue represent “actual" reflections, whereas those marked in green repre-

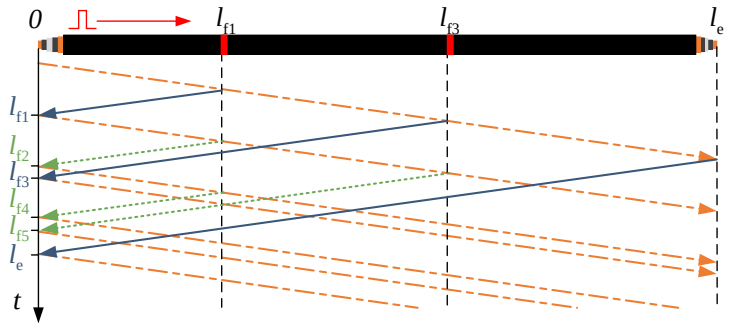


Fig. 3.18 Lattice diagram of the pulse propagation in the cable.

sent “fake" reflections. It is clear that “fake" reflections interfere with the accurate detection and localization of actual defects.

By analyzing the lattice diagram, it can be observed that the first reflected signal always corresponds to the first actual defect. Therefore, once the first defect is localized, its corresponding reflected signals can be removed, and the earliest remaining reflection must correspond to the second actual defect. By repeating this process, all actual defects in the cable can be localized. To implement this strategy, the following steps are required:

(1) Localize the first actual defect.

(2) Estimate the reflection coefficient of the defect.

(3) Reconstruct its reflected signal and remove it from the measured signal.

(4) Extract the remaining reflected signals.

(5) Iterate the process to localize all actual defects.

3.3.2 Estimation of Defect Characteristic Parameters

To reconstruct the reflected signals, the characteristic parameters of the defects must be determined. The two types of defects—lumped and distributed—have different parameter requirements. Lumped defects are relatively simple and are characterized by a single parameter: the local reflection coefficient. In contrast, the characteristic parameters of distributed defects include both the interface reflection coefficient and the defect length. The defect type can be identified using the CNN-based classification method proposed above.

Estimation of Lumped Defect Characteristic Parameters

Lumped defects can be classified into two categories: series resistance defects, which exhibit higher impedance than the healthy cable, and ground defects, which exhibit lower impedance.

The equivalent circuits for these two types of defects are shown in Fig. 2.10 and their TDR measurement results are shown as Fig. 3.19. Based on the relationship between the reflection coefficient and the defect resistance, as given in (2.12) and (2.13), the equivalent resistances of lumped defects can be estimated using the following expressions:

$$R_{\mathrm{s}} = Z_{\mathrm{c}} \frac{1+\Gamma_{\mathrm{s}}'}{1-\Gamma_{\mathrm{s}}'} - Z_{\mathrm{c}} \tag{3.30}$$

$$R_{\mathrm{g}} = -Z_{\mathrm{c}} \frac{1+\Gamma_{\mathrm{g}}'}{2\Gamma_{\mathrm{g}}'} \tag{3.31}$$

Here, Γ_{s}' and Γ_{g}' represent the local reflection coefficients of the series resistance and ground defects, respectively. R_{s} and R_{g} are the equivalent resistances of the defects.

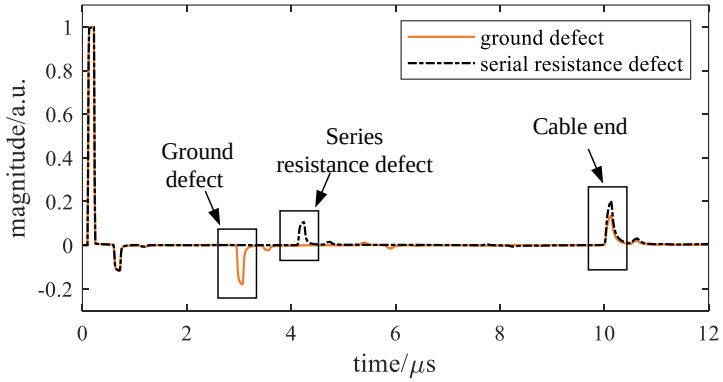


Fig. 3.19 Two typical TDR measurement results of cable with lumped defects

According to (3.30) and (3.31), the local reflection coefficient Γ_*' must be determined to calculate the equivalent resistance of the defect. Γ_*' can be extracted from the TDR measurement results. For a cable with a single defect located at l_{f1}, the transfer function of the reflected signal from the defect can be expressed based on (3.1) as follows [40]:

$$\mathrm{e}^{-2\gamma_{\mathrm{c}} l_{\mathrm{f1}}} \Gamma_{\mathrm{f1}}' = \frac{V_{5\mathrm{f1}}^{-}}{V_5^{+}} \tag{3.32}$$

where Γ_{f1}' is the local reflection coefficient of defect 1, and $V_{5\mathrm{f1}}^{-}$ represents the signal reflected from defect 1, as observed at point 5 in Fig. 3.1. Following the derivation steps of (3.16), (3.32) can be rewritten as:

$$\mathrm{e}^{-2\gamma_{\mathrm{c}} l_{\mathrm{f1}}} \Gamma_{\mathrm{f1}}' = \frac{V_{\mathrm{of1}} V_{\mathrm{os}}}{(V_{\mathrm{oD}})^2 - (V_{\mathrm{os}})^2} \tag{3.33}$$

According to (3.33), the interface reflection coefficient Γ_{f1}' can be directly estimated from the TDR measurement results, enabling the subsequent calculation of the defect's equivalent resistance using (3.30) or (3.31).

Equation (3.33) applies to cables with a single defect. For estimating the parameters of the n-th defect in a cable with multiple defects, this equation must be modified. Taking a cable with two defects as an example, the signal propagation along the cable is illustrated in Fig. 3.20. In this figure, V_6^+ represents the incident signal to defect 1, and V_7^+ is the transmitted signal after V_6^+ passes through defect 1. V_8^+ is the incident signal to defect 2, and V_{8f2}^- is the signal reflected from defect 2. V_{7f2}^- and V_{6f2}^- denote the reflected signals from defect 2, observed at point 7 and point 6, respectively. V_{5f2}^- is the reflected signal from defect 2 as observed at point 5. The relationships between V_6^+ and V_7^+, and between V_{7f2}^- and V_{6f2}^- can be expressed as follows:

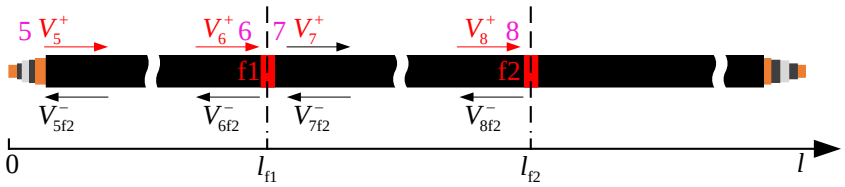


Fig. 3.20 The procedure of the signal propagating along a cable with two lumped defects

$$V_7^+ = V_6^+ \cdot T_{f1} \tag{3.34}$$

$$V_{6f2}^- = V_{7f2}^- \cdot T_{f1} \tag{3.35}$$

where T_{f1} denotes the transmission coefficient of defect 1. The expressions for T_{f1} are given as follows:

$$T_{f1} = 1 - |\Gamma'_{f1}| \tag{3.36}$$

where $|\Gamma'_{f1}|$ is the absolute value of the local reflection coefficient of defect 1.

Therefore, the relationship between Γ'_{f2} and TDR results can be expressed as follows:

$$e^{-2\gamma_c l_{f2}} \Gamma'_{f2} T_{f1}^2 = \frac{V_{of2} V_{os}}{(V_{oD})^2 - (V_{os})^2} \tag{3.37a}$$

$$T_{f1} = \begin{cases} 1 + \Gamma'_{f1}, & \text{ground defects} \\ 1 - \Gamma'_{f1}, & \text{series resistance defects.} \end{cases} \tag{3.37b}$$

Γ'_{f2} denotes the local reflection coefficient of defect 2. Furthermore, for the n-th defect, the estimation equation of its local reflection coefficient can be expressed as follows:

$$\Gamma'_{fn} = \frac{1}{e^{-2\gamma_c l_{fn}} \prod_{i=1}^{n-1} T_{fi}^2} \frac{V_{ofn} V_{os}}{(V_{oD})^2 - (V_{os})^2} \tag{3.38a}$$

$$T_{fi} = \begin{cases} 1 + \Gamma'_{fi}, & \text{ground defects} \\ 1 - \Gamma'_{fi}, & \text{series resistance defects.} \end{cases} \tag{3.38b}$$

where l_{fn} is the location of defect n, Γ'_{fn} is its local reflection coefficient, and T_{fi} is the transmission coefficient of defect i. Additionally, V_{ofn} denotes the TDR-measured reflected signal from defect n. As shown in (3.38a), the estimation accuracy of Γ'_{fn} strongly depends on the precision of defect localization. Therefore, the localization method based on TVMF is crucial for reliable defect parameter estimation.

Estimation of Distributed Defect Characteristic Parameters

According to the reflection coefficient expressions in (3.24) and (3.25), its characteristic parameters include the interface reflection coefficient Γ_{f1}^{+}, the defect length Δl_{f1}, and the propagation constant γ_{f1}. Equation (3.27) provides a simplified form of (3.24). Using Euler's formula and trigonometric identities, (3.27) can be rewritten as:

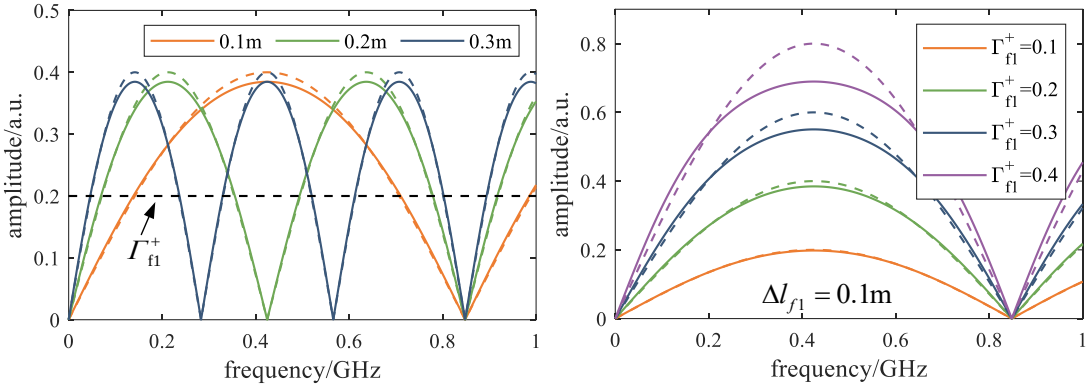
$$\Gamma'_{f1} = -2\Gamma_{f1}^{+} \sin\left(\beta_c \Delta l_{f1}\right) e^{j\left(\frac{\pi}{2} - \beta_c \Delta l_{f1}\right)} \tag{3.39}$$

Furthermore, as shown in (3.18b), β_c is frequency-dependent, and thus (3.39) can be rewritten as:

$$\Gamma'_{f1} = -2\Gamma_{f1}^{+} \sin\left(K_b \omega \Delta l_{f1}\right) e^{j\left(\frac{\pi}{2} - K_b \omega \Delta l_{f1}\right)} \tag{3.40}$$

As shown in (3.40), the local reflection coefficient of distributed defects are frequency-dependent and characterized by two parameters: the defect length Δl_{f1} and the interface reflection coefficient Γ_{f1}^{+}. Its frequency-dependent behavior is illustrated in Fig. 3.21. Fig. 3.21a shows how Γ'_{f1} varies with defect length. The amplitude of Γ'_{f1} exhibits a sinusoidal pattern, with the period decreasing as the defect length increases. In contrast to the interface reflection coefficient Γ_{f1}^{+}, which is typically constant, Γ'_{f1} increases with frequency in the low-frequency range. As a result, unlike lumped defects, the reflection intensity of distributed defects is affected by the frequency bandwidth of the injected signal. This implies that the magnitude of the reflected signal cannot directly indicate defect severity. Even when the injected signals have the same bandwidth, the severity of distributed defects cannot be compared without knowing their lengths. Fig. 3.21b illustrates the impact of Γ_{f1}^{+} on the accuracy of the approximation in (3.40). As shown, the approximation error increases around the peak as Γ_{f1}^{+} grows. However, according to the analysis in Section 2.1, even for severe distributed defects, Γ_{f1}^{+} is typically less than 0.3. Furthermore, the frequency components of practical measurement signals usually remain within several hundred megahertz. Therefore, the approximation in (3.40) remains valid even when Γ_{f1}^{+} is relatively large.

In Section 3.2, the results of the TVMF provide a coarse estimation of the distributed defect equivalent length. Therefore, when estimating the characteristic parameters of a distributed defect, the interface reflection coefficient Γ_{f1}^{+} remains the only unknown. Since the magnitude



(a) Various defect lengths (b) Various Γ_{f1}^{+}

Fig. 3.21 The frequency-dependent behavior of the reflection coefficient for distributed defects is illustrated. The solid lines represent the accurate results obtained from (3.24), while the dashed lines show the approximated results based on (3.40).

of the local reflection coefficient Γ_{f1}' exhibits a sinusoidal pattern and Γ_{f1}^{+} is the sole unknown variable, it can be estimated by fitting a sinusoidal function to the measured data.

When a cable contains multiple defects, the injected signal may be altered as it propagates through preceding distributed defects. Hence, to accurately estimate the characteristic parameters of the n-th distributed defect, the influence of prior defects on the propagating signal must be taken into account. The transmission characteristics of a distributed defect can be derived from (3.24) and (3.25). The signal propagation through a distributed defect is illustrated in Fig. 3.22, where Γ_{f1}' denotes the local reflection coefficient at the input of the defect, and Γ_{f1}^{+} represents the interface reflection coefficient at the output. The variables V_6^+, V_7^+, V_8^+, and V_9^+ denote the incident signals at different positions along the defect segment, while V_6^-, V_7^-, V_8^-, and V_9^- denote the corresponding reflected signals.

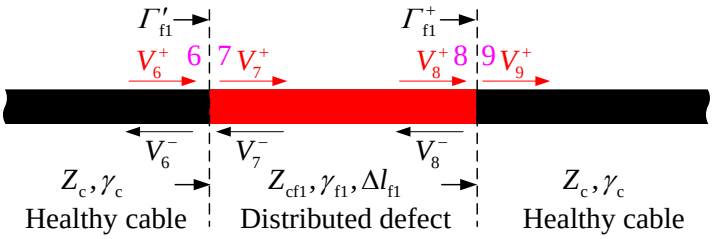


Fig. 3.22 The procedure of the signal propagating along a distributed defect

As illustrated in Fig. 3.22, the transmission coefficient T_{f1} can be derived based on the following principle:

$$V_6^+ + V_6^- = V_7^+ + V_7^- \tag{3.41a}$$

$$V_8^+ + V_8^- = V_9^+ \tag{3.41b}$$

The relationships between V_6^+ and V_6^-, V_7^+ and V_7^-, as well as between V_8^+ and V_9^+, are expressed as follows:

$$V_6^- = V_6^+ \Gamma_{\mathrm{f1}}' \tag{3.42}$$

$$V_7^- = V_7^+ \Gamma_{\mathrm{f1}}^+ \mathrm{e}^{-2\gamma_{\mathrm{f1}}\Delta l_{\mathrm{f1}}} \tag{3.43}$$

$$V_9^+ = V_8^+ \left(1+\Gamma_{\mathrm{f1}}^+\right) \tag{3.44}$$

By combining (3.41), (3.42), (3.43), and (3.44), the relationship between V_6^+ and V_9^+ can be expressed as follows:

$$V_9^+ = V_6^+ \frac{\mathrm{e}^{-\gamma_{\mathrm{f1}}\Delta l_{\mathrm{f1}}}\left(1+\Gamma_{\mathrm{f1}}'\right)\left(1+\Gamma_{\mathrm{f1}}^+\right)}{1+\Gamma_{\mathrm{f1}}^+ \mathrm{e}^{-2\gamma_{\mathrm{f1}}\Delta l_{\mathrm{f1}}}}. \tag{3.45}$$

According to (3.45), the transmission coefficient T_{f1} of the distributed defect is given by:

$$T_{\mathrm{f1}} = \frac{\mathrm{e}^{-\gamma_{\mathrm{f1}}\Delta l_{\mathrm{f1}}}\left(1+\Gamma_{\mathrm{f1}}'\right)\left(1+\Gamma_{\mathrm{f1}}^+\right)}{1+\Gamma_{\mathrm{f1}}^+ \mathrm{e}^{-2\gamma_{\mathrm{f1}}\Delta l_{\mathrm{f1}}}} \tag{3.46}$$

By neglecting the attenuation of the distributed defect and replacing β_{f1} with β_{c}, the transmission coefficient T_{f1} can be obtained by substituting (3.39) into (3.46), yielding:

$$T_{\mathrm{f1}} = \frac{\mathrm{e}^{-\mathrm{j}\beta_{\mathrm{c}}\Delta l_{\mathrm{f1}}}\left[1-2\Gamma_{\mathrm{f1}}^+ \sin\left(\beta_{\mathrm{c}}\Delta l_{\mathrm{f1}}\right)\mathrm{e}^{\mathrm{j}\left(\frac{\pi}{2}-\beta_{\mathrm{c}}\Delta l_{\mathrm{f1}}\right)}\right]\left(1+\Gamma_{\mathrm{f1}}^+\right)}{1+\Gamma_{\mathrm{f1}}^+ \mathrm{e}^{-2\mathrm{j}\beta_{\mathrm{c}}\Delta l_{\mathrm{f1}}}} \tag{3.47}$$

In (3.47), Γ_{f1}^+ and Δl_{f1} are the two characteristic parameters of the distributed defect, which have been estimated based on the TVMF results and reflection coefficient fitting. Thus, the transmission coefficient T_{f1} of the distributed defect can be determined.

By combining (3.38) and (3.47), the reflection coefficient of the n-th defect in a cable with multiple defects can be estimated as:

$$\Gamma_{\mathrm{f}n}' = \frac{1}{\mathrm{e}^{-2\gamma_{\mathrm{c}}l_{\mathrm{f}n}}\prod_{i=1}^{n-1} T_{\mathrm{f}i}^2} \frac{V_{\mathrm{of}n}V_{\mathrm{os}}}{\left(V_{\mathrm{oD}}\right)^2-\left(V_{\mathrm{os}}\right)^2} \tag{3.48a}$$

for lumped defects

$$T_{\mathrm{f}i} = \begin{cases} 1+\Gamma_{\mathrm{f}i}', & \text{ground defects} \\ 1-\Gamma_{\mathrm{f}i}', & \text{series resistance defects,} \end{cases} \tag{3.48b}$$

for distributed defects

$$T_{\mathrm{f}i} = \frac{\mathrm{e}^{-\mathrm{j}\beta_{\mathrm{c}}\Delta l_{\mathrm{f}i}}\left[1-2\Gamma_{\mathrm{f}i}^+ \sin\left(\beta_{\mathrm{c}}\Delta l_{\mathrm{f}i}\right)\mathrm{e}^{\mathrm{j}\left(\frac{\pi}{2}-\beta_{\mathrm{c}}\Delta l_{\mathrm{f}i}\right)}\right]\left(1+\Gamma_{\mathrm{f}i}^+\right)}{1+\Gamma_{\mathrm{f}i}^+ \mathrm{e}^{-2\mathrm{j}\beta_{\mathrm{c}}\Delta l_{\mathrm{f}i}}} \tag{3.48c}$$

$$\Gamma_{\mathrm{f}i}^+ = \frac{\Gamma_{\mathrm{f}i}'}{-2\sin\left(\beta_{\mathrm{c}}\Delta l_{\mathrm{f}i}\right)\mathrm{e}^{\mathrm{j}\left(\frac{\pi}{2}-\beta_{\mathrm{c}}\Delta l_{\mathrm{f}i}\right)}}. \tag{3.48d}$$

Equation (3.48) provides a unified approach for estimating the reflection coefficients of both lumped and distributed defects in a cable containing multiple defects and joints. When applying (3.48) to calculate the reflection coefficient from TDR measurement results, the reflected signal must correspond to an actual defect rather than a “fake" reflection. To distinguish reflections from actual defects, a pulse reconstruction method is proposed in the next section.

3.3.3 Implementation of Pulse Reconstruction

After estimating the characteristic parameters of the cable and defects, the reflected signal can be reconstructed. By reconstructing the reflections from known defects, “fake" reflections in the TDR measurement can be eliminated. This enables the sequential identification and localization of the actual defects.

To illustrate the detailed process of reflected pulse reconstruction, a cable with a single defect is first considered as an example. The process is similar for multiple defects, and the corresponding results are also provided. Fig. 3.23 shows a TDR measurement system used to detect a cable with a defect. As the TDR device is identical to that in Fig. 3.1, it is omitted in Fig. 3.23.

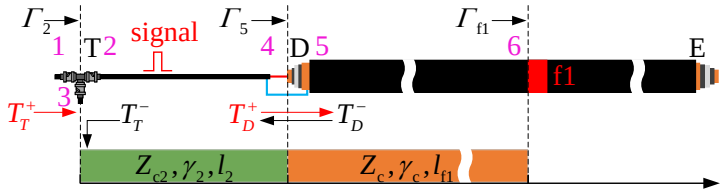


Fig. 3.23 The schematic of the TDR measurement system for a cable with a defect.

To reconstruct the measured reflected signal, the relationship between the measured signals and the cable model is analyzed. Based on the modeling method for cables with multiple defects described in Section 2.3, the measured reflected signals can be expressed in terms of the measured injected signals as follows:

$$V_{\mathrm{or}} = V_{\mathrm{oI}} \cdot \Gamma_2 \cdot T_{\mathrm{T}}^{-} \tag{3.49}$$

where Γ_2 represents the reflection coefficient at port 2. However, Γ_2 includes the influence of the connecting cable and connector D, whose parameters are unknown. Therefore, (3.49) should be considered a theoretical result rather than one suitable for practical application. To avoid calculating Γ_2, Γ_2 is expressed using Γ_5 and shown as follows:

$$\Gamma_2 = \Gamma_5 \mathrm{e}^{-2\gamma_2 l_2} T_{\mathrm{D}}^{+} T_{\mathrm{D}}^{-} \tag{3.50}$$

Furthermore, by substituting (3.9), (3.10), (3.13), and (3.15) into (3.50), the expression for Γ_2 can be rewritten as:

$$\Gamma_2 = \Gamma_5 e^{-2\gamma_2 l_2}\left(1 - \frac{V_{oD}^2}{V_{os}^2}\right) \tag{3.51}$$

The frequency spectrum of the TDR measurement result, V_{or}, can be reconstructed as:

$$V_{\mathrm{or}} = -\Gamma_5\left(\frac{V_{\mathrm{os}}^2 - V_{\mathrm{oD}}^2}{V_{\mathrm{os}}}\right) \tag{3.52}$$

Equation (3.52) provides the expression for reflected pulse reconstruction in the frequency domain. By applying the inverse Fourier transform, the time-domain waveform of the reconstructed reflection pulse can be obtained. Notably, (3.52) requires only the input reflection coefficient Γ_5 of the tested cable and does not rely on the reflection coefficients of the TDR device or connector D. For a cable with a single defect located at l_{f1}, as illustrated in Fig. 3.23, Γ_5 can be derived as follows:

$$\Gamma_5 = \Gamma_1 e^{-2\gamma_c l_{\mathrm{f1}}} \tag{3.53}$$

Here, Γ_1 denotes the reflection coefficient at the entrance of defect 1. For a cable with multiple defects, Γ_1 can be recursively calculated using (2.40). It is important to note that when reconstructing the reflected signals generated by the first n defects, the cable segment beyond the n-th defect is assumed to be an infinitely long, healthy cable.

Using (3.52), all multiple reflection pulses caused by the first n defects can be reconstructed. By subtracting these reconstructed signals from the TDR measurement results, the first reflection in the residual signal must correspond to the $(n+1)$-th defect. This defect can then be localized using the TVMF method, and its parameters can be estimated. By repeating this process until the end of the cable, all defects can be sequentially localized and their characteristic parameters determined.

3.3.4 Simulation and Validation

In this section, simulations are conducted to validate the detection and localization of multiple defects based on pulse reconstruction. First, to demonstrate the complete procedure of pulse reconstruction, a simulation involving a cable with two lumped defects is presented in detail. Then, simulation of a cable containing different defects—including both lumped and distributed types—is carried out to further verify the effectiveness of the proposed method for different types of defects.

Case I: Cable with two lumped defects

First, a model of a 600-meter-long cable, each containing two lumped defects, is constructed. The locations and types of the defects in the case are illustrated in Fig. 3.24. The defect resistances are $R_{\mathrm{p1}} = 50\,\Omega$ and $R_{\mathrm{s3}} = 80\,\Omega$.



Fig. 3.24 Case I: A model of long cable with multiple defects

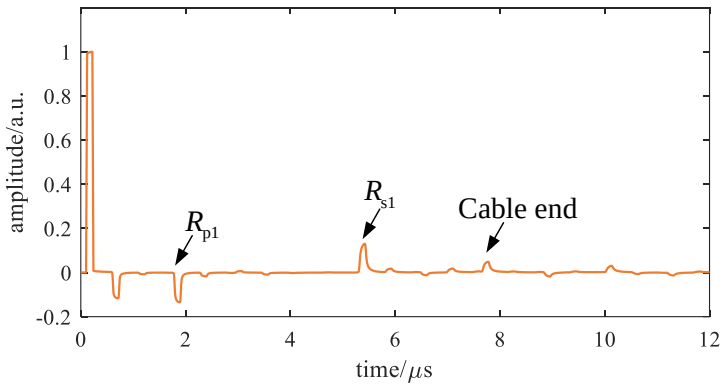


Fig. 3.25 TDR simulation results

The TDR simulation results for the cases is presented in Fig. 3.25. In the figure, multiple reflected pulses can be observed in the TDR measurement. The detailed steps of the proposed method for localizing multiple defects are as follows:

Step 1. Localize the first defect. The first reflection corresponds to the first defect. Using TVMF, the first defect in Fig. 3.25 was localized at 100.11 meters.

Step 2. Estimate the type and parameters of the first defect. The type of the first defect is determined based on whether the reflected signal is positive or negative. In Fig. 3.25, it is classified as ground defects. Then, using (3.30), (3.31), and (3.33), the equivalent resistance of the first defect Fig. 3.25 is estimated as 49.95 Ω.

Step 3. Reconstruct the reflected pulses by the first defect. By establishing equivalent models of the tested cable containing only the first defect and calculating the reflection coefficient of the tested cable, the reflected pulses are reconstructed according to (3.52), as shown in Fig. 3.26.

Step 4. Identification and Localization of the Second Actual Reflection Pulse. After the reconstructed pulses were subtracted from the measured results, the remaining reflection signals—excluding the first defect—were obtained. The first reflection pulse in the remaining signals was then localized. Due to estimation errors in the characteristic parameters of the

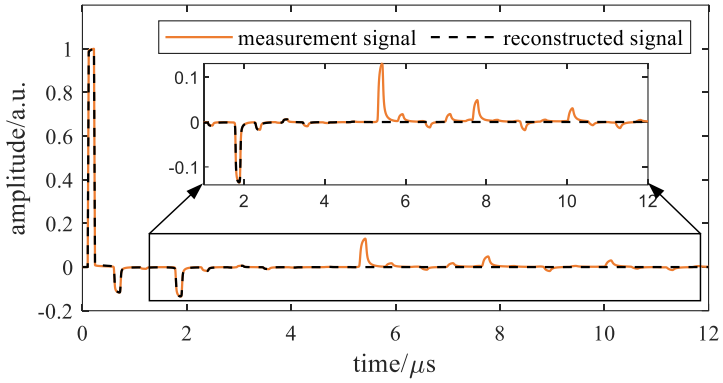


Fig. 3.26 Reconstruction of reflection pulses by the first Defect

tested cable and defects, as well as the influence of noise, small spurious peaks may appear in the TVMF localization results. To mitigate this, a threshold of ± 3 standard deviations was adopted to identify and localize the first significant reflection in the TVMF output. The TVMF localization results for the remaining signals are shown in Fig. 3.27, where the orange line represents the TVMF response and the green shaded region indicates the ± 3 standard deviation range, referred to as the error band. From the figure, the second actual reflection pulse is observed at approximately 5.2 μs, corresponding to a localized defect at 400.51 m.

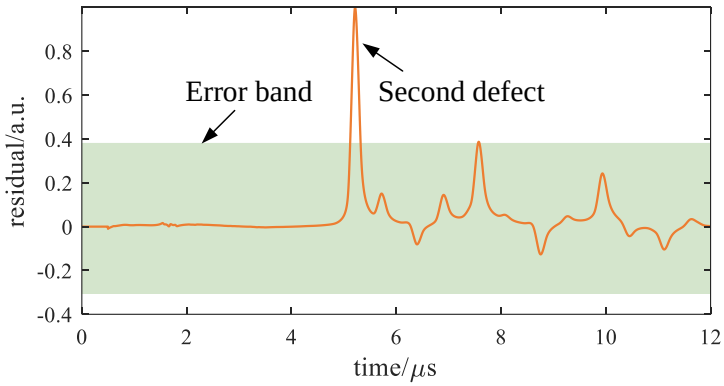


Fig. 3.27 The TVMF location results of the second actual reflection pulse

Step 5. Estimate the type and parameters of the second defect. According to (3.30), (3.31), and (3.48), for the cable shown in Fig. 3.24, the second defect is classified as series resistance defects, with an estimated equivalent resistance of 78.09 Ω.

Step 6. Reconstruct the reflection pulses by the first and second defects. By repeating Step 3, the reflection pulses caused by the first and second defects were reconstructed and compared, as shown in Fig. 3.28.

Step 7. Identify and localize the third actual reflection pulse. By repeating Step 4, the TVMF localization results for the remaining reflection pulses were obtained and are shown in Fig. 3.29. In the figure, the third reflection pulse occurs at approximately 7.5 μs, and the defect

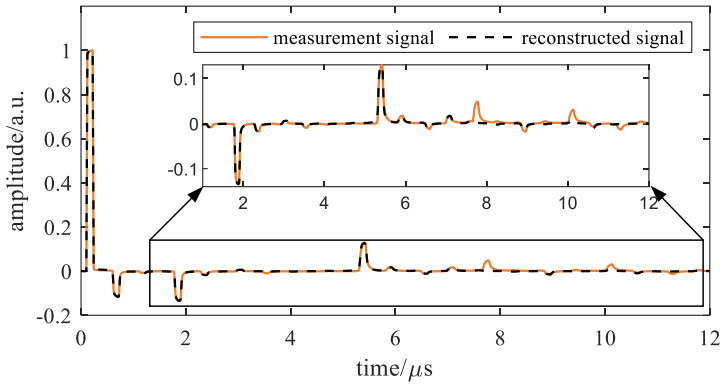


Fig. 3.28 Reconstruction of reflection pulses by the first and second defects

is localized at 600.8 meters. Considering the cable length, 600.8 meters is approximated to 600 meters; therefore, the third defect can be regarded as the reflection pulse from the cable end. Thus far, all defects in the cable have been identified and localized. The reflected pulses caused by all defects were reconstructed and are shown in Fig. 3.30. If the detected defects do not correspond to the cable end, Steps 2, 3, and 4 can be repeated to estimate and locate subsequent defects until the cable end is identified. The location and defect results for case I are summarized in Table 3.2.

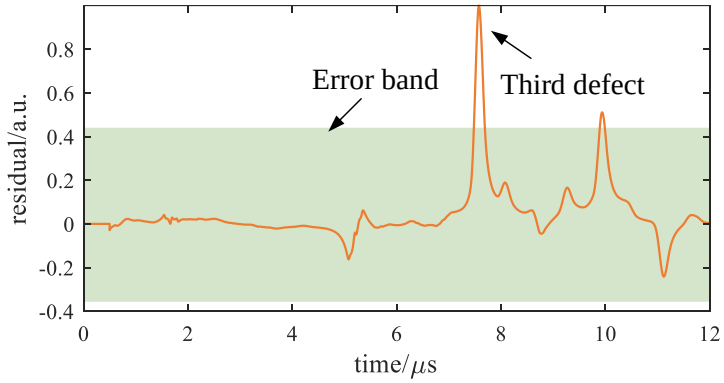


Fig. 3.29 The TVMF location results of the third actual reflection pulse

A flowchart illustrating the procedure for multiple defect identification and localization is also provided, as shown in Fig. 3.31.

Regarding the identification of the cable end, two scenarios are considered:

(1) **Known cable length:** If the cable length is known, a reflected pulse can be attributed to the cable end when the defect location approximately equals the total cable length.

(2) **Unknown cable length:** Since the cable end is typically open-circuited during TDR measurements, a reflected pulse can be identified as originating from the cable end if its equivalent impedance is significantly high, typically exceeding several kilo-ohms.

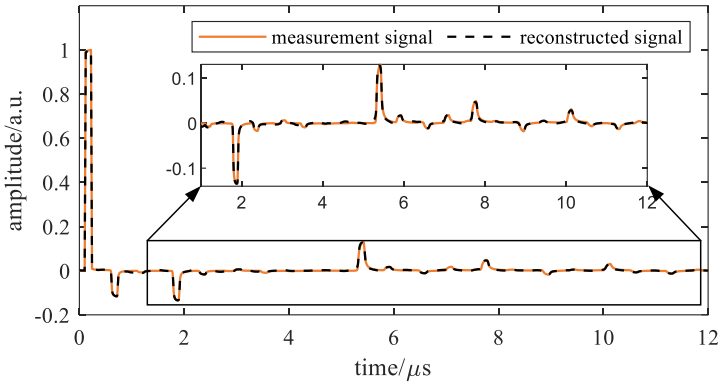


Fig. 3.30 Reconstruction of reflection pulses by the first, second defects and cable end

Table 3.2 Location and estimation results of defects in Case I

Defect	Property	Estimation	Reference	Error/%
1st	Location/m	100.11	100	0.11
	Resistance/Ω	49.95	50	0.10
	Type	Ground	Ground	–
2nd	Location/m	400.51	400	0.12
	Resistance/Ω	78.09	80	2.39
	Type	Series	Series	–
3rd	Location/m	600.08	600	0.01
	Type	Open circuit	Open circuit	–

Case II: Cable with a lumped defect and a distributed defect

In this case, a 600-meter-long cable with one lumped defect and one distributed defect is simulated. The lumped defect, located at 100 m, is a series resistance defect with a resistance of $R_{s4} = 30\,\Omega$. The distributed defect, located at 400 m, is a shield hole defect with a length of 2 m, an angle of 240°, and a characteristic impedance of $Z_{cf3} = 48.26\,\Omega$. The simulation schematic is shown in Fig. 3.32. The TDR simulation results are shown in Fig. 3.33. The first, second, and third reflection pulses correspond to the lumped defect, the distributed defect, and the cable end, respectively.

By repeating Steps 1 to 7 from the previous section, the reconstructed defect pulses are obtained, as shown in Fig. 3.34. As observed from the figure, the pulse reconstruction method accurately reconstructs the reflected pulses from each defect. This procedure effectively distinguishes multiple reflections caused by multiple defects and eliminates “fake" reflections.

The localization results for each defect, along with the estimated characteristic parameters, are presented in Table 3.3. The results demonstrate that the proposed method exhibits high accuracy and robustness when applied to a cable containing multiple defects of different types.

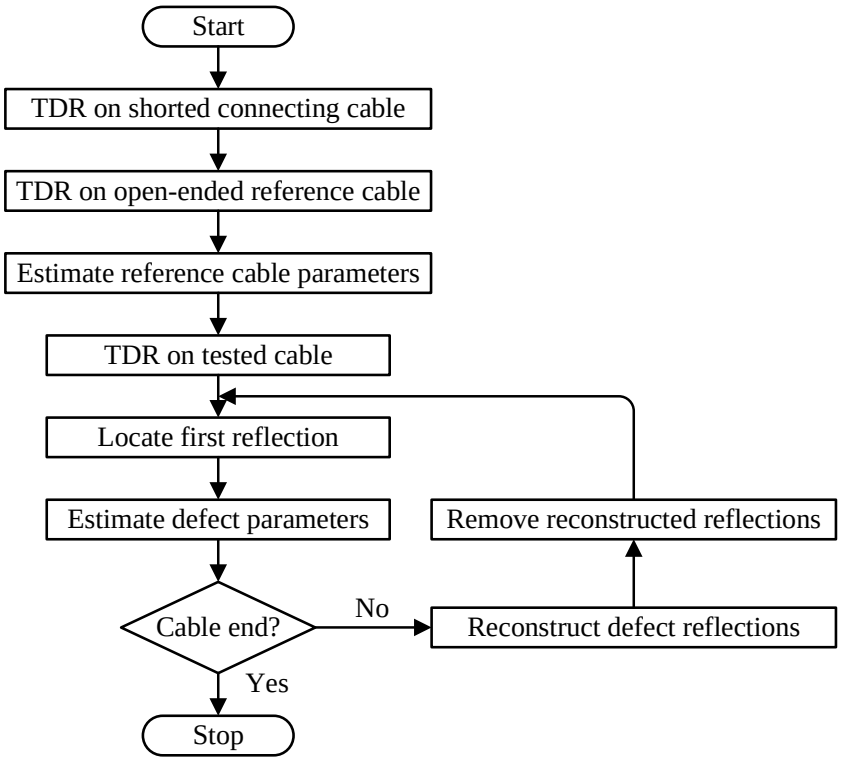


Fig. 3.31 Flowchart of multiple defect identification and localization. Note: the reference cable is a cable segment of the same type as the tested cable.



Fig. 3.32 The schematic of the cable with a lumped defect and a distributed defect

For the first defect, a lumped defect, the estimated location has a minimal error of 0.11 %, and the series resistance is accurately identified as 30 Ω, matching the reference value exactly. The second defect, a distributed defect, is located with an error of 0.26 %. Its interface reflection coefficient Γ_{f}^{+} is estimated to be -0.174, with a relative error of 2.96 %, and the estimated

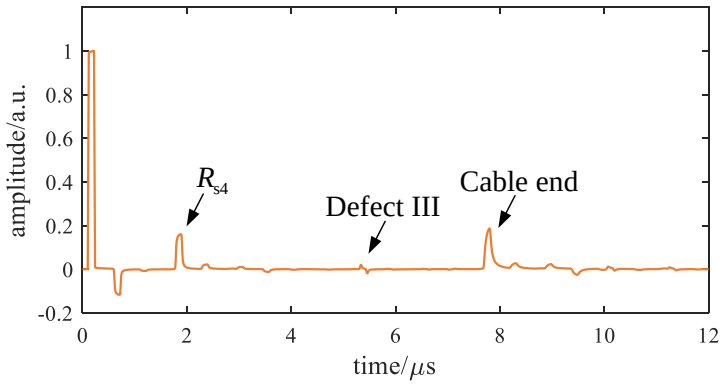
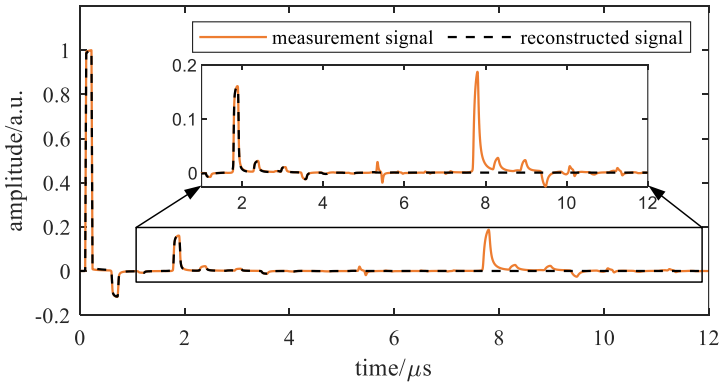
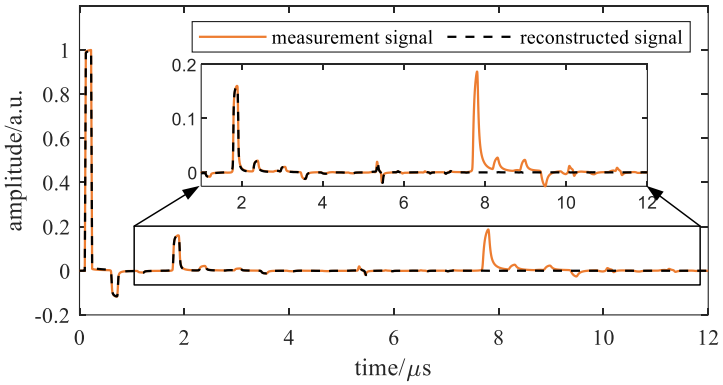


Fig. 3.33 TDR simulation results of the cable in case II

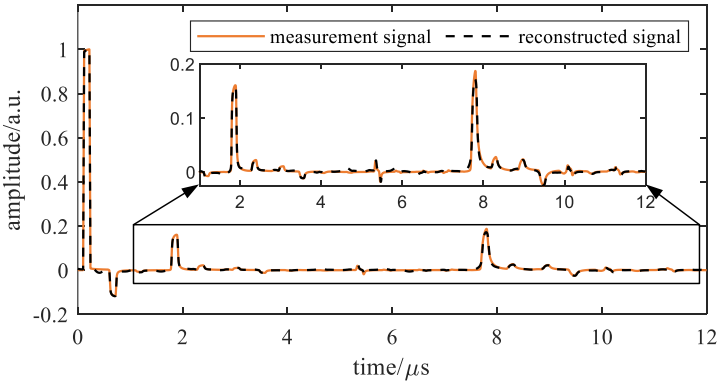
defect length is 2.20 m, corresponding to a 10 % error. Despite the 10 % length estimation error, the reconstructed waveform closely matches the simulated result in both shape and reflection timing, as shown in Fig. 3.34. This suggests that the estimated length represents an equivalent length under the assumption $\beta_f = \beta_c$. The third defect, corresponding to the open-circuited cable end, is localized with an error of 0.25 %, and its type is correctly identified, further validating the method's effectiveness in detecting hard faults. Overall, the proposed method accurately localizes various types of defects and estimates their characteristic parameters, demonstrating strong practical applicability for cable diagnostics.



(a) Reconstruction of first defect



(b) Reconstruction of first and second defects



(c) Reconstruction of first defect, second defect and cable end

Fig. 3.34 Reconstruction of reflection pulses in case II cable

Table 3.3 Location and estimation results of defects in Case II

defect	type	property	Estimation	Reference	Error/%
1st	lumped defect	location/m	100.11	100	0.11
		resistance/Ω	30	30	0
		type	series resistance	series resistance	–
2nd	distributed defect	location/m	401.02	400	0.26
		Γ_{f}^{+}	-0.174	-0.169	2.96
		Δl_{f}/m	2.20	2	10
3rd	open circuit	location/m	603.53	602	0.25
		type	open circuit	open circuit	–

In this section, a series of simulations was conducted to validate the accuracy of characteristic parameter estimation and defect localization for cables with multiple defects and the effectiveness of the pulse reconstruction method. The detailed process of identifying and locating actual defects using the reflected pulse reconstruction technique is illustrated. In the following section, the experimental results and performance of the proposed method are presented and analyzed.

3.4 Experimental Verification

In this section, experiments were conducted to validate the proposed methods. First, an experiment was performed to estimate the characteristic parameters of cables. Subsequently, two types of defects scenarios were tested: a cable with two series resistance defects, a cable with a series resistance defect and a ground defect. The experiment results were analyzed and the performance of the proposed method was evaluated.

3.4.1 Experimental Setup Measurement Platform

As the experiment aims to quantitatively validate the proposed method, preparing and testing samples at 10 kV is costly and impractical. For this reason, the experiment was conducted on a coaxial signal cable. The experimental platform consists of five main components: a pulse source, an oscilloscope, a computer, a connecting cable, and the test cable samples. A schematic diagram of the setup is shown in Fig. 3.35. The pulse source, a Keysight 33600A, is used to generate the required pulse signal and has an output impedance of 50 Ω. The oscilloscope, a PicoScope 5443D, samples both the injected and reflected signals from the cable under test and is impedance-matched at 75 Ω. The computer is used to control the pulse source and to analyze

data collected by the oscilloscope. In TDR measurements of power cables, the characteristic impedance of the connecting cable often differs from that of the tested cable. In this experiment, a 50 m-long RG179 cable with a characteristic impedance of 75 Ω was used as the connecting cable. The tested cable is an SYV50 with a characteristic impedance of 50 Ω. Defects were inserted into the tested cable using SMA connectors, which are impedance-matched to the tested cable to avoid additional interface reflections.

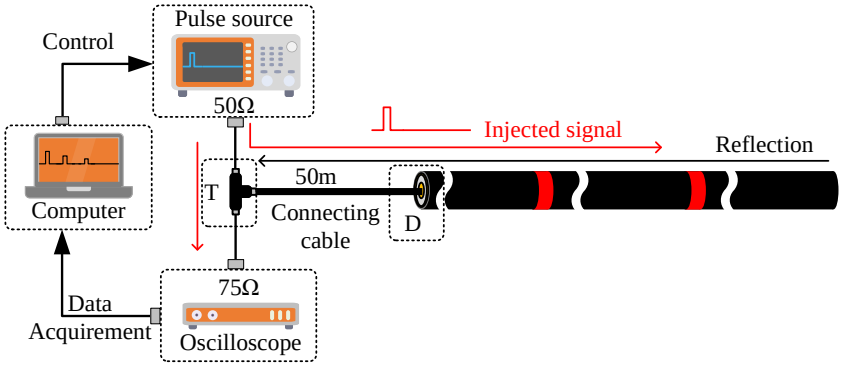


Fig. 3.35 The schematic of the experiment

The experimental settings are shown in Table 3.4. Case I validates the estimation of cable characteristic parameters using a 200 m-long defect-free cable. Case II involves two series resistance defects, while Case III has one ground defect and one series resistance defect.

Table 3.4 Parameters of defects in experiments

Case	Length/m	Location/m	Type	Defect parameters
case I	200	–	–	–
case II	600	200, 400	two series resistance defects	$R_{s1} = 20\,\Omega$, $R_{s2} = 100\,\Omega$
case III	600	200, 400	a ground defect, a series resistance defect	$R_{p1} = 100\,\Omega$, $R_{s3} = 100\,\Omega$

3.4.2 Experimental Results and Analysis

Cable Characteristic Parameter Estimation

In the experiment for cable characteristic parameter estimation, the tested cable was a 200 m-long healthy cable with an open-circuited end. The injected pulse had a rise time and fall time

of 20 ns each, and a pulse width of 100 ns. The corresponding TDR measurement result is shown in Fig. 3.36.

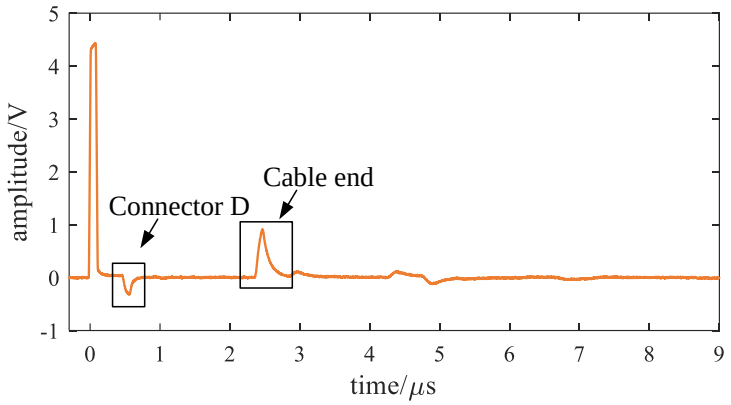


Fig. 3.36 The TDR measurement results of the 200-meter-long cable with an open-circuit.

Based on (3.16) and (3.17), along with the measurement results shown in Fig. 3.36, the characteristic parameters of the tested cable were estimated. The results are presented in Fig. 3.38. To validate these estimates, the same type of cable was measured using a VNA, and its S-parameters were obtained. The schematic of VNA measurement is shown as Fig. 3.37. The characteristic parameters were then calculated using (2.41) and (2.42). The results from the improved method are compared with those obtained from the VNA measurements, and the comparison is also shown in Fig. 3.38.

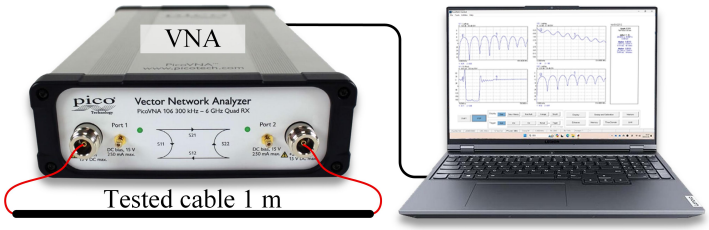
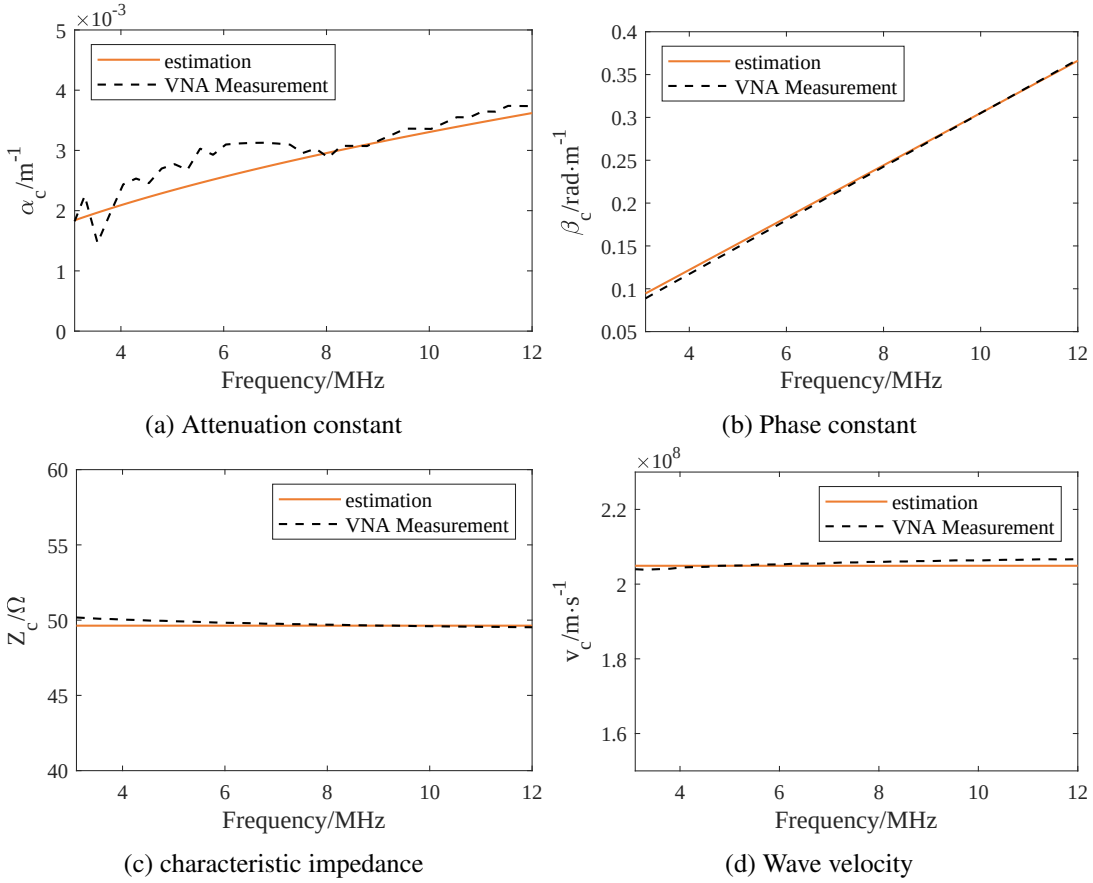


Fig. 3.37 The schematic of VNA measurement for cable characteristic parameters

In Fig. 3.38, the estimated characteristic impedance Z_c of the tested cable is 49.63 Ω, and the estimated wave velocity is 204.91 m/μs. These estimates are consistent with the VNA measurement results, indicating that the improved estimation method has high accuracy. Compared to VNA method, the improved method offers greater flexibility in practical measurement.

Detection of Multiple Defects

In these cases, lumped defects were implemented using non-inductive resistors. These defects were inserted into the healthy cable via SMA connectors. Photographs of the lumped defects

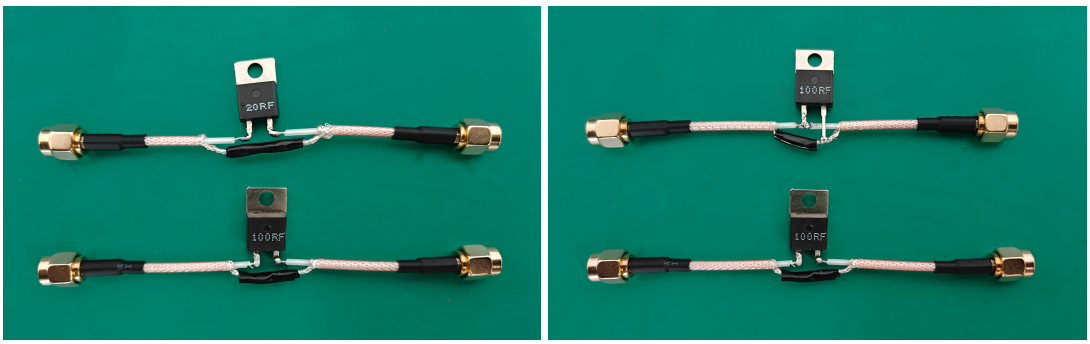


(a) Attenuation constant (b) Phase constant

(c) characteristic impedance (d) Wave velocity

Fig. 3.38 Comparison of cable characteristic parameters: estimation results by the improved method and measurement results from the VNA

are shown in Fig. 3.39. In this setup, Defect I and Defect II are configured according to the parameters specified for Case II and Case III in Table 3.4.

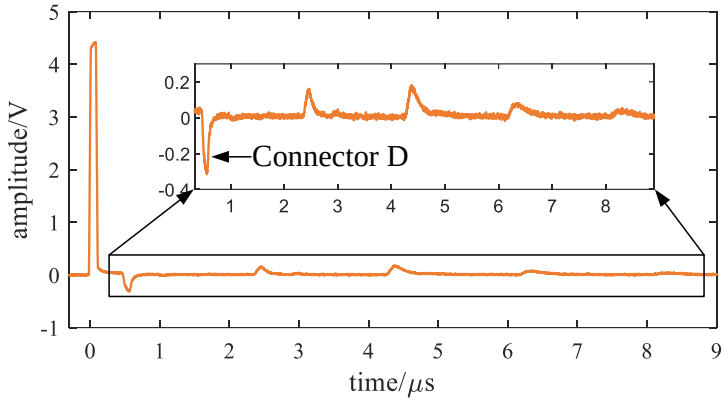


(a) Case II (b) Case III

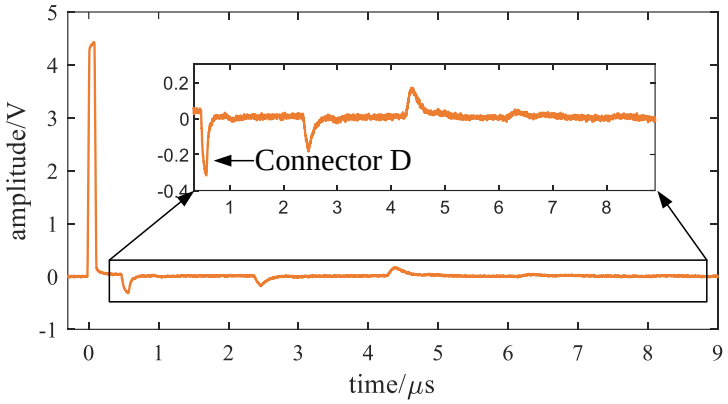
Fig. 3.39 Resistors used as lumped defects in experiments

The measurement results for Case II and Case III are shown in Fig. 3.40. Specifically, Fig. 3.40a presents the TDR measurement results for Case II, while Fig. 3.40b shows the results for Case III. The most notable difference between the two cases lies in the polarity of the second

reflection pulse. In Case II, the second reflected pulse is positive, whereas in Case III, it is negative.



(a) Case II

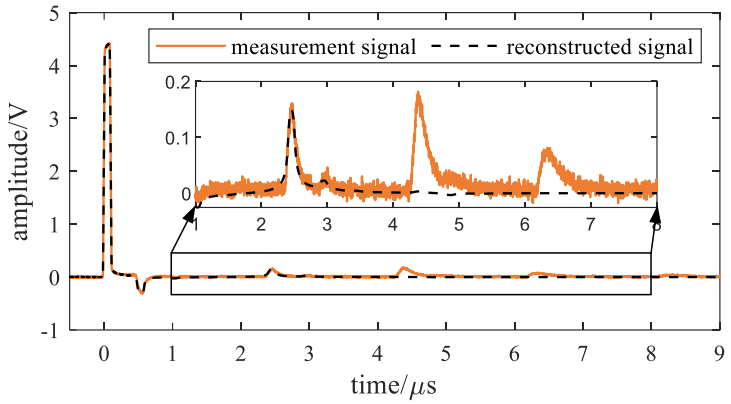


(b) Case III

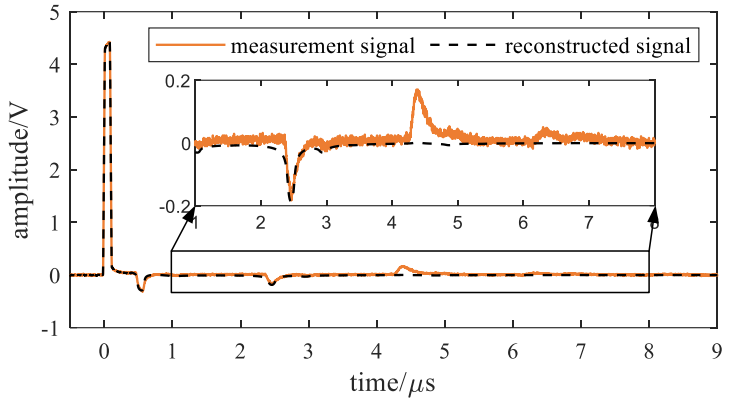
Fig. 3.40 The TDR measurement results of two lumped defects

In Fig. 3.40, the first reflected pulses appearing at 0.6 µs originate from connector D. The second pulses, observed at approximately 2.3 µs, correspond to the first cable defects. Using the TVMF method, the first defect locations in Case II and Case III were estimated to be 197.74 m and 198.35 m, respectively. The corresponding localization errors are 2.26 m and 1.65 m, with relative errors of 1.13 % and 0.83 %, respectively. Subsequently, the equivalent resistance and defect type were estimated using equations (3.33), (3.30), and (3.31). Based on the polarity of the reflected signals, the first defect in Case II was identified as a series resistance defect, while the first defect in Case III was classified as a ground defect. The estimated equivalent resistances were 19.19 Ω and 100.04 Ω, with relative errors of 4.55 % and 0.04 %, respectively. Using the estimated characteristic parameters, the reflected pulses from the first defect were reconstructed. The reconstruction results are shown in Fig. 3.41.

After subtracting the reconstructed reflection pulses of the first defect from the measurement results, the second defects were localized using the TVMF method. The localization results for the second defects in Case II and Case III are shown in Fig. 3.42.

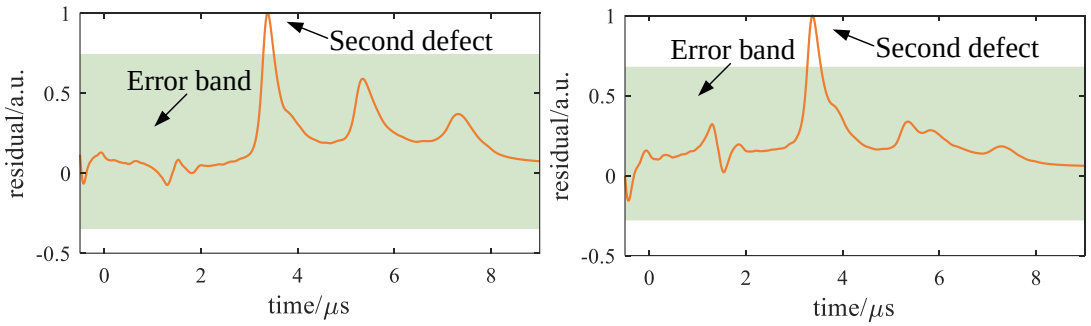


(a) Case II



(b) Case III

Fig. 3.41 The reconstruction reflection pulses by the first defect in Case II and Case III

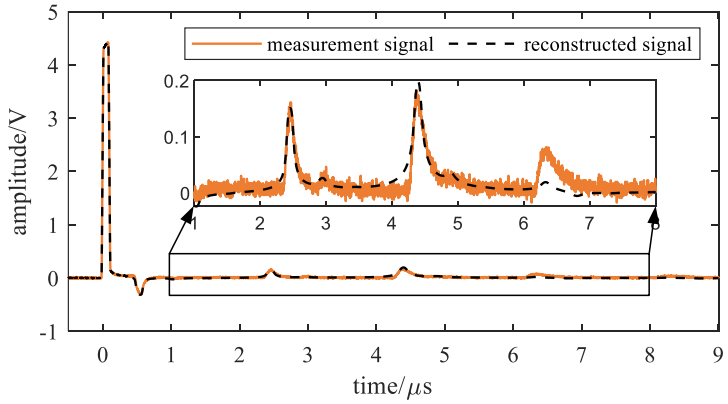


(a) Case II (b) Case III

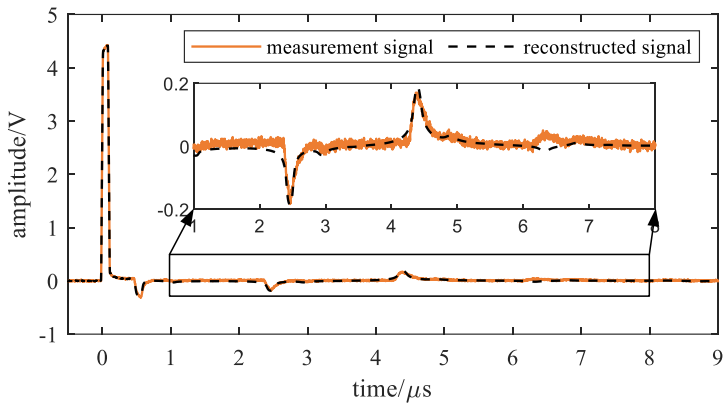
Fig. 3.42 The TVMF location results of the second defects

According to the localization results shown in Fig. 3.42, the second defects in Case II and Case III are located at 397.63 m and 397.42 m, respectively. Based on the polarity of the reflected signals, both defects were classified as series resistance defects, with estimated equivalent resistances of 95.58 Ω for Case II and 105.19 Ω for Case III. Following the same reflected pulse reconstruction procedure, the reflection pulses caused by both the first and second defects in Cases II and III were reconstructed. The results are shown in Fig. 3.43. As illustrated in the figure, the reconstructed reflected pulses closely match the measured TDR

responses, confirming the accuracy of the reconstruction. However, around 6 µs, a reflected signal is clearly observed in the TDR measurement results, whereas no corresponding reflection appears in the reconstructed signal. This discrepancy indicates the presence of an additional reflection around 6 µs, which is not accounted for by the two identified defects.



(a) Case II

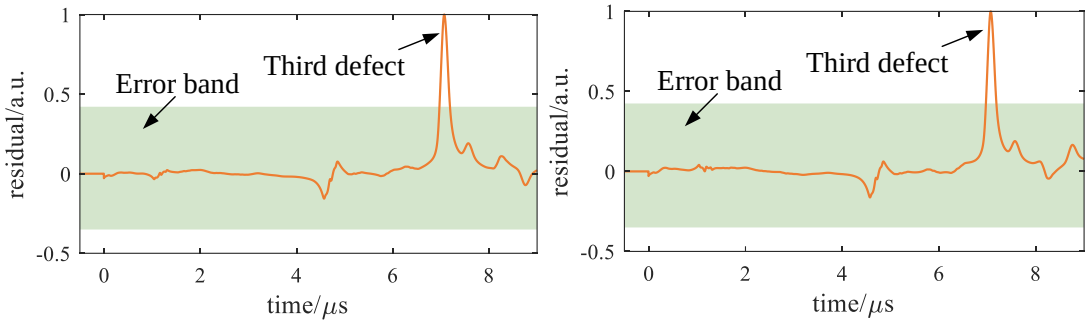


(b) Case III

Fig. 3.43 The reconstruction reflection pulses by the first and second defects in Case II and Case III

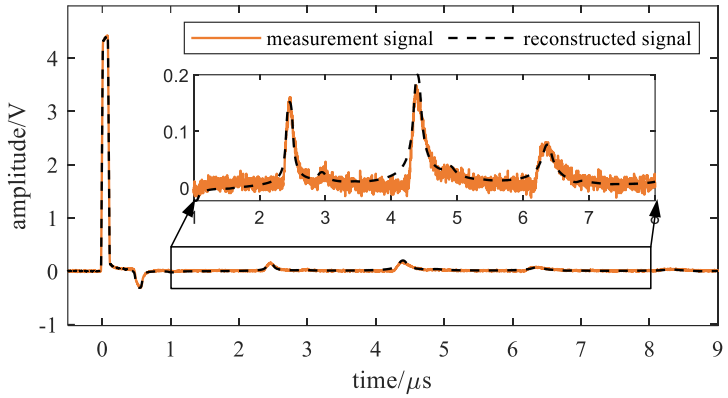
After removing the reconstructed signals of the first and second defects from the TDR measurement results, the third defect was localized using the TVMF method. The corresponding localization results are shown in Fig. 3.44. According to the peaks in Fig. 3.44, the third defects in Case II and Case III were located at 601.52 m and 597.52 m, respectively.

The third defects in both Case II and Case III were subsequently classified as series resistance defects, with estimated equivalent resistances of 1100.46 Ω and 1378.91 Ω, respectively. These high resistance values indicate that the defects are likely caused by open-circuit faults or correspond to the open-circuited cable ends. Considering the overall cable lengths, the associated reflection pulses are attributed to reflections from the cable ends. The reflection pulses caused by the first and second defects, as well as those from the cable ends, were reconstructed. The results are shown in Fig. 3.45.

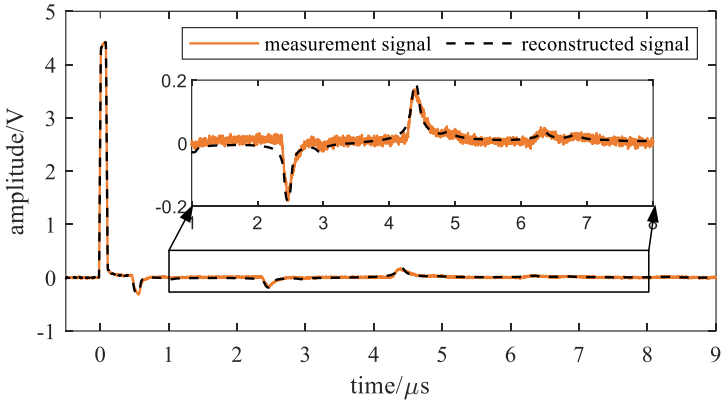


(a) Case II (b) Case III

Fig. 3.44 The TVMF location results of the third defects



(a) Case II



(b) Case III

Fig. 3.45 The reconstruction reflection pulses by all defects and cable ends in Case II and Case III

Using the TVMF method in combination with the pulse reconstruction technique, the defects in Case II and Case III were successfully localized and identified, and their equivalent resistances were estimated. The localization results and resistance estimations are summarized in Table 3.5 and Table 3.6, respectively.

From Table 3.5 and Table 3.6, it can be observed that the maximum estimation error for the equivalent defect resistances is 5.19 %, and all localization errors are below 1.5 %. These results demonstrate that the proposed method can accurately estimate equivalent resistances

Table 3.5 The location results of the defects in Case II and III

Case	Defect	Estimation/m	Reference/m	Error/%
II	1st	197.74	200	1.13
	2nd	397.63	400	0.59
	3rd	601.52	600	0.25
III	1st	198.35	200	0.83
	2nd	397.42	400	0.65
	3rd	597.52	600	0.41

Table 3.6 Equivalent resistance estimation results of defects in Case II and III

Case	Defect	Estimation		Reference		Error/%
		Value/Ω	Type	Value/Ω	Type	
II	1st	19.19	series resistance	20	series resistance	4.05
	2nd	95.58	series resistance	100	series resistance	4.42
	3rd	Open	–	Open	–	–
III	1st	100.04	ground	100	ground	0.04
	2nd	105.19	series resistance	100	series resistance	5.19
	3rd	Open	–	Open	–	–

and precisely localize defects. The experimental results validate the effectiveness and practical applicability of the proposed method for multi-defect localization and identification in cable TDR measurements.

3.5 Summary

In this chapter, a TVMF method is proposed to suppress the effect of noise and waveform distortion in TDR measurements and achieve accurate defect localization. A pulse reconstruction method is proposed to identify and localize multiple defects in a multiple-defect cable. Characteristic parameters of the cable and its defects are first estimated from TDR measurements. Based on the estimated characteristic parameters, the TVMF filter bank is constructed to localize defects. The pulse reconstruction method, based on the TVMF localization and parameter estimation results, reconstructs the reflected pulses from each defect and identifies each defect in a multiple-defect cable one by one using the multiple-cable RCS model. The proposed methods are effective in solving the problem of identifying repeated reflections in TDR measurements

of multiple-defect cables and significantly reduce the probability of misidentification. Their effectiveness and accuracy are verified through both simulations and experiments.

Chapter 4

Quantitative Severity Evaluation of Cable Defects Based on Double-Frequency TFDR

According to the research results on distributed defects presented in the last section, high-frequency signals are more sensitive to changes in defect severity. However, the high-frequency components of a pulse signal occupy a small proportion of its spectrum and are severely attenuated after propagating over a long distance. To address this, TFDR is used to estimate the severity of cable defects. It employs a chirp signal as the excitation source, enabling greater sensitivity to variations in defect severity. Based on this principle, a double-frequency TFDR method is proposed in this section. This method quantitatively estimates defect severity by determining the equivalent resistance of lumped defects and the physical dimensions of distributed defects. Simulations and experiments are conducted to verify its effectiveness.

4.1 Principles of TFDR-Based Cable Defect Detection

4.1.1 Principles of Detection and Localization

A Gaussian-enveloped linear frequency-modulated (LFM) signal, also known as a chirp signal, is a promising candidate for increasing the proportion of high-frequency components in the injected signal. The Gaussian envelope provides smooth edge transitions, distinguishing the signal from noise pulses. Meanwhile, linear frequency modulation enables the signal to span a broad band-pass frequency range, thereby enhancing measurement sensitivity. The injected signal used in TFDR can be expressed as [103]:

$$s(t) = A \cdot \mathrm{e}^{-\frac{\lambda (t-t_0)^2}{2} + \mathrm{j}\frac{\kappa (t-t_0)^2}{2} + \mathrm{j}\omega_0 (t-t_0)} \tag{4.1}$$

In this expression, the parameter λ defines the signal duration, while κ determines the slope of its instantaneous frequency. The variable t_0 denotes the time center of $s(t)$, and ω_0 represents its center frequency. The parameter A corresponds to the amplitude of $s(t)$.

A typical chirp signal with a 40 MHz bandwidth, a 40 MHz center frequency, and a 200 ns duration is shown in Fig. 4.1. In the time–frequency representation, a straight ridge is observed, which demonstrates that the signal possesses a linear time–frequency relationship. The energy spectral density (ESD) plot shows that the signal's frequency content follows a Gaussian distribution.

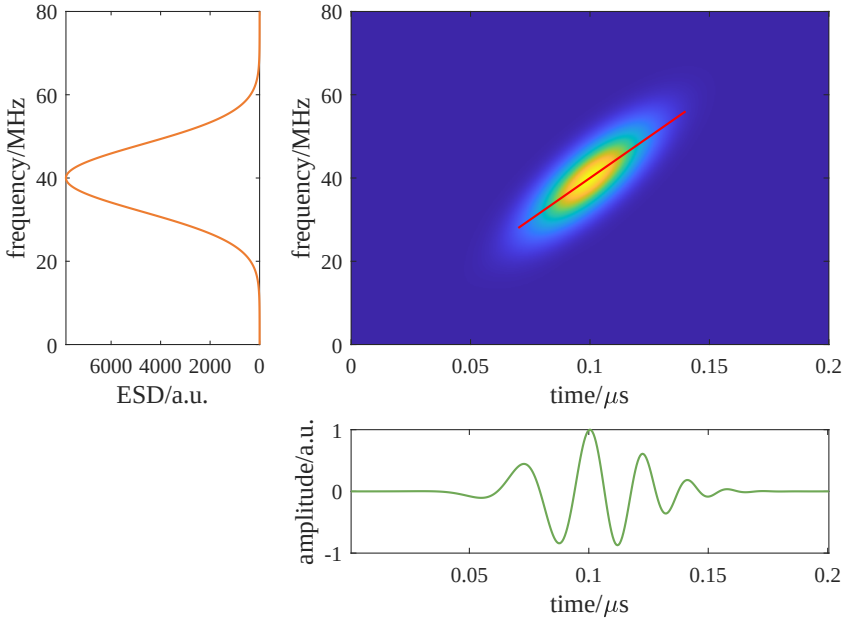


Fig. 4.1 Chirp signal with a 40 MHz bandwidth, a 40 MHz center frequency and a 200 ns duration time

In both the time and frequency domains, chirp signals exhibit characteristics that are markedly distinct from noise. Compared with conventional pulse signals, chirp signals are more easily distinguishable from noise, making them well-suited for signal detection in noisy environments.

As the signal $s(t)$ propagates through a cable with defects, reflections occur, producing a reflected signal $r(t)$. To localize defects in TFDR measurements, a time-frequency cross-correlation (TFCC) method is employed, leveraging the time-frequency characteristics of the chirp signal. In TFCC analysis, both the injected and reflected signals are transformed from the time domain to the time-frequency domain to obtain their respective time-frequency distributions. For time-frequency analysis of LFM signals, the Wigner-Ville distribution (WVD) offers superior time-frequency resolution. Therefore, WVD is employed in TFCC to calculate

the time-frequency distribution. The WVD of the injected signal $s(t)$ is defined as follows [101]:

$$\begin{aligned} W_{\mathrm{s}}(t,\omega) &= \int_{-\infty}^{+\infty} s\left(t+\frac{\tau}{2}\right) s^{*}\left(t-\frac{\tau}{2}\right) \mathrm{e}^{-\mathrm{j}\tau\omega}\,\mathrm{d}\tau \\ &= 2A^{2}\sqrt{\frac{\pi}{\lambda}}\mathrm{e}^{-\lambda(t-t_0)^{2}-\frac{1}{\lambda}(\omega-\kappa(t-t_0)-\omega_0)}. \end{aligned} \tag{4.2}$$

Similarly, the WVD of the reflected signal $r(t)$ is obtained by replacing $s(t)$ with $r(t)$ in (4.2),and is expressed as:

$$W_{\mathrm{r}}(t,\omega) = \int_{-\infty}^{+\infty} r\left(t+\frac{\tau}{2}\right) r^{*}\left(t-\frac{\tau}{2}\right) \mathrm{e}^{-\mathrm{j}\tau\omega}\,\mathrm{d}\tau. \tag{4.3}$$

The TFCC between the injected signal $s(t)$ and the reflected signal $r(t)$ is derived and expressed as (4.4) [104]:

$$C_{\mathrm{sr}}(t) = \frac{2\pi}{E_{\mathrm{s}}E_{\mathrm{r}}(t)} \times \int_{t'=t-T_{\mathrm{s}}}^{t'=t+T_{\mathrm{s}}} \int_{-\infty}^{+\infty} W_{\mathrm{r}}\left(t',\omega\right) W_{\mathrm{s}}\left(t'-t,\omega\right) \mathrm{d}\omega\,\mathrm{d}t' \tag{4.4}$$

Here, $W_{\mathrm{s}}(t,\omega)$ and $W_{\mathrm{r}}(t,\omega)$ denote the WVDs of the injected signal $s(t)$ and the reflected signal $r(t)$, respectively. The terms E_{s} and $E_{\mathrm{r}}(t)$ are used to normalize $C_{\mathrm{sr}}(t)$, ensuring that its value is bounded between 0 and 1. Their expressions are given as follows:

$$E_{\mathrm{s}} = \iint W_{\mathrm{s}}(t,\omega)\,\mathrm{d}t\,\mathrm{d}\omega \tag{4.5a}$$

$$E_{\mathrm{r}}(t) = \int_{t'=t-T_{\mathrm{s}}}^{t'=t+T_{\mathrm{s}}} \int_{-\infty}^{+\infty} W_{\mathrm{r}}\left(t',\omega\right) \mathrm{d}\omega\,\mathrm{d}t' \tag{4.5b}$$

The parameter T_{s} controls the integration length and is set to $T_{\mathrm{s}} = 3\sigma_t$, where σ_t is defined as follows [105]:

$$\sigma_{\mathrm{t}}^{2} = \int_{-\infty}^{\infty} (t-\mathrm{t}_0)^{2} \mid s(t) \mid^{2} \mathrm{d}t \tag{4.6}$$

If the cable contains defects, the $C_{\mathrm{sr}}(t)$ curve will exhibit peaks corresponding to the arrival times of the reflected signals. The defect locations can then be determined based on the wave propagation velocity. A typical TFDR measurement result is shown in Fig. 4.2.

Using (4.4), the $C_{\mathrm{sr}}(t)$ is computed, and the resulting curve is shown in Fig. 4.3. The curve exhibits five distinct peaks: the first corresponds to the start of the injected signal, the second to the initial reflection from the defect, the third to the second reflection from the defect, the fourth to the reflection from the cable end, and the fifth reflection is the defect's reflection excited by the reflection pulse from the cable end.

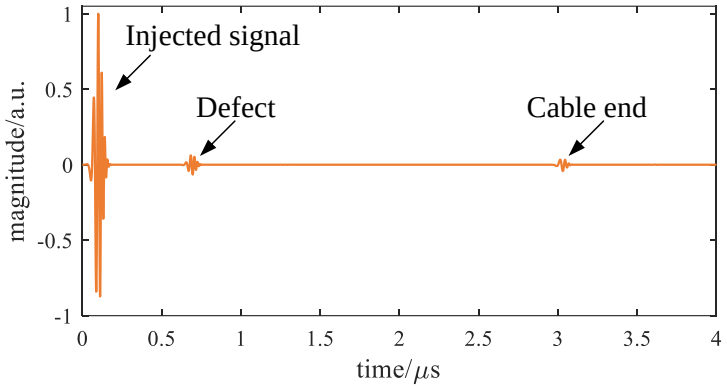


Fig. 4.2 A typical TFDR measurement result

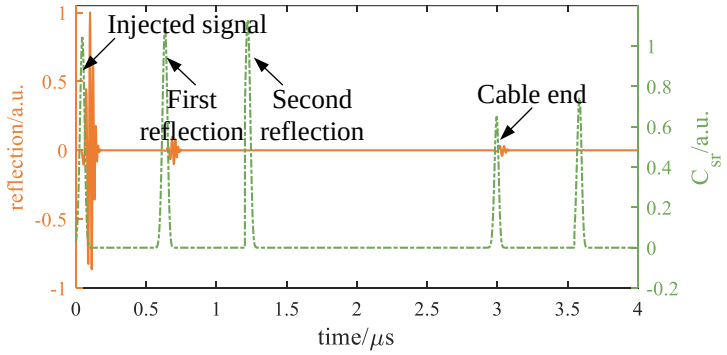


Fig. 4.3 The TFCC of the reflected signal

4.1.2 Design for Injected Signal Parameters

Unlike TDR, TFDR employs an chirp signal, whose parameter configuration is more complex and non-unique. Therefore, the first step in TFDR measurements typically involves designing the signal parameters. These include the center frequency f_0, bandwidth B, duration T_0, and amplitude. The amplitude is usually constrained by the injection source and the limitations of the measurement system. A higher amplitude enables stronger signal injection into the cable and facilitates the detection of weak defects and long cables; thus, it is typically set to the maximum level tolerable by the system. The remaining three parameters—center frequency, bandwidth, and duration—are primarily determined by the measurement conditions, such as the frequency-domain characteristics of the cable under test, its length, and the required localization accuracy. The following sections discuss the design of these three parameters in detail.

Center Freuqency f_0

The selection of the center frequency f_0 is influenced by multiple factors, including the frequency-dependent characteristics of the cable, the cable length, and the performance of the measurement system. On the one hand, high-frequency components are more susceptible to

attenuation as the signal propagates through the cable. On the other hand, higher frequencies provide greater sensitivity to defects, as illustrated in the analysis of Fig. 3.21. Therefore, the choice of f_0 requires a trade-off between signal attenuation and defect sensitivity.

The following principles should be considered when selecting the center frequency f_0:

(1) Ensure that the signal can propagate through the entire length of the cable.

(2) Maximize f_0 to enhance sensitivity to defects.

(3) Ensure that f_0 falls within the bandwidth of the measurement system.

Given a cable of length l_c and the maximum tolerable attenuation of the measurement system A_{max}, the relationship between the center frequency f_0 and the cable length L can be expressed as

$$A_{max} < \frac{V-}{V+} = \frac{V^+ e^{-2\alpha_c(f_0)l_c}}{V^+} \tag{4.7}$$

where V^+ is the amplitude of the injected signal and α_c is the attenuation constant of the tested cable. The attenuation constant α_c is frequency-dependent and can be measured using the method described in Section 3.1. The center frequency f_0 can then be calculated using the following equation:

$$\alpha_c(f_0) = -\frac{1}{2l_c} \ln A_{max} \tag{4.8}$$

Based on the curve of the attenuation constant α_c, the center frequency f_0 can be determined accordingly.

Frequency Bandwidth B_0

The frequency bandwidth B_0 of the signal is constrained by the required spatial resolution, the frequency-dependent characteristics of the cable, and the performance of the measurement system. The spatial resolution refers to the minimum distance between two adjacent defects that can be distinguished. It is determined by the signal bandwidth B_0 and the propagation velocity v_c of the signal in the cable. The required bandwidth B_0 can be calculated using the following equation [106]:

$$B_0 = \frac{v_c}{2\Delta l_{min}} \tag{4.9}$$

The frequency characteristics of the cable also play a critical role in determining the signal bandwidth B_0. The TFCC method is based on the assumption that the tested cable behaves as a linear system. Therefore, within the signal's frequency range, the cable must exhibit uniform phase characteristics—i.e., the phase velocity of all frequency components should remain constant—to avoid signal distortion. Based on the distributed-parameter model, for a

typical 10 kV cable, the phase velocity remains stable when the frequency exceeds 1 MHz [107]. The limitation imposed by the measurement system on the bandwidth B_0 is straightforward and is not the focus of this discussion.

Based on the above considerations, the selection of the bandwidth B_0 can follow the procedure below:

(1) Determine the required bandwidth B_0 based on the desired minimum spatial resolution $\Delta l_{\min}$.

(2) Verify whether the frequency range defined by f_0 and B_0 lies within the linear region of the cable. If not, increase B_0 to ensure it falls within the linear range.

(3) Check whether the resulting frequency range is within the bandwidth of the measurement system. If B_0 is outside the system bandwidth, adjust it accordingly to comply with the system's limitations.

Duration T_0

The duration T_0 of the signal is determined by the blind distance of the cable. Specifically, T_0 must be shorter than the arrival time of the first defect. This ensures that the reflected signal from the first defect does not overlap with the injected signal. Another constraint on T_0 is imposed by the performance of the injection source: T_0 must be longer than the rise/fall time of the source and must accommodate the frequency sweep capability of the source.

After determining the center frequency f_0, bandwidth B, and duration T_0 of the signal, the signal can be generated. However, the expression of the signal in (4.1) cannot be directly specified in terms of f_0, B, and T_0. The relationship between the signal parameters f_0, B, and T_0, and the parameters λ, κ, and ω_0 in (4.1), can be expressed as [21]:

$$T_0^2 = \int (t-t_0)^2 \, |s(t)|^2 \, \mathrm{d}t = \frac{\lambda}{2} \tag{4.10a}$$

$$\omega_0 = 2\pi f_0 \tag{4.10b}$$

$$B_0^2 = \int (\omega-\omega_0)^2 \, |S(\omega)|^2 \, \mathrm{d}\omega = \frac{\lambda^2+\kappa^2}{2\lambda} \tag{4.10c}$$

4.2 Principles of Double-Frequency TFDR for Defect Severity Estimation

According to the analysis in Section 2.1, the severity of lumped defects can be characterized by their equivalent resistance, while the severity of distributed defects is determined by their

characteristic impedance and physical length. To evaluate defect severity by estimating these parameters from TFDR measurement results, the reflected signals of defects are derived and analyzed.

4.2.1 Analytical Modeling of TFDR Defect Measurement Results

Lumped Defect Analysis

Lumped defects are relatively simple and amenable to theoretical analysis. The equivalent circuit of a lumped defect is shown in Fig. 2.10. The local reflection coefficient Γ'_{fl} is defined in (2.10) for ground defects and in (2.11) for series resistance defects. The TFDR measurement process for lumped defects can be analyzed theoretically as follows.

The frequency-domain representation of the injected signal $S(\omega)$ is given by:

$$S(\omega) = A\sqrt{\frac{2\pi}{\lambda - \mathrm{j}\kappa}}\mathrm{e}^{-\frac{(\omega-\omega_0)^2}{2(\lambda-\mathrm{j}\kappa)} - \mathrm{j}\omega t_0} \tag{4.11}$$

Here, $S(\omega)$ is the Fourier transform of the injected signal $s(t)$.

It is assumed that the cable segment located beyond the defect is sufficiently long, such that any time-domain reflected signal generated by the defect does not temporally overlap with subsequent reflections originating from the remote end of the cable. This separation ensures that the defect-induced reflection can be clearly distinguished in the time domain, without interference from other reflections. Under this condition, the reflected signal—which can be attributed solely to the defect—can be individually extracted for further frequency-domain analysis. Based on the modeling strategy and theoretical framework outlined in Section 2.3, the analytical expression for the reflected signal can be systematically derived as follows:

$$\begin{aligned} R(\omega) &= S(\omega)\cdot \mathrm{e}^{-2(\alpha_\mathrm{c}+\mathrm{j}\beta_\mathrm{c})l_{\mathrm{fl}}}\cdot \Gamma'_{\mathrm{fl}} \\ &= A\sqrt{\frac{2\pi}{\lambda - \mathrm{j}\kappa}}\mathrm{e}^{-\frac{(\omega-\omega_0)^2}{2(\lambda-\mathrm{j}\kappa)} - \mathrm{j}\omega t_0}\cdot \Gamma'_{\mathrm{fl}}\mathrm{e}^{-2(\alpha_\mathrm{c}+\mathrm{j}\beta_\mathrm{c})l_{\mathrm{fl}}}. \end{aligned} \tag{4.12}$$

Here, $R(\omega)$ is the Fourier transform of the reflected signal $r(t)$. The variable l_{fl} denotes the distance from the defect to the measurement point. α_c and β_c represent the attenuation and phase constants of the cable, respectively.

Given the characteristics of lumped defects, the local reflection coefficient Γ'_{fl} of the lumped defect can be considered frequency-independent. Therefore, by applying the inverse

Fourier transform to $R(\omega)$, the reflected signal $r(t)$ of the lumped defect can be expressed as:

$$r(t) = \Gamma'_{\mathrm{f1}} A \mathrm{e}^{\frac{\omega'^2 - \omega_0^2}{2(\lambda - \mathrm{j}\kappa)}} \mathrm{e}^{-\frac{\lambda}{2}(t-t')^2 + \frac{\mathrm{j}\kappa}{2}(t-t')^2 + \mathrm{j}\omega'(t-t')} \tag{4.13a}$$

$$\omega' = \omega_0 - 2\frac{\lambda^2 + \kappa^2}{\lambda} K_{\mathrm{a}} l_{\mathrm{f1}} \tag{4.13b}$$

$$t' = t_0 + 2K_{\mathrm{b}} l_{\mathrm{f1}} - 2\frac{\kappa}{\lambda} K_{\mathrm{a}} l_{\mathrm{f1}}. \tag{4.13c}$$

In (4.13), the attenuation constant α_{c} and the phase constant β_{c} are approximated as functions of frequency. K_{a} and K_{b} are the proportional coefficients of the attenuation constant α_{c} and the phase constant β_{c} with respect to frequency, respectively. By substituting (4.13) into (4.3), the WVD $W_{\mathrm{r}}(t, \omega)$ of the reflected signal can be derived as follows:

$$\begin{aligned} W_{\mathrm{r}}(t,\omega) = {} & 2A^2 \Gamma'^2_{\mathrm{f1}} \sqrt{\frac{\pi}{\lambda}} \mathrm{e}^{-4K_{\mathrm{a}} l_{\mathrm{f1}} \left(\omega_0 - \frac{\lambda^2 + \kappa^2}{\lambda} K_{\mathrm{a}} l_{\mathrm{f1}}\right)} \\ & \times \mathrm{e}^{-\lambda(t-t')^2 - \frac{1}{\lambda}[\omega - \omega' - \kappa(t-t')]^2} \end{aligned} \tag{4.14}$$

According to (4.5), E_{s} and $E_{\mathrm{r}}(t)$ can be derived and are expressed as:

$$E_{\mathrm{s}} = 2A^2 \pi \sqrt{\frac{\pi}{\lambda}} \tag{4.15a}$$

$$E_{\mathrm{r}}(t) = 2A^2 \Gamma'^2_{\mathrm{f1}} \pi \sqrt{\frac{\pi}{\lambda}} \mathrm{e}^{-4K_{\mathrm{a}} l_{\mathrm{f1}} \left(\omega_0 - \frac{\lambda^2 + \kappa^2}{\lambda} K_{\mathrm{a}} l_{\mathrm{f1}}\right)}. \tag{4.15b}$$

By substituting (4.2), (4.14), and (4.15) into (4.4), the $C_{\mathrm{sr}}(t)$ corresponding to the TFDR measurement results for lumped defects can be expressed as:

$$\begin{aligned} C_{\mathrm{sr}}(t) &= \frac{4A^4 \Gamma'^2_{\mathrm{f1}} \frac{\pi^3}{\lambda} \mathrm{e}^{-4K_{\mathrm{a}} l_{\mathrm{f1}} \left(\omega_0 - \frac{\lambda^2 + \kappa^2}{\lambda} K_{\mathrm{a}} l_{\mathrm{f1}}\right) - \frac{\lambda^2 + \kappa^2}{2\lambda}\left[(2K_{\mathrm{a}} l_{\mathrm{f1}})^2 + (t - 2K_{\mathrm{b}} l_{\mathrm{f1}})^2\right]}}{4A^4 \Gamma'^2_{\mathrm{f1}} \frac{\pi^3}{\lambda} \mathrm{e}^{-4K_{\mathrm{a}} l_{\mathrm{f1}} \left(\omega_0 - \frac{\lambda^2 + \kappa^2}{\lambda} K_{\mathrm{a}} l_{\mathrm{f1}}\right)}}, \\ &= \mathrm{e}^{-\frac{\lambda^2 + \kappa^2}{2\lambda}\left[(2K_{\mathrm{a}} l_{\mathrm{f1}})^2 + (t - 2K_{\mathrm{b}} l_{\mathrm{f1}})^2\right]} \end{aligned} \tag{4.16}$$

From (4.16), it can be observed that the TFCC result for lumped defects has the form of a Gaussian function. When the time satisfies $t = 2K_{\mathrm{b}} l_{\mathrm{f1}} = 2l_{\mathrm{f1}}/v_{\mathrm{c}}$, the $C_{\mathrm{sr}}(t)$ reaches its maximum value. Therefore, the time corresponding to the peak of the $C_{\mathrm{sr}}(t)$ curve represents the precise

arrival time of the reflected signal caused by the lumped defect. Moreover, the amplitude of $C_{\mathrm{sr}}(t)$ is independent of the defect's equivalent resistance and depends only on the defect's location.

By extracting the reflected signal caused by the lumped defect from the TFDR measurement results, the frequency-domain expression of the extracted signal $R_{\mathrm{e}}(\omega)$ can be written as:

$$\begin{aligned} R_{\mathrm{e}}(\omega) &= \mathscr{F}\left(r(t+2K_{\mathrm{b}}l_{\mathrm{f1}})\right) = R(\omega)\mathrm{e}^{\mathrm{j}2K_{\mathrm{b}}l_{\mathrm{f1}}\omega} \\ &= A\sqrt{\frac{2\pi}{\lambda-\mathrm{j}\kappa}}\mathrm{e}^{-\frac{(\omega-\omega_0)^2}{2(\lambda-\mathrm{j}\kappa)}-\mathrm{j}\omega t_0}\cdot\Gamma'_{\mathrm{f1}}\mathrm{e}^{-2\alpha_{\mathrm{c}}l_{\mathrm{f1}}} \end{aligned} \tag{4.17}$$

By comparing (4.17) with (4.11), it can be observed that the phase of the extracted signal $R_{\mathrm{e}}(\omega)$ is solely determined by the reflection coefficient Γ'_{f1}, while the amplitude of $R_{\mathrm{e}}(\omega)$ is influenced by both the characteristics of the tested cable and Γ'_{f1}.

Distributed Defect Analysis

Distributed defects are more complex than lumped defects, and their effects on TFDR measurements are correspondingly more intricate. According to the analysis in Section 3.3, the influence of a distributed defect on the injected signal can be described using a local reflection coefficient. As shown in (3.40), the approximation of the local reflection coefficient Γ'_{f1} for a distributed defect is given by:

$$\Gamma'_{\mathrm{f1}} = -2\Gamma^{+}_{\mathrm{f1}}\sin\left(K_{\mathrm{f1}}\omega\Delta l_{\mathrm{f1}}\right)\mathrm{e}^{\mathrm{j}\left(\frac{\pi}{2}-K_{\mathrm{f1}}\omega\Delta l_{\mathrm{f1}}\right)} \tag{4.18}$$

where K_{f1} denotes the slope of the phase constant β_{f1} with respect to the angular frequency ω for the distributed defect. Based on the RCS method, the spectrum $R(\omega)$ of the reflected signal from the distributed defect can be expressed as:

$$\begin{aligned} R(\omega) &= S(\omega)\cdot\mathrm{e}^{-2\left(\alpha_{\mathrm{c}}+\mathrm{j}\beta_{\mathrm{c}}\right)l_{\mathrm{f1}}}\cdot\Gamma'_{\mathrm{f1}} \\ &= A\sqrt{\frac{2\pi}{\lambda-\mathrm{j}\kappa}}\mathrm{e}^{\left[-\frac{(\omega-\omega_0)^2}{2(\lambda-\mathrm{j}\kappa)}-\mathrm{j}\omega t_0-2(\alpha_{\mathrm{c}}+\mathrm{j}\beta_{\mathrm{c}})l_{\mathrm{f1}}\right]} \\ &\quad\times -2\Gamma^{+}_{\mathrm{f1}}\sin(K_{\mathrm{f1}}\Delta l_{\mathrm{f1}}\omega)\mathrm{e}^{\mathrm{j}\left(\frac{\pi}{2}-K_{\mathrm{f1}}\Delta l_{\mathrm{f1}}\omega\right)} \end{aligned} \tag{4.19}$$

Using the inverse Fourier transform, the reflected signal $r(t)$ can be expressed as

$$r(t) = -\Gamma_{\mathrm{fl}}^{+} A \mathrm{e}^{\frac{\omega'^2-\omega_0^2}{2(\lambda-\mathrm{j}\kappa)}} \left(\mathrm{e}^{-\frac{\lambda}{2}(t-t')^2+\frac{\mathrm{j}\kappa}{2}(t-t')^2+\mathrm{j}\omega'(t-t')} - \mathrm{e}^{-\frac{\lambda}{2}(t-t'-2K_{\mathrm{bf1}}\Delta l_{\mathrm{f1}})^2+\frac{\mathrm{j}\kappa}{2}(t-t'-2K_{\mathrm{bf1}}\Delta l_{\mathrm{f1}})^2+\mathrm{j}\omega'(t-t'-2K_{\mathrm{bf1}}\Delta l_{\mathrm{f1}})} \right) \tag{4.20}$$

where t' and ω' are defined as in (4.13). By substituting (4.20) into (4.3), the WVD $W_{\mathrm{r}}(t,\omega)$ of the reflected signal can be derived as follows:

$$\begin{aligned} W_{\mathrm{r}}(t,\omega) = {} & 2A^2\Gamma_{\mathrm{fl}}^{+2}\sqrt{\frac{\pi}{\lambda}}\mathrm{e}^{-4K_{\mathrm{a}}l_{\mathrm{f1}}\left(\omega_0-\frac{\lambda^2+\kappa^2}{\lambda}K_{\mathrm{a}}l_{\mathrm{f1}}\right)} \\ & \times \left(\mathrm{e}^{-\lambda(t-t')^2-\frac{1}{\lambda}(\omega-\omega'-\kappa(t-t'))^2} \right. \\ & -2\cos(2K_{\mathrm{bf1}}\Delta l_{\mathrm{f1}}\omega)\,\mathrm{e}^{-\lambda(t-t'-K_{\mathrm{bf1}}\Delta l_{\mathrm{f1}})^2-\frac{1}{\lambda}(\omega-\omega'-\kappa(t-t'-K_{\mathrm{bf1}}\Delta l_{\mathrm{f1}}))^2} \\ & \left. +\mathrm{e}^{-\lambda(t-t'-2K_{\mathrm{bf1}}\Delta l_{\mathrm{f1}})^2-\frac{1}{\lambda}(\omega-\omega'-\kappa(t-t'-2K_{\mathrm{bf1}}\Delta l_{\mathrm{f1}}))^2} \right). \end{aligned} \tag{4.21}$$

Based on (4.5), $E_{\mathrm{r}}(t)$ can be derived and expressed as:

$$\begin{aligned} E_{\mathrm{r}}(t) = {} & 4A^2\Gamma_{\mathrm{fl}}^{+2}\pi\sqrt{\frac{\pi}{\lambda}}\mathrm{e}^{-4K_{\mathrm{a}}l_{\mathrm{f1}}\left(\omega_0-\frac{\lambda^2+\kappa^2}{\lambda}K_{\mathrm{a}}l_{\mathrm{f1}}\right)} \\ & \times \left(1-\mathrm{e}^{-\frac{\lambda^2+\kappa^2}{\lambda}(K_{\mathrm{bf1}}\Delta l_{\mathrm{f1}})^2}\cos\left(2K_{\mathrm{bf1}}\Delta l_{\mathrm{f1}}\omega'\right) \right). \end{aligned} \tag{4.22}$$

By substituting (4.2), (4.21), (4.15a), and (4.22) into (4.4), the $C_{\mathrm{sr}}(t)$ corresponding to the TFDR measurement results for distributed defects can be expressed as:

$$\begin{aligned} C_{\mathrm{sr}}(t) = {} & B\mathrm{e}^{-b(t-2K_{\mathrm{b}}l_{\mathrm{f1}})^2}+D\mathrm{e}^{-b(t-K_{\mathrm{bf1}}\Delta l_{\mathrm{f1}}-2K_{\mathrm{b}}l_{\mathrm{f1}})^2} \\ & +B\mathrm{e}^{-b(t-2K_{\mathrm{bf1}}\Delta l_{\mathrm{f1}}-2K_{\mathrm{b}}l_{\mathrm{f1}})^2} \end{aligned} \tag{4.23}$$

where B, D and b are expressed as

$$B = \frac{\mathrm{e}^{-2\frac{\lambda^2+\kappa^2}{\lambda}(K_{\mathrm{a}}l_{\mathrm{f1}})^2}}{2\left(1-\mathrm{e}^{-\frac{\lambda^2+\kappa^2}{\lambda}(K_{\mathrm{bf1}}\Delta l_{\mathrm{f1}})^2}\cos\left(2K_{\mathrm{bf1}}\Delta l_{\mathrm{f1}}\omega'\right)\right)} \tag{4.24a}$$

$$D = \frac{\mathrm{e}^{-2\frac{\lambda^2+\kappa^2}{\lambda}(K_{\mathrm{a}}l_{\mathrm{f1}})^2}}{2\left(1-\mathrm{e}^{-\frac{\lambda^2+\kappa^2}{\lambda}(K_{\mathrm{bf1}}\Delta l_{\mathrm{f1}})^2}\cos\left(2K_{\mathrm{bf1}}\Delta l_{\mathrm{f1}}\omega'\right)\right)}$$

$$\times -2\cos\left(2K_{\mathrm{bf1}}\Delta l_{\mathrm{f1}}\left(\omega_0-\frac{\lambda^2+\kappa^2}{\lambda}K_{\mathrm{a}}l_{\mathrm{f1}}\right)\right)\mathrm{e}^{-\frac{\lambda^2+\kappa^2}{2\lambda}(K_{\mathrm{bf1}}\Delta l_{\mathrm{f1}})^2} \tag{4.24b}$$

$$b = -\frac{\lambda^2+\kappa^2}{2\lambda}. \tag{4.24c}$$

From the expression in (4.23), it can be observed that the peak time value of $C_{\mathrm{sr}}(t)$ is influenced by both the defect location l_{f1} and the length of the defect segment Δl_{f1} and the interface reflection coefficient Γ_{f1}^{+} of the distributed defect has no effect on the amplitude of $C_{\mathrm{sr}}(t)$.

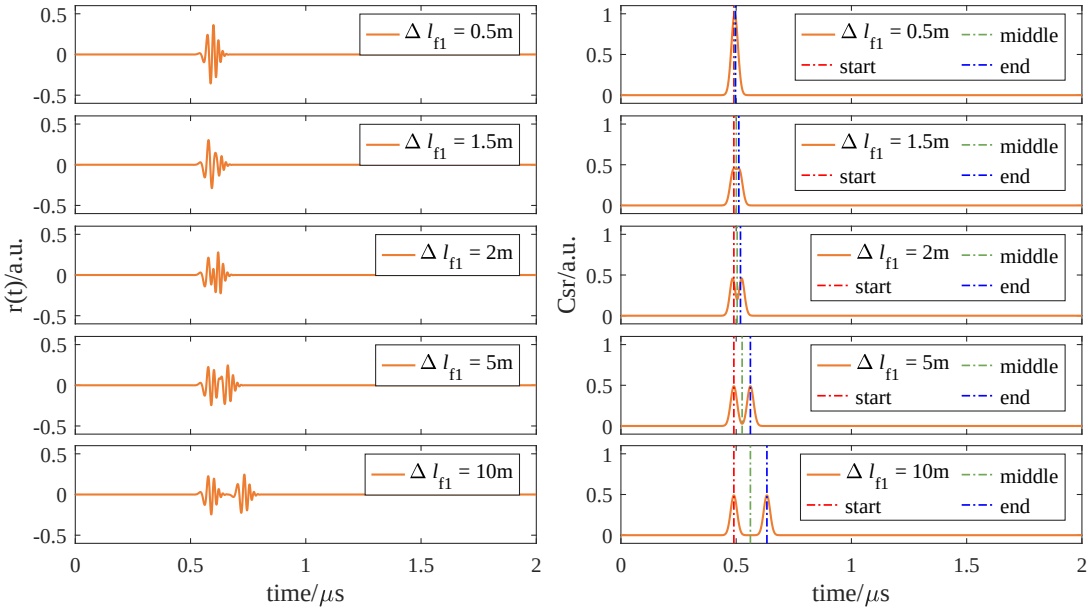
An analysis of the expression of $C_{\mathrm{sr}}(t)$ in (4.23) shows that it is a sum of three Gaussian functions. Therefore, its peaks can be determined by differentiation and Taylor expansion. The number of peaks in the $C_{\mathrm{sr}}(t)$ curve is determined by the length of the defect segment Δl_{f1}: when the segment is short, the curve has only one peak; as the segment length increases, two peaks appear with a local minimum between them. In the short-segment case, solving (4.23) yields the peak time t_1 from the following equation:

$$t_1 = 2K_{\mathrm{b}}l_{\mathrm{f1}} + K_{\mathrm{bf1}}\Delta l_{\mathrm{f1}} \tag{4.25}$$

According to (4.25), the peak time t_1 corresponds to the reflection from the midpoint of the defect segment, indicating that the localization result is also at this midpoint.

Based on (4.20) and (4.23), the reflected signals and corresponding TFCC curves for distributed defects of varying lengths are shown in Fig. 4.4. Fig. 4.4a presents the reflected signals without the injected signal. As the defect length increases, the reflected signal becomes increasingly stretched and eventually separates into two distinct parts when the defect is sufficiently long. Fig. 4.4b shows the TFCC curves corresponding to distributed defects of different lengths. When the defect is short, the TFCC curve exhibits a single peak. As the

length increases, the peak becomes lower and broader. For longer defects, the TFCC curve develops two distinct peaks. In Fig. 4.4b, the vertical red, green, and blue dashed lines indicate the actual start, midpoint, and end locations of the distributed defect, respectively. For long distributed defects, defect length can be estimated from the time interval between two TFCC peaks. However, for short distributed defects, it is difficult to estimate the length based on the TFCC curve. The spatial resolution of TFCC depends on the bandwidth of the injected signal, as described in (4.9). For an injected signal with a 40 MHz bandwidth, the corresponding spatial resolution is approximately 2.1 m for a 10 kV cable given in Table 2.2.



(a) Reflected signal (b) TFCC

Fig. 4.4 The reflected signal and TFCC of distributed defects with different lengths

4.2.2 Implementation of Double-Frequency TFDR Method

To estimate the length of a short distributed defect, a double-frequency TFDR method is proposed. Based on (4.11) and (4.17), the spectrum ratio P_{sr} between the reflected and injected signals can be expressed as:

$$P_{\mathrm{sr}} = \frac{R_{\mathrm{e}}(\omega)}{S(\omega)} = \Gamma'_{\mathrm{f1}} \mathrm{e}^{-2\alpha_{\mathrm{c}} l_{\mathrm{f1}}} \tag{4.26}$$

The spectrum ratio P_{sr} captures the combined effects of the local reflection coefficient Γ'_{f1} of the defect and the attenuation of the cable. The attenuation constant α_{c} can be estimated using the method described in Section 3.1. Accordingly, the local reflection coefficient Γ'_{f1} can be

estimated from the spectrum ratio P_{sr}, and its expression is given by:

$$\Gamma'_{\mathrm{f1}} = \frac{P_{\mathrm{sr}}}{\mathrm{e}^{-2\alpha_{\mathrm{c}} l_{\mathrm{f1}}}} \tag{4.27}$$

The local reflection coefficient Γ'_{f1} of distributed defects is given by (3.26), which can be reformulated as follows:

$$\Gamma'_{\mathrm{f1}} = -2\Gamma_{\mathrm{f1}}^{+} \sin\left(K_{\mathrm{bf1}}\,\omega\Delta l_{\mathrm{f1}}\right) \mathrm{e}^{\mathrm{j}\left(\frac{\pi}{2} - K_{\mathrm{bf1}}\,\omega\Delta l_{\mathrm{f1}}\right)} \tag{4.28}$$

The amplitude of the local reflection coefficient Γ'_{f1} depends on the interface reflection coefficient Γ_{f1}^{+}, the slope of the phase constant K_{bf1}, and the defect length Δl_{f1}. The interface reflection coefficient Γ_{f1}^{+} is typically a real, frequency-independent constant in the high-frequency range. K_{bf1} is dependent on type of defects, which can be identified by the characteristic impedance of defects or the interface reflection coefficient Γ_{f1}^{+}. To decouple the effects of Γ_{f1}^{+} and the defect length Δl_{f1} on the local reflection coefficient, an additional TFDR measurement is performed with a doubled center frequency. Based on this idea, the double-frequency TFDR method is proposed.

Double-frequency TFDR requires two TFDR measurements, where the center frequency of the injected signal in the second measurement is twice that of the first. To describe the procedure in detail, a damage factor ρ is defined to quantify the severity of the distributed defect. Its theoretical expression is given by:

$$\rho = \left|\Gamma_{\mathrm{f1}}^{+} \sin\left(K_{\mathrm{bf1}}\,\omega\Delta l_{\mathrm{f1}}\right)\right| \tag{4.29}$$

The damage factor ρ can be calculated from the TFDR measurement results. Based on (4.27) and (4.28), the measurement equation for the damage factor ρ is given by:

$$\rho = \frac{|P_{\mathrm{sr}}|}{2\mathrm{e}^{-2\alpha_{\mathrm{c}} l_{\mathrm{f1}}}} \tag{4.30}$$

Using the damage factors ρ obtained from the first and second TFDR measurements, the length of the defect can be estimated as follows:

$$\cos\left(\beta_{\mathrm{f1}}\Delta l_{\mathrm{f1}}\right) = \frac{\left|\Gamma_{\mathrm{f1}}^{+} \sin\left(K_{\mathrm{bf1}} 2\omega\Delta l_{\mathrm{f1}}\right)\right|}{2\left|\Gamma_{\mathrm{f1}}^{+} \sin\left(K_{\mathrm{bf1}}\,\omega\Delta l_{\mathrm{f1}}\right)\right|} = \frac{\rho_2}{2\rho_1} \tag{4.31}$$

where ρ_1 and ρ_2 are the damage factors obtained from the first and second TFDR measurements, respectively. The phase constant is given by $\beta_{\mathrm{f1}} = K_{\mathrm{bf1}}\omega$. Then, based on (4.31) the interface reflection coefficient Γ_{f1}^{+} and the characteristic impedance Z_{cf1} of the defect can be estimated as

follows:

$$\left|\Gamma_{\mathrm{f1}}^{+}\right| = \frac{\rho_1}{\sqrt{1-\cos\left(\beta_{\mathrm{f1}}\Delta l_{\mathrm{f1}}\right)}} = \frac{\rho_1}{\sqrt{1-\dfrac{\rho_2}{2\rho_1}}} \tag{4.32}$$

$$Z_{\mathrm{cf1}} = Z_c\frac{1-\Gamma_{\mathrm{f1}}^{+}}{1+\Gamma_{\mathrm{f1}}^{+}} \tag{4.33}$$

The polarity of Γ_{f1}^{+} can be determined from the phase difference between the injected and reflected signals. If the phase difference is in the range $(\pi, 3\pi/2)$, Γ_{f1}^{+} is positive; if it is in the range $(0, \pi/2)$, Γ_{f1}^{+} is negative.

Based on (4.31), (4.32) and (4.33), the length and characteristic impedance of distributed defects can be effectively estimated.

4.2.3 Quantitative Estimation of Severity Defects

Lumped and distributed defects are characterized by different parameters: lumped defects by equivalent resistance, and distributed defects by length and characteristic impedance. Therefore, before estimating defect severity, it is essential to first identify the defect type.

As analyzed in Fig. 3.21, the local reflection coefficient Γ'_{f1} of a distributed defect is a sinusoidal function of frequency and increases with frequency within a low-frequency range. In contrast, the local reflection coefficient of a lumped defect remains constant across frequencies. This difference can serve as a criterion for identifying defect types using the double-frequency TFDR method. The damage factor ρ, defined in (4.29), represents the amplitude of the local reflection coefficient Γ'_{f1}. Therefore, in the double-frequency TFDR measurement results, if the damage ratio ρ_2 at the higher frequency is greater than ρ_1, the defect is a distributed defect; otherwise, if ρ_1 is equal to ρ_2 approximately, it is classified as a lumped defect.

Charateristic Parameters Estimation of Lumped Defects

In the expression for the damage factor ρ of lumped defects, the local reflection coefficient Γ'_{f1} is equal to the interface reflection coefficient Γ_{f1}^{+}. Thus, the equivalent resistance of lumped defects can be estimated using the damage factor ρ. Based on (3.30) and (3.31), the equivalent resistance corresponding to ρ is given by

$$R_{\mathrm{s}} = Z_{\mathrm{c}}\frac{1+\rho}{1-\rho} - Z_{\mathrm{c}} \tag{4.34a}$$

$$R_{\mathrm{g}} = Z_{\mathrm{c}}\frac{1-\rho}{2\rho} \tag{4.34b}$$

The choice of the appropriate equation for estimating the equivalent resistance of lumped defects depends on the defect type. For series resistance defects, the equivalent resistance is estimated using (4.34a), while for ground defects, it is estimated using (4.34b). Therefore, the type of lumped defect must be identified prior to resistance estimation.

For a series resistance defect, Γ'_{f1} is a positive constant, and thus the extracted signal $R_{\mathrm{e}}(\omega)$ from the reflected signal has the same phase as the injected signal, i.e., $\Delta\phi = 0^\circ$. In contrast, for a ground defect, Γ'_{f1} is a negative constant, resulting in an extracted signal with a phase opposite to that of the injected signal, i.e., $\Delta\phi = 180^\circ$. Therefore, a phase-based method is proposed to identify the type of lumped defect.

To compute the phase of a signal, its analytic signal is first obtained. The analytic signal $\tilde{x}(t)$ of a real-valued signal $x(t)$ is defined as [108]

$$\tilde{x}(t) = x(t) + j\hat{x}(t) \tag{4.35}$$

where $\hat{x}(t)$ is the Hilbert transform of $x(t)$. The Hilbert transform of a signal $x(t)$ is defined as

$$\hat{x}(t) = \frac{1}{\pi}\mathrm{p.v.}\int_{-\infty}^{\infty}\frac{x(\tau)}{t-\tau}\,\mathrm{d}\tau \tag{4.36}$$

where p.v is the Cauchy principal value. The analytic signal $\tilde{x}(t)$ is a complex signal, and its phase $\phi(t)$ can be calculated as

$$\phi(t) = \arg\left(\tilde{x}(t)\right) = \arctan\left(\frac{\hat{x}(t)}{x(t)}\right) \tag{4.37}$$

Based on (4.37), the phases of the injected signal $s(t)$ and the reflected signal $r(t)$ can be calculated. By comparing the phase of the reflected signal with that of the injected signal, the type of lumped defect can be identified. This method can be also applied to identify the polarity of the interface reflection coefficient Γ_{f1}^{+} of distributed defects.

In summary, the procedure for estimating the equivalent resistance of lumped defects is as follows:

(1) Acquire the measurement results from the double-frequency TFDR.

(2) Calculate the damage factors ρ_1 and ρ_2 from the measurement results.

(3) Identify the defect type as a lumped defect.

(4) Classify the lumped defect as either a series resistance defect or a ground defect.

(5) Compute the local reflection coefficient Γ'_{f1} and the characteristic impedance Z_{cf1} using (4.32) and (4.33).

(6) Estimate the equivalent resistance of the lumped defect using (4.34).

Charateristic Parameters Estimation of Distributed Defects

If a defect is identified as a distributed defect, its length and characteristic impedance must be estimated using (4.31) and (4.33), respectively. Based on the estimated characteristic impedance Z_{cf1}, the type and other structural parameters of the distributed defect can be further determined. However, a limitation arises when estimating the segment length. As shown in (4.31), accurate estimation of the segment length Δl_{f1} requires prior knowledge of the phase constant β_{f1} of the defect. A practical solution to this issue is to first determine the defect type based on Z_{cf1} and then construct models of distributed defects covering all possible characteristic parameter values. From the simulation results of these models, the β_{f1} corresponding to Z_{cf1} can be obtained, and the defect length can then be estimated. Therefore, for distributed defects, the characteristic parameters can be estimated as follows and the corresponding flowchart is presented in Fig. 4.5.

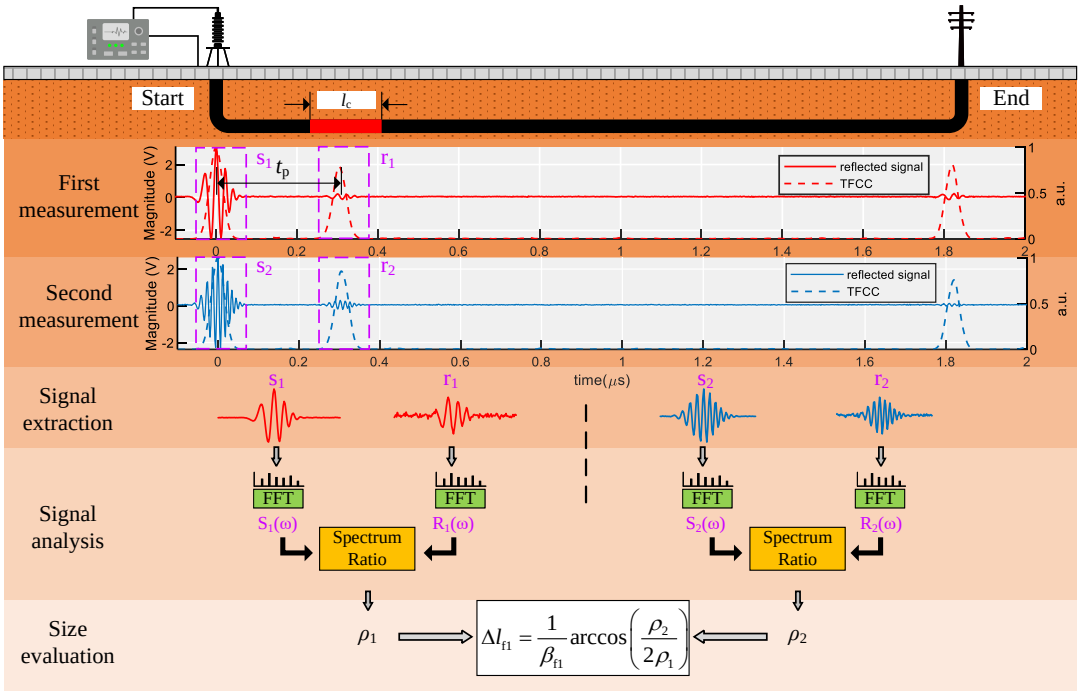


Fig. 4.5 Flowchart of the estimation of distributed defect

(1) Acquire the measurement results from the double-frequency TFDR.

(2) Calculate the damage factors ρ_1 and ρ_2 from the measurement results.

(3) Identify the defect type as a distributed defect.

(4) Estimate the characteristic impedance Z_{cf1} of the distributed defect using (4.33).

(5) Identify the type of distributed defect based on the estimated characteristic impedance Z_{cf1}.

(6) Model the distributed defect with all possible characteristic parameters using the FEM method and calculate all Z_{cf} and β_{f} of defects of this type.

(7) Determine certain structural parameters of the distributed defect, such as the angle of the shield hole, based on the estimated Z_{cf1}.

(8) β_{f1} is obtained based on Z_{cf1}, and the defect length is then estimated using (4.31).

4.2.4 Simulation and Validation

To validate the double-frequency TFDR method, a series of simulations were conducted on a 10 kV cable, with parameters listed in Table 2.2. These simulations primarily focused on estimating the sizes of distributed defects, including two typical types: shield corrosion and shield hole defects. The simulation setup for these distributed defects is illustrated in Fig. 4.6. The cable is 250 m long, excluding the length of the defect segment, and the defect is positioned 50 m from the beginning of the cable. Based on the criterion of signal design in Section 4.1, the first injected signal has a center frequency of 40 MHz, a bandwidth of 40 MHz, and a center time of 100 ns. The second injected signal has a center frequency of 80 MHz, with the same bandwidth and duration.

A Typical Shield Corrosion Defect

The first simulation case involves a cable with a shield corrosion defect. Following the procedure of the double-frequency TFDR method, the lengths of the defects are estimated accordingly.

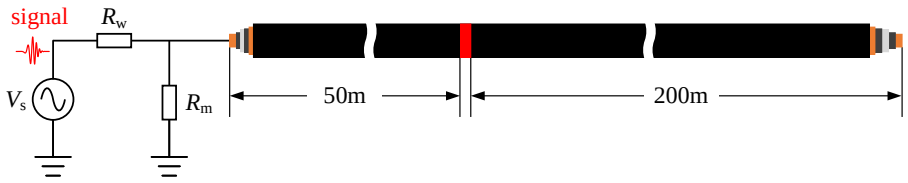


Fig. 4.6 Diagram of cable detection using TFDR

Step 1. Obtaining the measurement results of the double-frequency TFDR. The reflected signals from the cable were simulated using the double-frequency TFDR method. Taking the results of the first measurement as an example, the reflected signal $r(t)$ for various shield corrosion defects is shown in Fig. 4.7. In this figure, the signals observed near 0 µs correspond to the injected signal. The reflections from the defects appear at approximately 0.7 µs, while those near 3 µs result from reflections at the open end of the cable. By comparing

the reflected signals, it can be observed that the magnitude of the reflections increases with increasing defect length, and the arrival time of the reflected signals is delayed as the defect length increases. This observation is consistent with the findings reported in [69].

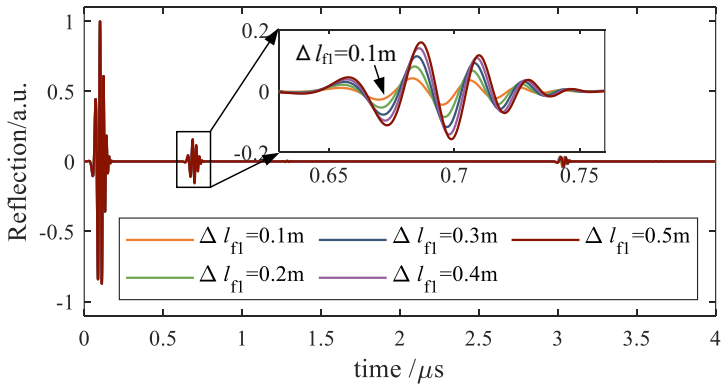


Fig. 4.7 Reflected signals from shield corrosion defects with different lengths

Step 2. Localizing the defects using the TFCC method. The defects shown in Fig. 4.7 are localized using the TFCC method, and the corresponding location curves are presented in Fig. 4.8. The defect locations are identified by the occurrence of the second peaks, while the peaks near 3 μs correspond to reflections from the open end of the cable. Analysis of the second peaks reveals that their occurrence time is delayed as the defect length increases. This observation is consistent with the theoretical result given by (4.25).

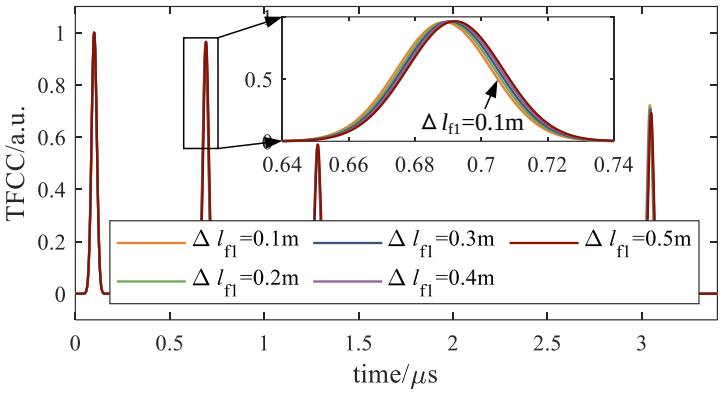


Fig. 4.8 Effect of various shield corrosion sizes on the location of the peak in TFCC curves

To validate the derivation of the peak time in (4.25), the simulation results were compared with the analytical results obtained from the equation. The comparison is shown in Fig. 4.9. As illustrated, there is good agreement between the simulation and analytical results. The peak time of the TFCC curve increases with the defect length, confirming the correctness of the derived expression for peak time. However, minor discrepancies between the simulation and analytical results are observed in Fig. 4.9. These differences are attributed to the simulation time step and the approximations used in (3.24) and (3.26).

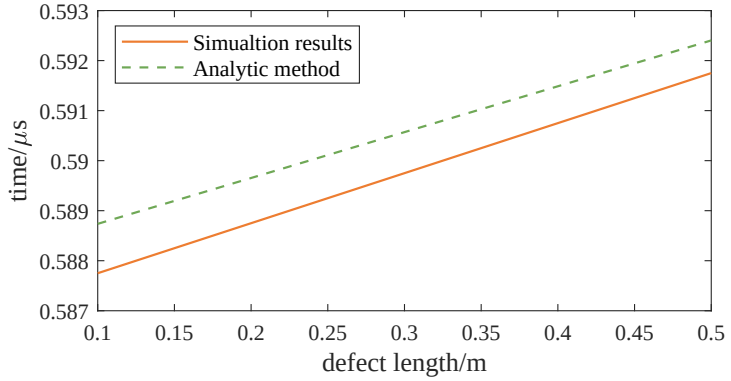


Fig. 4.9 Effect of the defect length on the location: comparison between simulations and equations

Step 3. Estimating the characteristic impedance of the defect. By extracting the reflected signal $r(t)$ from the double-frequency TFDR measurement results, the local reflection coefficient Γ'_{f1} of the shield corrosion defect can be calculated using (4.27). Subsequently, the characteristic impedance Z_{cf1} of the defect is computed using (4.33). The estimated characteristic impedance Z_{cf1} for the shield corrosion defect is shown in Fig. 4.10. Comparison with the reference value indicates that the estimated impedance closely matches the true value, with a maximum relative error of 2.25 %.

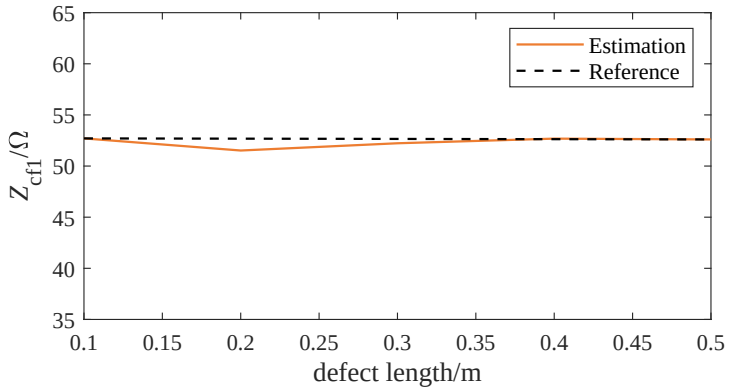


Fig. 4.10 Comparison of Z_{cf1} between the estimated value and the reference value

Step 4. Estimating the length of the defect. To estimate the length of shield corrosion defects, the characteristic parameter K_{bf1} must be known. K_{bf1} can be calculated as follows:

$$K_{\mathrm{bf1}} = \frac{\mathrm{d}\beta_{\mathrm{bf1}}}{\mathrm{d}\omega} \tag{4.38}$$

where β_{bf1} is the phase constant of the shield corrosion defect, which can be calculated using cable shield corrosion model in Section 2. For the cable specified in Table 2.2, the phase constant slope K_{bf1} of the shield corrosion defect is $9.1656 \times 10^{-9}\,\mathrm{s\,m^{-1}}$. The attenuation constant α_{c} is $0.0066\,\mathrm{m^{-1}}$ at a center frequency of 40 MHz, and $0.0119\,\mathrm{m^{-1}}$ at 80 MHz. The evaluation results for the corrosion defect lengths are shown in Fig. 4.11. As shown in Fig. 4.11,

the estimated defect lengths closely match the reference values. The maximum relative error is 11.32 %, occurring at a defect length of 0.2 m. This discrepancy is primarily caused by the simulation time step, and the approximation used in the reflection coefficient expression (3.26) also introduces a minor influence on the estimation accuracy.

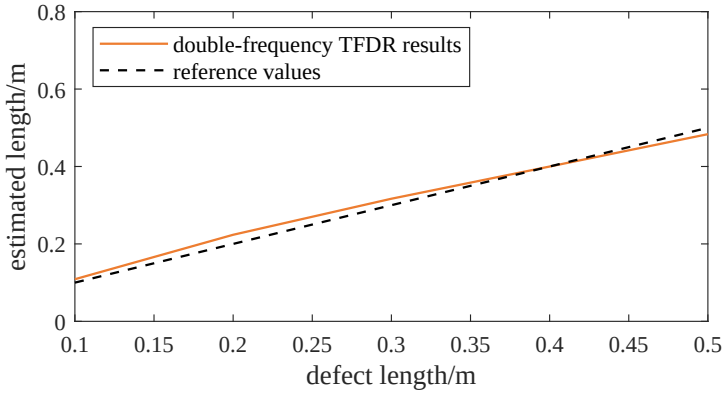


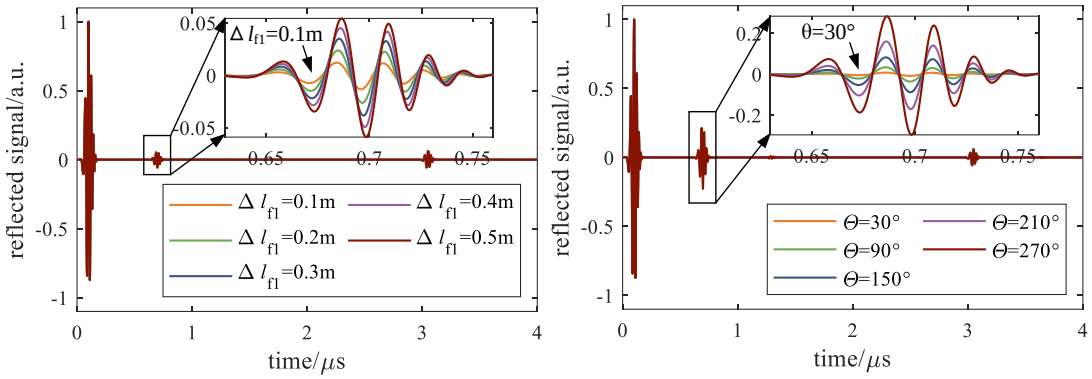
Fig. 4.11 Assessment results of shield corrosion size using the double-frequency TFDR

A Typical Shield Hole Defect

The second simulation case of the distributed defect involves a cable with a shield hole defect, as shown in Fig. 2.15. The simulation model and excitation signals are the same as those used in the shield corrosion defect simulations. Two groups of shield hole defects are modeled. In the first group, the defect length Δl_{f1} varies from 0.1 m to 0.5 m, with a fixed central angle $\theta = 150^{\circ}$. In the second group, the central angle θ varies from 30° to 270°, while the defect length is fixed at 0.5 m. Following the steps of the double-frequency TFDR method, the length, central angle, and characteristic impedance of the shield hole defects are estimated.

Step 1. Obtaining the measurement results of the double-frequency TFDR. The reflected signals of the cable excited by the first injected signal are shown in Fig. 4.12. In this figure, the signals near 0 µs correspond to the injected signal, those around 0.7 µs result from reflections caused by defects, and the signals near 3 µs originate from reflections at the open end of the cable. Fig. 4.12a shows that as the defect length increases, the reflected signal peaks are delayed and their magnitudes increase. In contrast, Fig. 4.12b demonstrates that while the peak time remains constant for varying defect angles, the peak magnitude increases with larger defect angles.

Analyzing the variation in the magnitude of the reflected signals in Fig. 4.12, it appears that the influences of defect length and defect angle are not equivalent. To investigate this further, the correlation between the reflected signal magnitude and both defect length and angle was analyzed. Simulations were performed for shield hole defects with lengths ranging from 0.1 m to 0.5 m and central angles ranging from 30° to 270°. The distribution of reflected



(a) Various shield hole lengths (b) Various shield hole angles

Fig. 4.12 Reflected signals for various shield hole defects

signal magnitudes is illustrated in Fig. 4.13. Using normalized partial derivative sensitivity analysis [109], the mean sensitivity values with respect to defect angle and length were found to be 2.363 and 0.886, respectively. This indicates that the defect angle has a greater impact on the reflected signal magnitude than the defect length.

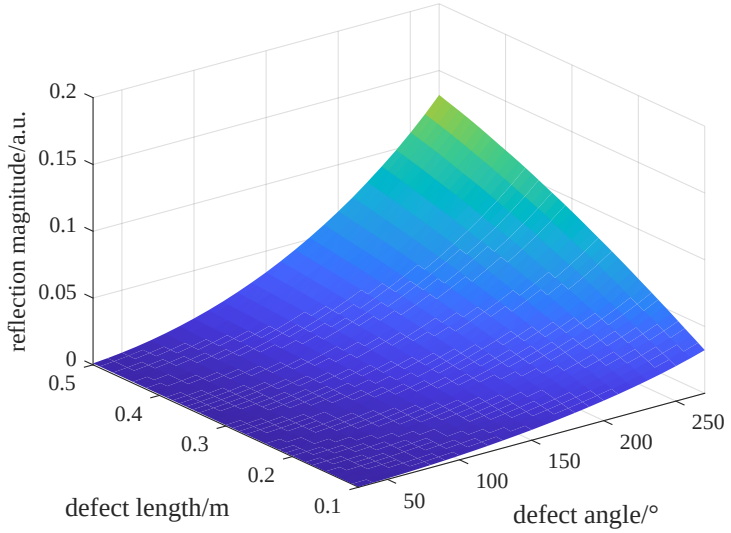
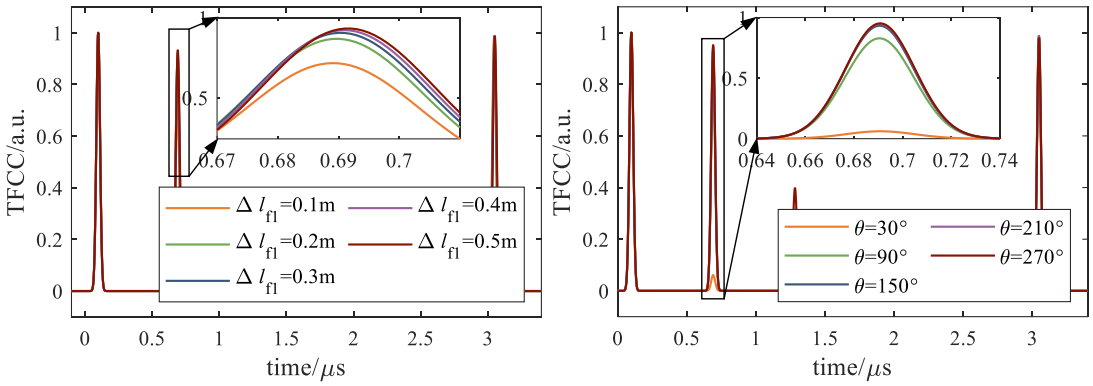


Fig. 4.13 Magnitude surface of the reflected signal for various defects

Step 2. Localizing the defects using the TFCC method. The defects shown in Fig. 4.12 are localized using the TFCC method, and the corresponding location curves are presented in Fig. 4.14. The time associated with defect locations is identified by the occurrence of the second peaks in the TFCC curves. In Fig. 4.14a, the location results are observed to be delayed as the defect length increases. In Fig. 4.14b, defects with small angles exhibit smaller peak values. However, the theoretical peak values in the TFCC curves should not depend on the defect angle. This discrepancy is attributed to numerical errors arising from the computation of the WVD. The smaller the angle of the shield hole defect, the more significant the influence of numerical errors becomes.



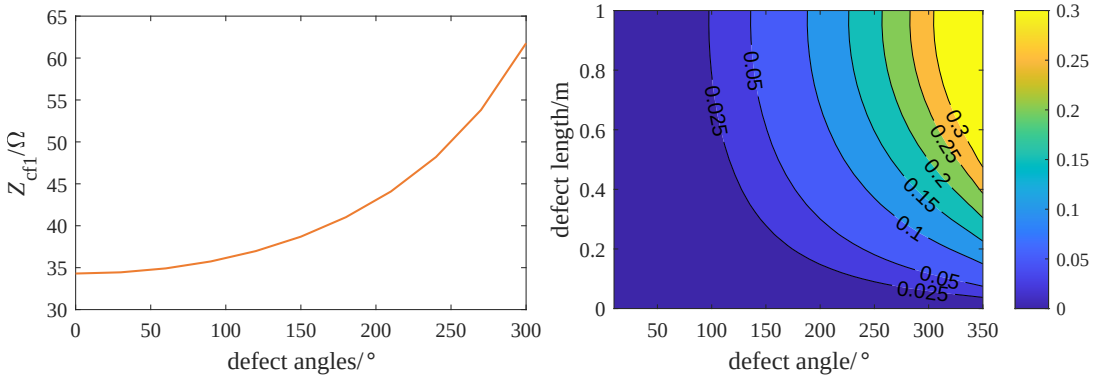
(a) Various lengths (b) Various angles

Fig. 4.14 TFCC curves of reflected signals from shield corrosion hole defects of various sizes

.

Step 3. Estimating the characteristic impedance and central angle of the shield hole defect. By extracting the reflected signal $r(t)$ from the double-frequency TFDR measurement results, the damage ratio ρ of the shield hole defect can be calculated using (4.30). The corresponding characteristic impedance Z_{cf1} can then be determined using (4.33). Based on the analysis of shield hole defects, the characteristic impedance Z_{cf1} is primarily influenced by the central angle θ of the defect. Therefore, θ can be estimated from the calculated value of Z_{cf1}. To facilitate this estimation, a reference relationship between Z_{cf1} and θ was established using FEM simulations. The simulated values of Z_{cf1} for various central angles are shown in Fig. 4.15a.

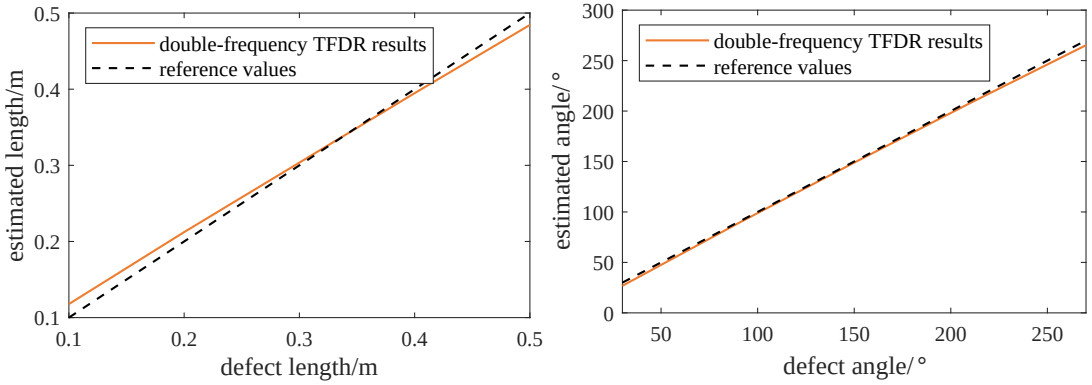
Step 4. Estimating the length of the shield hole defect. The defect length can be estimated using (4.31). Alternatively, a more convenient approach is to use FEM results to obtain the reference damage factor ρ for various defect lengths and central angles. The defect length can then be determined by matching the measured damage factor ρ_1 with the corresponding reference value. The relationship between ρ, defect central angle, and defect length is presented in Fig. 4.15b.



(a) Reference Z_{cf1} (b) Reference ρ

Fig. 4.15 Reference characteristic impedance Z_{cf1} and reference ρ of the shield hole defects

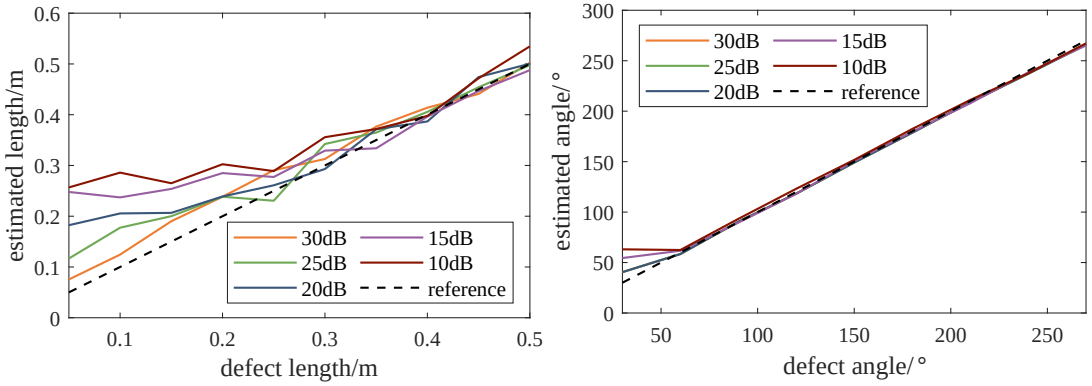
In the contour plot of the reference ρ, the defect length can be estimated by locating the corresponding length that matches the measured ρ_1 at the known central angle θ of the shield hole defect. Based on this approach, the estimation results for the shield hole defects in the simulations are presented in Fig. 4.16. The results shown in Fig. 4.16 indicate that the maximum error in defect length estimation is 1.8 cm at $l_c = 0.15$ m, corresponding to a relative error of 12 %. Although this 12 % error may appear significant, it is primarily attributed to the simulation time step. In the simulation, the maximum frequency is 2 GHz, resulting in a time step of 0.5 ns. Given the signal propagation velocity of 172 m µs^{-1}, the corresponding spatial resolution is approximately 2.15 cm, introducing a discretization error in the simulated reflected signals. For angle estimation, the maximum absolute error is 4.75° at $\theta = 300°$, corresponding to a relative error of 1.76 %. The estimation error increases as the angle approaches 360°, which is due to the fact that radiated energy becomes non-negligible at large angles, violating the assumption in (3.24). Ignoring discretization effects, the evaluation results demonstrate that the double-frequency TFDR method is both valid and accurate for assessing the length and angle of shield hole defects.



(a) Estimated lengths (b) Estimated angles

Fig. 4.16 Size evaluation of shield hole defects

Next, the impact of noise on the proposed method was analyzed. Noise typically originates from environmental sources such as electromagnetic interference, equipment-related factors (e.g., thermal noise), and stochastic disturbances in power grids. These are commonly modeled as white noise, as discussed in [12]. Based on this understanding, the performance of the proposed method was evaluated under various SNRs. For each defect at each SNR level, 20 simulation trials were conducted, and the mean results are presented in Fig. 4.17. The figure shows that defect length estimation is more sensitive to noise than angle estimation. In the case of length estimation, the error is larger for short defects at low SNR levels and decreases as SNR increases. Angle estimation is generally more robust, with significant errors occurring only at small angles under low SNR conditions.

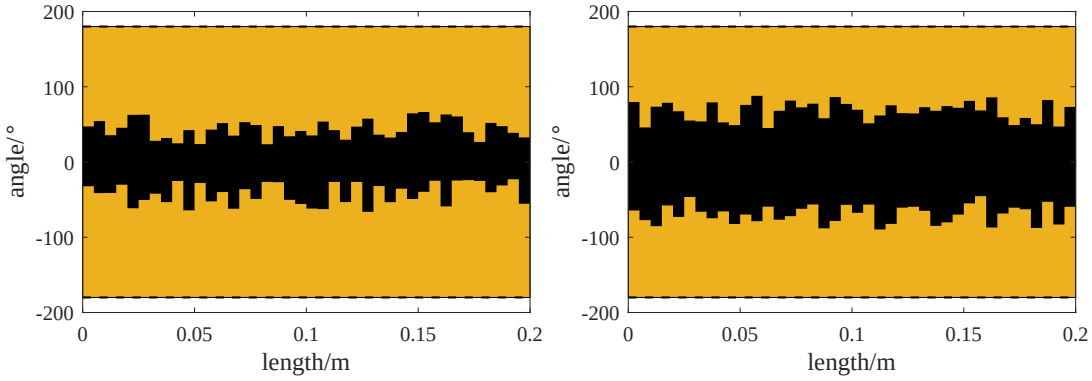


(a) Defect length (b) Defect angle

Fig. 4.17 Size evaluation of shield hole defects under the signals with various SNR

Irregular Shield Hole Defects

In practice, shield holes often exhibit irregular geometries. To evaluate the robustness of the proposed method, simulations were conducted for irregular shield holes. A total of 12 irregular defects were modeled. The irregular holes were constructed in the FEM model as follows: first, a regular hole is defined by specifying an average central angle θ_g and a length Δl_{fc}. This hole is then divided into multiple small segments along the cable axis. An angle variation range $\Delta\theta_g$ is defined, and angle perturbations within this range are randomly assigned to each segment to simulate geometric irregularity. The structural parameters of the modeled irregular shield corrosion holes are listed in Table 4.1, and examples of the typical irregular holes are illustrated in Fig. 4.18.

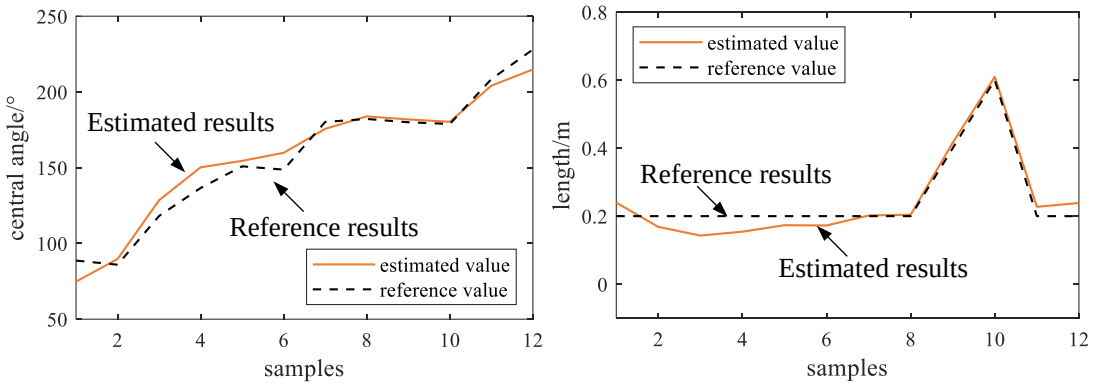


(a) Sample 2 (b) Sample 4

Fig. 4.18 Irregular shield hole defects in Table 4.1

The estimated sizes of the irregular shield holes are presented in Fig. 4.19. These estimated values are compared with the average geometric parameters of the corresponding holes. The comparison shows that the estimated values closely match the average values and follow a consistent trend. Although the estimation errors for both angle and length are slightly larger

for irregular shield corrosion holes compared to regular ones, the deviations remain within an acceptable range. These results demonstrate that the proposed method can reliably evaluate the sizes of irregular shield holes.



(a) Angle comparison (b) Length comparison

Fig. 4.19 Size evaluation of irregular shield corrosion holes

Table 4.1 Angle and length parameters of the samples in the simulation

Sample	θ_g/°	$\Delta\theta_g$/°	Δl_{fc}/m	Average/°
1	90	±15	0.2	88.69
2	90	±45	0.2	85.97
3	120	±15	0.2	118.18
4	135	±45	0.2	136.62
5	150	±15	0.2	150.90
6	150	±60	0.2	148.72
7	180	±15	0.2	180.22
8	180	±60	0.2	182.16
9	180	±60	0.4	179.99
10	180	±60	0.6	178.85
11	210	±60	0.2	208.49
12	225	±45	0.2	228.01

In this section, a double-frequency TFDR method is proposed to estimate the equivalent resistance of lumped defects and the physical dimensions of distributed defects. Validated by simulations and experiments, the method achieves good performance even for irregular defects.

4.3 Experimental Verification

To validate the performance of the double-frequency TFDR method in practical applications, a series of experiments were conducted.

4.3.1 Experimental Setup and Measurement Platform

In the experiment, an SYV50 coaxial cable with a characteristic impedance of 50 Ω and total length of 180 m was used. A defect was introduced at approximately 30 m from the cable's start, connected via SMA connectors between two segments. The setup, shown in Fig. 4.20, includes an arbitrary waveform generator, oscilloscope, computer, and the test cable. The experiment platform is shown Fig. 4.21. In the platform, the arbitrary waveform generator used is the Keysight 33621A, and the oscilloscope is the Tektronix MSO5204B.

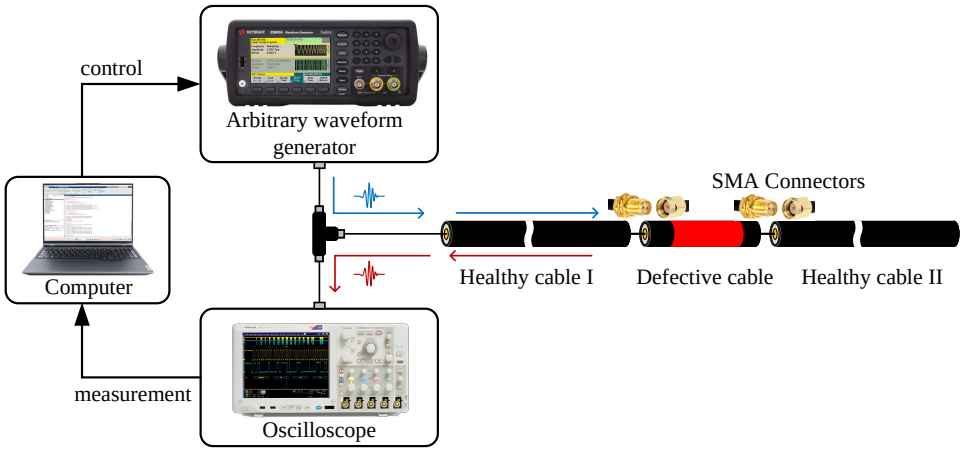


Fig. 4.20 Experiment setup

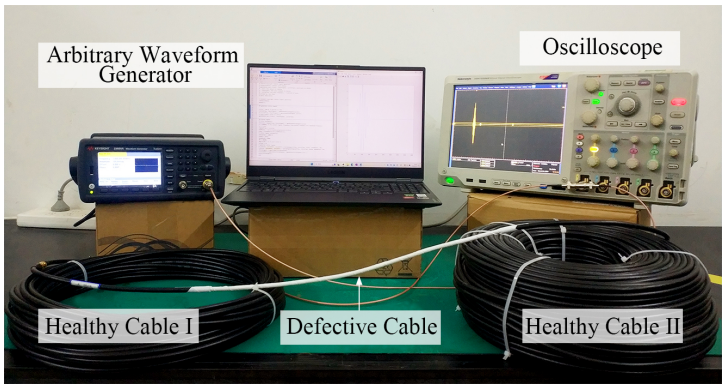
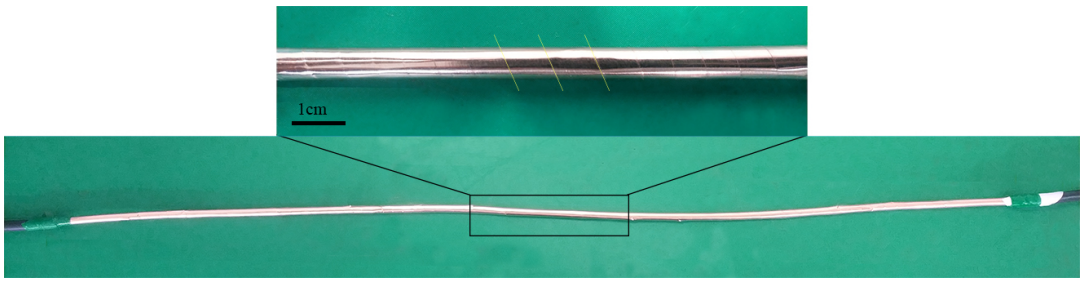


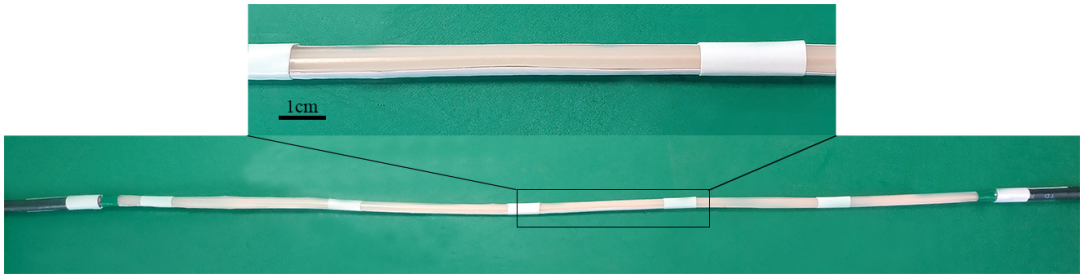
Fig. 4.21 Experiment platform

Three types of defects were fabricated for the experiment. The first type is the shield corrosion defect. According to the structural characteristics of shield corrosion, the primary cause is the isolation between adjacent layers of shielding tapes. To simulate this condition, a thin layer of Scotch tape was inserted between the shielding layers to mimic the insulation effect. The second type is the shield hole defect. To replicate such defects, apertures were cut into the shielding layer using the following procedure: the shield, composed of long strips of copper foil with a width corresponding to the perimeter of the cable insulator, was first separated

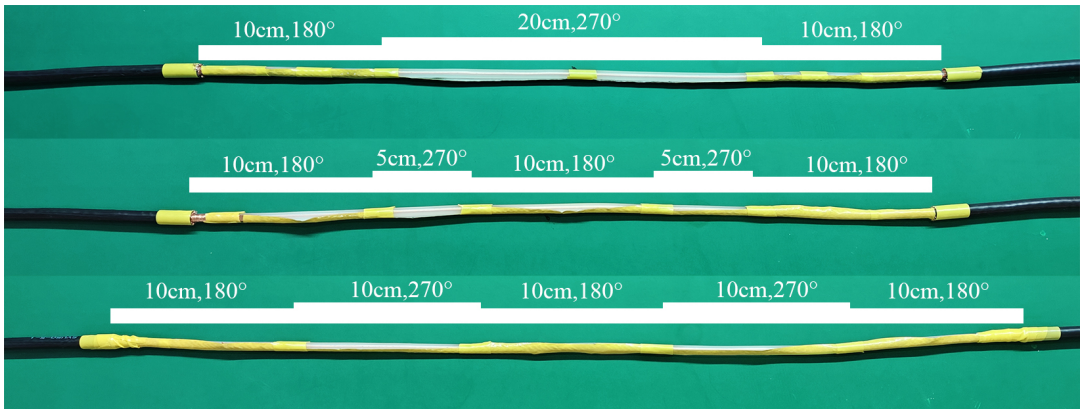
from the insulation after removing the outer sheath. The required aperture width was calculated based on the desired hole angle. The shielding foil was then flattened, the removal area was measured and marked, and the copper foil was cut using a knife. Finally, the processed shield was re-wrapped around the insulation. The third type is the irregular shield hole defect. The fabrication method is similar to that of the regular shield hole defect, with the only difference being that the shield hole angle varies along the length, resulting in a non-uniform aperture. Samples of the defective cables are shown in Fig. 4.22.



(a) Cable samples mimicking shield corrosion defects



(b) Cable samples mimicking shield hole defects



(c) Cable samples mimicking irregular shield hole defects

Fig. 4.22 Cable samples with defects

4.3.2 Experimental Results and Analysis

The signals used in the experiments are determined by the signal selection criterion in Section 4.1. The first injected signal has a center frequency of 40 MHz, a bandwidth of 40 MHz,

and a center time of 100 ns. The second injected signal has a center frequency of 80 MHz, with the same bandwidth and center time. The experimental results are shown as follows.

Shield Corrosion Defect

In the shield corrosion defect experiment, defects with lengths of 20 cm and 30 cm were fabricated. The reflected signals from the cables containing these defects are shown in Fig. 4.23. It can be observed that the reflected signal corresponding to the longer defect exhibits a larger magnitude.

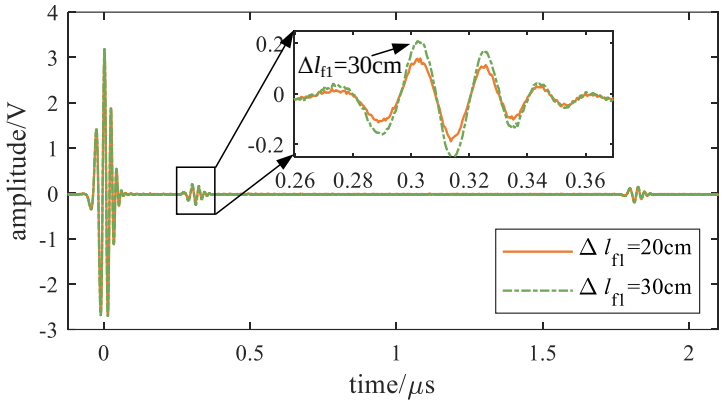
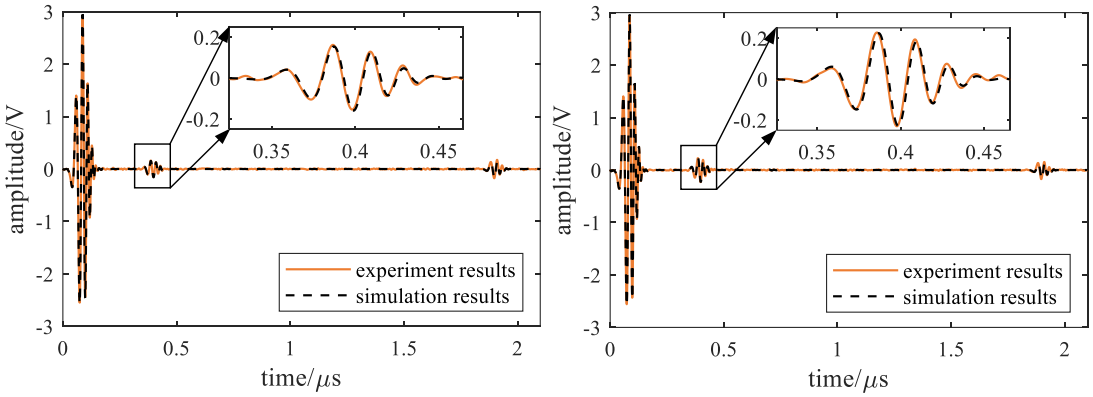


Fig. 4.23 Measured results of shield corrosion defects by the first injected signal

In addition, to validate the consistency between the shield corrosion defect model established in Chapter 2 and the actual physical defects, the experimental setup was modeled and simulated. A comparison between the simulation results and the experimental measurements is shown in Fig. 4.24. The comparison indicates that the simulation results closely match the experimental data, confirming that the shield corrosion defect model is valid and provides a reliable reference for cable defect estimation using the double-frequency TFDR method.

The defects are then located using the TFCC method. The TFCC curves corresponding to the reflected signals are shown in Fig. 4.25. Peaks are observed at the start and end of the cable, as well as at the positions of the defects. Therefore, defects can be identified by determining the times at which these peaks occur. By calculating the time difference between the first and second peaks, the arrival time of the reflected signal is determined to be 0.295 μs.

Furthermore, to determine the defect locations and estimate their lengths, the wave velocity v_c and attenuation constant α_c of the SYV50 cable were measured using a healthy cable of known length. The parameter K_b was then calculated according to (3.18b). The measured wave velocity v_c is 204.08 m μs^{-1}, and the attenuation constants α_c are 0.0072 m^{-1} at 40 MHz and 0.0085 m^{-1} at 80 MHz. The corresponding value of K_b is 7.1695×10^{-9} s m^{-1}.



(a) 20 cm (b) 30 cm

Fig. 4.24 Comparison between the reflected signals obtained with the experiment and in simulation for shield corrosion defects

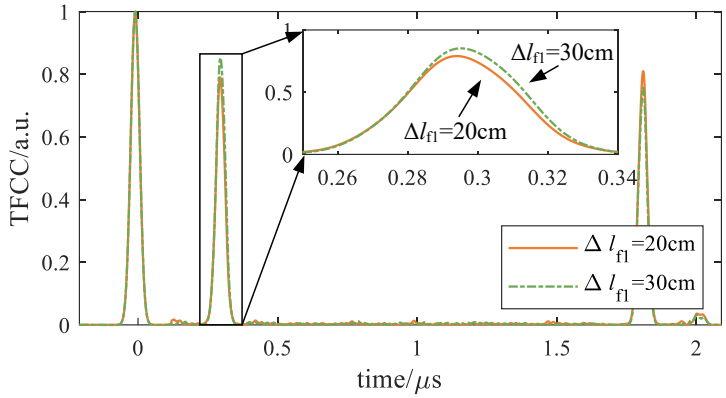


Fig. 4.25 TFCC curves of the defect location in the experiment

Using (4.31), the defect lengths in the experiment were estimated, and the results are summarized in Table 4.2. The comparison shows that the double-frequency TFDR method provides highly accurate estimations of shield corrosion defect sizes, with errors of less than 1 % between the measured and estimated values. The small discrepancies can be attributed to the approximation used in the reflection coefficient model, as described in (3.26), as well as to the influence of measurement noise.

Table 4.2 Comparison of actual and estimated defect sizes

Defect	Length/cm	Estimated Length/cm	Error/%
1	20	20.006	0.3
2	30	30.001	0.03

Additionally, the characteristic impedance Z_{cfl} of the shield corrosion defects was calculated based on its distributed-parameter model, and the measured values were compared with those

obtained from the shield corrosion models. The simulated and experimental results are presented in Table 4.3. The error between the measured and simulated values is less than 2.4 %.

Table 4.3 Comparison between simulated and measured values of Z_{cf1}

Defect	Size/cm	Simulated Z_{cf1}/Ω	Measured Z_{cf1}/Ω	Error/%
1	20	72.84	74.58	2.40
2	30	72.84	72.21	0.87

Sheild Hole Defect

In this experiment, to detect shield hole defects with various central angles and lengths, eight cable samples with varying angles and lengths were prepared. Six of the samples feature apertures with lengths of 30 cm, 40 cm, and 50 cm, each with central angles of either 90° or 180°. In addition, one sample has an aperture of 60 cm with an angle of 190°, and another is 60 cm long with a 230° angle.

Fig. 4.26 presents the measured reflected signals from the defective cable samples. In the plot, different colors represent different defect lengths, while different line styles correspond to different aperture angles. The reflected signals caused by the defects appear between 0.25 μs and 0.35 μs. Analyzing the relationship between signal magnitude and defect geometry, it can be observed that the magnitude of the reflected signals increases with increasing defect length when the aperture angle is fixed. Likewise, for a fixed defect length, the magnitude increases with larger aperture angles.

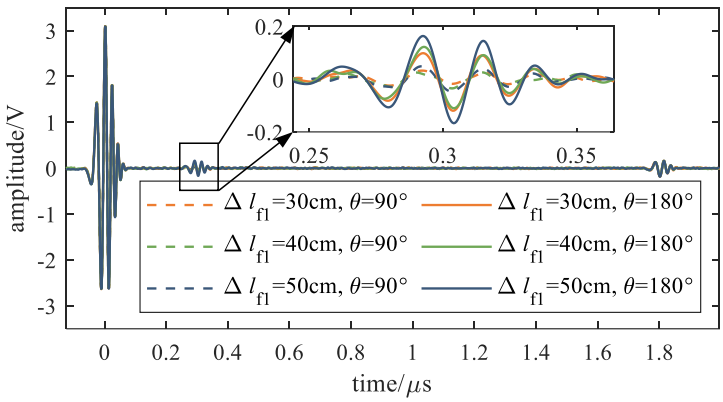
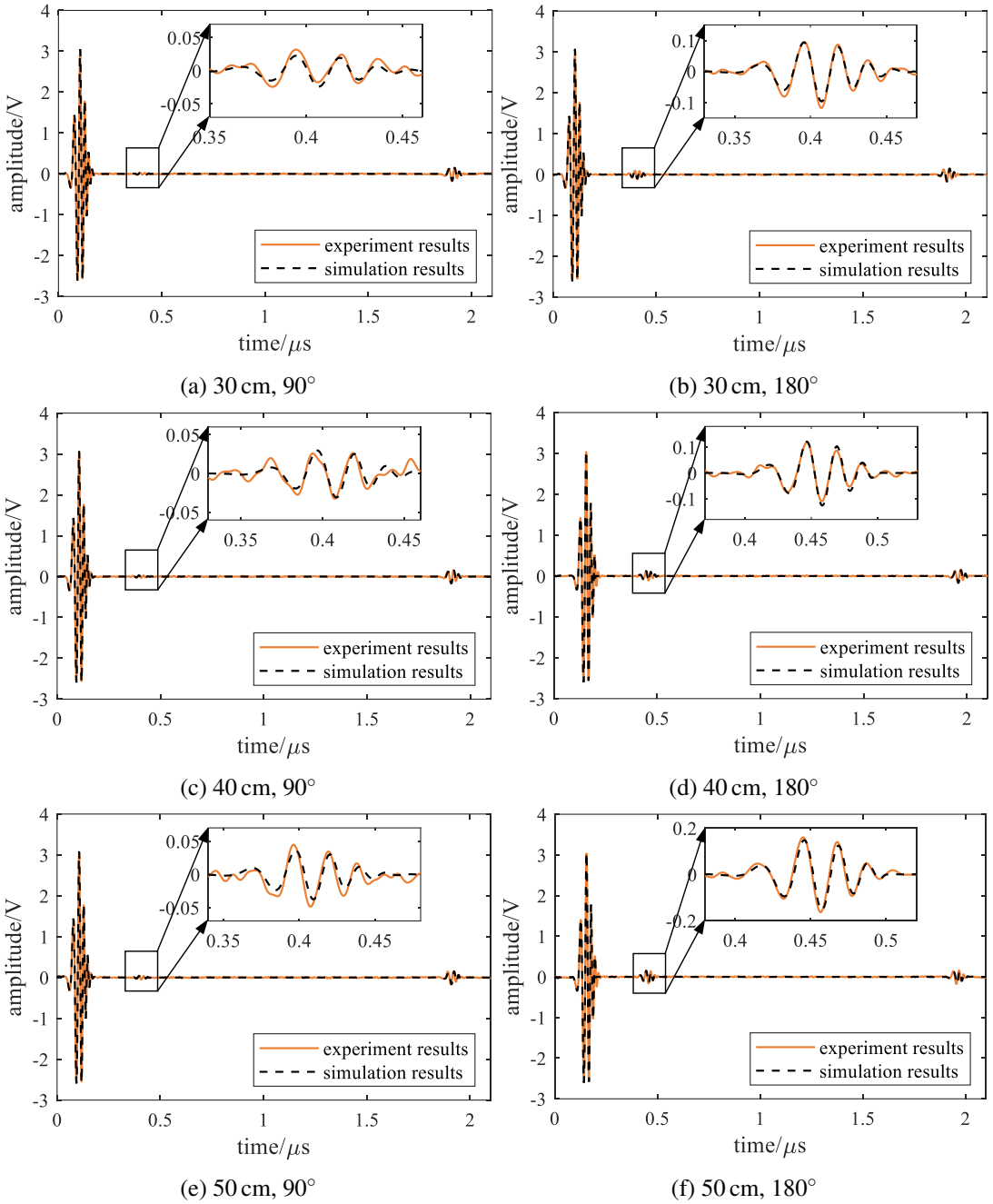


Fig. 4.26 The TFDR measurement results of cables with shield hole defects

Cables in the experiment are simulated using the method proposed in Section 2. The TFDR measurement results are compared with the simulation results in Fig. 4.27. The good agreement between the experimental and simulated curves demonstrates the accuracy of the shield hole

defect model. This confirms the efficacy of the simulation model as a reliable representation of real-world cable shield hole defects. Therefore, the simulation models can be effectively used to generate reference datasets for ρ_1 and Z_{cf1}.



(a) 30 cm, 90° (b) 30 cm, 180°

(c) 40 cm, 90° (d) 40 cm, 180°

(e) 50 cm, 90° (f) 50 cm, 180°

Fig. 4.27 Comparison between the reflected signals obtained with the experiment and in simulation for shield hole defects

Defects are located using the TFCC method, and the corresponding TFCC curves of the reflected signals are shown in Fig. 4.28. Peaks in these curves appear at the start and end points of the cable, as well as at the defect locations. Defects are identified by locating the occurrence

of these peaks, which for the defects in Fig. 4.28 occurs at 0.295 µs. The experimental results are consistent with the simulation results shown in Fig. 4.14. Specifically, the TFCC magnitude is larger for long and wide shield hole defects compared to short and narrow ones. However, in the case of varying defect angles, a discrepancy is observed: in simulations, the TFCC magnitude differences between defects with large central angles are relatively small, whereas in the experiments, the differences are more pronounced. This is primarily due to the influence of noise, which particularly distorts small reflected signals, thereby increasing the apparent difference between defects with small and large central angles.

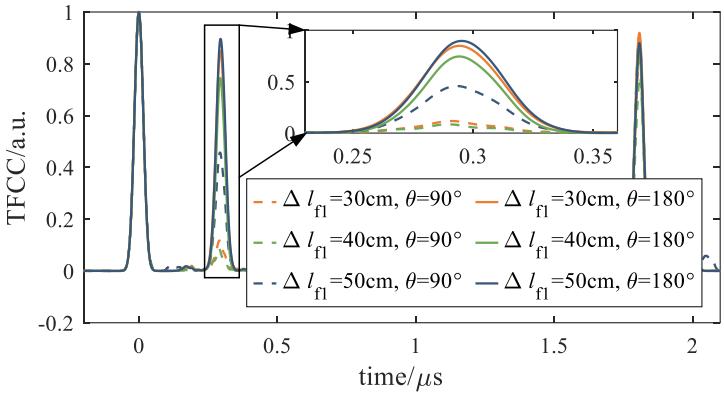
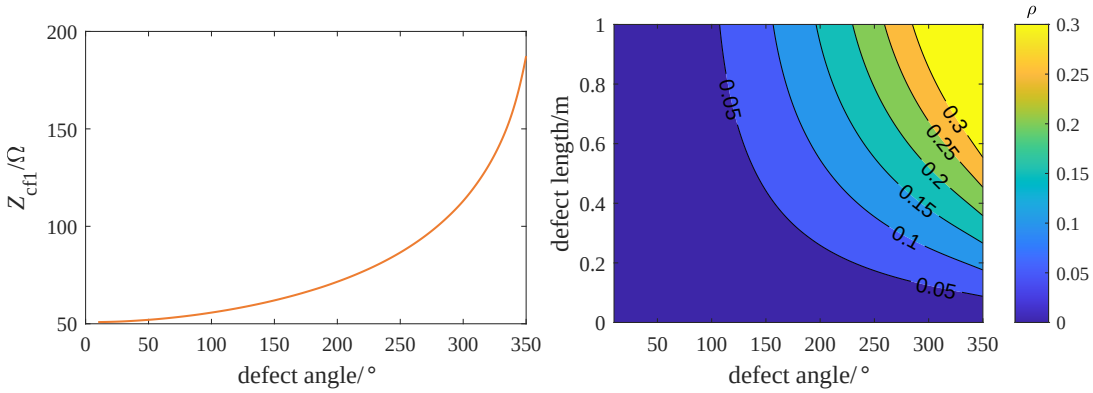


Fig. 4.28 TFCC curves showing the location of cable defects

To estimate the angle and length of the shield hole defect, the reference curve of the characteristic impedance Z_{cf1} and the reference contour of the damage ratio ρ_1 were calculated using the FEM method. The reference curve of Z_{cf1} is shown in Fig. 4.29a, and the reference contour of ρ_1 is presented in Fig. 4.29b.



(a) Z_{cf1} (b) ρ_1

Fig. 4.29 Reference sets of Z_{cf1} and ρ_1 for evaluating the size of the shield hole defects

The reference and measured values of ρ_1 are compared in Table 4.4. The maximum observed error between the reference and measured values is 7.93 %. This error arises partly from measurement noise and partly from imperfections in the physical fabrication of the defects.

In particular, for longer defects, it is difficult to maintain a uniform and consistent aperture angle along the entire length of the cable segment, which contributes to deviations. Despite these sources of uncertainty, Table 4.4 demonstrates that the measured ρ_1 values closely match the reference values obtained from simulation, thereby confirming the validity and reliability of the model used to derive ρ_1. Furthermore, these experimentally validated models can serve as the basis for establishing a reference database to support the accurate diagnosis and quantitative evaluation of cable shield hole defects in practical applications.

Table 4.4 Comparison of ρ_1 between reference and measured values in experiments

Defect	Size	Reference ρ_1	Measured ρ_1	Error/%
1	30 cm, 90°	0.0137	0.0136	0.73
2	30 cm, 180°	0.0480	0.0485	1.04
3	40 cm, 90°	0.0180	0.0183	1.67
4	40 cm, 180°	0.0630	0.0630	0.00
5	50 cm, 90°	0.0220	0.0237	7.73
6	50 cm, 180°	0.0770	0.0787	2.21
7	60 cm, 190°	0.0990	0.1050	6.06
8	60 cm, 230°	0.1387	0.1277	7.93

Using (4.33), the characteristic impedance Z_{cf1} was calculated. The reference and measured values of Z_{cf1} are compared in Table 4.5. From the table results,it can be observed that the error between the measured and reference values is less than 2.3 %, demonstrating that the double-frequency TFDR method can accurately measure the characteristic impedance of cable shield hole defects.

Table 4.5 Comparison of Z_{cf1} between the reference and measured values in experiments

Defect	Size	Reference Z_{cf1}/Ω	Measured Z_{cf1}/Ω	Error/%
1	30 cm, 90°	54.79	54.39	0.73
2	30 cm, 180°	67.26	68.81	2.30
3	40 cm, 90°	54.79	54.52	0.49
4	40 cm, 180°	67.26	67.23	0.04
5	50 cm, 90°	54.79	54.91	0.22
6	50 cm, 180°	67.26	66.63	0.94
7	60 cm, 190°	69.30	68.67	0.91
8	60 cm, 230°	79.68	79.03	0.82

The length and angle of the defective cable samples were evaluated using the double-frequency TFDR method. The evaluated results are compared with the reference values in Table 4.6. The results confirm that the proposed double-frequency TFDR method is effective for evaluating the size of cable shield hole defects. However, discrepancies between the

evaluated and actual values are observed. These errors primarily arise from measurement noise and limitations in the precision of defect fabrication. Notably, the discrepancies are smaller for angle evaluations, indicating higher accuracy in estimating defect angles. In contrast, length evaluations exhibit larger errors, suggesting a greater susceptibility to inaccuracies. This difference can be attributed to the influence of noise. Angle estimation is based on the ratio between results from two separate measurements, which helps to mitigate the effect of noise. In contrast, length estimation is derived from a single measurement and is therefore more vulnerable to noise-induced errors. Furthermore, since length estimation depends on the accuracy of the angle estimation, any error in the angle evaluation can propagate and further degrade the accuracy of the length estimation.

Table 4.6 Comparison of defect sizes between actual and estimated values

Defect	Size	Estimated Δl_{f1}/cm	Error/%	Estimatedθ/°	Error/%
1	30 cm, 90°	32.90	9.67	85.42	5.09
2	30 cm, 180°	32.85	9.50	172.44	4.20
3	40 cm, 90°	43.73	9.32	86.93	3.41
4	40 cm, 180°	40.10	0.25	179.84	0.09
5	50 cm, 90°	52.94	5.88	91.39	1.54
6	50 cm, 180°	53.16	6.32	176.76	1.80
7	60 cm, 190°	66.74	11.23	187.04	1.56
8	60 cm, 230°	55.42	7.63	228.06	0.84

Irregular Shield Hole Defect

The irregular shield hole defects shown in Fig. 4.22c were also evaluated using the same procedure. The evaluation results for these irregular defects are presented in Table 4.7.

Table 4.7 Comparison between actual sizes and estimation results of irregular shield holes

Defect size	Estimated Δl_{f1}/cm	Error/%	Estimated θ/°	Error/%
40 cm, 225°	37.64	5.91	237.93	5.75
40 cm, 202.5°	42.67	6.68	208.99	3.21
50 cm, 216°	51.70	3.40	223.88	3.65

The angle in defect sizes is the weighted average angle of the irregular shield hole, which is calculated as $\theta_{\mathrm{ave}} = \frac{\sum_{i=1}^{N} \theta_i l_{\mathrm{ci}}}{\sum_{i=1}^{N} l_{\mathrm{ci}}}$.

As shown, the lengths of the irregular shield holes were estimated with high accuracy, with a maximum error of 6.68 %. The angles estimated by the proposed method represent the average angular distribution of each defect and show good agreement with the actual weighted average angles, with a maximum error of 5.75 %. In practical applications, shield holes may exhibit more complex geometries, which could lead to increased estimation errors. Nevertheless, both simulation and experimental results demonstrate that the proposed method can still provide a reliable and indicative evaluation of the size characteristics of irregular shield holes.

4.4 Summary

In this chapter, a double-frequency TFDR technique is proposed to estimate the equivalent resistance and physical sizes of cable defects. In this method, a two-sequential TFDR measurement strategy is employed, where the second injected signal has a center frequency twice that of the first. The damage ratio of a defect is defined as the modulus ratio of the reflected signal to the injected signal. The equivalent resistance of lumped defects and the physical sizes of distributed defects are then estimated from these damage ratios. Using the estimated equivalent resistance and physical sizes, the defect severity is quantitatively evaluated. The proposed method is validated through simulations and experiments, which demonstrate that it can accurately estimate the equivalent resistance of lumped defects as well as the length and angle of distributed defects, even for irregularly distributed defects.

Chapter 5

Development of a TDR System with HV Pulse Injection and Fast Range Switching

Although the double-frequency TFDR method can estimate defect severity quantitatively and accurately, its high-frequency injected signal is greatly attenuated and the detectable distance is short. Due to the limitations of current high-frequency signal generators, double-frequency TFDR is mainly used for defect estimation of short cables (hundreds of meters). In multiple-defect and long-cable defect detection, defect localization is the primary task. However, due to attenuation of the cable and reflections from defects and joints, the detectable distance of traditional TDR is limited when testing cables with multiple defects. An effective method to address this is to enhance the strength of the injected signal; however, this requires that measurement devices have higher voltage withstand levels and wider dynamic ranges. In this chapter, a TDR with HV pulse injection and fast range switching (HVFRS-TDR) is designed. The system incorporates a HV pulse generator with continuously adjustable amplitude and pulse width to enhance the energy of the injected signal. A fast-switching, multi-ratio voltage divider is also developed to measure the reflected signal, ensure the safety of the measurement system, and improve the visibility of weak reflected signals. The designed TDR system is validated through experiments.

5.1 Tunable HV Pulse Generator

The amplitude of the reflected signal in a TDR system is directly affected by the injected pulse amplitude. A higher-amplitude pulse enhances the reflected signals of weak reflection defects, thereby extending the measurement range. Besides amplitude, the pulse width also influences the measurable distance. A wider pulse carries more energy and can propagate farther, supporting long-range detection. However, increasing the pulse width shifts the frequency

content to lower frequencies, reducing spatial resolution and making it harder to distinguish closely spaced defects. To balance detection distance and resolution, a HV pulse generator with adjustable amplitude and pulse width is developed for the HVFRS-TDR system.

5.1.1 Hardware Design and Simulation Analysis

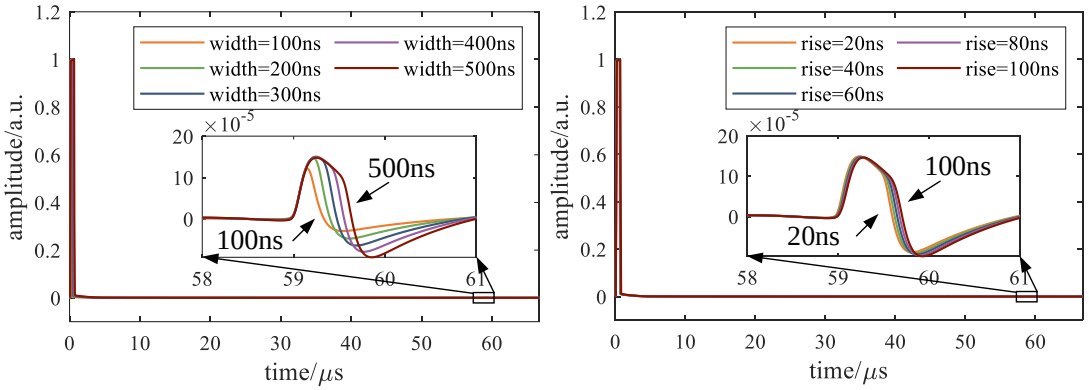
To design a HV pulse generator with continuously adjustable amplitude and pulse width, the required performance specifications are first defined. Subsequently, the hardware design is presented, including the selection of key components and the development of the pulse circuit. Finally, signal integrity simulations are conducted to verify the performance of the designed pulse generator and to optimize circuit parameters.

Identify the Required Performance of the Pulse Generator

To identify the required performance of the pulse generator, the testing conditions of the HVFRS-TDR system are first determined. A typical power cable of type 8.7/15 kV-35 mm^2 is selected as the test line. In cable TDR measurements, the primary objective is to detect and localize cable joints. Therefore, the detection and localization of all joints along the cable is set as the measurement target of the equipment. For a 10 kV cable, the total length typically ranges from 3 km to 5 km, with joints usually located every 300 m to 500 m [110]. Accordingly, the pulse generator must be capable of generating pulses sufficient for detecting and localizing joints at 5 km. Based on the analysis in the Section 2.1, the equivalent input impedance of a joint in this type of cable ranges from 36.18 Ω to 43.08 Ω. Therefore, the TDR response of a cable with a joint at 5 km can be simulated to determine the required performance specifications of the pulse generator.

The reflected signal is shown in Fig. 5.1. According to the simulation results, the reflected signal of a joint at 5 km is extremely weak, with an amplitude of only 0.000147 times that of the injected signal. In practical measurement environments, the noise typically ranges from several tens to several hundreds of millivolts. Therefore, based on practical experience, the amplitude of the reflected signal should be no less than 0.5 V to ensure reliable detection of the reflected signal. Based on this requirement, the injected signal must exceed 3.4 kV to ensure that the reflected signal rises above the noise and can be effectively captured.

As shown in the simulation results in Fig. 5.1a, the amplitude of the reflected signal increases with the pulse width. However, when the pulse width exceeds 400 ns, the improvement in the reflection magnitude becomes insignificant. Therefore, the maximum output pulse width of the source should be set longer than 400 ns. Fig. 5.1b presents the simulation results of reflected signals from a joint located at 5 km, excited by pulses with varying rise times. It



(a) Injected signals with various pulse width (b) Injected signals with various rise time

Fig. 5.1 TDR simulation results of a cable with a joint at 5 km

can be observed that variations in rise time have little effect on the amplitude of the reflected signal. This is because the high-frequency components of the injected pulse are significantly attenuated as the signal propagates through the long cable, even if the rise time of the injected signal is very short. Thus, rise time is not a critical factor for improving reflection amplitude in long-distance detection. Nonetheless, rise time remains an important parameter for the TDR system. A shorter rise time improves the system's temporal resolution and enhances the accuracy of defect localization. Therefore, the rise time of the injected pulse should be made as short as possible. Based on these analyses, a HV pulse generator with an amplitude exceeding 3.4 kV, a continuously adjustable pulse width, and a maximum output pulse width greater than 400 ns must be developed to meet the requirements of long cable detection.

Design of the Pulse Generator

A HV negative pulse generator based on series-stacked MOSFETs is designed, which is driven by an active gate driver and can precisely control the pulse and has low isolation requirements. The pulse generator comprises a HV DC source, isolated drivers, a gate drive circuit, a switching circuit, and a control module. Its topology is shown in Fig. 5.2. In the figure, the source is a HV DC supply, which is controlled by a P-channel MOSFET M_{h} used to switch the HV DC on and off. The resistor R_{c} serves as a charging resistor to limit the inrush charging current, while the capacitor C_{c} stores energy for pulse generation. The MOSFETs M_1, M_2, ..., M_n are connected in series and function as the main switching elements for generating HV negative pulses. The components R_{b} and C_{b} form the buffer circuit, which limits the voltage slew rate and assists in dynamic voltage balancing during switching. The resistor R_{sv} serves as the static voltage balancing resistor to ensure uniform voltage distribution across the MOSFETs in the steady state. The isolated drivers serve to electrically isolate the control signals and supply isolated power to the active gate drivers. The gate drive circuit interfaces between the isolated drivers and the series-stacked MOSFETs to ensure proper switching control. The control module

manages the overall operation of the pulse generator, including the regulation of output pulse amplitude and width. The load is represented by the resistance R_{L}.

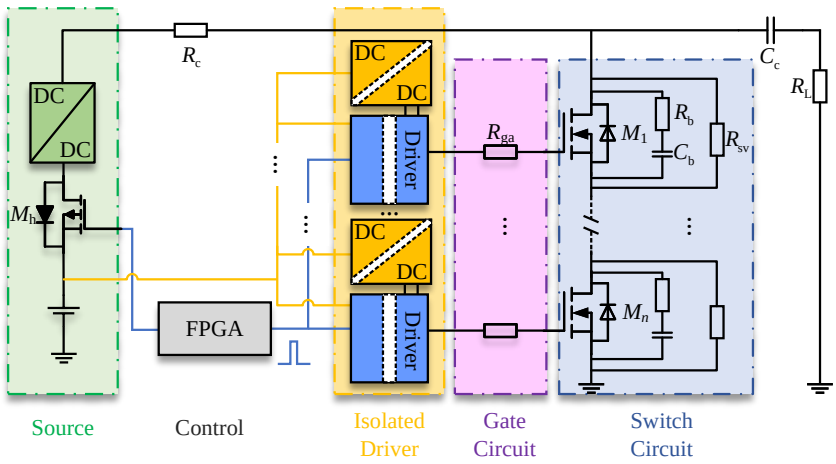
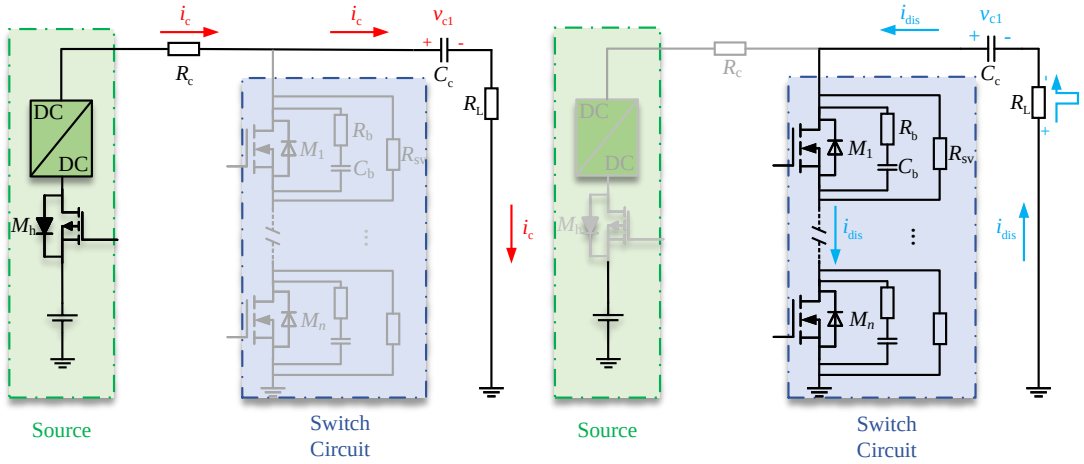


Fig. 5.2 Topology of the HV negative pulse generator

The pulse generator operates in two phases: the charging phase and the discharging phase. During the charging phase, the P-channel MOSFET M_{h} is turned on, while the series-stacked MOSFETs M_1, M_2, ..., M_n are turned off. In this state, the capacitor C_{c} is charged through the charging resistor R_{c} and the load resistor R_{L}. The circuit operation in the charging phase is illustrated in Fig. 5.3a. The operating state of the MOSFETs during the discharging phase is opposite to that in the charging phase. During the discharging phase, M_{h} is turned off and the series-stacked MOSFETs M_1, M_2, ..., M_n are turned on, allowing the capacitor C_{c} to discharge through the stacked MOSFETs and the load resistor R_{L}. As a result, a HV negative pulse is generated across the load resistor R_{L}. The circuit operation in the discharging phase is illustrated in Fig. 5.3b.



(a) Charging phase (b) Discharging phase

Fig. 5.3 Circuit of the pulse generator in charging and discharging phase

Selection of Key Components

In the HV pulse generator, the MOSFET is the most critical component. The component selection process begins with the MOSFETs, as they largely determine the performance of the system. To realize a pulse generator with continuously adjustable amplitude and pulse width, the selected MOSFETs must feature high breakdown voltage, fast switching speed, and low on-state resistance. In this design, the C3M0040120K SiC MOSFET from Wolfspeed is chosen as the switching device. This device has a breakdown voltage of 1200 V, a rise time of 17 ns, and a fall time of 9 ns. Its peak current capability is limited by junction temperature; however, for pulse widths shorter than 200 µs, the device can handle peak currents exceeding 160 A. Due to the short duration of the output pulses in this application, the peak current is not a limiting factor. The C3M0040120K also features an input capacitance of 2.9 nF, an output capacitance of 103 pF, and a reverse transfer capacitance of 5 pF. Due to the relatively large input capacitance of the MOSFETs, the gate driver must be capable of supplying high drive current. In this design, the UCC21520 from Texas Instruments is selected as the gate driver for the C3M0040120K. The UCC21520 is an isolated gate driver with an isolation voltage of 5.7 kV, and it can provide a source current of 4 A and a sink current of 6 A, which is sufficient to drive the selected MOSFETs. The typical gate-source voltage for the C3M0040120K is −4 V to 15 V. Therefore, a dual isolated power supply providing 15 V and −4 V is used to power the gate driver. The HV DC source is a commercial unit with a maximum output voltage exceeding 3.4 kV. An adjustable HV DC power supply with a maximum output of 5 kV is employed.

Based on the selected components, a HV pulse generator is designed. The circuit layout of the pulse generator is shown in Fig. 5.4.

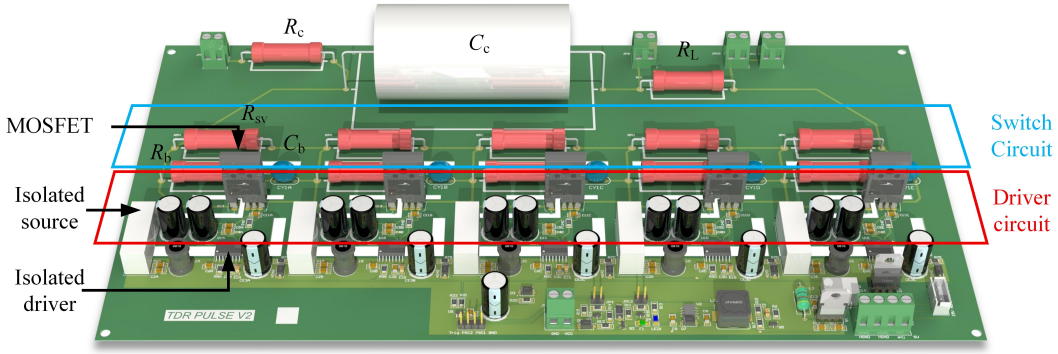


Fig. 5.4 Design circuit of the HV pulse generator

Determination of the Parameters of Basic Circuits

In the pulse generator shown in Fig. 5.2, the basic circuit consists of two main parts: the charging circuit and the static voltage balancing circuit. The charging circuit includes the HV

DC source, the charging resistor R_c, the storage capacitor C_c, and the equivalent load resistor R_L. The static voltage balancing circuit consists of the static balancing resistors R_{sv}. In the charging circuit, the selection of the charging resistor R_c primarily depends on the power rating and output voltage of the HV DC source. The maximum charging current i_{cmax} must satisfy the following condition:

$$i_{cmax} \leq \frac{P_{HVmax}}{V_{HVout}} \tag{5.1}$$

where P_{HVmax} is the maximum power rating of the HV DC source, and V_{HVout} is its output voltage. Since the equivalent load resistance R_L is much smaller than the charging resistor R_c, its influence on the charging process can be neglected. Therefore, the value of R_c can be selected according to the following criterion:

$$R_c \geq \frac{V_{HVout}}{i_{cmax}} \tag{5.2}$$

Given that the maximum power rating of the HV DC source is 5 W, the charging resistor R_c can be selected as 5 MΩ, and its voltage rating should exceed 5 kV.

The selection of the capacitor C_c mainly depends on the output pulse width and the allowable voltage drop during the discharging phase. The required pulse width is greater than 400 ns, while the designed maximum pulse width is 1 µs. Taking a 50 Ω load as an example, to ensure that the voltage drop is less than 10 % of the output voltage during a maximum output pulse width of 1 µs, the capacitance C_c can be calculated as follows:

$$e^{-\frac{t_w}{\tau_{dis}}} \geq 0.9 \tag{5.3a}$$

$$C_c = \frac{\tau_{dis}}{R_L} \tag{5.3b}$$

where t_w is the output pulse width and τ_{dis} is the discharging time constant. According to (5.3), the required capacitance C_c is greater than 189.75 nF. In this design, C_c is selected as 220 nF. The breakdown voltage of the capacitor should exceed 5 kV. Notably, under pulsed conditions, the partial discharge inception voltage is typically lower than the rated DC voltage of the capacitor. Therefore, a capacitor rated at 8 kV is selected for C_c to ensure reliable operation.

The selection of the static voltage balancing resistor R_{sv} is straightforward. The resistance of R_{sv} should satisfy the following equation:

$$R_{sv} \leq \frac{1}{10} R_{dsoff} \tag{5.4}$$

where R_{dsoff} is the off-state resistance of the MOSFETs. According to the datasheet of the C3M0040120K, the minimum value of R_{dsoff} is 24 MΩ. Therefore, the resistance of the static

voltage balancing resistor R_{sv} should not exceed 2.4 MΩ. If R_{sv} is too small, the static voltage balancing circuit may consume excessive power. R_{sv} is selected as 2 MΩ.

5.1.2 Signal Integrity Simulation and Parameter Optimization

In the design of the HV pulse generator, the buffer circuit and gate circuit must be carefully adjusted to ensure both the performance of the generator and the safe operation of the MOSFETs. The buffer circuit is used to limit the voltage slew rate ($\mathrm{d}v/\mathrm{d}t$) and suppress overvoltage on the drain-source voltage V_{ds} during switching transitions. The gate circuit controls the switching speed of the MOSFETs. Excessively fast switching may lead to V_{ds} overshoot and output pulse oscillations, while overly slow switching increases the rise and fall times of the output pulse. Therefore, the parameters of both the buffer circuit and gate circuit should be optimized by performing signal integrity simulations to balance the requirements of performance and device protection.

The signal integrity simulation is conducted using CST Studio Suite. The PCB layout of the HV pulse generator is first designed in Altium Designer and then imported into CST Studio Suite, which is shown in Fig. 5.5.

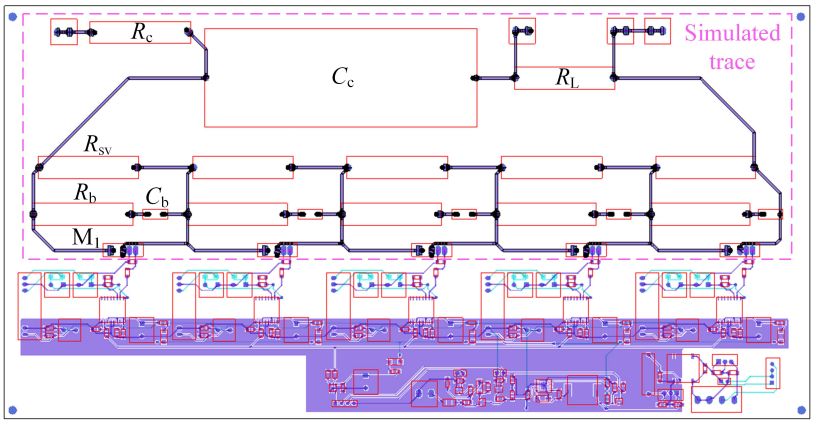
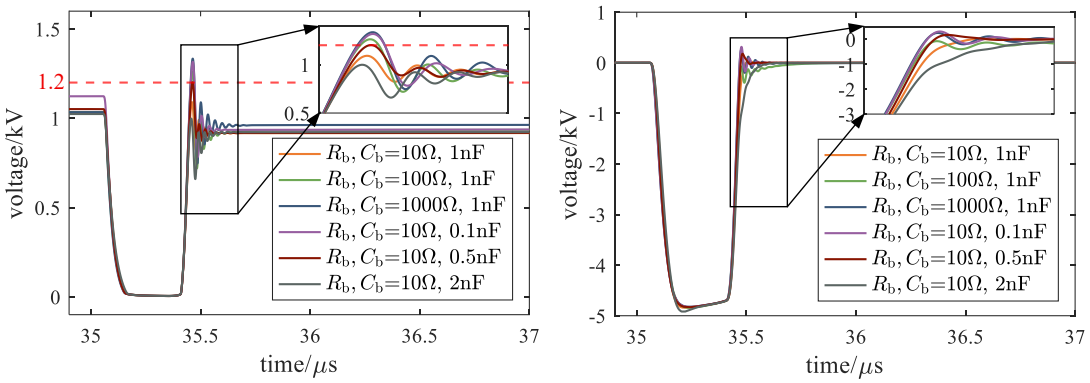


Fig. 5.5 PCB model of the HV pulse generator for signal integrity simulation

In CST, the parasitic parameters of the PCB are extracted, and a SPICE model of the PCB is generated. By combining this PCB SPICE model with the SPICE models of the components, a complete signal integrity simulation model of the HV pulse generator is established. As the parasitic parameters of the power supply circuit do not affect the output pulse shape, they are excluded from the simulation. To determine suitable parameters for the buffer circuit, simulations are performed under various buffer configurations. The results are shown in Fig. 5.6. Fig. 5.6a presents the simulated drain-source voltage V_{ds} of the MOSFET closest to the HV terminal under different buffer parameters. The results show that V_{ds} is influenced during MOSFET turn-off: increasing the buffer resistance R_b leads to higher V_{ds}, while increasing

the buffer capacitance C_b reduces V_{ds}. Given the breakdown voltage limit of the MOSFETs, V_{ds} must remain below 1200 V. Therefore, R_b is selected as 10 Ω, and C_b should be greater than 0.5 nF. Fig. 5.6b shows the output pulse waveform under different buffer parameters. The simulation results indicate that the buffer circuit significantly affects the fall time of the output pulse. When R_b is fixed at 10 Ω, reducing C_b from 2 nF to 1 nF shortens the fall time. Based on these results, R_b is selected as 10 Ω, and C_b is selected as 1 nF.



(a) V_{ds} (b) V_{out}

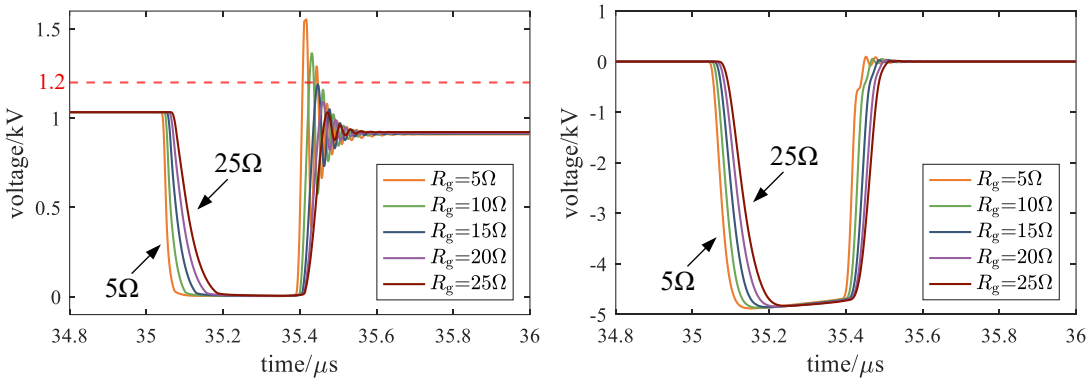
Fig. 5.6 Simulation of the HV pulse generator with various parameters of the buffer circuit

The gate circuit controls the switching speed of the MOSFETs by regulating the rise time of the gate–source voltage V_{gs}. V_{gs} is determined by the gate resistance R_{ga} and the gate capacitance C_{gs} of the MOSFET. To determine a suitable gate resistance R_{ga}, the pulse generator is simulated with various values of R_{ga}. The simulation results are shown in Fig. 5.7. As observed, increasing the gate resistance leads to longer rise and fall times of the output pulse. At the same time, the peak voltage of the V_{ds} oscillations during MOSFET turn-off decreases with increasing R_{ga}. According to the simulation results, a gate resistance greater than 15 Ω is required to ensure the safe operation of the MOSFETs. However, higher gate resistance also slows down the switching transitions. To balance fast switching performance with device safety, the gate resistance R_{ga} is ultimately selected as 20 Ω.

5.1.3 Experimental Testing and Performance Evaluation

Based on the above design, a prototype of the HV pulse generator was constructed and tested. The prototype is shown in Fig. 5.8.

The prototype HV pulse generator was validated experimentally, as shown in Fig. 5.9. Fig. 5.9a shows the measured drain-source voltages V_{ds} of the series-stacked MOSFETs under a 200 Ω load. All waveforms remain below 1200 V with no significant oscillations, indicating that each MOSFET operates within its safe operating area. The voltage distribution is well balanced, with minimal differences between devices. Fig. 5.9b presents output pulses with



(a) V_{ds} (b) V_{out}

Fig. 5.7 Simulation of the HV pulse generator with various parameters of the gate resistance

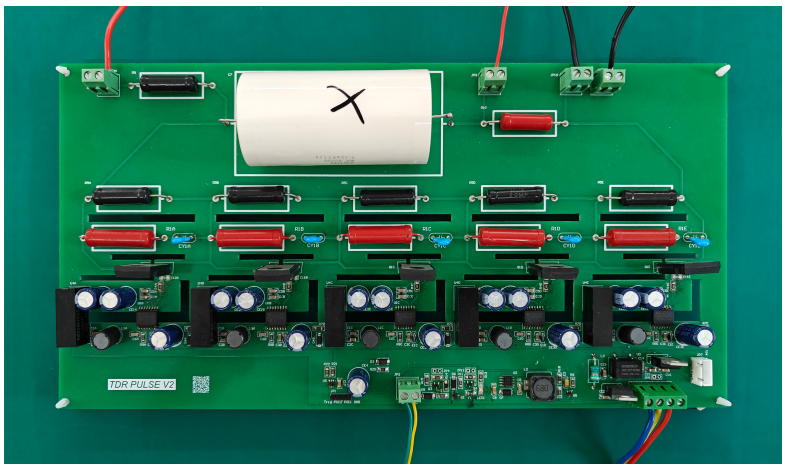
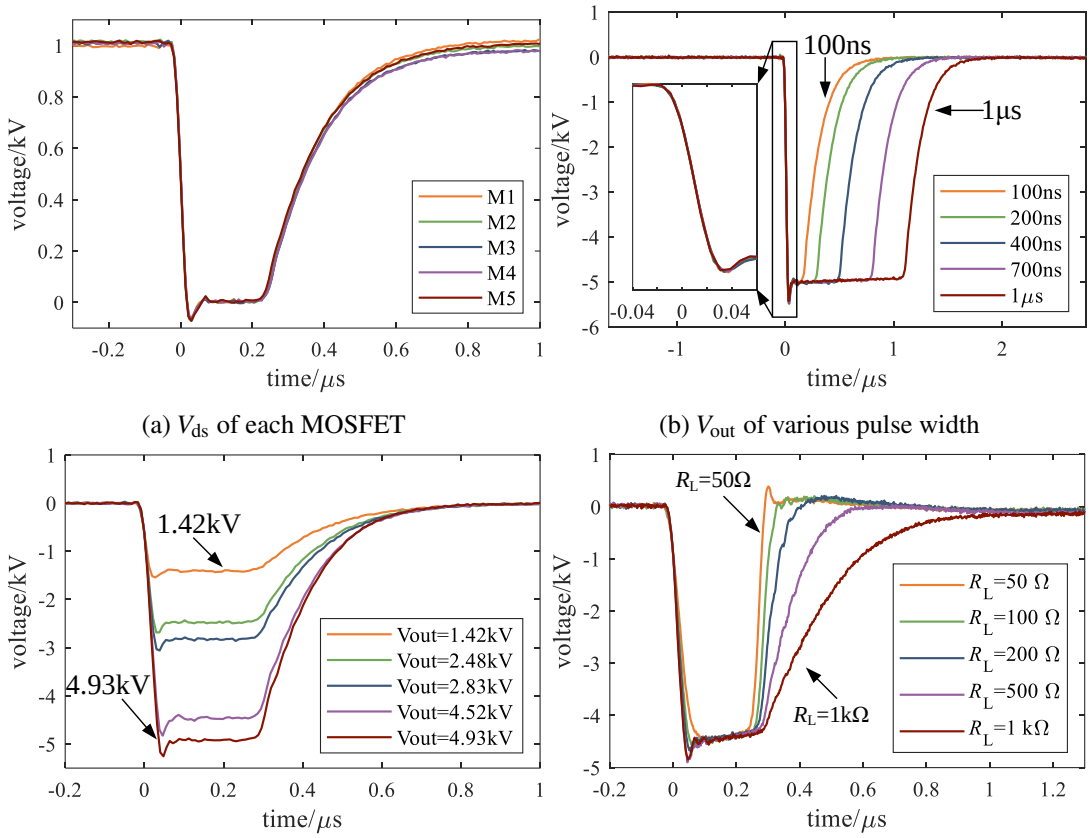


Fig. 5.8 Prototype of the HV pulse generator

different widths under the same load. The pulses exhibit sharp rising edges with a typical rise time of about 60 ns, and the pulse width is continuously adjustable from 100 ns to 1 µs. Even at the widest pulse, the voltage drop is only 3.27 %. Fig. 5.9c shows output pulses with different amplitudes, with a maximum output amplitude of 4.93 kV. Fig. 5.9d shows the output pulses under various load resistances. As the load resistance increases, the fall time of the output pulse also increases, indicating that the fall time is determined by the load resistance.

5.2 Fast-Switching Multiple-Ratio Voltage Divider

HV pulse generators significantly enhance the performance of TDR systems. However, as the amplitude of the injected pulse increases, measuring the TDR signal becomes more challenging. When a HV pulse is injected into the cable, the injected signal can be measured using a high-attenuation voltage divider. If the reflected signal has a relatively high amplitude, it can be measured through the same high-attenuation divider. However, if the reflected signal is



(a) V_{ds} of each MOSFET

(b) V_{out} of various pulse width

(c) V_{out} of various pulse magnitude

(d) V_{out} of various load resistance

Fig. 5.9 Test results of the HV pulse generator

significantly weak, it may become too small to be detect accurately after passing through a high-attenuation divider. Therefore, a fixed-ratio voltage divider is not suitable for measuring reflected signals with a wide range of amplitudes. To address this issue, a multi-ratio voltage divider is required.To enable dynamic selection of the appropriate division ratio at different time intervals during TDR measurements, it is essential for the multi-ratio voltage divider to have fast switching capability. As a result, a fast-switching multi-ratio voltage divider (FSMRVD) is designed.

5.2.1 Topology and Operational Principle of the FSMRVD

FSMRVD provides two primary functions: multi-ratio voltage division and fast switching. The multi-ratio voltage division is achieved by incorporating multiple voltage dividers with different division ratios. Fast switching is realized through a high-speed switching circuit. The overall topology of the FSMRVD is shown in Fig. 5.10. In the topology, VD1 to VD4 represent four RC voltage dividers with different division ratios. In each divider, R_{Hn} and R_{Ln} are the resistors in the HV and low-voltage (LV) arms, respectively. C_{Hn} and C_{Ln} are the corresponding compensation capacitors, used to extend the bandwidth of the voltage divider. AP1 to AP4

represent the active protection circuits, each protecting the low arm of a voltage divider. They consist of two series-connected MOSFETs in a back-to-back configuration. VF1 to VF4 represent the four voltage follower circuits that provide mutual isolation between the voltage dividers. FS1 to FS4 represent the fast switching circuits and share the same structure as the active protection circuit. The working procedure of the FSMRVD is as follows: when a voltage divider is selected for signal measurement, the corresponding active protection circuit is opened and the other active protection circuits are closed. The fast switching circuit corresponding to the selected divider is closed, while the others are opened.

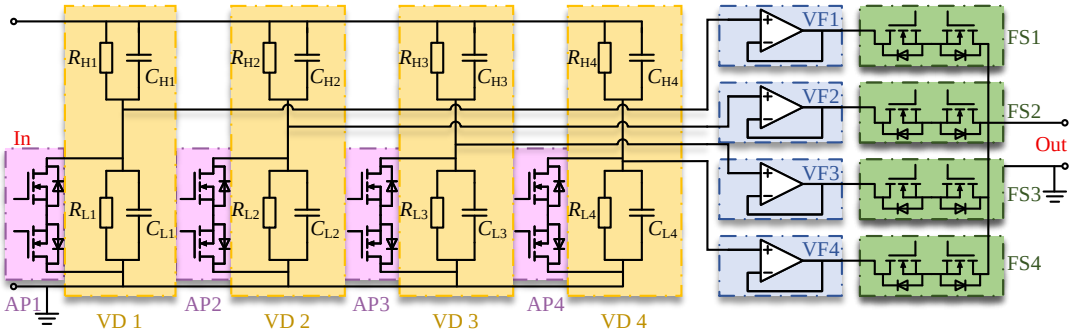


Fig. 5.10 Topology of the FSMRVD

Based on the above principle, the FSMRVD PCB model is designed and shown in Fig. 5.11. The PCB consists of five parts: the voltage divider circuit, active protection circuit, fast switching circuit, voltage follower circuit, and the required power supply circuit. The voltage divider section includes four RC dividers with different ratios. Their outputs are first connected to corresponding voltage follower circuits, and then routed through four fast switching circuits to the final output. To protect the LV arms of the dividers, four active protection circuits are implemented on the PCB. In both the active protection and fast switching circuits, back-to-back series-connected MOSFETs are used. Due to this configuration, isolated gate drivers and isolated power supplies are required to properly drive the MOSFETs.

5.2.2 Key Parameter Selection and System Implementation

To determine the required performance of the FSMRVD and select appropriate components, the characteristics of the measured signal must first be identified. As described in the previous section, the HV pulse generator can produce pulses with continuously adjustable amplitude and pulse width. The maximum output voltage is 5 kV, and the minimum rise time of the output pulse is approximately 60 ns. According to the relationship between rise time and bandwidth [111], the required bandwidth of the voltage divider can be calculated as follows:

$$f_{\mathrm{BW}} \geq \frac{0.35}{t_{\mathrm{r}}} \tag{5.5}$$

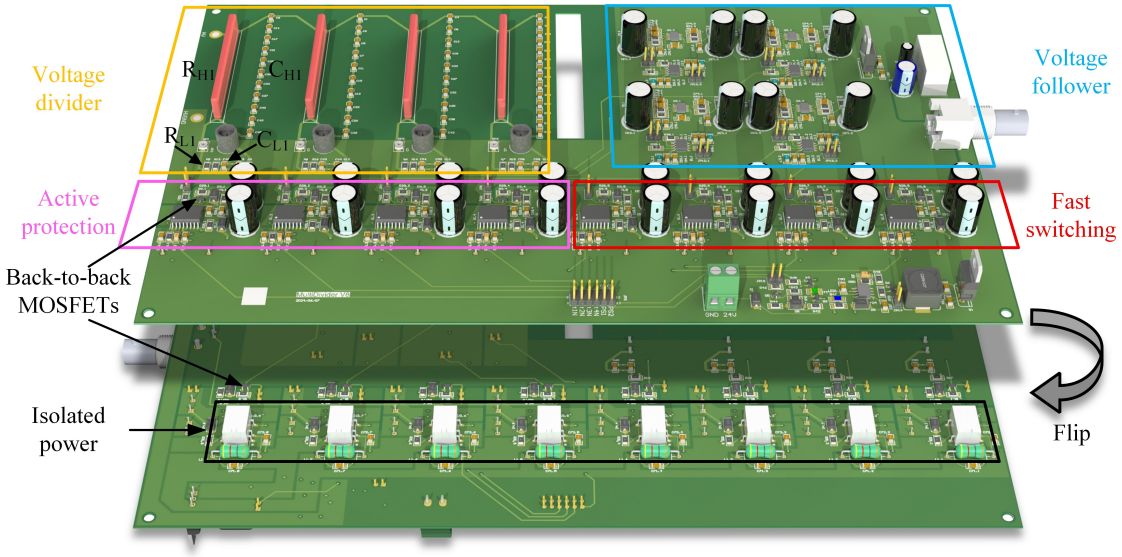


Fig. 5.11 PCB model of the FSMRVD

where f_{BW} is the required bandwidth of the voltage divider, and t_r is the rise time of the output pulse. To satisfy the requirement of HV pulse source, the bandwidth of the voltage divider should exceed 5.83 MHz. In addition to bandwidth, switching speed is another critical performance requirement for the FSMRVD. Since the joint detection is a common TDR application, the FSMRVD must be capable of switching fast enough to capture reflections from cable joints. Typically, joints in power cables are spaced at intervals of 300-500 m. The FSMRVD must complete the switching operation within the time window between reflections from adjacent joints. Based on the expected reflection time and joint spacing, the required switching time of the FSMRVD should be less than 3.5 µs.

Parameter Selection of the Voltage Divider

The voltage divider is an RC parallel voltage divider, in which the resistors and capacitors in the HV and LV arms satisfy the following relationships:

$$R_H = K_{VD} \cdot R_L \tag{5.6a}$$

$$C_L = K_{VD} \cdot C_H \tag{5.6b}$$

where R_H and C_H are the resistance and capacitance of the HV arm, R_L and C_L are those of the LV arm, and K_{VD} is the voltage division ratio. To achieve high resolution across a wide range of signal amplitudes, the voltage division ratios K_{VD} of the four voltage dividers are selected as 1/500, 1/100, 1/10, and 1/2, respectively.

To ensure sufficient bandwidth of the voltage divider, the capacitance of the HV arm C_H should be kept small. The bandwidth of the voltage divider can be calculated as follows [112]:

$$f_{BW} \approx \frac{1}{2\pi R_w C_H} \tag{5.7}$$

where f_{BW} is the bandwidth of the voltage divider, R_w is the resistance of the signal source under test, and C_H is the capacitance of the HV arm. In the TDR system, the connected cable typically has a characteristic impedance of 50 Ω, so the source resistance R_w is taken as 50 Ω. According to (5.7), the required capacitance C_H of the HV arm can be calculated as follows:

$$C_H \leq \frac{1}{2\pi R_w f_{BW}} \tag{5.8a}$$

Hence, the total capacitance of each HV arm C_H should be less than 545.6 pF.

The design procedure of the voltage divider is as follows, taking the 1/2 ratio divider as an example. If the resistance is too small, it leads to excessive power consumption, whereas an overly large resistance may cause DC offset issues in this application. Therefore, the resistance of the LV arm is commonly set to 1 MΩ. Due to the parasitic parameters of the MOSFETs in the active protection circuit, the operational amplifier in the voltage follower circuit, and the PCB itself, the LV arm has a minimum inherent capacitance. The output capacitance of the MOSFETs used in the LV circuit ranges from 10 to 50 pF. The input capacitance of the operational amplifier is usually on the order of a few tens of picofarads. Additionally, the parasitic capacitance of the PCB in the LV arm was measured to be approximately 25.9 pF using a LCR meter. Therefore, the equivalent capacitance of the LV arm C_L is estimated to be approximately 150 pF. According to (5.6), the resistance and capacitance of the HV arm R_H and C_H are determined to be 1 MΩ and 150 pF, respectively. The remaining three voltage dividers are designed using the same method. The final design parameters of the voltage dividers are summarized in Table 5.1.

Table 5.1 Designed parameters of the voltage dividers.

Voltage dividers	ratio	R_H/MΩ	C_H/pF	R_L/MΩ	C_L/pF
VD1	1:500	499	0.3	1	150
VD2	1:100	99	1.52	1	150
VD3	1:10	9	16.67	1	150
VD4	1:2	1	150	1	150

When selecting resistors and capacitors in HV arms, HV non-inductive components should be used in the HV arms. Flat glass glaze film resistors, capable of withstanding up to 20 kV, are selected as the HV resistors. However, due to limited available resistance values, the closest match to the design values is chosen. To maintain the desired voltage division ratio, the

resistance of the LV arm R_L is adjusted accordingly. The HV arm capacitors are composed of multiple capacitors connected in series. To precisely adjust the voltage division ratio, a tunable capacitor is included in the LV arm to fine-tune the total capacitance C_L. The parameters of the selected components are listed in Table 5.2. According to these parameters, the total capacitance of the HV arms C_H is 174 pF, which is below the upper limit of 545.6 pF, indicating that the design requirements for the voltage dividers are satisfied.

Table 5.2 Designed parameters of the voltage dividers.

Voltage dividers	ratio	R_H/MΩ	C_H	R_L/MΩ	C_L/pF
VD1	1:500	500	3.9 pF/11	1.002	150
VD2	1:100	100	15 pF/10	1.01	150
VD3	1:10	10	150 pF/10	1.11	150
VD4	1:2	1	2.2 nF/14	1	150

Components Selection of the Active Protection Circuit

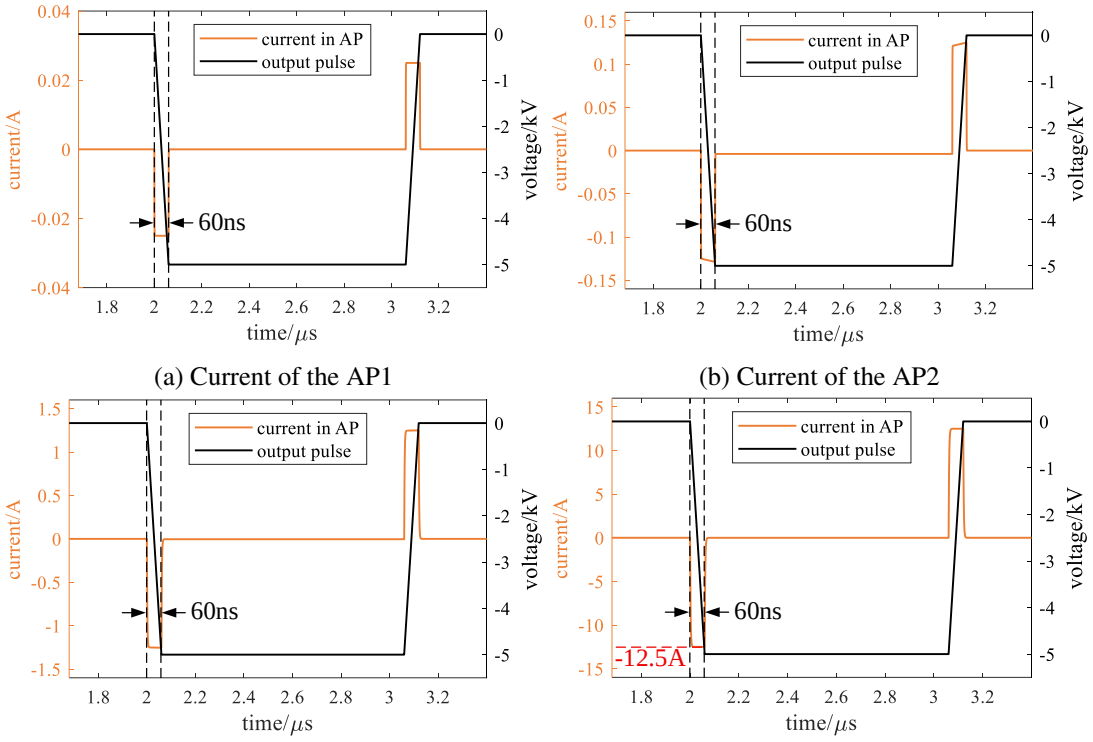
In the active protection circuit, MOSFETs are employed as switching devices. Under normal operating conditions, the voltage across the MOSFETs is theoretically less than 10 V, so breakdown voltage is not a critical parameter. Instead, to meet the bandwidth requirements of the voltage divider described above, the output capacitance of the MOSFETs must be minimized, making it a key selection criterion. Another important parameter is the drain current. When the active protection circuit is triggered, the MOSFETs conduct the current from each voltage divider. For dividers with low ratios, the current is relatively large. Therefore, the selected MOSFETs must have sufficiently high pulsed drain current ratings to ensure reliable operation.

Based on the component values listed in Table 5.2, the current through the MOSFETs in the active protection circuit is simulated under an injected pulse of 5 kV with a pulse width of 1 µs. The simulation results are shown in Fig. 5.12. As seen, the highest current occurs in the 1/2 ratio voltage divider, reaching 12.5 A. Therefore, the MOSFETs used in the active protection circuit should support a pulsed drain current exceeding 12.5 A.

Table 5.3 Required Parameters of MOSFETs in the Active Protection Circuit.

Parameters	Required Value	2N7002K
Drain-to-source voltage/V	≥ 10	60
Output capacitance/pF	≤ 50	8
Pulsed drain current (t_p=120 ns)/A	≥ 12.5	–

The required specifications for the MOSFETs used in the active protection circuit are summarized in Table 5.3. The 2N7002K MOSFET from ON Semiconductor is selected for this



(a) Current of the AP1

(b) Current of the AP2

(c) Current of the AP3

(d) Current of the AP4

Fig. 5.12 Current simulation results of the active protection circuits

application. The parameters of the selected device are also listed in Table 5.3. The drain-to-source breakdown voltage of the 2N7002K is 60 V, which meets the requirement of exceeding 10 V. Its output capacitance is 8 pF, well below the 50 pF threshold, making it suitable for maintaining the bandwidth of the voltage divider. The pulsed drain current of the selected MOSFET is not explicitly specified in the datasheet. However, it can be reasonably estimated from the effective transient thermal resistance $R_{\theta JC}$ curve provided therein. Based on the curve in the datasheet and the known thermal and electrical parameters, the pulsed drain current I_{DM} can be calculated as follows [113]:

$$I_{DM} = \sqrt{\frac{T_{Jmax} - 25\,^{\circ}C}{R_{\theta JC}(t_p) \times R_{DS(on)}^{T_{Jmax}}}} \tag{5.9}$$

where T_{Jmax} is the maximum junction temperature, specified as 150 °C in the datasheet. $R_{\theta JC}(t_p)$ denotes the effective transient thermal resistance corresponding to the pulse width t_p and is $0.279\,^{\circ}C\,W^{-1}$ for $t_p = 120$ ns. $R_{DS(on)}^{T_{Jmax}}$ is the drain-to-source on-resistance at T_{Jmax}, given as 1.91 Ω. Based on (5.9), the maximum pulsed drain current I_{DM} of the 2N7002K is calculated to be 15.32 A, which comfortably exceeds the required current of 12.5 A. Therefore, the 2N7002K can be safely employed in the active protection circuit without risking thermal or electrical overstress.

Selection of Op-Amp in the Voltage Follower Circuit

The voltage follower circuit is used to isolate different circuits, thereby reducing interference between them and eliminating the influence of the measurement device's input impedance. The output pulse ranges from $-10\,\mathrm{V}$ to $10\,\mathrm{V}$, so the output voltage swing of the operational amplifier must exceed this range. Since the resistance of the voltage divider's LV arm is approximately $1\,\mathrm{M\Omega}$, the op-amp should have a very high input impedance to ensure proper operation. Additionally, its input bias current should be very low to minimize DC offset in the voltage divider. The input signal has a bandwidth of $5.83\,\mathrm{MHz}$, so the op-amp's bandwidth must exceed this value. As the measured signal is a pulse, the slew rate is also a critical parameter. Based on the pulse amplitude and rise time, the required slew rate of the op-amp can be calculated as follows:

$$\mathrm{SR} \geq \frac{V_{\mathrm{out}}}{t_{\mathrm{r}}} \tag{5.10}$$

where V_{out} is the maximum amplitude of the output pulse from the voltage divider, and t_{r} is the rise time of the output pulse. Given the minimum rise time of $60\,\mathrm{ns}$, the required slew rate of the op-amp is calculated as $166.67\,\mathrm{V\,\mu s^{-1}}$. The required specifications for the op-amp used in the voltage follower circuit are summarized in Table 5.4. A Texas Instruments THS4631 is selected as the op-amp for this application, and its parameters are also listed in Table 5.4.

Table 5.4 Required Parameters of MOSFETs in the Active Protection Circuit.

Parameters	Required Value	THS4631
Output voltage swing/V	$\geq \pm 10$	± 13
Common-mode input resistance/MΩ	≥ 100	1000
Input bias current/pA	≤ 1000	100
Bandwidth/MHz	≥ 5.83	325
Slew rate/$\mathrm{V\,\mu s^{-1}}$	≥ 166.67	1000

The MOSFETs used in the fast switching circuit do not have stringent requirements; thus, the same MOSFETs as those used in the active protection circuit are selected. Other auxiliary circuits in the FSMRVD, such as the power supply circuit and the MOSFET driver circuit, are designed according to the system requirements. Two types of power supply circuits are employed in the FSMRVD: one is an isolated power supply for the MOSFET driver circuit; the other is a bipolar power supply for the op-amp in the voltage follower circuit.

5.2.3 Experimental Testing and Performance Evaluation

Based on the above design, a prototype of the FSMRVD was constructed, as shown in Fig. 5.13. To validate the design, the performance of circuit was experimentally tested.

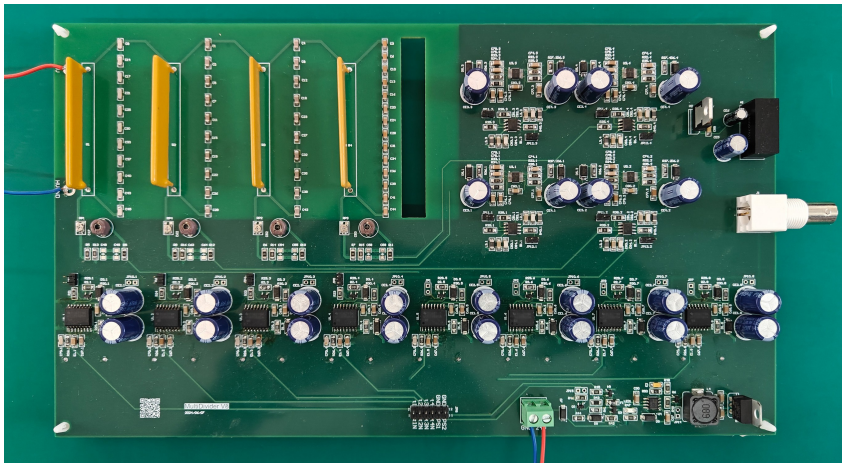


Fig. 5.13 Prototype of the FSMRVD

Bandwidth Test

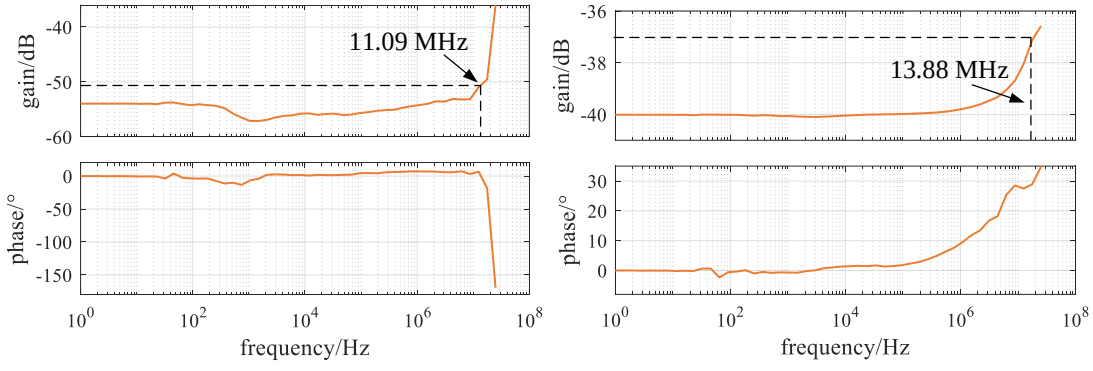
The bandwidth of the FSMRVD was evaluated by injecting sinusoidal signals of various frequencies and measuring the corresponding output responses. During the bandwidth test of VD*i*, the corresponding AP*i* is left open and FS*i* is closed, while all other APs are closed and all other FSs are open. Bandwidth test results are presented in Fig. 5.14, which shows the frequency response of the FSMRVD from 1 Hz to 25 MHz. VD1, with a voltage division ratio of 1:500, exhibits a bandwidth of approximately 11.09 MHz, while VD2, with a 1:100 ratio, achieves about 13.88 MHz. Both VD3 (1:10 ratio) and VD4 (1:2 ratio) demonstrate bandwidths exceeding 25 MHz.

The relatively lower bandwidths of VD1 and VD2 compared to VD3 and VD4 are primarily due to the smaller capacitance values in their HV arms, which make them more sensitive to the parasitic capacitance of the PCB. In addition, VD1 and VD2 are positioned on the far left of the PCB, while their corresponding access points (FS1, FS1) and the output terminals are on the right side. This spatial arrangement introduces greater parasitic inductance, further degrading their high-frequency performance. Nevertheless, the bandwidths of VD1 and VD2 exceed 5.83 MHz, satisfying the design requirements.

Switching Speed Test

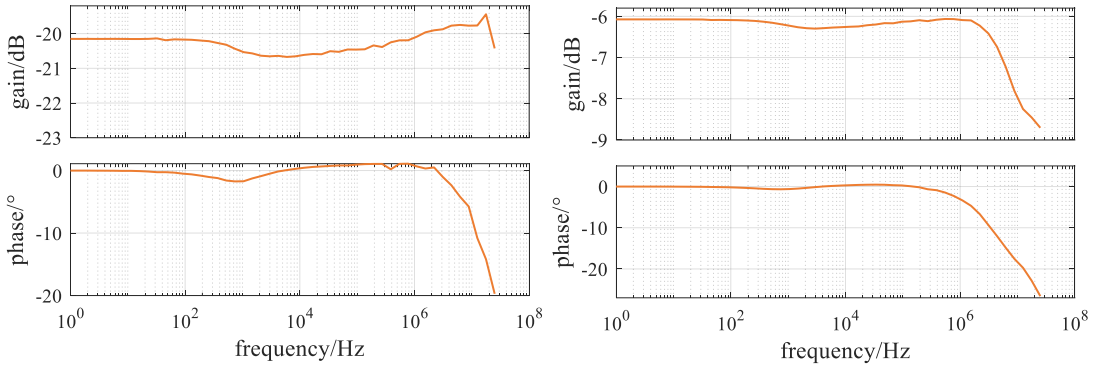
The switching speed of the FSMRVD was evaluated by measuring the time difference between the control signal and the output signal of the FSMRVD. During the switching speed test of AP*i* and FS*i*, a DC signal is applied across the LV arm of VD*i*, while all other APs are turned on and all other FSs are turned off as shown in Fig. 5.15.

The control signal is a pulse signal with a width of 200 ns. The measurement results of the control signal and the output signal of the FSMRVD are shown in Fig. 5.16. From the results,



(a) Frequency response of the VD1

(b) Frequency response of the VD2



(c) Frequency response of the VD3

(d) Frequency response of the VD4

Fig. 5.14 Bandwidth test results of FSMRVD

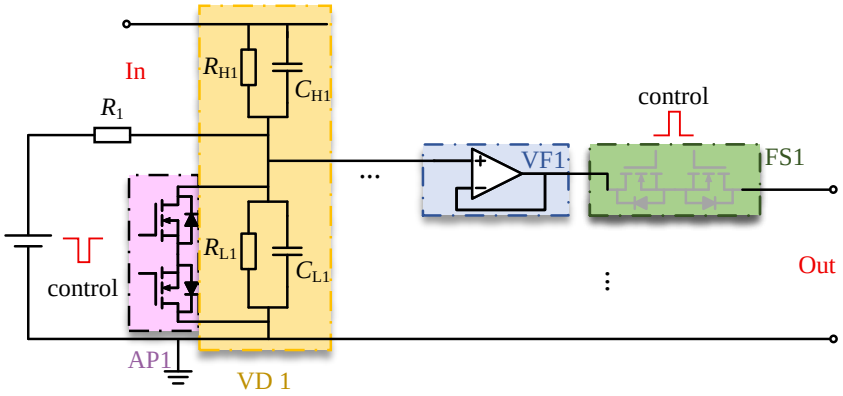


Fig. 5.15 Schematic of the switching speed test of the FSMRVD

it can be observed that the delay time t_D between the control signal and the output signal is approximately 70 ns, and the fall time t_f is approximately 13 ns. Therefore, to ensure the safety of the FSMRVD and the measurement device, the switching time t_{switch} between two voltage dividers should satisfy the following condition:

$$t_{switch} \geq t_D + t_f + t_{margin} \tag{5.11}$$

where t_{margin} is the safety margin time to protect the FSMRVD, and t_{margin} can be set to 50 ns. Therefore, the switching time of the FSMRVD should be greater than 133 ns.

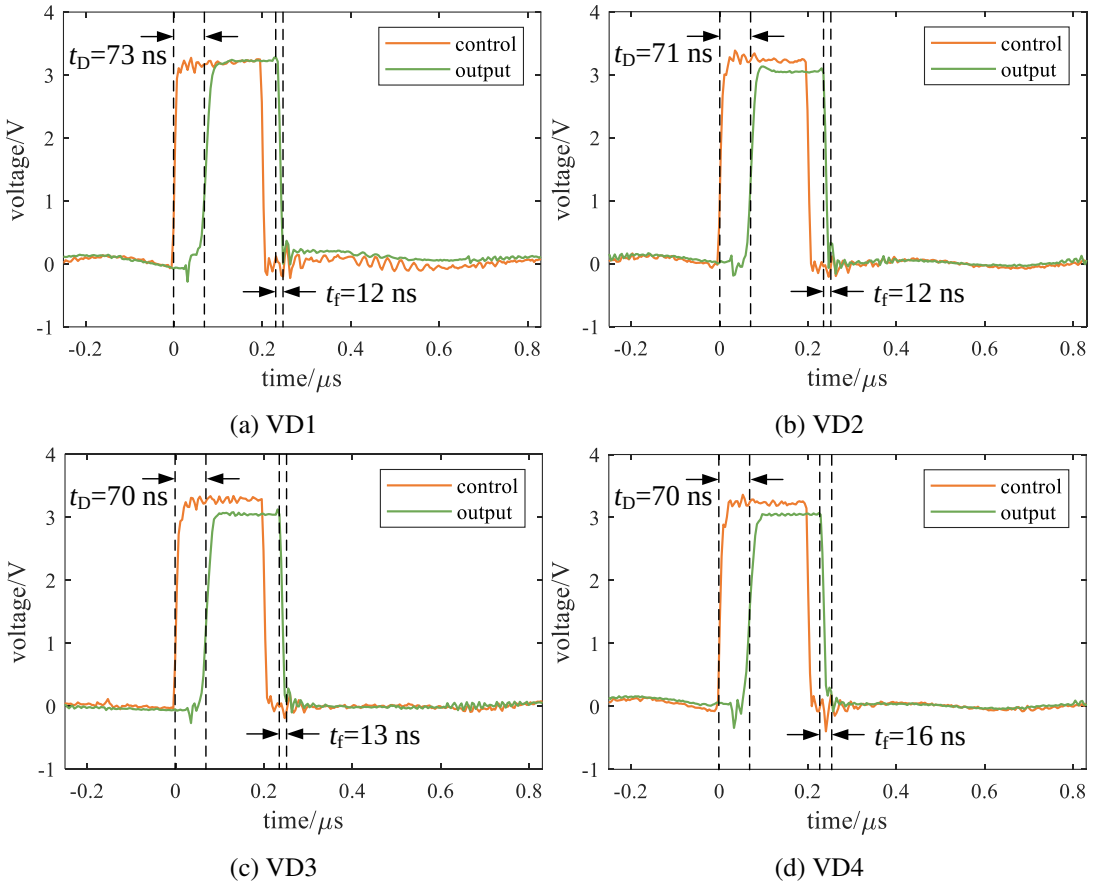


Fig. 5.16 Switching speed test results of the FSMRVD

5.3 Experimental Validation of HVFRS-TDR System

In the preceding sections, the HV pulse generator and the FSMRVD were independently designed, implemented, and experimentally validated. To evaluate the integrated functionality of the HVFRS-TDR system, an integration experiment was conducted. This experiment aimed to verify the coordination between the two components and demonstrate the overall operation of the system. Therefore, it was conducted in the laboratory using a coaxial signal cable as the test cable.

5.3.1 Experimental Platform and Testing Procedure

The experiment was conducted in the laboratory. In the experiment, the tested cable is an SYV-50 coaxial cable with a length of approximately 685 m. Three types of weak defects

were fabricated: Type 1—a series resistance of 1.5 Ω; Type 2—a ground defect of 1 kΩ; and Type 3—a ground defect of 4.3 kΩ. Three cases were tested in the experiment: Case 1—the cable with a 1.5 Ω series resistance defect at 535 m; Case 2—the cable with a 1 kΩ ground defect at 380 m and a 1.5 Ω series resistance defect at 535 m; and Case 3—the cable with a 4.3 kΩ ground defect at 380 m and a 1.5 Ω series resistance defect at 535 m. The defects were connected to the cable via SMA connectors. The details of the three cases are summarized in Table 5.5.

Table 5.5 Tested cases in the experiment

Case	Defect 1			Defect 2		
	Type	Parameter/Ω	Location/m	Type	Parameter/Ω	Location/m
Case 1	Series resistance	1.5	535	–	–	–
Case 2	Ground defect	1000	380	Series resistance	1.5	535
Case 3	Ground defect	4300	380	Series resistance	1.5	535

The measurement device is a PicoScope 5000D series oscilloscope, used to measure the output signal of the FSMRVD. A computer is employed to control both the HV pulse generator and the FSMRVD, as well as to process the measured data. The experimental platform is shown in Fig. 5.17. The tested cable consists of four sections: the first section is 180 m long, the second is 200 m, the third is 155 m, and the fourth is 130 m.

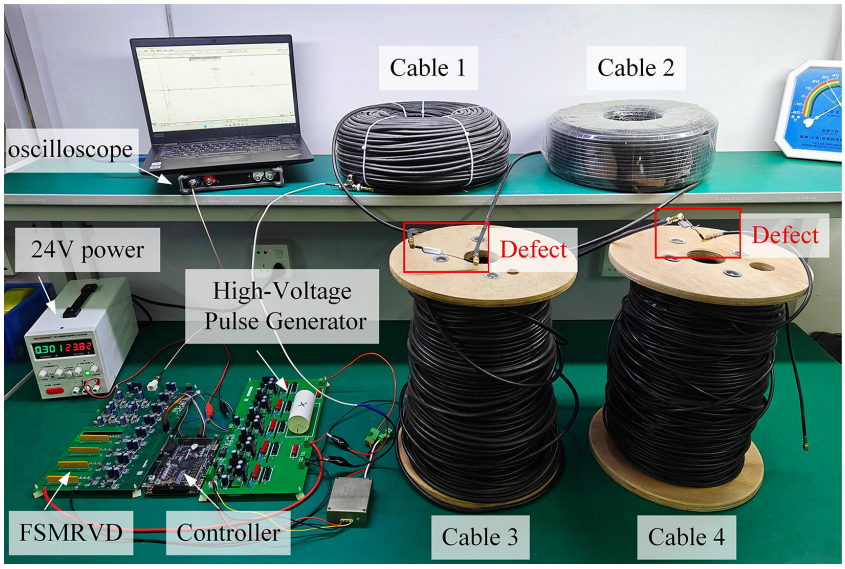


Fig. 5.17 Experiment platform of the HVFRS-TDR system

The operation procedure of the HVFRS-TDR system is as follows:

(1) **Set the parameters of the injected pulse.** The amplitude and pulse width of the injected pulse are configured via the computer.

(2) **Select the initial ratio of the FSMRVD.** The FSMRVD is initially set to a safe ratio such that the maximum output voltage remains below the safety threshold of the measurement device.

(3) **Measure the tested cable.** The cable is tested and the reflection signal is acquired.

(4) **Analyze the reflection signal and configure the switching time and ratio of the FSMRVD.** In the time interval where no obvious reflections are observed, a lower voltage division ratio is selected. The switching time and corresponding ratio are then configured.

(5) **Re-inject the pulse.** The HV pulse is injected into the tested cable again, and the reflection signal is measured again.

(6) **Repeat Steps 4 and 5 until the FSMRVD is set to the lowest ratio.**

Following the above procedure, the experiment is carried out. Due to the insulation limitation of the tested cable, the maximum output voltage of the HV pulse generator is limited to 800 V, and the pulse width is set to 200 ns.

5.3.2 Experimental Results and Analysis

The initial safety ratio of the FSMRVD is set to 1:100. For Case 1, the first measurement result is shown in Fig. 5.18. From the measurement results, an obvious reflection signal is observed at 6.6 µs, which corresponds to the reflection from the end of the cable. At other time instances, no significant reflection signals are observed.

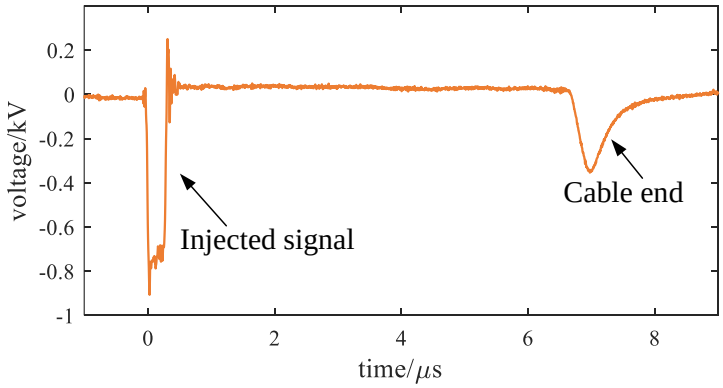


Fig. 5.18 The first measurement result of the Case 1

Therefore, the FSMRVD is set to the ratio of 1:10 from 3.9 µs to 6.3 µs, while maintaining a ratio of 1:100 at other times. The second measurement result is shown in Fig. 5.19. From

the results, it can be seen that the reflected signal within the interval from 3.9 µs to 6.3 µs is amplified, and an obvious reflection is observed at 5.4 µs, corresponding to the series resistance defect. Fig. 5.19 also compares the results obtained with and without the FSMRVD. It is evident that the FSMRVD significantly enhances the detection capability of the TDR system. The series resistance defect is only 1.5 Ω, with a reflection coefficient of just 0.0148, which is very small.

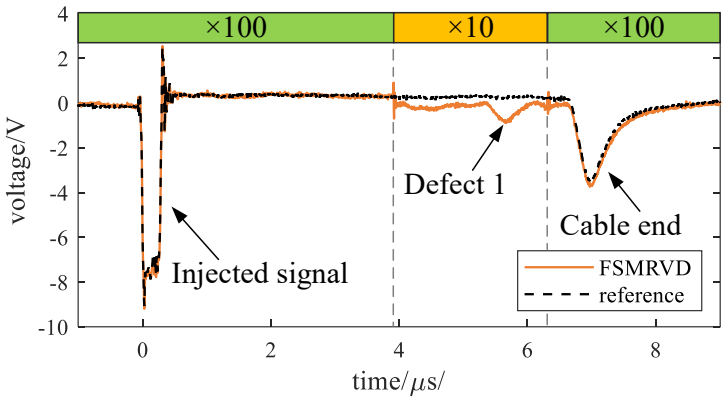


Fig. 5.19 The second measurement result of the Case 1

Cases 2 and 3 were tested using the same procedure. The first defects in both cases simulate high-resistance faults. By calculating the reflection coefficient of the ground defects, the first defect in Case 2 is found to have a reflection coefficient of −0.0224, and the first defect in Case 3 has a reflection coefficient of −0.0058. The measurement results of Cases 2 and 3 are shown in Fig. 5.20 and Fig. 5.21, respectively. Fig. 5.20 shows that, from 1.96 µs to 6.3 µs, the FSMRVD operates in the 1:10 voltage division mode. A reflection signal appears at 3.8 µs, corresponding to the 1 kΩ ground defect. Similarly, in Fig. 5.21, a reflection signal is observed at 3.8 µs, corresponding to the 4.3 kΩ ground defect. Both figures also compare the measurement results obtained with and without the FSMRVD. It can be clearly seen that without using the FSMRVD, it is difficult to identify the reflection signals of high-resistance faults.

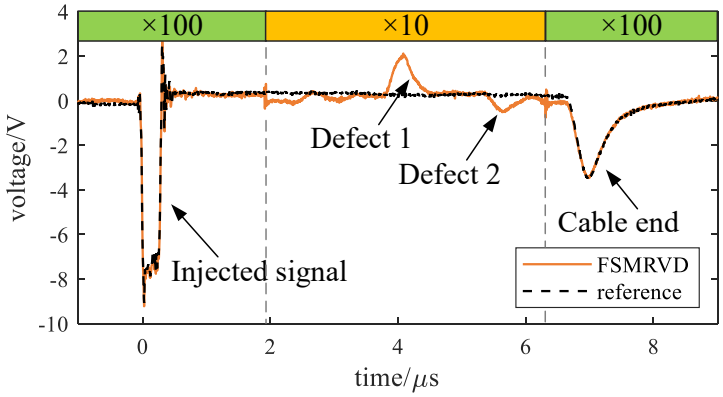


Fig. 5.20 The measurement result of the Case 2

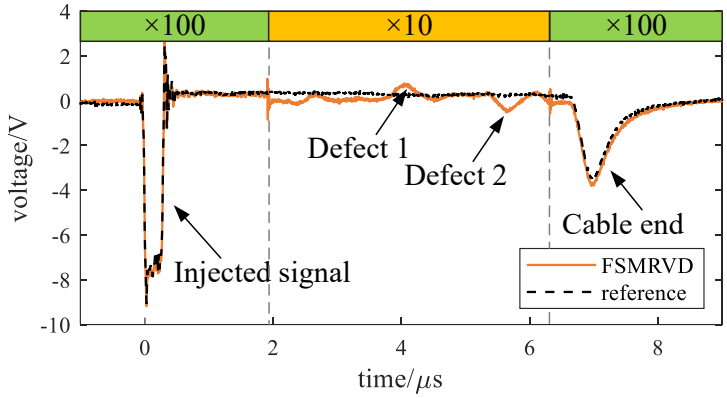


Fig. 5.21 The measurement result of the Case 3

Using the TVMF method described in Section 3.2, the defects in Case 1, Case 2, and Case 3 were successfully located. The localization results are summarized in Table 5.6. As shown in the table, the maximum localization error in the experiment is 1.2 %. These results demonstrate that, with the assistance of the TVMF method, the HVFRS-TDR system is capable not only of effectively detecting small defects in long cables, but also of accurately locating them.

Table 5.6 Localization results of defects in three test cases.

Case	Defect 1			Defect 2		
	l_{f1}/m	Reference/m	Error/%	l_{f2}/m	Reference/m	Error/%
Case 1	538.8	535	0.71	–	–	–
Case 2	384.7	380	1.2	538.1	535	0.65
Case 3	377.5	380	0.66	540.2	535	0.97

Based on the measurement results of Case 1, Case 2, and Case 3, it can be concluded that the HVFRS-TDR system significantly enhances the detection capabilities of conventional TDR by combining HV pulse injection with an FSMRVD. The HV pulse injection increases the amplitude of the reflected signals from weak defects, while the FSMRVD improves the visibility of week reflected signals. Overall, the HVFRS-TDR system provides a practical and effective solution for detecting weak defects in long cables.

5.4 Summary

In this chapter, a HVFRS-TDR system is developed for detecting defects in multiple-defect cables. The system consists of a HV pulse generator and a FSMRVD. The HV pulse generator adopts a series-stacked MOSFET configuration to generate HV pulses with continuously adjustable amplitude and pulse width. Its maximum output voltage is 4.93 kV, with a rise

time of 60 ns and a voltage drop of less than 5 % over a 1 µs pulse width. The FSMRVD uses MOSFETs to switch among voltage dividers with ratios of 1:500, 1:100, 1:10, and 1:2, extending the dynamic range of the measurement system. It can switch ratios within 133 ns and has a minimum bandwidth of 11.09 MHz. Experimental validation demonstrates that the HVFRS-TDR system can effectively detect defects in multiple-defect cables, enhance improve the visibility of weak reflected signals and improve the detectable range of the TDR system.

Chapter 6

Conclusions and Future Work

6.1 Conclusions

To address the limitations of traditional cable TDR techniques in multi-defect detection, localization, and severity estimation, a high-voltage pulse injection and fast range switching TDR system is designed, a multiple-defect identification and localization method based on pulse reconstruction is proposed, and a quantitative evaluation method for defect severity based on double-frequency TFDR is developed. These methods are developed through a series of theoretical derivations, and their effectiveness is verified through simulations and scaled experiments. The research results primarily address the challenges of long-distance and multiple-defect detection in cable TDR, and they have important theoretical and practical significance for ensuring the safe and reliable operation of power cables. With the expansion of distributed cable networks, the importance of this research becomes increasingly prominent. The main contributions of this work are summarized as follows:

(1) Cable joints and defects were modeled, and their propagation characteristics were analyzed. Using the distributed-parameter method and FEM simulation, it is found that the characteristic impedances of cable joints, shield corrosion defects, shield hole defects, and series resistance defects are higher than those of intact cables, whereas those of ground defects and water ingress defects are lower. The combination of reflection waveform and characteristic impedance can be used to distinguish different defect types.

(2) To address the challenge of simulating reflection signals in multiple-defect cables, a general simulation method based on the RCS was proposed. Using transmission line theory and the cascading of two-port networks, the RCS of a cable with multiple defects was derived. The time-domain reflection signal under various excitation conditions was then obtained via the TDFD method. The RCS approach incorporates accurate frequency-dependent models of both

cables and defects, enabling precise calculation of reflected signals while fully accounting for their propagation characteristics. This provides a solid theoretical foundation for TDR reflection analysis.

(3) A pulse reconstruction method was proposed to address the interference caused by multiple reflections in TDR-based detection of multiple-defect cables. The method combines TVMF for accurate defect localization with a defect parameter estimation algorithm, enabling sequential localization and parameter estimation of defects. The TVMF provides high localization accuracy and strong anti-noise capability, effectively suppressing the influence of attenuation, dispersion, and multiple reflections. By reconstructing the reflected pulses and eliminating multiple reflections, the method can effectively separate, identify, and locate multiple defects. Simulations and experiments validated its effectiveness and accuracy. The results demonstrated that the proposed method accurately identified the number of defects in the cables, with a maximum localization error of 1.13 %. Overall, this method effectively prevents misjudgment of defect numbers caused by multiple reflections and accurately reveals the spatial distribution of multiple defects in cables.

(4) The double-frequency TFDR method was proposed for the quantitative evaluation of defect severity. It performs two TFDR measurements, where the second injected signal has a center frequency one octave higher than the first. By decoupling the effects of characteristic impedance and the physical size of defects, the method can estimate the equivalent resistance of lumped defects and the physical dimensions of distributed defects. Using the equivalent resistance and physical size, defect severity can be quantitatively evaluated. The method was validated through simulations and experiments, demonstrating that the characteristic impedances of defects and the physical sizes of short distributed defects with lengths ranging from about ten centimeters to several meters can be accurately estimated. From the experimental results, the maximum estimation error of defect characteristic impedance was 2.4 %, and the maximum error of defect length was 11.23 %. The double-frequency TFDR approach provides an effective and practical solution for the quantitative assessment of cable defect severity.

(5) An HVFRS-TDR system was developed for multiple-defect cable detection with an extended measurement range. The system integrates a high-voltage pulse source and a fast-switching multi-ratio voltage divider. Compared with conventional TDR systems, it can generate pulses with amplitudes ranging from 0 to 4.93 kV and pulse widths from 200 ns to 1 μs, thereby extending the propagation distance of injected signals and improving the SNR of reflected signals. The voltage divider can rapidly switch between four different ratios within 133 ns to ensure the visibility of reflected signals with varying amplitudes. The combination of high-voltage pulse injection and fast range switching significantly enhances the measurement capability of TDR, providing a reliable and effective solution for long-distance and multiple-defect cable detection.

6.2 Future Work

To further enhance the capabilities of TDR-based cable diagnostics, several directions for future research and development are identified:

(1) Conducting more on-site experiments for validating the proposed method on combined cable defects. Real cable defects often have more complex structures, as they may combine multiple defect types with complicated propagation characteristics. To ensure reliable validation, appropriate signal pre-processing techniques, such as baseline removal and de-noising, will be required.

(2) Identification of combination defects using deep learning. Some defects in cables are not single-type defects, but rather consist of multiple coexisting defect types, such as water ingress coupled with corrosion or mechanical damage. These defect types may interact and influence the overall reflection characteristics in complex ways, making accurate detection more challenging. Deep learning models can be trained to recognize these intricate patterns and interactions, enabling the identification of combination defects that traditional methods may fail to detect.

(3) Developing online double-frequency TFDR monitoring systems. Due to high-frequency signal injection, TFDR can be applied for online measurement, and this system integrates TFDR technology with online signal injection and measurement to enable periodic acquisition of reflected signals. The evolution of defects can be monitored by comparing measurement results at different times. This approach would greatly improve the reliability and maintainability of cables.

References

[1] Shu-Ran Liu and Konstantinos Kopsidas. Risk-based underground cable circuit ratings for flexible wind power integration. *IEEE Transactions on Power Delivery*, 36(1):145–155, February 2021.

[2] Peng Chi. *Research on fault state diagnosis andcondition assessment of 10 kV cable based on data driven*. PhD thesis, China University of Mining and Technology, Xu Zhou, 2022.

[3] 2024 annual report on electric power reliability in china. Technical report, National Energy Administration, Beijing, March 2025.

[4] Electric Power Research Institute. Failure rates of underground cable systems. Accessed: 2025-06-26.

[5] Yi-Feng Zhao. *Modeling study on discharge-to-breakdown evolution at the insulation interface of 10 kV cable joints*. PhD thesis, South China University of Technology, Guang Zhou, 2024.

[6] Guo-Chang Li, Xiao-Jian Liang, Jia-Hao Zhang, Xue-Jing Li, Yan-Hui Wei, Chun-Cheng Hao, Qing-Quan Lei, and Sheng-Tao Li. Insulation properties and interface defect simulation of distribution network cable accessories under moisture condition. *IEEE Transactions on Dielectrics and Electrical Insulation*, 29(2):403–411, April 2022.

[7] Power cables with extruded insulation and their accessories for rated voltages from 1 kV (um=1.2 kV) up to 35 kV (um=40.5 kV) – part 2: cables for rated voltages from 6 kV (um=7.2 kV) up to 30 kV (um=36 kV), 2020.

[8] IEEE guide for field testing of shielded power cable systems using very low frequency (VLF) (less than 1 Hz), 2013.

[9] Yi Lu, Yuan-Xiang Zhou, Xiao-Long Huang, Dang-Guo Xu, Wen-Peng Li, Peng Zhao, Ya-Mei Li, and Yan-Feng Gao. AC and DC withstand voltage tests in commissioning test procedure designed for ±535 kV HVDC cable. In *2025 7th Asia Energy and Electrical Engineering Symposium (AEEES)*, pages 271–274, Chengdu, March 2025. IEEE.

[10] Li Wang, Sai-Ke Yang, Xiao-Kai Guo, Ting-Xi Sun, Hong-Jie Li, Hong-Xiao Wu, and Bao-Feng Nan. Development of a compact very low frequency cosine-rectangular and damped alternating current voltage generator for insulation testing of medium-voltage power cables. *IET Generation, Transmission & Distribution*, 14(26):6450–6456, December 2020.

[11] Sai-Ke Yang, Li Wang, Xiao-Kai Guo, Ting-Xi Sun, Yu-Xin Lu, Yuan Yan, and Hong-Jie Li. Implementation of a novel very low frequency cosine-rectangular voltage generator for insulation testing of power cables. *IEEE Transactions on Power Electronics*, 36(7):7679–7692, July 2021.

[12] Yuan Yan, Riccardo Trinchero, Igor Simone Stievano, and Hong-Jie Li. Implementation of adaptive partial discharge denoising in resource-limited embedded systems via efficient time-frequency matrix factorization. *IEEE Transactions on Instrumentation and Measurement*, 73:1–13, March 2024.

[13] Rong Li, Kai Zhou, Xianjie Rao, Min Xie, Hao Yuan, Jianbo Xiang, and Zikang Wang. Localization of damp defects and analysis of moisture characteristics for cable body in the distribution grid. *Zhongguo Dianji Gongcheng Xuebao/Proceedings of the Chinese Society of Electrical Engineering*, 42(9):3470–3479, May 2022.

[14] Meng-Xin Zhu, Fang-Zhou Shi, Li Wang, Jun-Bai Chen, Yuan Yan, Xin Xia, and Hong-Jie Li. Measuring the dissipation factor of capacitive equipment under damped ac voltage. *IEEE Transactions on Instrumentation and Measurement*, 73:1–12, January 2024.

[15] IEEE guide for detection, mitigation, and control of concentric neutral corrosion in medium-voltage underground cables, 2007.

[16] Cynthia M. Furse, Moussa Kafal, Reza Razzaghi, and Yong-June Shin. Fault diagnosis for electrical systems and power networks: a review. *IEEE Sensors Journal*, 21(2):888–906, January 2021.

[17] Paul Smith, Cynthia Furse, and Jacob Gunther. Analysis of spread spectrum time domain reflectometry for wire fault location. *IEEE Sensors Journal*, 5(6):1469–1478, December 2005.

[18] Wafa Ben Hassen, Nicolas Ravot, Antoine Dupret, Armando Zanchetta, Freddy Morel, Laurent Pillon, Nicolas Imbert, Nicolas Boisrivent, and Charles Chuc. OMTDR-based embedded cable diagnosis for mutliple fire zones detection and location in aircraft engines. In *2017 IEEE SENSORS*, pages 1–3, Glasgow, October 2017. IEEE.

[19] Jian Guo Zhang, Hang Xu, Bing Jie Wang, Li Liu, Peng Cheng Su, and Jing Xia Li. Wiring fault detection with boolean-chaos time-domain reflectometry. *Nonlinear Dynamics*, 80(1):553–559, January 2015.

[20] Fabrice Auzanneau. Natural amplification of soft defects signatures in cables using binary time domain reflectometry. *IEEE Sensors Journal*, 21(2):937–944, January 2021.

[21] Y. Shin, E. Powers, T. Choe, C. Hong, E. Song, J. Yook, and J. Park. Application of time-frequency domain reflectometry for detection and localization of a fault on a coaxial cable. *IEEE Transactions on Instrumentation and Measurement*, 54(6):2493–2500, December 2005.

[22] Cynthia Furse and Nilesh Kamdar. An inexpensive distance measuring system for navigation of robotic vehicles. *Microwave and Optical Technology Letters*, 33(2):84–87, March 2002.

[23] C. Furse, You Chung Chung, R. Dangol, M. Nielsen, G. Mabey, and R. Woodward. Frequency-domain reflectometery for on-board testing of aging aircraft wiring. *IEEE Transactions on Electromagnetic Compatibility*, 45(2):306–315, May 2003.

[24] Pedro J. Medelius and Howard J. Simpson. Non-intrusive impedance-based cable tester, December 1999.

[25] P. Tsai, Chet Lo, You Chung Chung, and C. Furse. Mixed-signal reflectometer for location of faults on aging wiring. *IEEE Sensors Journal*, 5(6):1479–1482, December 2005.

[26] Mostafa Kamel Smail, Lionel Pichon, Marc Olivas, Fabrice Auzanneau, and Marc Lambert. Detection of defects in wiring networks using time domain reflectometry. *IEEE Transactions on Magnetics*, 46(8):2998–3001, August 2010.

[27] Shekoufeh Abdollahi, Somayyeh Chamaani, and Jurgen Sachs. Time-domain reflectometry for measuring scattering parameters: comparison of m-sequence device and step-generator TDR. In *2020 14th European Conference on Antennas and Propagation (EuCAP)*, pages 1–5, Copenhagen, March 2020. IEEE.

[28] Zhi-Qiang Zhou, Dan-Dan Zhang, Jun-Jia He, and Meng-Hu Li. Local degradation diagnosis for cable insulation based on broadband impedance spectroscopy. *IEEE Transactions on Dielectrics and Electrical Insulation*, 22(4):2097–2107, August 2015.

[29] Chet Lo and Cynthia Furse. Noise-domain reflectometry for locating wiring faults. *IEEE Transactions on Electromagnetic Compatibility*, 47(1):97–104, February 2005.

[30] Ola Breien and Inge Johansen. Attenuation of travelling waves in single-phase high-voltage cables. *Proceedings of the Institution of Electrical Engineers*, 118(6):787, June 1971.

[31] L. M. Wedepohl and D. J. Wilcox. Transient analysis of underground power-transmission systems. system-model and wave-propagation characteristics. *Proceedings of the Institution of Electrical Engineers*, 120(2):253, January 1973.

[32] Peter van der Wielen. *On-line detection and location of partial discharges in medium-voltage power cables*. PhD thesis, Eindhoven University of Technology, Eindhoven, 2005.

[33] Zi-Jian Wang, Kai Zhou, Guang-Ya Zhu, Zhong-Ying Liang, Zi-Kang Wang, and Yao Fu. Moisture diagnosis method for cold-shrinkable intermediate joints of distribution cables based on time-frequency domain conversion. *High Voltage Engineering*, 48(6):2178–2186, June 2022.

[34] Y. Norouzi, S. Braun, C. Frohne, S. Seifi, and P. Werle. Effect of cable joints on frequency domain analysis. In *2018 IEEE Conference on Electrical Insulation and Dielectric Phenomena (CEIDP)*, pages 288–292, Cancún, October 2018. IEEE.

[35] Yu-Xiao Hu, Lu Chen, Ying Liu, and Yang Xu. Principle and verification of an improved algorithm for cable fault location based on complex reflection coefficient spectrum. *IEEE Transactions on Dielectrics and Electrical Insulation*, 30(1):308–316, February 2023.

[36] Yuhui Yu. Research on the localization of power cable joints based on frequency-domain reflectometry. Master's thesis, Huazhong University of Science and Technology, Wuhan, 2023.

[37] Yan Li, Peter A. A. F. Wouters, Paul Wagenaars, Peter C. J. M. van der Wielen, and E. Fred Steennis. Power cable joint modelin high frequency. In *2012 IEEE International Conference on Condition Monitoring and Diagnosis*, pages 76–79, Bali, September 2012. IEEE.

[38] Zuo-Xin Tang, Kai Zhou, Ye-Fei Xu, and Jing-Tao Huang. Cable defect length and type identification method based on frequency-domain reflectometry signal attenuation strength evaluation. *Insulating Materials*, 57(08):130–137, July 2024.

[39] Laurent Sommervogel. Various models for faults in transmission lines and their detection using time domain reflectometry. *Progress In Electromagnetics Research C*, 103:123–135, June 2020.

[40] Li-Xin Wang, Kai-Xing Chang, Gang Zhang, Xin He, and Xin Xin. Multiple faults location and evaluation in shielded cable based on joint analysis of reflection coefficient spectrum and matched filter matrix. *IEEE Transactions on Industrial Electronics*, 71(11):14977–14987, November 2024.

[41] G. Chen, S. Sun, D. Pommerenke, J. Drewniak, G. Greene, R. McDaniel, A. Belarbi, and H. Mu. Crack detection of a full-scale reinforced concrete girder with a distributed cable sensor. *Smart Materials and Structures*, 14(3):S88–S97, May 2005.

[42] Jim Jun Guo and Steven A. Boggs. High frequency signal propagation in solid dielectric tape shielded power cables. *IEEE Transactions on Power Delivery*, 26(3):1793–1802, July 2011.

[43] Clayborne Taylor and Charles Harrison. On the excitation of a coaxial line by an incident field propagating through a small aperture in the sheath. *IEEE Transactions on Electromagnetic Compatibility*, EMC-15(3):127–131, August 1973.

[44] G. Cerri, R. De Leo, and V. M. Primiani. "Thermic end-fire" interstitial applicator for microwave hyperthermia. *IEEE Transactions on Microwave Theory and Techniques*, 41(6):1135–1142, July 1993.

[45] C. Buccella, M. Feliziani, and G. Manzi. Identification and localization of defects in shielded cables by a numerical/experimental procedure. In *2003 IEEE Symposium on Electromagnetic Compatibility*, pages 213–218, Istanbul, August 2003. IEEE.

[46] W. Ben Hassen and M. Kafal. Shielding damage characterization in twisted pair cables using M-based reflectometry and inverse problems. In *2019 PhotonIcs & Electromagnetics Research Symposium - Spring (PIERS-Spring)*, pages 3093–3101. IEEE, June 2019.

[47] Evert Frederik Steennis. *The behaviour of water trees in extruded cable insulation*. PhD thesis, Delft University of Technology, Netherlands, 1989.

[48] Y. Ohki, Y. Ebinuma, and S. Katakai. Space charge formation in water-treed insulation. *IEEE Transactions on Dielectrics and Electrical Insulation*, 5(5):707–712, October 1998.

[49] Xiao Ma, Kang-Le Li, Kai Zhou, Yuan Li, and Ke-Rong Huang. PDC branch parameter characteristics of water tree aged cables based on the microstructural characteristics of water trees. *High Voltage Engineering*, 48(2):716–723, February 2022.

[50] Gavita Mugala, Roland Eriksson, and Per Pettersson. High frequency characteristics of water-tree degraded XLPE insulation in power cables. *IEEE Transactions on Dielectrics and Electrical Insulation*, 14(5):1271–1277, October 2007.

[51] Kai Zhou, Ming Huang, Wen-Biao Tao, Min He, and Ming-Liang Yang. A possible water tree initiation mechanism for service-aged XLPE cables: conversion of electrical tree to water tree. *IEEE Transactions on Dielectrics and Electrical Insulation*, 23(3):1854–1861, June 2016.

[52] F. H. Kreuger, M. G. Wezelenburg, A. G. Wiemer, and W. A. Sonneveld. Partial discharge. xviii. errors in the location of partial discharges in high voltage solid dielectric cables. *IEEE Electrical Insulation Magazine*, 9(6):15–22, November 1993.

[53] Reinoud Sleeman and Torild van Eck. Robust automatic p-phase picking: an on-line implementation in the analysis of broadband seismogram recordings. *Physics of the Earth and Planetary Interiors*, 113(1–4):265–275, June 1999.

[54] Jochen H. Kurz, Christian U. Grosse, and Hans-Wolf Reinhardt. Strategies for reliable automatic onset time picking of acoustic emissions and of ultrasound signals in concrete. *Ultrasonics*, 43(7):538–546, June 2005.

[55] P. Wagenaars, P. A. A. F. Wouters, P. C. J. M. Van Der Wielen, and E. F. Steennis. Accurate estimation of the time-of-arrival of partial discharge pulses in cable systems in service. *IEEE Transactions on Dielectrics and Electrical Insulation*, 15(4):1190–1199, August 2008.

[56] Redy Mardiana and Charles Su. Partial discharge location in power cables using a phase difference method. *IEEE Transactions on Dielectrics and Electrical Insulation*, 17(6):1738–1746, February 2010.

[57] Yong-June Shin, Eun-Seok Song, Joo-Won Kim, Jin-Bae Park, Jong-Gwan Yook, and Edward J. Powers. Time-frequency domain reflectometry for smart wiring systems. In *2002 International Symposium on Optical Science and Technology*, page 86, Washington, December 2002. SPIE.

[58] TokSon Choe, Ki-Seok Kwak, Yong-June Shin, Jin Bae Park, and Tae Sung Yoon. The load impedance measurement in the time-frequency domain reflectometry system. In *2005 IEEE Instrumentationand Measurement Technology Conference Proceedings*, pages 497–500, Ottawa, May 2005. IEEE.

[59] A. M. Bruckstein and T. Kailath. Inverse scattering for discrete transmission-line models. *SIAM Review*, 29(3):359–389, September 1987.

[60] Ching-Wen Hsue and Te-Wen Pan. Reconstruction of nonuniform transmission lines from time-domain reflectometry. *IEEE Transactions on Microwave Theory and Techniques*, 45(1):32–38, January 1997.

[61] M.K. Smail, H.R.E.H. Bouchekara, L. Pichon, H. Boudjefdjouf, and R. Mehasni. Diagnosis of wiring networks using particle swarm optimization and genetic algorithms. *Computers & Electrical Engineering*, 40(7):2236–2245, October 2014.

[62] Simon Blum, Michael Ulrich, and Bin Yang. A continuous cost function for the reconstruction of wired networks from reflection measurements. In *2017 25th European Signal Processing Conference (EUSIPCO)*, pages 2551–2555, Kos, August 2017. IEEE.

[63] Chun-Kwon Lee and Yong-June Shin. Detection and assessment of I&C cable faults using time–frequency r-cnn-based reflectometry. *IEEE Transactions on Industrial Electronics*, 68(2):1581–1590, February 2021.

[64] C. Ho, W. Lee, and Y. Hung. Signature representation of underground cables and its applications to cable fault diagnosis. In *1993 2nd International Conference on Advances in Power System Control, Operation and Management (APSCOM-93)*, pages 861–865, Hong Kong, December 1993.

[65] Chun-Kwon Lee, Gu-Young Kwon, and Yong-June Shin. Condition assessment of I&C cables in nuclear power plants via stepped-frequency waveform reflectometry. *IEEE Transactions on Instrumentation and Measurement*, 68(1):215–224, January 2019.

[66] Gu-Young Kwon, Chun-Kwon Lee, and Yong-June Shin. Diagnosis of shielded cable faults via regression-based reflectometry. *IEEE Transactions on Industrial Electronics*, 66(3):2122–2131, March 2019.

[67] L. A. Griffiths, R. Parakh, C. Furse, and B. Baker. The invisible fray: a critical analysis of the use of reflectometry for fray location. *IEEE Sensors Journal*, 6(3):697–706, June 2006.

[68] Andrea Cozza and Lionel Pichon. Echo response of faults in transmission lines: models and limitations to fault detection. *IEEE Transactions on Microwave Theory and Techniques*, 64(12):4155–4164, December 2016.

[69] Anthony Manet, Abelin Kameni, Florent Loete, Jerome Genoulaz, Lionel Pichon, and Odile Picon. Equivalent circuit model of soft shield defects in coaxial cables using numerical modeling. *IEEE Transactions on Electromagnetic Compatibility*, 59(2):533–536, April 2017.

[70] Xu Hua, Li Wang, and Yao-Jia Zhang. Analysis and diagnosis of shielded cable faults based on finite-element method and time-reversal time-frequency domain reflectometry. *IEEE Transactions on Industrial Electronics*, 69(4):4205–4214, April 2022.

[71] Xing-Yu Zou, Hai-Bao Mu, Hao-Tian Zhang, Lan-Qing Qu, Yi-Fan He, and Guan-Jun Zhang. An efficient cross-terms suppression method in time–frequency domain reflectometry for cable defect localization. *IEEE Transactions on Instrumentation and Measurement*, 71:1–10, April 2022.

[72] Manfred Bawart, Massimo Marzinotto, and Giovanni Mazzanti. A deeper insight into fault location on long submarine power cables. *e & i Elektrotechnik und Informationstechnik*, 131(8):355–360, December 2014.

[73] Manfred Bawart, Massimo Marzinotto, and Giovanni Mazzanti. Diagnosis and location of faults in submarine power cables. *IEEE Electrical Insulation Magazine*, 32(4):24–37, July 2016.

[74] Andrea Cataldo, Egidio De Benedetto, Antonio Masciullo, and Giuseppe Cannazza. A new measurement algorithm for TDR-based localization of large dielectric permittivity variations in long-distance cable systems. *Measurement*, 174:109066, April 2021.

[75] Ren-Yu Zhang, Chang-Yu Chen, and Chang-Zhang Wang. *High voltage testing technology*. Tsinghua University Press, Beijing, 2009.

[76] Ren-Yu Zhang. *High voltage testing technology*. Tsinghua University Press, Beijing, 2003.

[77] Woongje Sung and B. J. Baliga. On developing one-chip integration of 1.2 kV SiC mosfet and JBS diode (JBSFET). *IEEE Transactions on Industrial Electronics*, 64(10):8206–8212, October 2017.

[78] A. Chaney and R. Sundararajan. Simple mosfet-based high-voltage nanosecond pulse circuit. *IEEE Transactions on Plasma Science*, 32(5):1919–1924, October 2004.

[79] Yong-Gang Wang, Qian-Rong Bian, Zi Li, and Song Jiang. Research of high-voltage pulse generator based on marx circuit and pulse transformer. *IEEE Transactions on Plasma Science*, 53(6):1250–1257, June 2025.

[80] Lei Pang, Tian-Jun Long, Kun He, Yong-Rui Huang, and Qiao-Gen Zhang. A compact series-connected SiC mosfets module and its application in high voltage nanosecond pulse generator. *IEEE Transactions on Industrial Electronics*, 66(12):9238–9247, December 2019.

[81] Robert Moller, Jan Vocke, Artur Muhlbeier, and Ralf Puffer. Development of a test bench for the investigation of the breakdown voltage of insulation materials at medium frequency rectangular voltages. *IEEE Transactions on Power Electronics*, 36(3):2621–2628, March 2021.

[82] Hyun-Bin Jo, Jae-Beom Ahn, Woo-Cheol Jeong, Joo-Young Lee, Min-Kyu Choi, and Hong-Je Ryoo. Compact design of 40 kV 100 A high-voltage pulsed-power modulator for driving x-band magnetrons. *IEEE Transactions on Power Electronics*, 38(6):7598–7609, June 2023.

[83] Ya-Lu Shao, Jian Wang, Cun-Suo Pang, and Yan Han. High-resolution acquisition design method for large dynamic signals. *Journal of Transducer Technology*, 35(02):148–153, February 2022.

[84] G. Small, A. Budovsky, I.and Gibbes, and J. Fiander. Precision three-stage 1000 V/50 Hz inductive voltage divider. *IEEE Transactions on Instrumentation and Measurement*, 54(2):600–603, April 2005.

[85] S. Mašlán and M. Šíra. Design and characterisation of 1 kV multirange resistive voltage divider. In *Proceedings of the 25th IMEKO TC4 International Symposium and 23rd International Workshop on ADC and DAC Modelling and Testing*, pages 57–62, Brescia, September 2022. IMEKO TC-4, IMEKO.

[86] Clayton R. Paul. *Analysis of multiconductor transmission lines*. IEEE, New York, 2007.

[87] David M. Pozar. *Microwave engineering: theory and techniques*. John wiley & sons, Hoboken, 2021.

[88] Emad S. Ibrahim. Corrosion control in electric power systems. *Electric Power Systems Research*, 52(1):9–17, October 1999.

[89] Clayton R. Paul. *Inductance: loop and partial*. John Wiley & Sons, 2011.

[90] IEEE guide for assessment, mitigation, and control of corrosion of metallic shields for extruded dielectric cables rated 5 kV to 46 kV, 2022.

[91] Jian-Ming Jin. *Theory and computation of electromagnetic fields*. Wiley–IEEE, Hoboken, 2010.

[92] Rong Li, Kai Zhou, Hang Wan, Min Xie, Li Liu, Xian-Jin Wang, and Xiao Ma. Moisture location of 10 kV cable joints in medium voltage distribution grid based on frequency domain reflection. *Dianwang Jishu/Power System Technology*, 45(2):825–832, February 2021.

[93] Klaehn W. Burkes, Elham B. Makram, and Ramtin Hadidi. Water tree detection in underground cables using time domain reflectometry. *IEEE Power and Energy Technology Systems Journal*, 2(2):53–62, June 2015.

[94] Gavita Mugala. *High frequency characteristics of medium voltage XLPE power cables*. PhD thesis, KTH Royal Institute of Technology, Stockholm, 2005.

[95] Joel P. Dunsmore. *Handbook of microwave component measurements: with advanced vna techniques*. John Wiley & Sons, Ltd, Hoboken, 2012.

[96] Joel Dunsmore, Ning Cheng, and Yong-Xun Zhang. Characterizations of asymmetric fixtures with a two-gate approach. In *77th ARFTG Microwave Measurement Conference*, Baltimore, June 2011. IEEE.

[97] R. Papazyan and R. Eriksson. Calibration for time domain propagation constant measurements on power cables. *IEEE Transactions on Instrumentation and Measurement*, 52(2):415–418, April 2003.

[98] A. Cataliotti, A. Daidone, and G. Tine. Power line communication in medium voltage systems: characterization of mv cables. *IEEE Transactions on Power Delivery*, 23(4):1896–1902, October 2008.

[99] Mourad Barkat. *Signal detection and estimation*. Artech, Boston, 2005.

[100] Saeed V. Vaseghi. *Advanced digital signal processing and noise reduction*. John Wiley & Sons, Hoboken, February 2008.

[101] Boualem Boashash. *Time-frequency signal analysis and processing*. Academic Press, Oxford, second edition edition, 2016.

[102] Jay Karhade, Shaswati Dash, Samit Kumar Ghosh, Dinesh Kumar Dash, and Rajesh Kumar Tripathy. Time–frequency-domain deep learning framework for the automated detection of heart valve disorders using pcg signals. *IEEE Transactions on Instrumentation and Measurement*, 71:1–11, March 2022.

[103] Geon Seok Lee, Gu-Young Kwon, Su Sik Bang, Yeong Ho Lee, Seung Jin Chang, Song-Ho Sohn, Kijun Park, and Yong-June Shin. Time–frequency-based insulation diagnostic technique of high-temperature superconducting cable systems. *IEEE Transactions on Applied Superconductivity*, 26(4):1–5, June 2016.

[104] Su Sik Bang, Seung Hyun Yoon, Yeong Ho Lee, Yun Mook Lim, and Yong-June Shin. Local corrosion monitoring of prestressed concrete strand via time-frequency domain reflectometry. In *2018 International Conference on Diagnostics in Electrical Engineering (Diagnostika)*, pages 1–4, Pilsen, September 2018. IEEE.

[105] Eunseok Song, Yong-June Shin, Philip E. Stone, Jing-Jiang Wang, Tok-Son Choe, Jong-Gwan Yook, and Jin Bae Park. Detection and location of multiple wiring faults via time–frequency-domain reflectometry. *IEEE Transactions on Electromagnetic Compatibility*, 51(1):131–138, February 2009.

[106] Bai-Xiao Chen. *Modern radar system analysis and design*. Xidian University Press, Xi'an, 2012.

[107] Wei Zhang. *Detection and localization of partial discharge in distribution cables under damped AC voltage and its application*. PhD thesis, Xi'an Jiaotong University, Xi'an, 2014.

[108] Stéphane Mallat. *A wavelet tour of signal processing*. Academic Press, San Diego, 2 edition, 1999.

[109] Emanuele Borgonovo. *Global sensitivity analysis*. Springer International Publishing, Cham, 2017.

[110] Saike Yang. *Study on improving the sensitivity of partial discharge detection and the accuracy of localization in on-site oscillating wave tests for distribution cables*. PhD thesis, Xi'an Jiaotong University, Xi'an, 2022.

[111] Howard Johnson. *High speed digital design: a handbook of black magic*. Pearson Education India, Noida, 1993.

[112] Adel S. Sedra, Kenneth C. Smith, Tony Chan Carusone, and Vincent Gaudet. *Microelectronic circuits*. Oxford University Press, Oxford, 8 edition, 2020.

[113] John Wallace. Using M transient thermal impedance curves in your design. Application Note ZHCADJ1, Texas Instruments, 2023.

Achievements

Papers:

1. **Zhao K**, Grivet-Talocia S, Manfredi P, et al. Size assessment of power cable shield corrosion defects using double-frequency time-frequency-domain reflectometry[J].IEEE Transactions on Instrumentation and Measurement, 2025, 74: 1-11. (SCI:001445070100015; EI:20251017981917).

2. **Zhao K**, Grivet-Talocia S, Manfredi P, et al. Detection and evaluation of shield damage defects in power cables using an improved dual-frequency time-frequency domain reflectometry[J]. Energies. 2025, 18(19): 1-15. (SCI:001593626800001; EI:20254319369077).

3. **Zhao K**, Wang T T, Chen J B, et al. A method to assess shield corrosion sizes in cable defects detection based on time-frequency domain reflectometry[C]//Proc. 7th Asia Conf. Energy and Electr. Eng. (ACEEE), Chengdu, China, 2024, pp. 62-68. (EI:20243817048934).

4. Zhang M, **Zhao K**, Yan Y, et al. A double-terminal traveling-wave-based method using novel noncontact sensors for fault location in transmission cable lines[J].IEEE Access, 2021, 9: 80797-80805.(SCI:000673898600001; EI:20212310472834).

5. **Zhao K**, Grivet-Talocia S, Manfredi P, et al. Multiple Defect Detection in Time-Domain Reflectometry for Power Cable Based on Time-Varying Matched Filtering and Reflected Pulse Reconstruction[J]. IEEE Transactions on Instrumentation and Measurement. (under review).

Patents:

1. Li H J, **Zhao K**, Chen J B, et al. A cable shield breakage and damage-size detection method, system, device and storage medium based on double-frequency measurement and stepwise evaluation method: China, ZL202411565675.0[P].

2. Li H J, **Zhao K**, Chen J B, et al. A measurement device and detection method of multiple defects in power cables based on pulse reconstruction: China, ZL202510379316.4[P].

3. Li H J, **Zhao K**, Chen J B, et al. A Cable Defect Identification and Localization Method and Device Based on Time-Varying Matched Filtering: China, ZL202510366715.7[P].